# Réduction du bruit de photon à l'aide d'un asservissement sur des faisceaux jumeaux produits par un oscillateur paramétrique optique

Jérome Mertz

DEPARTEMENT DE PHYSIQUE

DE L'ECOLE NORMALE SUPERIEURE

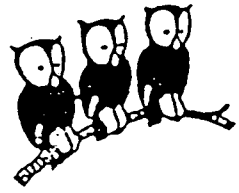

**Thèse de Doctorat de l'Université Pierre et Marie Curie**

Spécialité : Physique Quantique

*présentée par*

**Jerome MERTZ**

*pour obtenir le titre de Docteur de l'Université Pierre et Marie Curie*

*Sujet :*

# REDUCTION DU BRUIT DE PHOTON A L'AIDE D'UN ASSERVISSEMENT SUR DES FAISCEAUX JUMEAUX PRODUITS PAR UN OSCILLATEUR PARAMETRIQUE OPTIQUE

soutenue le 12 Novembre 1991 devant le jury composé de :

M. B. CAGNAC (président)
M. I. ABRAM
M. G. CAMY
M. C. FABRE
M. P. GRANGIER
M. P. KUMAR

**DEPARTEMENT DE PHYSIQUE**
**DE L'ECOLE NORMALE SUPERIEURE**

**Thèse de Doctorat de l'Université Pierre et Marie Curie**

spécialité : Physique Quantique

*présentée par*

**Jerome MERTZ**

*pour obtenir le titre de Docteur de l'Université Pierre et Marie Curie*

# REDUCTION DU BRUIT DE PHOTON A L'AIDE D'UN ASSERVISSEMENT SUR DES FAISCEAUX JUMEAUX PRODUITS PAR UN OSCILLATEUR PARAMETRIQUE OPTIQUE

# PHOTON NOISE REDUCTION USING ACTIVE CONTROL ON TWIN BEAMS GENERATED BY AN OPTICAL PARAMETRIC OSCILLATOR

soutenue le 12 Novembre 1991 devant le jury composé de :

M. B. CAGNAC (Président)
M. I. ABRAM
M. G. CAMY
M. C. FABRE
M. P. GRANGIER
M. P. KUMAR

Je remercie Jacques Dupont-Roc de m'avoir accueilli au Laboratoire de Spectroscopie Hertzienne de l'E.N.S. et permis de passer trois années à Paris qui s'avérèrent très agréables, ainsi que Claude Fabre et Elisabeth Giacobino pour m'avoir invité dans leur groupe d'optique "vraiment" quantique, et pour avoir dirigé ce travail de thèse. En particulier, je remercie Claude pour son aide considérable à la rédaction de la thèse et pour m'avoir souvent secouru lors de problèmes administratifs.

Je remercie Antoine Heidmann pour sa patience et sa perspicacité vraisemblablement illimitées. Son assistance et son soutien constants furent à la base d'une majeure partie de cette thèse, et ce fut un plaisir de travailler avec lui.

Je remercie aussi les autres membres du groupe: Serge Reynaud, Thierry Debuisschert, et Laurent Hilico pour leurs conseils et aide tout au long de mon travail; ainsi que Bernard Cagnac, Iso Abram, Georges Camy, Philippe Grangier, et Prem Kumar qui ont accepté de participer au jury.

Je tiens aussi a remercier le personnel technique, Francis Trehin, Marc Thommé, Jean Quilbeuf, Bernard Clergeaud et le personnel du secrétariat, Marie-Noëlle Ollivier et Brigitte Enrique, ainsi que Mlle Gazan et M. Manceau qui ont assuré le tirage.

Je suis reconnaissant à l'Ambassade de France aux Etats-Unis et à la DRET pour leur soutien financier, et à l'Université Paris VI pour m'avoir permis de rediger ma thèse en anglais. Etant donné mes origines anglophones, cela fut un agrément pour l'auteur et ce sera certainement un agrément pour les lecteurs qui n'auront pas à subir du français mal écrit.

Pour terminer, je remercie chaleureusement mes amis et ma famille pour m'avoir offert un soutien moral souvent très nécessaire.

# TABLE OF CONTENTS


INTRODUCTION ET RESUME EN FRANCAIS iii

I. INTRODUCTION 1

II. FORMALISM 8

a: Correlation functions and spectrum 8

b: Signal to noise ratio 9

c: Shot noise 10

d: Detection loss 12

e: Parametric interaction 12

f: Semi-classical theory 14

g: Amplitude and intensity correlations 16

III. OPTICAL PARAMETRIC OSCILLATOR 18

a: Evolution equations 18

b: Stationnary solutions 19

c: Field fluctuations in balanced OPO 20

d: Field fluctuations in unbalanced OPO 25

IV. TWIN BEAM EXPERIMENT 33

Reprint: Optics Letters 34

a: Pump laser: experimental details 37

b: OPO: experimental details 38

c: Detection mechanism: experimental details 41

d: Detection balance and linearity 42

e: Twin beam separator: experimental details 43

f: Conclusion 46

V. CONTROL THEORY 47

a: Linear transfer 47

b: Feedback 51

c: Nyquist analysis 52

d: Root-locus analysis 53

e: Bode analysis 56

f: Conditional stability 59

g: Time delay in feedback 61

VI. CONTROL WITH TWIN BEAMS 63
a: Basic model 63
b: Balanced beams 65
c: Examples of control mechanisms 66
d: Channel imperfections 69
e: Realization of variable attenuator 70
f: Application to twin beams generated by OPO 72
g: Gain error analysis 74
h: Stability analysis 78
i: Feedforward versus feedback 80
VII. FEEDFORWARD CONTROL EXPERIMENT 82
Reprint: Physical Review Letters 83
a: Pump laser: experimental details 87
b: Feedforward channel: experimental details 87
c: Sum/difference circuitry 94
d: Detection linearity 95
e: Conclusion 96
VIII. FEEDBACK CONTROL EXPERIMENT 98
a: Experimental layout and specifications 98
b: Results and discussion 101
APPENDIX 106
a: Photon model 106
b: Simulation algorithm 110
c: Statistical parameters 114
d: Results 116
REFERENCES 121

# INTRODUCTION ET RESUME EN FRANCAIS

Les systèmes d'asservissement sont utilisés depuis de nombreuses années pour réduire les fluctuations de divers paramètres physiques. En particulier dans le domaine optique, on emploie couramment des systèmes de contrôle opto-électroniques pour réduire les fluctuations d'intensité d'un laser.

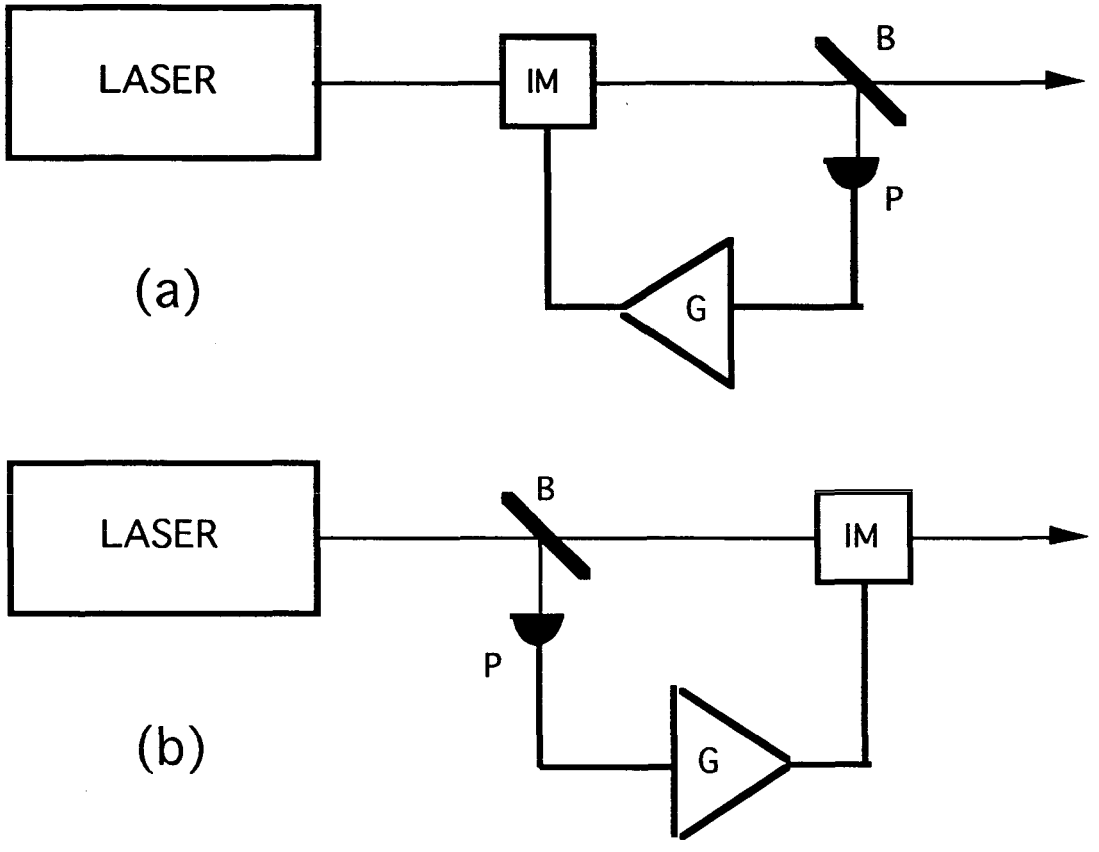


Figure 1 : Configurations d'asservissement "amont" et "aval". B: lame semi-réfléchissante. P : photodiode. G : amplificateur. IM : modulateur d'intensité.

En général, ces dispositifs comprennent une lame partiellement réfléchissante B qui prélève une partie du faisceau (voir figure 1), un photodétecteur P qui mesure l'intensité lumineuse, et un système électronique de modulation du faisceau laser permettant de corriger ses fluctuations. Cette correction peut être appliquée avant (configuration "amont" : figure 1.a), ou bien après la lame B (configuration "aval" : figure 1.b). Les limites à la réduction du bruit que l'on peut atteindre avec de tels dispositifs peuvent être séparées en deux catégories. Il y a tout d'abord des limites techniques, liées aux performances du système d'asservissement, comme par exemple son bruit propre ou sa bande passante. Lorsque le

système d'asservissement est parfait, il est en mesure de corriger le bruit d'intensité "classique", ou "technique", du faisceau laser, dû à des vibrations mécaniques, des fluctuations thermiques, des instabilités variées, etc.. Il ne peut en revanche pas corriger le bruit "quantique" d'intensité qui provient de la nature corpusculaire du photon. Ce bruit, appelé bruit de "grenaille" ou bruit de photons, est la deuxième limite, de caractère plus fondamental, à laquelle se heurte tout système d'asservissement d'intensité.

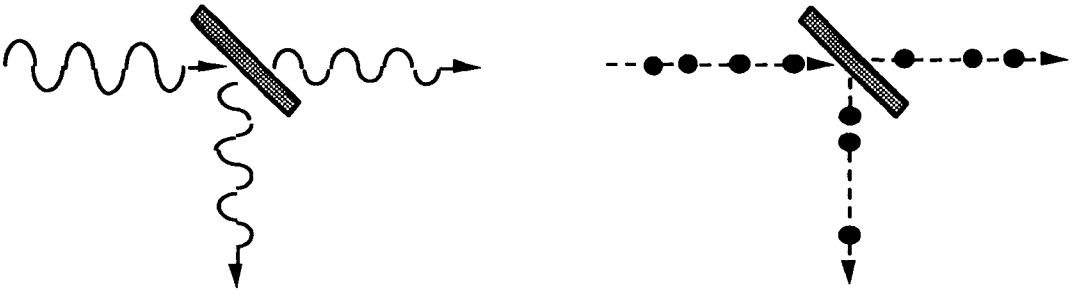

Figure 2 : La lame semi-réfléchissante envisagée d'un point de vue "classique" (à gauche), ou "quantique" (à droite).

Considérons en effet se qui se passe au niveau de la lame semi-réfléchissante utilisée dans le système d'asservissement (figure 2) : dans une description classique, l'onde lumineuse incidente se partage en deux ondes identiques, dont les variations sont donc parfaitement corrélées. Si l'on raisonne maintenant quantiquement, les photons qui arrivent sur la lame ne peuvent évidemment pas se partager en deux : ils sont transmis ou réfléchis de manière aléatoire. Ils en résulte que les répartitions des photons dans les faisceaux transmis ou réfléchis ne sont pas complètement corrélées. L'information contenue dans le faisceau réfléchi n'est donc pas suffisante pour corriger les fluctuations du faisceau transmis. Une autre explication de cette décorrélation au niveau de la lame, que nous verrons dans le chapitre II, consiste à dire que les fluctuations du vide entrent par la voie d'entrée inutilisée de la lame et se couplent aux deux voies de sortie.

On a longtemps tenu le bruit de photon comme la limite à jamais infranchissable du bruit d'intensité d'un faisceau lumineux. On sait maintenant que cette limite, appelée aussi limite quantique standard, n'est valable que pour un sous-ensemble particulier d'états de la lumière, les états "classiques", mais non pour d'autres, que l'on qualifie d'états "non-classiques", ou d'états "comprimés". La question des limites ultimes d'un asservissement d'intensité s'est donc reposée sous un jour nouveau après la démonstration expérimentale qu'on pouvait effectivement produire des états comprimés [Slu 85].

La lumière comprimée [Sque87] est caractérisée par une réduction des fluctuations en dessous de la limite quantique standard pour une composante de quadrature déterminée. En

particulier, on appelle lumière comprimée en amplitude un état de la lumière où les fluctuations de la composante d'amplitude sont réduites. La mesure de l'intensité d'un tel état est caractérisée, à la limite des faibles fluctuations, par une statistique de comptage sub-Poissonienne.

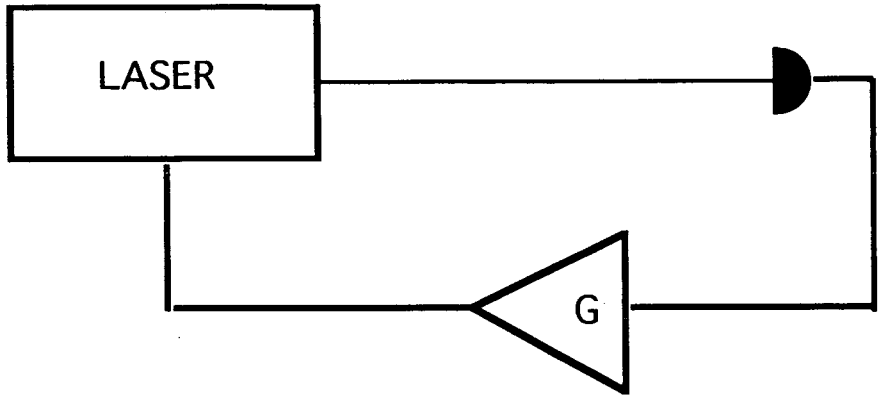


Figure 3 : Asservissement utilisant l'intensité totale du faisceau à asservir.

Il revient à Yamamoto et à ses collaborateurs [Mac86] d'avoir les premiers montré expérimentalement que l'on pouvait créer une lumière comprimée en amplitude à l'aide d'un asservissement électronique, en utilisant un dispositif dans lequel l'intensité d'une diode laser était mesurée et utilisée comme signal d'erreur dans le système de régulation du courant d'injection de la diode (figure 3). Cette expérience, bien que conceptuellement simple, fut importante car elle montra que les fluctuations quantiques n'étaient pas une limite fondamentale dans les systèmes actifs, et qu'elles pouvaient être réduites par des moyens électroniques au même titre que les fluctuations classiques. La différence importante entre le schéma de la figure 3 et ceux de la figure 1 est l'existence ou non d'un faisceau de sortie. Dans le cas de l'expérience de Yamamoto, l'asservissement a besoin de l'intégralité du faisceau lumineux pour pouvoir réduire les fluctuations en dessous du bruit de photon. La lumière sub-Poissonienne y a donc une existence éphémère, entre le laser et le détecteur, et elle ne peut pas être utilisée (si on met une lame dans le faisceau pour en extraire une partie, on se retrouve dans la configuration de la figure 1.a).

Plusieurs solutions furent proposées pour obtenir un signal utilisable dans l'asservissement sans détruire la corrélation d'intensité avec le faisceau à asservir. L'une d'entre elles consiste à utiliser une "mesure quantique non-destructive" [Lev86, LaP89, Gran91] de l'intensité du faisceau pour obtenir le signal d'erreur utilisable dans la boucle [Yam86, Haus86]. Une manière de réaliser une telle mesure quantique non-destructive consiste à utiliser un milieu Kerr, dont l'indice dépend de l'intensité du faisceau à corriger. Un faisceau auxiliaire mesure par une technique interférométrique le déphasage résultant.

Une autre solution consiste à revenir à la configuration de la figure 1, mais en injectant un "vide comprimé" [Slu85, Kim86] dans l'entrée inutilisée de la lame semi-réfléchissante pour supprimer la décorrélation entre les fluctuations des faisceaux transmis et réfléchis. Une troisième solution consiste à remplacer la lame semi-réfléchissante de la figure 1 par un "séparateur paramétrique" ("parametric beamsplitter"), au niveau duquel les photons incidents, au lieu de se répartir aléatoirement sur les deux voies de sortie, sont effectivement coupés en deux photons distincts par le processus de conversion paramétrique (figure 4). Il en résulte une corrélation parfaite entre les intensités des deux faisceaux de sortie, dont l'un est utilisé dans le système d'asservissement [Fab86, Yuen86, Sha87, Bjo88]. C'est à l'étude de cette dernière solution qu'est consacré le présent mémoire.

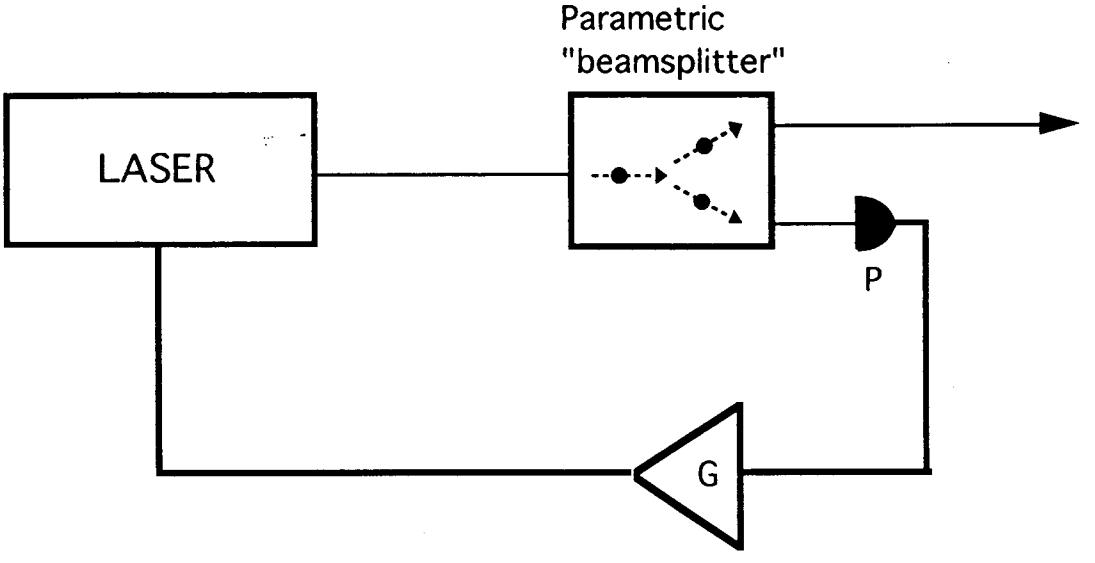


Figure 4 : Asservissement utilisant un "séparateur paramétrique".

Le fait que les photons créés par conversion paramétrique sont émis exactement simultanément a été prouvé expérimentalement par Weinberg [Bur70] et Mandel [Fri84]. On s'est rapidement rendu compte de l'intérêt de ces photons corrélés, ou photons jumeaux, dans des systèmes d'asservissement fonctionnant en régime de comptage de photons : la statistique de photon d'un des faisceaux est ajustée dans une boucle d'asservissement, en utilisant des techniques digitales d'ouverture ou de fermeture de portes optiques [Wal85, Sal85, Jak85, Hon86, Sto86], et la lumière est extraite en utilisant l'autre élément de la paire, créée soit par fluorescence paramétrique, soit par une cascade atomique. Dans le régime de comptage de photons, à cause de la faible efficacité quantique des compteurs de photons, la réduction du bruit quantique mesurée était modeste [Rar87], ou bien les flux obtenus très faibles [Hon86, Sto86, Rar87, Gra86]. Des expériences similaires récentes utilisant des détecteurs analogiques de bien meilleur rendement quantique ont nettement amélioré ces performances, et une réduction de bruit d'intensité de plus de 20 % a été récemment observée dans une

expérience de correction "amont" utilisant la fluorescence paramétrique [Tap88]. Les faisceaux générés dans cette expérience n'étaient cependant pas de très forte intensité ni de grande cohérence spatiale et temporelle, ce qui les rendait peu aptes à des applications pratiques.

Une autre source de faisceaux corrélés est l'Oscillateur Paramétrique Optique (OPO), formé d'un milieu paramétrique inséré dans une cavité optique [Bru77, Yar71, Shen84]. Bien que les faisceaux issus d'un tel OPO ne soient corrélés en intensité que pour des fréquences de bruit à l'intérieur de la bande passante de la cavité optique [Rey87], ils présentent le notable avantage d'avoir les mêmes propriétés qu'un faisceau émis par un laser (haute intensité, cohérence, faible largeur spectrale). C'est à l'étude d'un tel système que nous nous sommes plus particulièrement attachés dans cette thèse.

Le mémoire est divisé en deux parties principales, centrées autour de deux expériences dont nous avons inclus les publications. La première est consacrée à l'étude de la génération de faisceaux corrélés (ou "jumeaux") à l'aide d'un Oscillateur Paramétrique Optique (OPO). La seconde étudie les possibilités de réduction du bruit de photons sur un des faisceaux jumeaux en utilisant l'autre faisceau dans le système d'asservissement. Nous présentons maintenant un résumé de chaque chapitre :

**Chapitre I :** Introduction.

**Chapitre II :** Il comprend un résumé du formalisme mathématique utilisé dans cette thèse. Le lien entre la fonction d'autocorrélation et le spectre de puissance est établi, ainsi que la définition du bruit de grenaille, ou "shot noise", d'un faisceau lumineux. Nous présentons ensuite les expressions de transformation entrée-sortie des opérateurs quantiques de fluctuations dans le cas d'une lame semi-réfléchissante et d'une faible interaction paramétrique. Ces transformations sur les opérateurs quantiques du champ, étant linéaires et canoniques, sont équivalentes aux transformations sur les variables classiques du champ. Il en résulte que les transformations portant sur les moyennes quantiques de tout opérateur quantique symétrique (descriptibles en termes de fonction de Wigner) sont identiques aux transformations portant sur les moyennes stochastiques des variables classiques correspondantes. Nous ramenons donc le problème de transformations des opérateurs quantiques à un problème de transformations de variables fluctuantes classiques dérivées des équations de l'électrodynamique classique, dans lequel il faut tenir compte des modes vides couplés au système étudié, et qui sont source de fluctuations entrantes dans le système. C'est le principe de la méthode dite "semi-classique". Nous définissons finalement quelques paramètres qui seront utiles dans la suite, et qui caractérisent les corrélations entre les deux faisceaux.

**Chapitre III :** Ce chapitre est une étude théorique de l'Oscillateur Paramétrique Optique, formé d'un milieu faiblement paramétrique dans une cavité optique résonnante. Nous donnons les équations d'évolution des champs en interaction dans l'OPO sous une forme entrée-sortie, en incluant l'effet des modes vides entrants, et nous linéarisons ces équations autour des valeurs stationnaires des champs pour obtenir des équations d'entrée-sortie pour les fluctuations. Nous étudions les propriétés des faisceaux jumeaux émis par l'OPO, en particulier les spectres de bruit d'intensité de chaque faisceau, ainsi que le spectre de la différence d'intensité, qui caractérise les corrélations d'intensité entre les faisceaux jumeaux. Les expressions analytiques de ces spectres sont données dans le cas où l'OPO est équilibré (caractéristiques de l'OPO identiques pour les deux modes jumeaux), et aussi dans le cas général et beaucoup plus compliqué où l'OPO est déséquilibré, et où les différents champs ne sont pas nécessairement à résonance exacte avec les modes propres de la cavité. Dans le cas équilibré, le spectre de la différence des intensités prend la forme d'une Lorentzienne dont la largeur est égale à la bande passante de la cavité. Le bruit résiduel à fréquence nulle est égal au rapport entre les pertes de la cavité et la somme de ces pertes et de la transmission du miroir de sortie. Les corrélations quantiques d'intensité entre les faisceaux sont donc d'autant plus grandes que la transmission de la cavité pour les modes jumeaux est grande et que les pertes sont faibles.

**Chapitre IV** : Ce chapitre comprend une étude expérimentale de la corrélation d'intensité entre les faisceaux jumeaux produits par un OPO. Il contient la reproduction d'un article à Optics Letters présentant nos résultats. Nous avons mesuré une réduction de bruit de 86 % en dessous de la limite quantique standard dans le spectre de la différence des intensités, limitée à peu près également par les pertes optiques dans l'OPO et par l'efficacité quantique non parfaite des détecteurs. Ce résultat représente une amélioration substantielle par rapport aux mesures que nous avions effectuées précédemment. Il constitue à ce jour l'une des plus importantes réduction de bruit jamais observées dans le monde. Nous corroborons nos résultats à l'aide d'un atténuateur calibré, qui démontre que la réduction de bruit par rapport au bruit de grenaille est éliminée par les pertes optiques, et ce d'une manière strictement proportionnelle. Nous présentons aussi des détails supplémentaires sur l'expérience qui ne sont pas inclus dans l'article, notamment sur le laser YAG doublé qui produit le faisceau pompe, sur le système d'asservissement de l'intensité moyenne de l'OPO, sur l'électronique de détection, incluant une vérification de l'équilibrage et de la linéarité des photodétecteurs, et finalement sur le système de séparation des faisceaux jumeaux qui sert également à calibrer le niveau de bruit de grenaille dans l'expérience. Au cours de cette dernière discussion, nous présentons une analyse des différentes causes d'erreur dans la mesure de la réduction de bruit.

**Chapitre V** : Ayant maintenant bien établi la nature quantique des corrélations d'intensité dans l'OPO, il nous reste à exploiter ces corrélations pour produire, par un système d'asservissement, un faisceau ayant un bruit d'intensité comprimé. Dans ce but, nous commençons par donner un rappel de la théorie des asservissements linéaires, et en particulier des méthodes de boucle de contre-réaction. Nous présentons pour ce dernier type d'asservissement diverses méthodes d'analyse de stabilité, notamment la méthode de Nyquist, la méthode des pôles, et la méthode de Bode. Nous envisageons diverses méthodes pour améliorer les performances de ce système, soit en déplaçant la fréquence de résonance de l'asservissement, soit en utilisant une contre-réaction à stabilité conditionnelle. Nous étudions aussi les différents effets produits par un retard pur dans un asservissement contre-réactif. Ce chapitre de synthèse est conçu pour pouvoir être utilisé indépendamment du reste de la thèse.

**Chapitre VI** : La théorie des asservissements qui vient d'être esquissée est appliquée au problème de la correction des fluctuations d'intensité d'un faisceau lumineux en utilisant la mesure des fluctuations d'intensité d'un autre faisceau, présumé corrélé avec le premier. La fonction de transfert caractérisant cet asservissement sera dénommée gain de contrôle et notée G. Nous développons dans ce chapitre une théorie générale, indépendante du mécanisme particulier de ce transfert. A partir du spectre d'intensité de deux faisceaux quelconques, et du spectre de leur différence d'intensité, nous déterminons le spectre d'intensité du faisceau asservi, et parvenons à une expression pour la réduction optimale de bruit sur un faisceau à l'aide d'une telle méthode, ainsi que celle du gain de contrôle nécéssaire pour une telle réduction. Dans le cas où les deux faisceaux sont équilibrés, ce gain de contrôle est réel dans l'espace de Fourier. Pour des faisceaux parfaitement corrélés, G vaut à 1 et la réduction du bruit de grenaille peut être totale. Pour des faisceaux décorrélés, G est nul, et l'on ne peut pas descendre en dessous du bruit de photons. Nous considérons ensuite le cas des configurations d'asservissement amont ou aval, en tenant compte de la possibilité d'imperfections dans la chaine de transfert. On montre que les deux mécanismes sont formellement équivalents du point de vue de la réduction ultime de bruit, mais présentent différents avantages ou inconvénients dans leurs mises en oeuvre expérimentales. Finalement, nous précisons ces résultats en étudiant le cas spécifique de faisceaux jumeaux produits par un OPO, et d'un mécanisme de transfert comprenant un modulateur d'intensité électro-optique. Le désaccord entre la réduction de bruit idéale et une réduction de bruit réaliste est trouvé proportionnel au carré de la distance (dans le plan complexe) entre le gain théorique idéal (non réalisable en général) et le gain réaliste, compte tenu des contraintes imposées par la causalité et la stabilité du système. Cette distance permet de caractériser les performances d'un asservissement réaliste.

**Chapitre VII** : Il traite de l'étude expérimentale d'un asservissement en configuration aval, c'est-à-dire comprenant un transfert direct des fluctuations d'intensité d'un faisceau à l'autre. Les résultats de cette expérience sont présentés sous la forme d'un article publié à Physical Review Letters que nous incluons à la tête du chapitre. Nous avons mesuré dans le spectre du faisceau asservi une réduction de bruit de 24 % en dessous du bruit de grenaille autour d'une fréquence de 5 MHz, ce qui représente la première observation d'un faisceau sub-Poissonien généré par une telle méthode d'asservissement. Le faisceau sub-Poissonien produit présente l'intérêt d'être en même temps intense et de faible largeur spectrale. Les résultats sont vérifiés par la même méthode d'atténuation que celle décrite au chapitre IV. De plus, des détails supplémentaires sont fournis, concernant le laser pompe, les caractéristiques de la chaine de contrôle et de l'électronique de détection, ainsi qu'une analyse des performances de l'asservissement que nous avons employé.

**Chapitre VIII** : Nous présentons une expérience similaire à celle du chapitre précédent, mais dans laquelle l'asservissement est en configuration amont : la correction est maintenant appliquée sur l'intensité du faisceau pompe. Bien que cette expérience n'ait pas réussi à produire un faisceau asservi ayant un bruit réduit par rapport au bruit de grenaille, à cause des problèmes de tendance à l'auto-oscillation d'un tel dispositif, elle démontre cependant que ce tyupe d'asservissement est bien compris. Nous y analysons les performances de la boucle de contrôle utilisée, ainsi que les améliorations nécessaires pour parvenir à une réduction du bruit quantique dans cette configuration.

**Appendice** : Tout au long de ce mémoire, nous avons utilisé un formalisme semi-classique pour étudier les fluctuations quantiques d'intensité. Ce modèle est un modèle essentiellement classique, dans lequel les effets quantiques supplémentaires proviennent de l'existence des fluctuations du vide couplées avec le système étudié. Dans cet appendice, nous présentons brièvement un modèle complètement différent, dénommé modèle "corpusculaire", dans lequel chaque photon est considéré comme un évènement localisé dans le temps. En utilisant des arguments de comptage de ces photons, nous arrivons au même résultat que dans le modèle semi-classique pour le spectre d'un faisceau en configuration aval. Bien que ce modèle ne soit évidemment applicable que pour des systèmes dans lesquels la phase du champ électromagnétique ne joue aucun rôle, il présente l'avantage d'être intrinsèquement non-linéaire, et permet donc une étude du bruit d'intensité à des ordres supérieurs par rapport aux méthodes de linéarisation. Nous donnons en outre les résultats d'une simulation numérique de l'asservissement en configuration aval en générant par ordinateur deux trains de faisceaux jumeaux, corrélés ou décorrélés, et possédant des statistiques Poissoniennes ou superPoissoniennes. Les résultats numériques ainsi obtenus sont en bon accord avec les résultats de la méthode semi-classique.

# I. INTRODUCTION

The use of active control for the reduction of fluctuations in various physical parameters is prevalent both in electronics and in optics. In particular, the use of opto-electronic control for the reduction of laser intensity fluctuations has now become routine. Possible configurations for such control use a beamsplitter and photodetector to sample the laser intensity, and an intensity modulator to correct the laser intensity either before (feedback control) or after (feedforward control) the beamsplitter (see fig. 1.1).

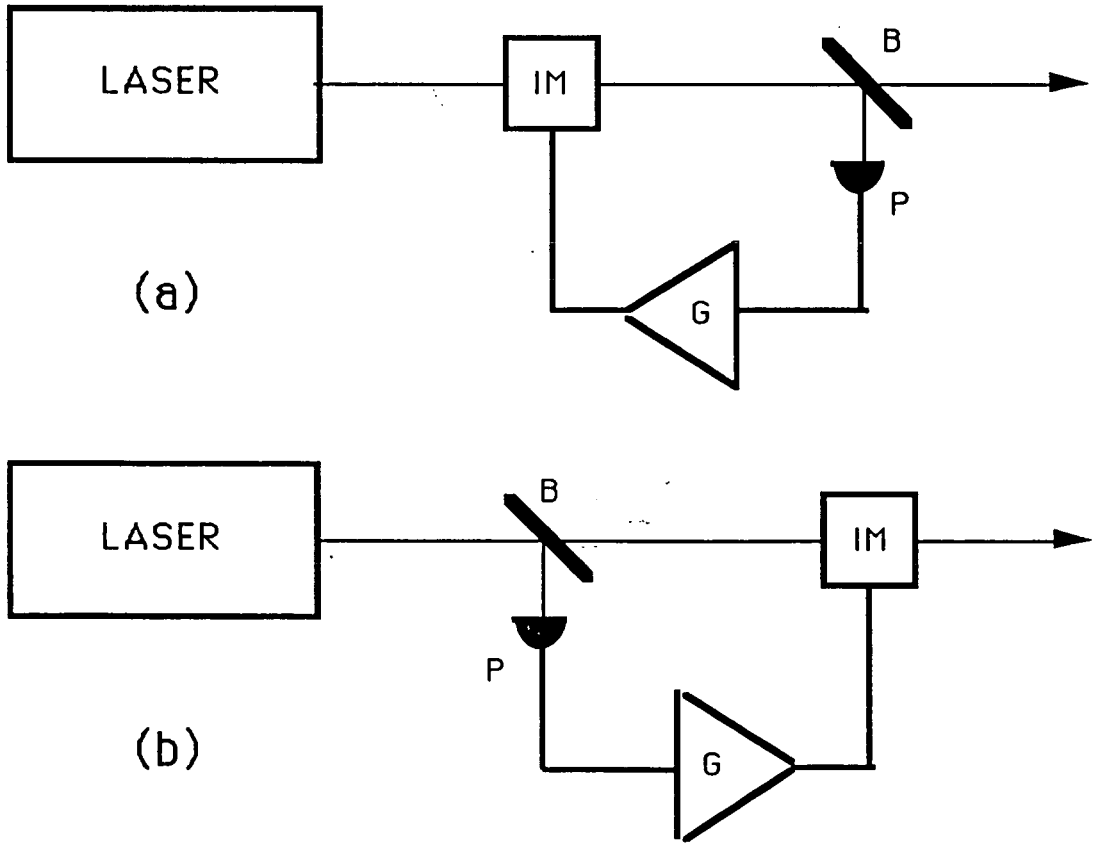


Figure 1.1: Feedback (a) and feedforward (b) control configurations. B: beamsplitter. P: photodiode. G: amplifier. IM: intensity modulator.

The limits to the reduction in noise obtained by the control configurations above may be separated into two categories. The first limit depends on the performance of the control channel itself, including such design specifications as channel noise and bandwidth. This limit is technical in nature. When the control channel is ideal, the above configurations correct the "classical" intensity noise in a laser which arises from thermal or mechanical source vibrations, mode instabilities, etc.. They cannot, however, correct the "quantum" noise in the laser intensity which arises from the discretized photon nature of light. The latter noise, referred to as photon noise, provides the second more fundamental limit to the intensity noise reduction that may be obtained with active control. The distinction between the two limits may be appreciated by considering the different effects of the sampling beamsplitter in a "classical" picture and in a "quantum" picture (see fig. 1.2). In the classical picture, the light wave incident on the beamsplitter is split into two light waves whose fluctuations are perfectly correlated. In the "quantum" picture, the photons incident on the beamsplitter are randomly transmitted or reflected (observed by the sampling photodiode), but not both. The resultant transmitted and reflected photon streams are therefore *not* rigorously correlated, and perfect noise control is unattainable. An alternative interpretation of this decorrelation, as we will see in chapt. II, is that it arises from the coupling of vacuum fluctuations through the unused beamsplitter input port.

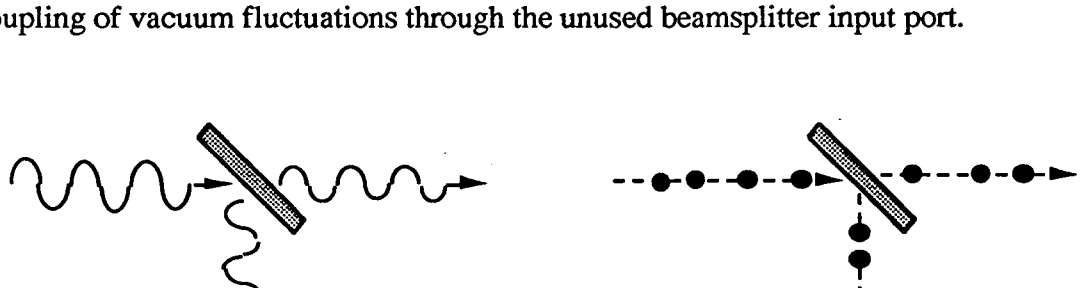

Figure 1.2: Beamsplitter in "classical" (left) and "quantum" (right) picture.

Until recently, quantum noise presented a lower limit to the noise in a laser beam intensity, variously known as the shot noise limit, the standard quantum limit (SQL), or the vacuum fluctuation level. Noise reduction below this limit was considered impossible. It is now recognized, however, that this limit applies only to certain categories of light, known as "classical" states, and not to other categories, known as "nonclassical" or "squeezed" states. With the experimental demonstration of these latter states [Slu85], interest has been renewed in the potential of active control for the reduction of laser noise below the quantum level.

Squeezed light [Sque87] is characterized by a reduction in the fluctuations of some field component below the shot noise level. Amplitude squeezed light, in particular, is defined by a reduction in the fluctuations of the amplitude component of the field. In the small fluctuation limit such light exhibits sub-Poissonian photon statistics. The generation of

amplitude squeezed light using external control was first demonstrated by Yamamoto et al [Mac86] using a scheme where the intensity of a semiconductor laser was monitored and used to regulate the laser drive current (see fig. 1.3). Although conceptually simple, this experiment was significant in demonstrating that quantum fluctuations were, in fact, not a fundamental limit to active noise control and that they could be reduced as well as classical fluctuations. The underlying difference, however, between the control configuration described here and the control configurations described above is that, in the latter, the controlled beams are available for external use. This is not the case in the Yamamoto experiment where the feedback signal required the monitoring of the *total* laser intensity for noise reduction below the shot noise level. The controlled sub-Poissonian light was restricted, therefore, only to the span between the laser and the detector and could not be extracted for external use. (Insertion of a beamsplitter into the controlled beam, for example, would be equivalent to the configuration of fig. 1.1a.)

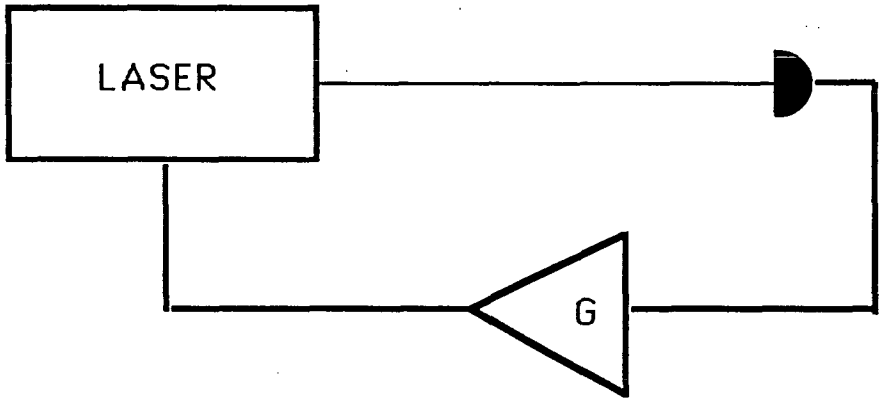


Figure 1.3: Feedback control monitors total intensity of control beam.

Several solutions were proposed to provide a control signal without destroying the control beam of interest. One solution makes use of quantum non-demolition (QND) measurement [Lev86, LaP89, Gran91] of the control beam intensity to provide the control signal [Yam86, Haus86]. A possible candidate for such a QND measurement is a Kerr medium inside which the intensity of one beam can non-destructively be inferred from the phase shift induced in an auxiliary monitor beam (see fig. 1.4).

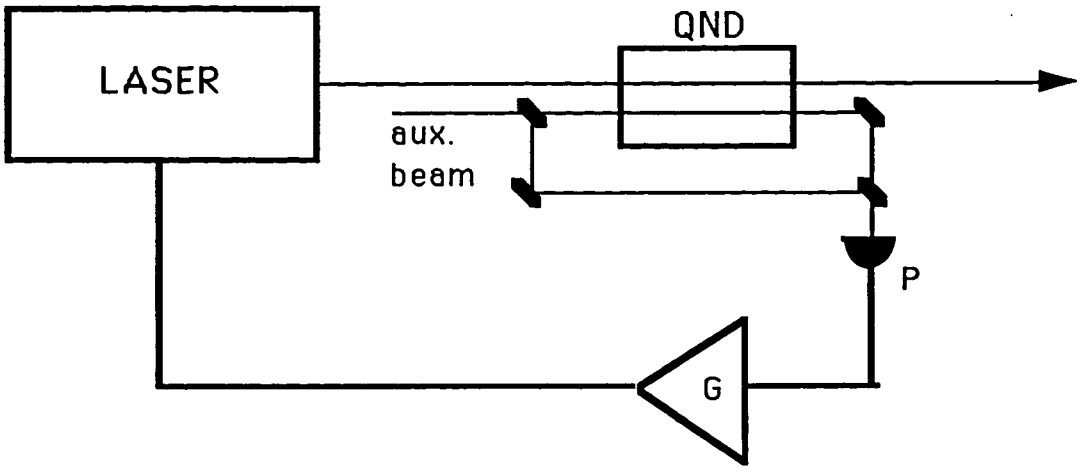


Figure 1.4: Feedback control using QND measurement. Intensity of control beam changes index of refraction in Kerr medium. Resultant phase shift in auxiliary beam is monitored by interferometric detection.

A second solution reverts to the configurations shown in fig. 1.1 for noise control but makes use of an injected squeezed vacuum [Slu85, Kim86] through the unused beamsplitter port [Cav89] to counteract the incurred quantum decorrelation in the transmitted and reflected beams (see fig. 1.5).

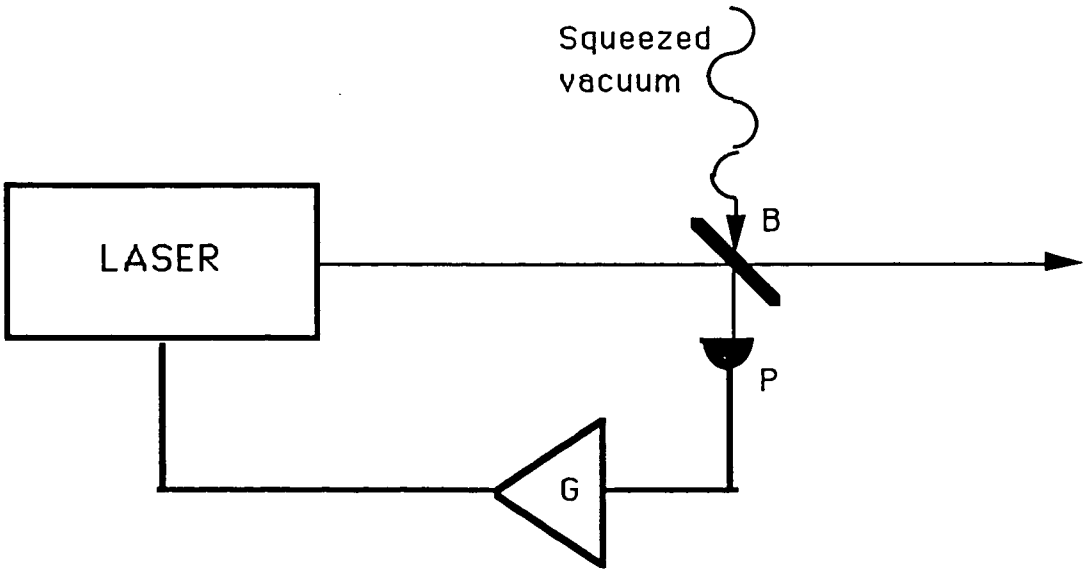


Figure 1.5: Feedback control in which squeezed vacuum is injected through unused beamsplitter port.

A third solution replaces the standard beamsplitters in fig. 1.1 by parametric "beamsplitters" in which the incident photons, instead of being randomly routed into either the control or the monitor paths, are instead split into two separate photons by parametric down-conversion (see fig. 1.6). The intensity correlations in the control and monitor paths are thus rigorously ensured [Fab86, Yuen86, Sha87, Bjo88]. We will concentrate on this latter solution.

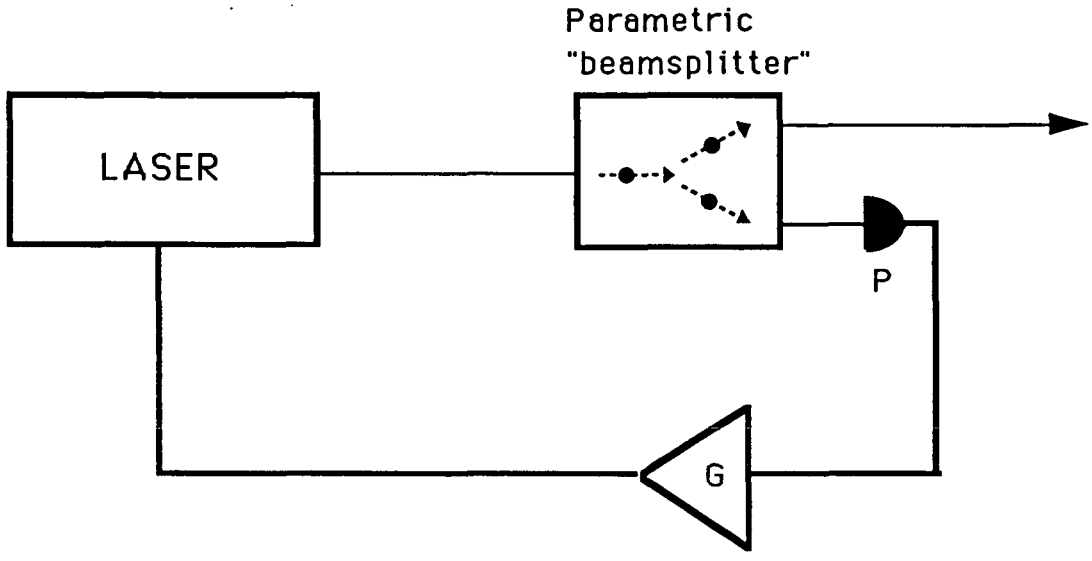


Figure 1.6: Feedback control using parametric "beamsplitter".

The property of parametric down-conversion that the emitted photons are generated simultaneously in time was originally established in experiments by Weinberg [Bur70] and Mandel [Fri84]. The interest in such correlated photons for noise control was first realized in the photon counting regime, where the statistics of a photon stream were tailored in a closed loop system, and sub-Poissonian light was extracted using the photon pairs generated by parametric fluorescence and also by atomic cascade. The photon count rate was measured and the information used to react directly on the controlled photon stream using gating techniques [Wal85, Sal85, Jak85, Hon86, Sto86]. Experiments in this photon counting regime yielded modest amounts of quantum noise reduction [Rar87] or very low photon fluxes [Hon86, Sto86, Rar87, Gra86] because of the poor quantum efficiency of photon counters. Similar control experiments using analog photodetectors with high quantum efficiency have fared better. Intensity noise reductions of more than 20% below the shot noise level have been recently reported for a feedback control experiment with parametric fluorescence [Tap88]. The light beams in this experiment, however, were

neither high intensity nor monomode, making them impractical for experimental applications. An alternative correlated beam source is the optical parametric oscillator (OPO), which comprises a parametric medium inside an optical cavity [Bru77, Yar71, Shen84] Although the output beams of an OPO are correlated in intensity only to within the optical cavity bandwidth [Rey87], they present the notable experimental advantage of being laser-like (high intensity, mono-mode, etc.) and easy to manipulate.

The purpose of this thesis is to study active control schemes using correlated beams. The structure of the thesis is is two parts, centered about the experimental articles included in chapters IV and VII. Following a brief introduction to formalism (chapt. II), the first part presents a theoretical (chapt. III) and experimental (chapt. IV) study of the optical parametric oscillator for its use as a correlated beam source. In practice, the amount of correlation between the OPO output beams is limited only by spurious optical losses undermining the pairwise detection of the beam photons (again, to within the cavity bandwidth). These losses will be included in our treatment of the OPO, as well as cavity detunings and beam imbalances, to correspond as closely as possible to the experimental situation [Hei87, Deb89, Nab90, Leo90] where the generated output beams are not perfectly correlated. Much of the first part of this thesis serves as an extension to the theoretical work by Fabre et al [Fab89] and to the experimental work by Debuisshert *et al* [Deb90] where it was established that OPOs are particularly effective generators of correlated beams. We demonstrate in chapter IV a quantum noise reduction of 86% below the shot noise level in the correlated beam intensity difference spectrum, which is the largest quantum noise reduction observed to date.

The second part of the thesis addresses the problem of, given two correlated (or partially correlated) beams, to what extent intensity noise reduction is possible when one beam is used to control the other. A brief review of linear control theory is presented in chapter V, written so it may be used stand-alone. A general theory is then presented in chapter VI for linear noise control using any two beams. The beams are specified only by their initial intensity correlations and their respective intensity noises, whereupon we examine the conditions necessary for noise reduction below the shot noise level. The theory developed in this chapter is independent of the details of the correlated beam source or of the control mechanism. We compare the noise reduction obtained using an idealized control channel with the noise reduction obtained using a realistic control channel. An analysis is included of gain error and of the constraints imposed by channel stability. In particular, we examine the case where the correlated beam source is an OPO and where the control mechanism is opto-electronic. Finally, we present results for control experiments using both the feedforward configuration (chapt VII) and feedback configuration (chapt. VIII). In the feedforward configuration, a reduction up to 24% below the shot noise level is observed in the controlled beam intensity noise power. This is the first demonstration of quantum noise reduction using active control with high intensity beams.

The formalism used throughout the thesis is a semiclassical input-output formalism [Rey89], since this is well adapted to control theory and to the study of OPOs in the small fluctuation limit. This formalism as well as the mathematical baggage necessary for the

study of intensity noise is given in chapter II. An alternative interpretation of intensity noise is given in the appendix, where a light beam is considered as a stream of discrete photons . The same result derived in chapter VI for twin beam control is re-derived with this interpretation using a simple photon counting argument for the case when the twin beams are Poissonian. Noise control is illustrated for this case by using computer simulation.

# II. FORMALISM

The purpose of this chapter is to introduce the mathematical formalism used throughout this thesis. We start by briefly introducing the notation used for the treatment of fluctuations in quantum optics. We introduce a semi-classical formalism where the quantum operators for these fluctuations are replaced by classical stochastic variables. Finally, we define the notation used to characterize the correlations between two light fields.

### a: *Correlation functions and spectrum*

We consider a field with a single propagation direction and a single polarization. In the Heisenberg representation, such a field is described by an electric field operator $\hat{E}(t)$, written as

$$\hat{E}(t) = \hat{E}^{+}(t) + \hat{E}^{-}(t). \tag{2.1}$$

$\hat{E}^{+}$ and $\hat{E}^{-}$ are respectively the positive and negative frequency components of the electric field. We will assume this field to be narrow in bandwidth centered about some carrier frequency $\omega_0$. The electric field operator may be separated into Fourier components:

$$\begin{aligned} \hat{E}^{+}(t) &= \int \frac{d\Omega}{2\pi} E_0(\omega_0)\hat{a}(\Omega)e^{-i(\omega_0+\Omega)t} \\ \hat{E}^{-}(t) &= \int \frac{d\Omega}{2\pi} E_0(\omega_0)\hat{a}^{\dagger}(\Omega)e^{i(\omega_0+\Omega)t}, \end{aligned} \tag{2.2}$$

where the range of integration is from $-\omega_0$ to $\infty$, but for narrowband fields will be approximated by the integration range $-\infty$ to $\infty$. (Unless otherwise specified, this will be the range for all the integrals in this thesis). $E_0(\omega_0)$ is a scaling constant chosen in such a way that the photon destruction and annihilation operators $\hat{a}(\Omega)$ and $\hat{a}^{\dagger}(\Omega')$ obey the commutation relation

$$\left[\hat{a}(\Omega), \hat{a}^{\dagger}(\Omega')\right] = 2\pi\delta(\Omega - \Omega'), \tag{2.3}$$

when $\Omega$, $\Omega' << \omega_0$ [Fab90]. Writing the time-dependent operators as

$$\hat{a}(t) = \int \frac{d\Omega}{2\pi}\hat{a}(\Omega)e^{-i\Omega t}, \tag{2.4}$$

the corresponding commutation relation is

$$\left[\hat{a}(t), \hat{a}^{\dagger}(t')\right] = \delta(t - t'). \tag{2.5}$$

We define an "intensity" operator $\hat{I}(t)$ as a measure of the instantaneous flux of photons

$$\hat{I}(t) = \hat{a}^{\dagger}(t)\hat{a}(t). \tag{2.6}$$

This differs from the standard definition of intensity which is the incident energy per unit time [Gla65], and corresponds instead to the quantity measured by a photodetector, which is number of incident photons per unit time. The fluctuations in this intensity are given by the operator

$$\delta\hat{I}(t) = \hat{I}(t) - \langle\hat{I}(t)\rangle, \tag{2.7}$$

where <..> denotes a quantum ensemble average over a given state $|\psi>$. In order to characterize the statistical properties of a field, we introduce two correlation functions. The first we define as the autocorrelation function of the intensity [Pap81]

$$C_I(t,t') = \langle\hat{I}(t)\hat{I}(t')\rangle - \langle\hat{I}\rangle^2 = \langle\delta\hat{I}(t)\delta\hat{I}(t')\rangle. \tag{2.8}$$

The second we define as the photon correlation function (variously known as the second order degree of coherence [Lou83]), related to the probability of detecting a photon at time t and another photon at time t'.

$$C(t,t') = \frac{\langle:\hat{I}(t)\hat{I}(t'):\rangle}{\langle\hat{I}\rangle^2}, \tag{2.9}$$

where <: :> denotes normal ordering. One finds then

$$C_I(t,t') = \langle\hat{I}\rangle\delta(t-t') + \langle\hat{I}\rangle^2(C(t,t')-1). \tag{2.10}$$

For a stationary field, $C_I(t,t')$ depends only on the quantity $\tau$=t-t'. The photon noise spectrum is defined as the Fourier transform of $C_I(\tau)$

$$S_I(\Omega) = \int d\tau\, C_I(\tau)\, e^{i\Omega\tau}, \tag{2.11}$$

or

$$S_I(\Omega) = \langle\hat{I}\rangle(1+Q(\Omega)), \tag{2.12}$$

where we have introduced the Mandel Q parameter

$$Q(\Omega) = \langle\hat{I}\rangle\int d\tau(C(\tau)-1)e^{i\Omega\tau}. \tag{2.13}$$

**b:** ***Signal to noise ratio***

Associated with any experimental measurement of intensity is a response function characterizing the detection response. We will denote this function $f(\tau)$, assumed causal and real. The *measured* intensity is the convolution:

$$I_f(t) = \int d\tau f(\tau)\langle \hat{I}(t-\tau)\rangle \tag{2.14}$$

We introduce the function $F(\Omega)=f(-\Omega)f(\Omega)$, defined from the Fourier transform of $f(\tau)$

$$f(\Omega) = \int d\tau e^{i\Omega\tau} f(\tau). \tag{2.15}$$

The spectrum of the measured intensity is then

$$S_{I_f}(\Omega) = F(\Omega) S_I(\Omega) \ , \tag{2.16}$$

and the variance of the measured intensity is

$$\Delta I_f^2 = \int \frac{d\Omega}{2\pi} \ F(\Omega)\langle \hat{I}\rangle(1+Q(\Omega)) \ . \tag{2.17}$$

Using the standard definition for the detection bandwidth B [Pap81]

$$2B = F(0)^{-1} \int \frac{d\Omega}{2\pi} \ F(\Omega) \ , \tag{2.18}$$

and assuming the detection filter is normalized so that

$$\int d\tau \ f(\tau) = 1 \ , \tag{2.19}$$

eqtn. 2.17 in the intensity may be rewritten as

$$\Delta I_f^2 = 2B\langle \hat{I}\rangle(1+Q_f) \ . \tag{2.20}$$

It is of practical importance to assign a signal to noise ratio to a detection measurement. For a signal defined proportional to the mean intensity: $S = \xi \langle \hat{I} \rangle$, one obtains

$$\frac{S}{N} = \xi \sqrt{\frac{\langle \hat{I}\rangle}{2B(1+Q_f)}} \ . \tag{2.21}$$

Methods for increasing this signal to noise ratio involve an increase in the intensity, a decrease in the detection bandwidth (assuming the signal bandwidth remains much smaller than the detection bandwidth), or a decrease in the Mandel parameter $Q_f$. The subject of this thesis is the latter of these methods.

### c: *Shot noise*

The term "shot noise" is used for the intensity fluctuation level when the photons in a field are incident on a detector at random times, that is, the probability of detecting a photon at time t is independent of the probability of detecting a photon at time t'. In this case, $C(\tau)=1$ and $Q(\Omega)=0$. The variance in the measured field intensity is then simply

$$\Delta I_f^2 = 2B\langle \hat{I}\rangle \ , \tag{2.22}$$

and the photon statistics are Poissonian. This is the case for a coherent field.

When the photon arrival times are correlated so that $Q(\Omega) > 0$, the field is super-Poissonian and contains "classical excess noise". When they are correlated so that $-1 \leq Q(\Omega) < 0$, the field is sub-Poissonian. The latter regime may only be described in a quantum treatment of the radiation.

For a field with general photon statistics, the standard method for measuring its associated shot noise level is with the use of two detectors (assumed ideal) and a beamsplitter (assumed lossless) as shown in fig. (2.1).

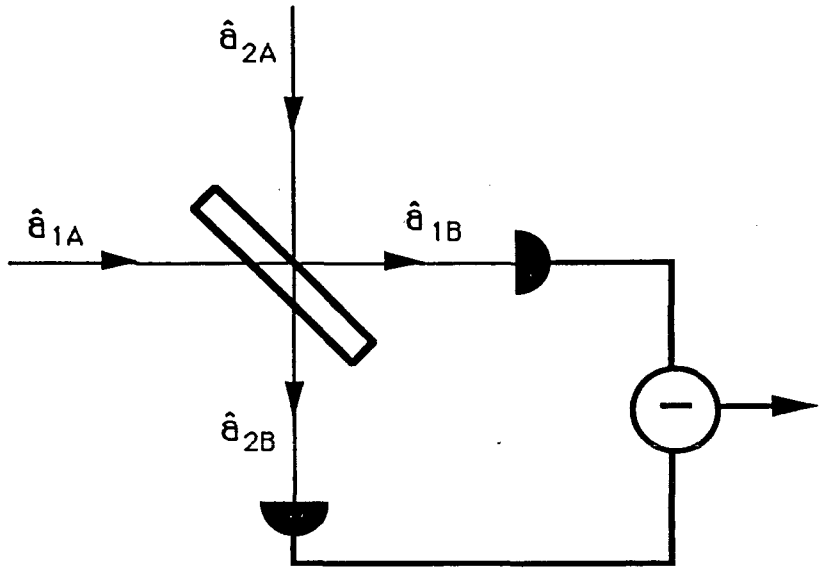


Figure 2.1

Denoting $\hat{a}_{1A}$ and $\hat{a}_{2A}$ as the modes incident on the beamsplitter, and $\hat{a}_{1B}$ and $\hat{a}_{2B}$ as the outgoing modes incident on the detectors, their relation is

$$\begin{aligned} \hat{a}_{1B} &= t\ \hat{a}_{1A} - r\ \hat{a}_{2A} \\ \hat{a}_{2B} &= r\ \hat{a}_{1A} + t\ \hat{a}_{2A} \end{aligned} \tag{2.23}$$

where r and t are the beamsplitter reflection and transmission coefficients. For the case when $r = t = 1/\sqrt{2}$ and when $\hat{a}_{2A}$ is unoccupied (in the vacuum state), then the measured noise spectrum of $\hat{I}_{1B}$-$\hat{I}_{2B} = \delta\hat{I}_{1B}$-$\delta\hat{I}_{2B}$ is $2B\langle\hat{I}_{1A}\rangle$. This is independent of the photon statistics in mode 1A, and is exactly the shot noise level associated with the total intensity in mode 1A.

We see in this example that the intensity fluctuations in the two modes $\hat{a}_{1B}$ and $\hat{a}_{2B}$ are not perfectly correlated since the resultant intensity difference spectrum is larger than zero. This may be interpreted using the model given in the introduction in which the beamsplitter randomly routes the incident photons from mode $\hat{a}_{1A}$ into either outgoing

mode $\hat{a}_{1B}$ or outgoing mode $\hat{a}_{2B}$. The numbers of photons counted in each outgoing mode are therefore not strictly equal (although they are equal on average).

**d: *Detection loss***

In practice, the photodiodes used to measure the field intensity are never perfect, and each photon incident on the detector photoactive region ejects an electron only with a probability $\eta$. This probability is the detector quantum efficiency. An imperfect detector ($\eta<1$) may be modeled as a perfect detector ($\eta=1$) with in front of it a beamsplitter of transmission coefficient $\sqrt{\eta}$ . Such a beamsplitter modifies not only the mean photon intensity but also the photon statistics. On measurement with an imperfect detector one obtains

$$\langle \hat{I} \rangle \rightarrow \eta \langle \hat{I} \rangle , \tag{2.24}$$

$$S_I(\Omega) \rightarrow \eta \langle \hat{I} \rangle (1 + \eta Q(\Omega)) . \tag{2.25}$$

The loss incurred by the field has the effect, therefore, of tending $S_I(\Omega)$ towards the shot noise level $\eta\langle\hat{I}\rangle$ linearly with $\eta$. This is independent of whether the field is sub or super Poissonian. For the detection of sub-Poissonian statistics, it is evidently important to keep the detection loss at a minimum.

**e: *Parametric interaction***

We have examined modes $\hat{a}_{1B}$ and $\hat{a}_{2B}$ when they emanate from a beamsplitter. (see fig. 2.1) We will show in the following chapters that if $\hat{a}_{1B}$ and $\hat{a}_{2B}$ are instead the two downconverted modes generated by a $\chi^{(2)}$ parametric interaction, then their intensity difference spectrum will fall below the associated shot noise level.

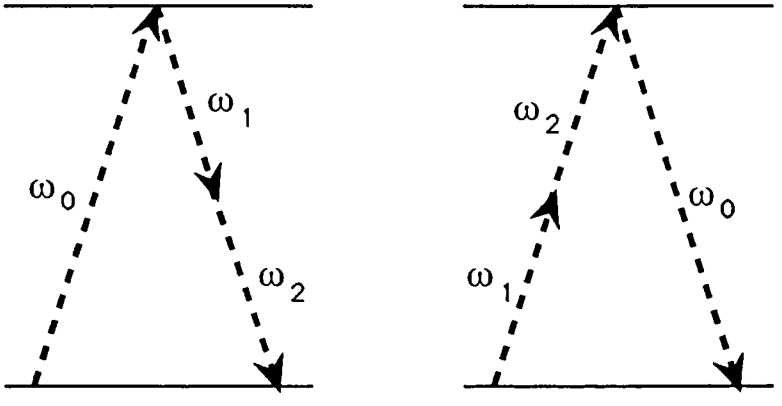


Figure 2.2: Parametric interaction: pump photon $\omega_0$ is downconverted to signal and idler photons $\omega_1$ and $\omega_2$ (left), or vice versa (right).

A $\chi^{(2)}$ parametric interaction is a three photon process where one photon is down-converted into two photons, or vice versa (see fig. 2.2). The absorbed photon is called the pump photon (indexed 0) and the down-converted photons are called the signal and idler photons (indexed 1 and 2). The energy conservation condition requires that $\omega_0=\omega_1+\omega_2$. The phase matching condition $\vec{k}_0 = \vec{k}_1 + \vec{k}_2$ (where $\vec{k}_i = \omega_i \vec{n}_i / c$; $\vec{n}_i$ = index of refraction) governs the conversion efficiency.

The Hamiltonian for the interaction is given by [Shen84]

$$H_I = -i\hbar\chi^{(2)}\left(\hat{a}_1^\dagger\hat{a}_2^\dagger\hat{a}_0 - \hat{a}_0^\dagger\hat{a}_1\hat{a}_2\right), \tag{2.26}$$

and the time dependence of the field operators by

$$\frac{d}{dt}\hat{a}_i(t) = \frac{i}{\hbar}\left[\hat{H}_I, \hat{a}_i\right]. \tag{2.27}$$

When taken to first order in $\chi^{(2)}$ and to first order in the interaction time $t_I$ during which the modes propagate through the parametric medium, the above equation may be written as a transformation equation relating incoming modes, indexed A, to outgoing modes, indexed B (see fig. 2.3):

$$\hat{a}_{iB} = \hat{a}_{iA} + t_I \frac{i}{\hbar}\left[\hat{H}_I, \hat{a}_{iA}\right]. \tag{2.28}$$

We note here that the operator $\hat{a}^\dagger_1\hat{a}_1$ - $\hat{a}^\dagger_2\hat{a}_2$ commutes with $H_I$. In other words, the difference in the signal and idler photon numbers is conserved before and after the parametric transformation [Gra84]. This is not the case with the beamsplitter transformation (eqtn. 2.23), and will be the underlying basis for the generation of intensity correlated beams.

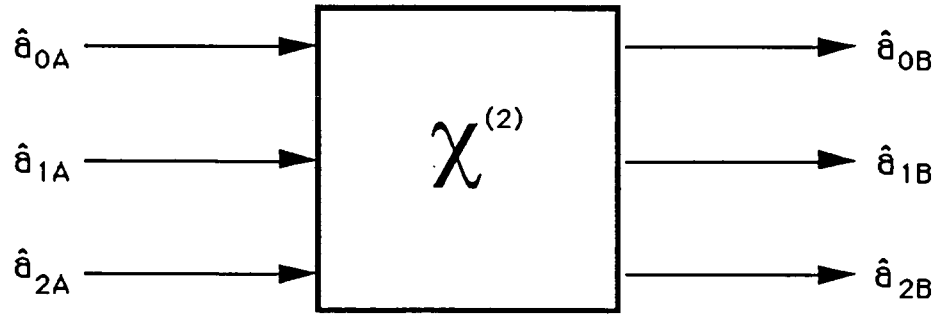


Figure 2.3: Parametric transformation of incoming modes (indexed A) to outgoing modes (indexed B).

For a linearized treatment of the field fluctuations, valid when the parametric interaction is a small perturbation (see eqtn. 2.7 for definition of the field fluctuation operator), the parametric input-output transformation may be written as

$$\begin{aligned}
\delta\hat{a}_{0B} &= \delta\hat{a}_{0A} + \chi\langle\hat{a}_{1A}\rangle\delta\hat{a}_{2A} + \chi\langle\hat{a}_{2A}\rangle\delta\hat{a}_{1A} \\
\delta\hat{a}_{1B} &= \delta\hat{a}_{1A} - \chi\langle\hat{a}_{0A}\rangle\delta\hat{a}^{\dagger}_{2A} - \chi\langle\hat{a}^{\dagger}_{2A}\rangle\delta\hat{a}_{0A} \\
\delta\hat{a}_{2B} &= \delta\hat{a}_{2A} - \chi\langle\hat{a}_{0A}\rangle\delta\hat{a}^{\dagger}_{1A} - \chi\langle\hat{a}^{\dagger}_{1A}\rangle\delta\hat{a}_{0A}
\end{aligned} \tag{2.29}$$

where $\chi=\chi^{(2)}t_I$. We note here that the field fluctuation operators are governed by the same transformation equations as the field variables are in a classical treatment [Shen84].

**f:** ***Semi-classical theory***

We adopt a semi-classical theory in which a quantum ensemble average is replaced by a classical ensemble average over an appropriately chosen probability distribution. In particular, we replace the field operators $\hat{a}_i(t)$ by classical stochastic variables $\alpha_i(t)$ whose classical ensemble average coincides with the quantum ensemble average when the field operators are symmetrically ordered [Rey90, Fab90]. The appropriate probability distribution is the Wigner distribution $W(\alpha,\alpha^*)$ defined by

$$\left\langle X\left(\hat{a},\hat{a}^{\dagger}\right)\right\rangle = \int d\alpha d\alpha^*\ X(\alpha,\alpha^*)\ W(\alpha,\alpha^*)\ , \tag{2.30}$$

where X an arbitrary symmetrically ordered function of $\hat{a}$ and $\hat{a}^{\dagger}$. The advantage of using the Wigner distribution over other semi-classical distributions (such as the Glauber P distribution or the Q distribution) is that it is invariant under a linear canonical transformation [Eke90]. That is, for incoming modes A and outgoing modes B that are linearly related and obey the same commutation relations:

$$\left[\hat{a}_{iB},\hat{a}^{\dagger}_{iB}\right] = \left[\hat{a}_{iA},\hat{a}^{\dagger}_{iA}\right]\ , \tag{2.31}$$

then

$$W\left(\alpha_{iB},\alpha^*_{iB}\right) = W\left(\alpha_{iA},\alpha^*_{iA}\right)\ . \tag{2.32}$$

Quantum and classical ensemble averages (left and right hand side of eqtn. 2.30) which coincide before the transformation, therefore, coincide after the transformation as well.

A linear canonical transformation is defined as

$$\hat{a}_{iB} = \sum_j \left(u_{i,j}\hat{a}_{jA} + v_{i,j}\hat{a}^{\dagger}_{jA}\right)\ , \tag{2.33}$$

where u and v satisfy the relations

$$\begin{aligned}
\sum_j \left(u_{i,j}u^*_{k,j} - v_{i,j}v^*_{k,j}\right) &= \delta_{i,k} \\
\sum_j \left(u_{i,j}v_{k,j} - v_{i,j}u_{k,j}\right) &= 0
\end{aligned} \tag{2.34}$$

We note that the input-output transformations for field fluctuations through a beamsplitter (eqtn. 2.23) and through a weakly parametric medium (eqtn. 2.29) are both linear canonical, as defined above. We use in our experiments an optical parametric oscillator (OPO) which comprises exactly these two elements. The semi-classical formalism is therefore well adapted for the treatment of the OPO, in the weak interaction limit. The fields are written as

$$\alpha_i(t) = \bar{\alpha}_i + \delta\alpha_i(t) \ , \tag{2.35}$$

where $\bar{\alpha}_i$ is the steady state field amplitude and $\delta\alpha_i$ are classical stochastic field fluctuations. The classical input field fluctuations are chosen to fit the Wigner distribution of the corresponding quantum input field fluctuations. The resultant output field fluctuations are obtained then from the OPO transformation given by equations 2.23 and 2.29. This method is closely connected to the linear stability analysis [Gib85], and has been shown to be equivalent to the standard quantum linearization method for the case of parametric oscillators [Rey89, Fab90a].

The operator we will be interested in is the intensity operator defined by eqtn. 2.6. This is not symmetrically ordered. In a linear fluctuation analysis where the mean fields are large, however, one may approximate the intensity operator by a symmetrically ordered intensity operator

$$\hat{I}(t) \equiv \tfrac{1}{2}\left(\hat{a}^\dagger(t)\hat{a}(t) + \hat{a}(t)\hat{a}^\dagger(t)\right) \ , \tag{2.36}$$

and hence by the intensity function

$$I(t) = |\alpha(t)|^2 \ . \tag{2.37}$$

The corresponding intensity fluctuations are

$$\delta I(t) = \bar{\alpha}\,\delta\alpha^*(t) + \bar{\alpha}^*\,\delta\alpha(t) \ . \tag{2.38}$$

For a mean field that is real, the real and imaginary components of the fluctuations correspond to the fluctuation components in phase and out of phase with the mean field. The first we denote as the amplitude fluctuations $\delta p$, and the second by the phase fluctuations $\delta q$, defined by

$$\delta p(t) = \delta\alpha(t) + \delta\alpha^*(t) \quad \leftrightarrow \quad \delta p(\Omega) = \delta\alpha(\Omega) + \delta\alpha^*(-\Omega) \tag{2.39}$$

$$\delta q(t) = -i\left(\delta\alpha(t) - \delta\alpha^*(t)\right) \quad \leftrightarrow \quad \delta q(\Omega) = -i\left(\delta\alpha(\Omega) - \delta\alpha^*(-\Omega)\right) \tag{2.40}$$

and the intensity fluctuations become

$$\delta I(t) = \bar{\alpha}\,\delta p(t) \quad \leftrightarrow \quad \delta I(\Omega) = \bar{\alpha}\,\delta p(\Omega) \ . \tag{2.41}$$

The corresponding intensity noise spectrum is related to the amplitude fluctuations through

$$S_I(\Omega) = \bar{I}\, S(\Omega) \tag{2.42}$$

where

$$S(\Omega) = \langle \delta p(-\Omega)\delta p(\Omega) \rangle \tag{2.43}$$

and S is equal to 1 when $\delta p$ represents vacuum fluctuations, that is, S is normalized to the shot noise level. (<..> will denote from now on a *classical* ensemble average.) We note that in this semi-classical formalism, the fluctuations $\delta p$ represent both the classical and quantum field fluctuations. $S(\Omega)$ less than 1 indicates that the fluctuations are smaller than the vacuum fluctuations whereas $S(\Omega)$ larger than 1 indicates the presence of extra classical noise.

We emphasize that in this semi-classical approach, the Wigner distribution of a vacuum mode is non-zero. We refer, for example, to the measurement of the shot noise level described in section II.c (fig. 2.1). When beam 2A is in the vacuum state, then $\delta I_{B1} - \delta I_{B2} = |\ \overline{\alpha_{1A}}|\delta p_{vac}$, obtaining in the same way the shot noise level of beam 1A, that is, $S_{B1-B2}(\Omega) = \bar{I}_{1A}$. The shot noise is interpreted in this semi-classical approach as the result of the vacuum fluctuations coupled through the unused beamsplitter port.

### g: *Amplitude and intensity correlations*

Throughout this thesis we will be interested in the amplitude and intensity correlations between two beams (indexed 1 and 2). We introduce for this an amplitude correlation parameter $S_{12}(\Omega)$, where

$$S_{12}(\Omega) = \langle \delta p_1(-\Omega)\delta p_2(\Omega) \rangle\ . \tag{2.44}$$

One notes

$$S_{12}{}^*(\Omega) = S_{12}(-\Omega) = S_{21}(\Omega) \tag{2.45}$$

obtaining a Cauchy-Schwartz inequality:

$$|S_{12}(\Omega)|^2 \le S_1(\Omega)S_2(\Omega)\ . \tag{2.46}$$

$S_{12}(\Omega)$ provides a scale for the amplitude correlations. The lower bound $S_{12}=0$ means the two beams are uncorrelated. The upper bound $|S_{12}| = \sqrt{S_1 S_2}$ means the fluctuations $\delta p_1$ and $\delta p_2$ are proportional ($\delta p_1 = \varkappa \delta p_2$), such as when the two beams are perfectly correlated ($\varkappa = 1$, $S_{12} = S_1 = S_2$) or when they are perfectly anti-correlated ($\varkappa = -1$, $S_{12} = -S_1 = -S_2$). Two beams are defined as balanced if $S_1 = S_2$ and $S_{12}(\Omega) = S_{21}(\Omega)$.

$S_{12}(\Omega)$ is not a true spectrum since it is complex in general (and for this reason is written in italics). The meaning of its real and imaginary components may be understood by defining the cross-correlation function

$$C_{12}(\tau) = \langle \delta p_1(t)\delta p_2(t+\tau) \rangle \tag{2.47}$$

The relations then hold:

$$\begin{aligned} \mathrm{Re}\, S_{12}(\Omega) &= \mathrm{F.T.}\left(C_{12}^{\mathrm{even}}(\tau)\right) \\ \mathrm{Im}\, S_{12}(\Omega) &= \mathrm{i\ F.T.}\left(C_{12}^{\mathrm{odd}}(\tau)\right) \end{aligned} \tag{2.48}$$

$C_{12}(\tau)$ may be measured using the standard procedure of Hanbury Brown and Twiss [Han74]. Asymmetry about the $\tau = 0$ axis corresponds to a relative time delay between the two beams. The imaginary component of $S_{12}(\Omega)$ is a measure, therefore, of this time delay, which may be frequency dependent in general. If beams 1 and 2 are balanced, then no such time delay exists and $S_{12}(\Omega)$ is real.

An alternative means for evaluating the amplitude correlations between beams 1 and 2 is from their amplitude difference fluctuations, defined by

$$\delta p_{-}(\Omega) = \tfrac{1}{\sqrt{2}}\left(\delta p_1(\Omega) - \delta p_2(\Omega)\right) . \tag{2.49}$$

The noise spectrum of these amplitude difference fluctuations is written

$$S_{1-2}(\Omega) = \left\langle \delta p_{-}(-\Omega)\delta p_{-}(\Omega)\right\rangle \tag{2.50}$$

where $S_{1\text{-}2}(\Omega)$ is normalized to the associated shot noise level of a beam with intensity $2\sqrt{\bar{I}_1\,\bar{I}_2}$. The relation between $S_{1\text{-}2}(\Omega)$ and $S_{12}(\Omega)$ is given by

$$S_{1-2}(\Omega) = \tfrac{1}{2}\left(S_1(\Omega) + S_2(\Omega)\right) - \mathrm{Re}\, S_{12}(\Omega) . \tag{2.51}$$

It is clear from the above equation that $S_{1\text{-}2}(\Omega)$ provides only incomplete information on the beam correlations when the two beams are unbalanced, since it is independent of the imaginary component of $S_{12}(\Omega)$. It presents the notable advantage, however, that it is a genuine (real) noise spectrum.

In experiment, photodetection monitors not the amplitude fluctuations but rather the intensity fluctuations of beams 1 and 2. The observed intensity difference fluctuations are defined by:

$$\delta I_{-}(\Omega) = \left(\delta I_1(\Omega) - \delta I_2(\Omega)\right) \tag{2.52}$$

and the corresponding noise spectrum of these intensity difference fluctuations is written

$$S_{I1-I2}(\Omega) = \left\langle \delta I_{-}(-\Omega)\, \delta I_{-}(\Omega)\right\rangle . \tag{2.53}$$

The relation between $S_{I1\text{-}I2}(\Omega)$ and $S_{12}(\Omega)$ is given by

$$S_{I1-I2}(\Omega) = \left(\bar{I}_1\, S_1(\Omega) + \bar{I}_2\, S_2(\Omega)\right) - 2\sqrt{\bar{I}_1\,\bar{I}_2}\ \mathrm{Re}\, S_{12}(\Omega) . \tag{2.54}$$

One notes that when the beams are of equal intensity, then $S_{I1\text{-}I2}(\Omega)$ is equal to $2\bar{I}S_{1\text{-}2}(\Omega)$.

# III. OPTICAL PARAMETRIC OSCILLATOR

A theoretical model is presented for the operation of an OPO [Bru77]. We use the semi-classical formalism introduced above, which is well adapted for treating the OPO as a quantum network where incoming mode fluctuations are transformed into outgoing mode fluctuations. The equations governing the mode transformations through the parametric medium were introduced in section II.e (eqtns. 2.29). We start here by presenting the equations governing the mode evolutions when this medium is placed inside an optical cavity. These equations are linearized and the correlations in the intensity fluctuations of the outgoing modes 1 and 2 are analyzed

### a: *Evolution equations*

We examine OPO operation in the non-degenerate regime where the downconverted modes 1 and 2 are separable either by frequency or by polarization. The modes inside and outside the cavity are coupled through a port mirror. Incoming mode 0 is the pump field channel and incoming modes 1 and 2 are assumed in the vacuum state, while outgoing modes 1 and 2 are the channels for the signal and idler output fields (see fig. 3.1).

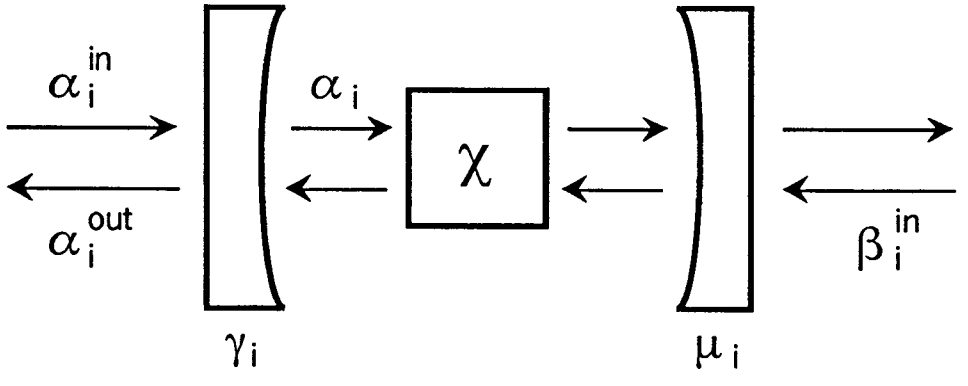


Figure 3.1: Input-output model for OPO.

For small one-pass gain and losses, the semi-classical equations governing the field evolutions during a cavity round trip of time $\tau$ (assumed the same for all fields) can be written as first order differential equations [Fab89]:

$$\begin{aligned}
\tau\dot{\alpha}_0 &= -2\chi\alpha_1\alpha_2 - \gamma_0'(1+i\varphi_0)\alpha_0 + \sqrt{2\gamma_0}\ \alpha_0^{in} + \sqrt{2\mu_0}\ \beta_0^{in} \\
\tau\dot{\alpha}_1 &= 2\chi\alpha_0\alpha_2^* - \gamma_1'(1+i\varphi_1)\alpha_1 + \sqrt{2\gamma_1}\ \alpha_1^{in} + \sqrt{2\mu_1}\ \beta_1^{in} \\
\tau\dot{\alpha}_2 &= 2\chi\alpha_0\alpha_1^* - \gamma_2'(1+i\varphi_2)\alpha_2 + \sqrt{2\gamma_2}\ \alpha_2^{in} + \sqrt{2\mu_2}\ \beta_2^{in}
\end{aligned} \tag{3.1}$$

The first terms on the right represent the parametric coupling due to the nonlinear susceptibility $\chi$ of the medium (see section II.e). The second terms represent the field damping due in part to the port mirror ($\gamma_i$) and in part to extraneous cavity losses ($\mu_i$), where $\gamma_i'=\gamma_i+\mu_i$. The damping parameters $\gamma_i$ ($\gamma_i << 1$) are defined by the reflection and transmission coefficients of the port mirror through

$$r_i = 1-\gamma_i \quad ; \quad t_i = \sqrt{2\gamma_i} \tag{3.2}$$

and $\mu_i$ are similarly related to a "transmission" of the second mirror which models all other loss mechanisms (see fig. 3.1). Detuning is also included in eqtns. 3.1 where the phase shift from resonance of each field after a round trip is $\gamma_i'\varphi_i$. The last terms in eqtns. 3.1 represent the coupling to the external modes, respectively through the port mirror (external modes $\alpha_i^{in}$) and through the losses (external modes $\beta_i^{in}$). Note: the fields here are assumed to propagate in the single circulation direction shown in fig. 3.1. When both circulation directions are taken into account in a linear cavity, the above equations remain essentially unchanged except that the "in" terms comprise incident fields from both directions and $\chi$ must be adjusted by a form factor that takes into account the spatial structure of the modes inside the cavity [Deb90].

The outgoing fields $\alpha_i^{out}$ are obtained simply from the superposition of the intracavity fields leaking out the port mirror and the incident fields reflected directly off the port mirror (see eqtn. 2.23; port mirror is assumed high reflectivity).

$$\alpha_i^{out} = \sqrt{2\gamma_i}\ \alpha_i - \alpha_i^{in} \ . \tag{3.3}$$

b: *Stationary solutions for OPO*

The stationary mean field solutions $\overline{\alpha_i}$ are obtained from eqtns. 3.1, noting that all the external mean fields are equal to zero except for the pump field $\overline{\alpha_0}^{in}$. When the pump field is large enough, the solutions for $\overline{\alpha_1}$ and $\overline{\alpha_2}$ become non-zero and the OPO is set in oscillation [Fab89]. This oscillation imposes the constraints that the detunings are equal ($\varphi_1=\varphi_2=\varphi$). The sum of the signal and idler phase is fixed, whereas the difference undergoes phase diffusion, much as does the phase of standard laser beam. We neglect in this treatment this phase diffusion since it occurs on time scales much longer than the fluctuation dynamics that are of interest [Cou91]. A phase reference is chosen so that the stationary solutions for the intracavity signal and idler fields are real:

$$\begin{aligned}
\overline{\alpha}_0 &= \frac{\sqrt{\gamma_1'\gamma_2'}}{2\chi}(1+i\varphi) \\
\overline{\alpha}_1 &= \frac{1}{2\chi}\sqrt{\gamma_0'\gamma_2'(\sigma-1)} \\
\overline{\alpha}_2 &= \frac{1}{2\chi}\sqrt{\gamma_0'\gamma_1'(\sigma-1)}
\end{aligned} \tag{3.4}$$

where $\sigma$ is a pump parameter related to the incident pump amplitude $|\overline{\alpha_0}^{in}|$ by

$$\sigma = \left[ \frac{8\chi^2 \gamma_0 |\overline{\alpha_0}^{in}|^2}{\gamma_0' \gamma_1' \gamma_2'} - (\varphi_0 + \varphi)^2 \right]^{1/2} + \varphi_0 \varphi \tag{3.5}$$

and $\sigma = 1$ corresponds to OPO threshold. The stationary solutions above provide the working point about which the field fluctuations will be studied.

### c: *Field Fluctuations in Balanced OPO*

The dynamics of the field fluctuations derive essentially from the linear expansion of eqtns. 3.1. To begin, we skirt a general treatment of the OPO and adopt several simplifications. In particular, we assume the OPO is balanced ($\gamma_1=\gamma_2=\gamma$ and $\mu_1=\mu_2=\mu$). The signal and idler output intensities are therefore the same. In addition, we assume the pump is resonant with the cavity ($\varphi_0=0$), considered here in a bad cavity limit ($\gamma' << \gamma_0'$). These assumptions do not greatly affect the underlying physics but considerably simplify an analysis. A more general treatment of the OPO will be made in section III.d.

The intracavity fields are written in a symmetric and antisymmetric form

$$\alpha_\pm = (\alpha_1 \pm \alpha_2)/\sqrt{2} \tag{3.6}$$

and the rate equations for the intracavity fields separate conveniently into

$$\begin{aligned} \tau \delta\dot{\alpha}_+ &= -2\gamma'(i - \varphi) Im(\delta\alpha_+) - \lambda \delta\alpha_+ + \sqrt{2\gamma}\ \delta\alpha_+^{in} + \sqrt{2\mu}\ \delta\beta_+^{in} + \sqrt{2\lambda}\ \delta\alpha_p^{in} \\ \tau \delta\dot{\alpha}_- &= -2\gamma'(1 + i\varphi) Re(\delta\alpha_-) + \sqrt{2\gamma}\ \delta\alpha_-^{in} + \sqrt{2\mu}\ \delta\beta_-^{in} \end{aligned} \tag{3.7}$$

where $\lambda = 2\gamma'(\sigma - 1)$ characterizes the parametric coupling to the pump mode and

$$\delta\alpha_p^{in} = \sqrt{\xi_0}\ \delta\alpha_0^{in} + \sqrt{1 - \xi_0}\ \delta\beta_0^{in} \tag{3.8}$$

is an effective pump noise; $\xi_0 = \gamma_0/\gamma_0'$.

An advantage of these equations is that the incident fluctuations are all uncorrelated with one another. The symmetric and anti-symmetric components of the fields can be treated therefore independently (see fig. 3.2).

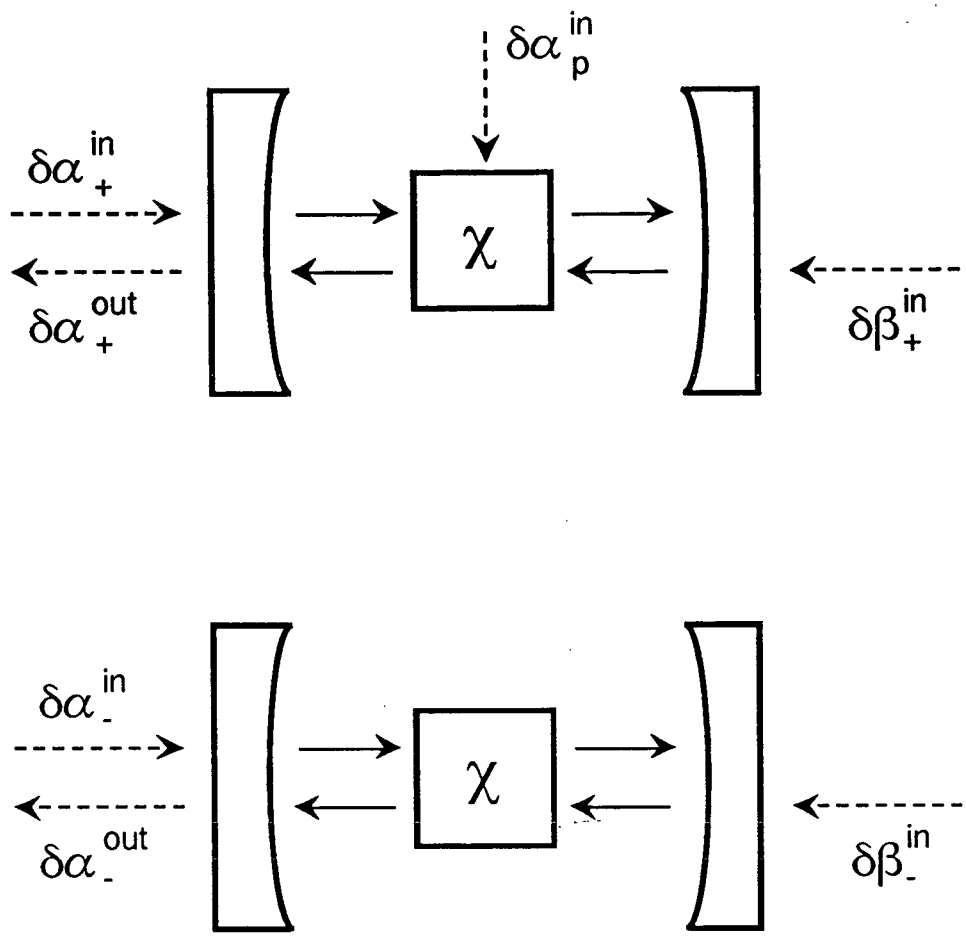


Figure 3.2: Input-output model for symmetric (top) and anti-symmetric (bottom) OPO field fluctuations.

The intracavity fields are coupled to external modes via three channels, admitting the vacuum fluctuations $\delta\alpha_{\pm}^{in}$ through the port mirror, the vacuum fluctuations $\delta\beta_{\pm}^{in}$ through the other intracavity losses, and the fluctuations in the pump modes $\delta\alpha_p^{in}$ through the parametric conversion process. The intracavity fluctuations are driven only by these incident fluctuations. This differs from the standard quantum treatment of the OPO where the intracavity fluctuations are said to originate entirely from the nonlinear medium [Fab90a, Dru81]. With eqtn. 3.3 relating the output fields to the input intracavity fields, the OPO can be viewed as a quantum network [Yur84] where input fluctuations are transferred to output fluctuations.

By writing the complex fields as column matrices with real and imaginary components [*Re* $\delta\alpha$, *Im* $\delta\alpha$], and taking the Fourier transform, eqtns. 3.7 become

$$\left[\delta\alpha_+^{out}(\Omega)\right] = \left(\sqrt{2\gamma}\ C_+ - 1\right)\left[\delta\alpha_+^{in}(\Omega)\right] + \sqrt{2\mu}\ C_+\left[\delta\beta_+^{in}(\Omega)\right] + \sqrt{2\lambda}\ C_+\left[\delta\alpha_p^{in}(\Omega)\right]$$
$$\left[\delta\alpha_-^{out}(\Omega)\right] = \left(\sqrt{2\gamma}\ C_- - 1\right)\left[\delta\alpha_-^{in}(\Omega)\right] + \sqrt{2\mu}\ C_-\left[\delta\beta_-^{in}(\Omega)\right] \qquad (3.9)$$

where the coefficients multiplying each column matrix are the transfer functions for the separate input fluctuations. The matrices $C_\pm$ are defined here as

$$C_+ = \frac{\sqrt{2\gamma}}{2\gamma'(\sigma + i\Omega)(\sigma - 1 + i\Omega)}\begin{bmatrix} \sigma + i\Omega & \varphi \\ 0 & \sigma - 1 + i\Omega \end{bmatrix}$$
$$C_- = \frac{\sqrt{2\gamma}}{2\gamma' i\Omega(1 + i\Omega)}\begin{bmatrix} i\Omega & 0 \\ -\varphi & 1 + i\Omega \end{bmatrix} \qquad (3.10)$$

with $\Omega$ normalized to the cavity bandwidth $2\gamma'/\tau$.

It is apparent from the above equations that both quadratures of the fluctuations remain uncoupled on resonance ($\varphi$=0) during the transfer process and are subject to simple low pass filtering in the cavity with differing time constants. At frequencies above the cavity bandwidth, $C_\pm$ tends towards zero and the output fluctuations tend towards the vacuum level. The output fluctuations are attributable then only to those input contributions that are not subject to cavity filtering, that is, to the vacuum fluctuations reflected directly off the port mirror.

The effects of being off resonance ($\varphi \neq 0$) are a reduction in the pump parameter $\sigma$ (see eqtn. 3.5), and a mixing of the field quadratures.

We note here that the intracavity and output mean fields are of the same (real) phase. The real and imaginary components of their fluctuations correspond therefore to their amplitude and phase fluctuations respectively. The intensity noise power spectra of the output fields are obtained from eqtn. 2.43. For the case of a balanced OPO, one finds $S_1$=$S_2$=S, where

$$S(\Omega) = 1 + \frac{\xi/2}{(\sigma - 1)^2 + \Omega^2}\left[\frac{\sigma(2 - \sigma)}{1 + \Omega^2} + \frac{\varphi^2(2\sigma - 1)}{\sigma^2 + \Omega^2}\right] \qquad (3.11)$$

and $\xi = \gamma/\gamma'$. $S(\Omega)$ is plotted in fig. 3.3 for $\xi = 1$ and for various values of $\sigma$, without (solid lines) and with (dotted lines) a detuning of $\varphi = 0.5$. The shot noise level is 1. For $\sigma$ near threshold ($\sigma \approx 1$), there is a large amount of excess noise at low frequencies. This excess noise is reduced with larger pumping. For $\sigma = 2$, the noise spectrum of each output beam is exactly at the shot noise level. For $\sigma > 2$, the noise spectrum drops below the shot noise level and approaches 1/2 at zero frequency for large $\sigma$. The output signal and idler fields become then sub-Poissonian. In general, detuning plays little role except that of introducing some additional noise at low frequency.

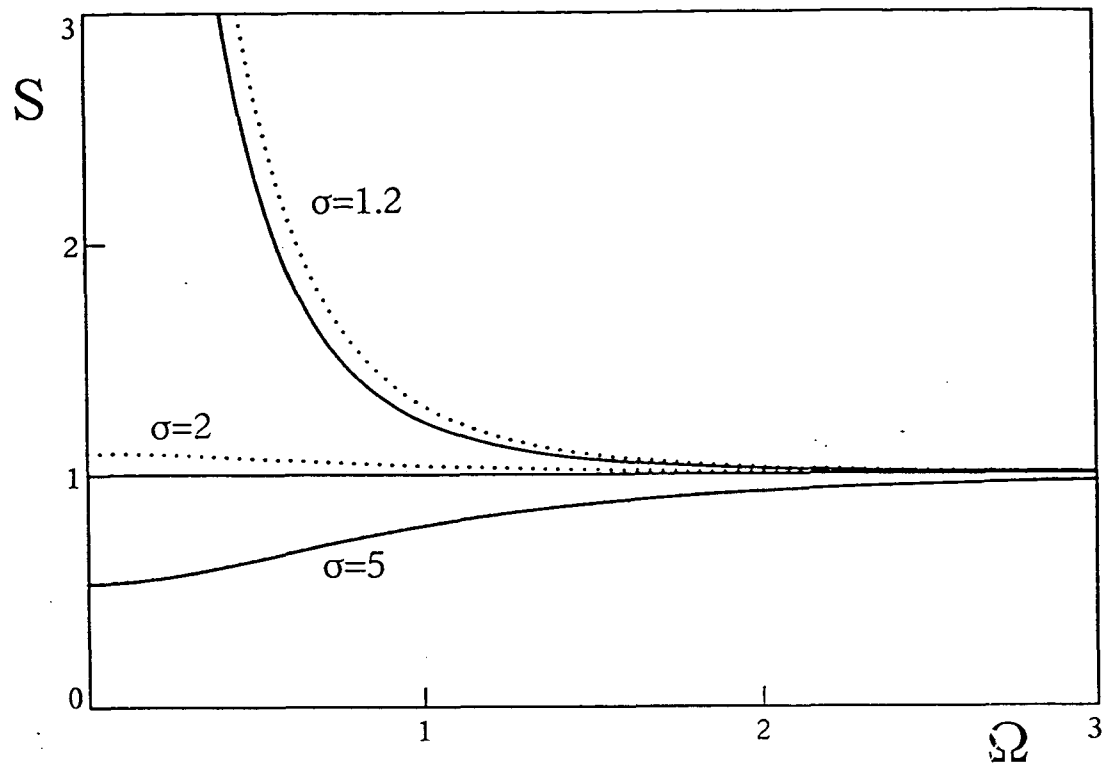


Figure 3.3: Single beam intensity spectrum with (dotted) and without (solid) a cavity detuning of $\varphi = 0.5$.

We are interested in the intensity correlations of the output fields. It was shown in section II.g that when the output fields are balanced, then the amplitude difference spectrum $S_{1-2}(\Omega)$ provides complete information on these correlations. Again, from section II.g,

$$S_{1-2}(\Omega) = \langle \delta p_-(-\Omega)\delta p_-(\Omega) \rangle \tag{3.12}$$

where $S_{1-2}(\Omega)$ is normalized to its associated shot noise level. It is simply related to $S_{12}$ by

$$S_{1-2}(\Omega) = S(\Omega) - S_{12}(\Omega) \tag{3.13}$$

since $S_{12}(\Omega)$ is real when the OPO is balanced.

$S_{1-2}(\Omega)$ provides a scale for the intensity correlations, in which $S_{1-2}=0$ indicates the signal and idler beams are perfectly correlated and $S_{1-2}=S$ indicates they are uncorrelated. For $0 < S_{1-2} < 1$, we will denote the correlations as "quantum". For $1 \leq S_{1-2} < S$, we will denote the correlations as "classical". We note that the latter situation can be obtained for two beams emanating from a beamsplitter, whereas the former cannot (see chapter I).

When all input fluctuations correspond to vacuum fluctuations (including the pump field fluctuations when the pump field is in a coherent state), one finds from eqtns. 3.9 and 3.12:

$$S_{1-2}(\Omega) = 1 - \frac{\xi}{1+\Omega^2} \,. \tag{3.14}$$

The intensity difference spectrum is *below* the shot noise level for frequencies within the cavity bandwidth. The signal and idler beams have non-classical correlations then, and their intensities are correlated to the quantum level. For this reason, they are commonly referred to as "twin beams" [Rey87]. We note that the intensity difference spectrum $S_{1-2}(\Omega)$ is independent of the pumping level and of detuning. At zero frequency, it is simply equal to the proportion $1-\xi$ of the cavity damping due to extraneous losses (see fig. 3.4).

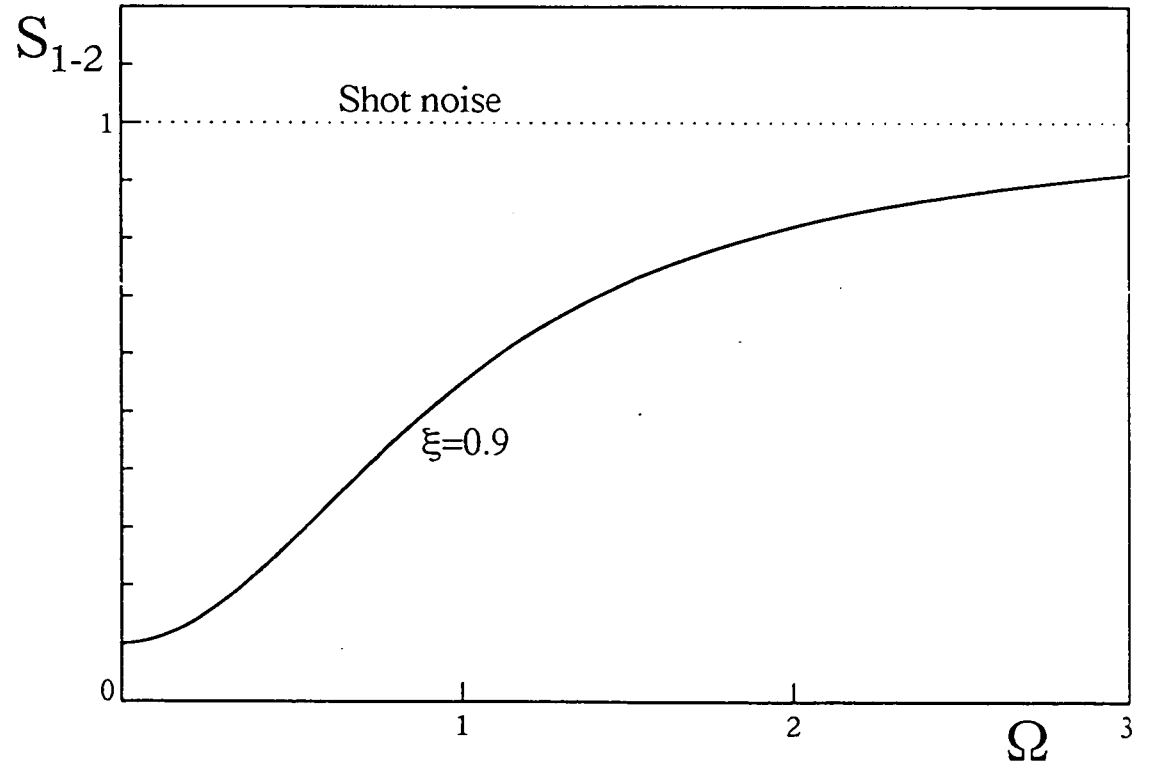


Figure 3.4: Intensity difference noise spectrum. $\xi = 0.9$.

In the event of detector loss, parametrized by a detector quantum efficiency $\eta$ (see section II.d), then the observed noise spectra are modified to

$$\begin{aligned} \tilde{S}(\Omega) &= \eta S(\Omega) + 1 - \eta \\ \tilde{S}_{1-2}(\Omega) &= \eta S_{1-2}(\Omega) + 1 - \eta \end{aligned} \tag{3.15}$$

and it suffices to replace $\xi$ in eqtns. 3.11 and 3.14 by $\eta\xi$.

An intuitive interpretation of the above results is afforded with a photon model [Rey87a]. In this model, the signal and idler photons are generated simultaneously inside the OPO cavity (see fig. 3.5). On generation, therefore, they are perfectly correlated. These photons remain inside the cavity for an average cavity storage time $\tau_c$. Because their exit times are independent, however, the number of photons in the output signal and idler beams remain equal only when counted over times longer than the cavity storage time. In other words, the correlation in the output beams subsists only for frequencies below the cavity bandwidth $\tau_c^{-1}$. This correlation is degraded by losses which undermine the pairwise detection of the output photons. These losses occur both in the OPO (parametrized by $\xi$) and in the detectors (parametrized by $\eta$). This photon model will be examined in more detail in the Appendix.

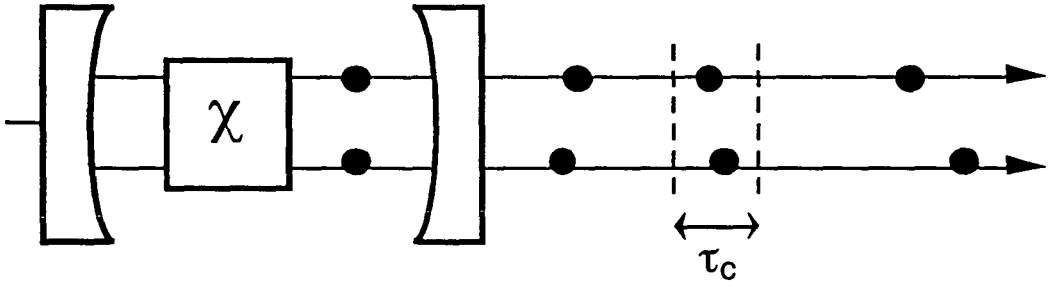


Figure 3.5: Photon model for twin beam decorrelation. Cavity storage time is $\tau_c$.

### d: *Field Fluctuations in Unbalanced OPO*

The above calculations can be extended to include pump detuning ($\varphi_0 \neq 0$) and cavity imbalance ($\gamma_1' \neq \gamma_2'$), which is the general case in experiment. The beams generated by the OPO are no longer balanced and the evolution equations for the fluctuations do not conveniently separate into symmetric and anti-symmetric components. In addition, the amplitude difference spectrum $S_{1-2}(\Omega)$ provides only incomplete information on the field correlations, and an evaluation of $S_{12}(\Omega)$ is necessary (see section II.g).

We calculate now $S_1$, $S_2$, and $S_{12}$ for an unbalanced, detuned OPO with the assumption only that the round trip time $\tau$ is the same for all modes and that we are still in a "bad cavity limit" for the pump mode. The stationary fields are those calculated in section III.b. The intracavity pump fluctuations are

$$\delta\alpha_0(\Omega)=\frac{1}{\sqrt{\gamma_0'}}\frac{1-i\varphi_0}{1+\varphi_0^2}\left(\sqrt{2}\,\delta\alpha_p^{in}(\Omega)-\sqrt{\gamma_1'(\sigma-1)}\delta\alpha_1(\Omega)-\sqrt{\gamma_2'(\sigma-1)}\delta\alpha_2(\Omega)\right) \quad (3.16)$$

where $\sigma$ and $\delta\alpha_p^{in}$ are defined from eqtns 3.5 and 3.8 and $\Omega$ is again normalized to the cavity bandwidth $2\gamma'/\tau$. We define the variables

$$\gamma'=\sqrt{\gamma_1'\gamma_2'}\ ,\ \xi_i=\frac{\gamma_i}{\gamma_i'}\ ,\ \zeta=\sqrt{\frac{\gamma_1'}{\gamma_2'}}\ ,\ \text{and}\ \ \varkappa=\frac{\sigma-1}{1+\varphi_0^2}\ . \quad (3.17)$$

The intracavity signal and idler fluctuations are then

$$\left(\frac{\zeta}{2}(1+i\varphi)+\frac{\zeta\varkappa}{2}(1-i\varphi_0)+i\Omega\right)\delta\alpha_1(\Omega)=\frac{1}{2}(1+i\varphi)\delta\alpha_2{}^*(-\Omega)-\frac{\varkappa}{2}(1-i\varphi_0)\delta\alpha_2(\Omega)+$$

$$+\frac{1}{\sqrt{2\gamma'}}\left(\sqrt{\zeta\varkappa}\,\frac{1-i\varphi_0}{\sqrt{1+\varphi_0^2}}\delta\alpha_p^{in}(\Omega)+\sqrt{\xi_1\varkappa}\,\delta\alpha_1^{in}(\Omega)+\sqrt{(1-\xi_1)\varkappa}\,\delta\beta_1^{in}(\Omega)\right). \quad (3.18)$$

We separate these fluctuations into their amplitude and phase components. The pump field is phase shifted with reference to the (real) signal and idler fields, and its respective phase and amplitude components are

$$\delta p_p^{in}(\Omega)=\frac{1}{\sqrt{1+\varphi_0^2}}\left((1-i\varphi_0)\delta\alpha_p^{in}(\Omega)+(1+i\varphi_0)\delta\alpha_p^{*in}(-\Omega)\right) \quad (3.19)$$

$$\delta q_p^{in}(\Omega)=\frac{1}{\sqrt{1+\varphi_0^2}}\left(-(i+\varphi_0)\delta\alpha_p^{in}(\Omega)+(i-\varphi_0)\delta\alpha_p^{*in}(-\Omega)\right) \quad (3.20)$$

which satisfy the relations

$$\left\langle\delta p_p^{in}(-\Omega)\delta p_p^{in}(\Omega)\right\rangle=\left\langle\delta q_p^{in}(-\Omega)\delta q_p^{in}(\Omega)\right\rangle=1 \quad (3.21)$$

$$\left\langle\delta p_p^{in}(\Omega)\delta q_p^{in}(\Omega)\right\rangle=0\ . \quad (3.22)$$

The above equations may be condensed into matrix form, where we write

$$[\delta\alpha]=\begin{bmatrix}\delta p_1\\ \delta q_1\\ \delta p_2\\ \delta q_2\end{bmatrix}\ ,\ \left[\delta\alpha_p^{in}\right]=\begin{bmatrix}\delta p_p^{in}\\ \delta q_p^{in}\end{bmatrix} \quad (3.23)$$

and define

$$M=\frac{1}{2}\begin{bmatrix}(1+\varkappa)\zeta & (\varkappa\varphi_0-\varphi)\zeta & \varkappa-1 & \varkappa\varphi_0-\varphi\\ (\varphi-\varkappa\varphi_0)\zeta & (1+\varkappa)\zeta & -\varkappa\varphi_0-\varphi & \varkappa+1\\ \varkappa-1 & \varkappa\varphi_0-\varphi & (1+\varkappa)/\zeta & (\varkappa\varphi_0-\varphi)/\zeta\\ -\varkappa\varphi_0-\varphi & \varkappa+1 & (\varphi-\varkappa\varphi_0)/\zeta & (1+\varkappa)/\zeta\end{bmatrix} \tag{3.24}$$

$$T=\begin{bmatrix}\sqrt{\xi_1\zeta} & 0 & 0 & 0\\ 0 & \sqrt{\xi_1\zeta} & 0 & 0\\ 0 & 0 & \sqrt{\xi_2/\zeta} & 0\\ 0 & 0 & 0 & \sqrt{\xi_2/\zeta}\end{bmatrix} \tag{3.25}$$

L is identical to T with $\xi_i$ replaced by 1-$\xi_i$, and

$$Q=\begin{bmatrix}\sqrt{\varkappa\zeta} & 0\\ 0 & \sqrt{\varkappa\zeta}\\ \sqrt{\varkappa/\zeta} & 0\\ 0 & \sqrt{\varkappa/\zeta}\end{bmatrix}. \tag{3.26}$$

The equations relating the input and output fluctuations become then

$$(M+i\Omega)[\delta\alpha]=\frac{1}{\sqrt{2\gamma'}}\left(T\left[\delta\alpha^{in}\right]+L\left[\delta\beta^{in}\right]+Q\left[\delta\alpha_p^{in}\right]\right) \tag{3.37}$$

$$\left[\delta\alpha^{out}\right]=\sqrt{2\gamma'}\,T[\delta\alpha]-\left[\delta\alpha^{in}\right] \tag{3.28}$$

obtaining for the output fluctuations

$$\left[\delta\alpha^{out}\right]=\left(T(M+i\Omega)^{-1}T-1\right)\left[\delta\alpha^{in}\right]+T(M+i\Omega)^{-1}\left(L\left[\delta\beta^{in}\right]+Q\left[\delta\alpha_p^{in}\right]\right). \tag{3.29}$$

Denoting $V(\Omega)$ the covariance matrix defined by

$$V(\Omega)=\left\langle[\delta\alpha(-\Omega)][\delta\alpha(\Omega)]^t\right\rangle \tag{3.30}$$

we are interested in the components

$$S_1(\Omega)=V_{1,1}^{out}(\Omega)\ ,\ S_2(\Omega)=V_{3,3}^{out}(\Omega)\ ,\ \text{and}\ S_{12}(\Omega)=V_{3,1}^{out}(\Omega)\ . \tag{3.31}$$

For input fluctuations at the vacuum level, that is for $V^{in}(\Omega)=1$, one finds

$$V^{out}(\Omega)=1+T(M-i\Omega)^{-1}D\left(M^t+i\Omega\right)^{-1}T \tag{3.32}$$

where

$$D = \left(T^2 + L^2 + QQ^t - M - M^t\right) = \begin{bmatrix} 0 & 0 & 1 & \varphi \\ 0 & 0 & \varphi & -1 \\ 1 & \varphi & 0 & 0 \\ \varphi & -1 & 0 & 0 \end{bmatrix}. \tag{3.33}$$

These calculations are completed using a symbolic mathematics program. Defining the parameters U,V, and Z as

$$\begin{aligned} U &= \varphi - \varkappa\varphi_0 \\ V &= (1+\varkappa)^2 + U^2 \\ Z &= \tfrac{1}{2}(\zeta + 1/\zeta) \end{aligned} \tag{3.34}$$

one obtains finally

$$S_i(\Omega) = 1 + \frac{\xi_i}{2}\left( \frac{Z^2V(2(1+\varkappa) + 2\varphi U - V) - U^2\left(1+\varphi^2\right) + \Omega^2\left(1 - \varkappa^2 + U^2 + 2\varkappa\varphi U\right)}{Z^2\left(\left(1+2\Omega^2\right)(1+\varkappa) + \varphi U - V\right)^2 + \Omega^2\left(Z^2V + \varkappa - \varphi U - \Omega^2\right)^2} \right) \tag{3.35}$$

and

$$S_{12}(\Omega) = 1 + \frac{\sqrt{\xi_1\xi_2}}{2}\left( \frac{S_r - i\Omega(\zeta - 1/\zeta)S_i}{Z^2\left(\left(1+2\Omega^2\right)(1+\varkappa) + \varphi U - V\right)^2 + \Omega^2\left(Z^2V + \varkappa - \varphi U - \Omega^2\right)^2} \right) \tag{3.36}$$

with

$$\begin{aligned} S_r = {} & Z^2\left(V(V - 2\varkappa - 2\varphi U) + 2\varphi U(2 + 2\varkappa + \varphi U) - 2U^2\right) - U^2\left(1+\varphi^2\right) + \\ & + 2Z^2\Omega^2\left(V + 2(1+\varkappa)\varphi U - 2U^2\right) + \Omega^2\left(1 + \varkappa^2 - 2U^2 - 2\varkappa\varphi U + 2\Omega^2\right) \end{aligned} \tag{3.37}$$

and

$$S_i = Z^2V(1 + \varkappa + \varphi U) - U^2\left(1+\varphi^2\right) + \Omega^2(1 + \varkappa - \varphi U) \tag{3.38}$$

These results are rather cumbersome. One notes immediately, however, that if the output efficiencies $\xi_1$ and $\xi_2$ are equal, then $S_1$ and $S_2$ are equal and independent of of the imbalance parameter $\zeta$ (for the pumping parameter $\sigma$ constant). $S_1(\Omega)$ is plotted in fig. 3.6 for $\xi_1 = \xi_2 = 0.9$ and for various values of $\sigma$, without (solid lines) and with (dotted lines) an imbalance of $\zeta = 0.5$. The effect of imbalance is a slight reduction in the bandwidth where $S_1(\Omega)$ is different from the shot noise level.

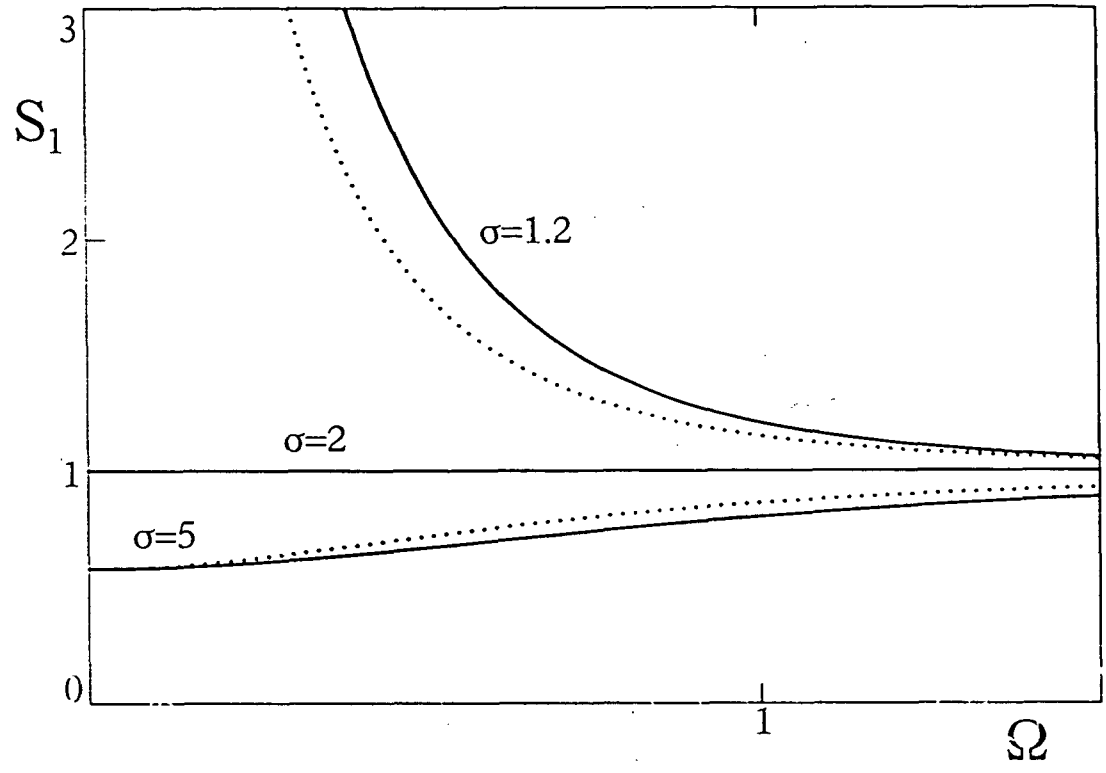


Figure 3.6: Single beam intensity spectrum with (dotted) and without (solid) a cavity imbalance of $\zeta = 0.5$.

Pump detuning plays a similar role as does the signal and idler detuning, and has the effect only of introducing additional noise in $S_i(\Omega)$ at low frequencies.

In fig. 3.7, the real (curves a) and imaginary (curve b) components of $S_{12}(\Omega)$ are plotted for the balanced case $\zeta=1$ (dotted) and for the unbalanced case $\zeta=0.5$ (solid), with parameters $\sigma = 1.2$, $\xi_1 = \xi_2 = 0.9$, and no detuning. (For $\zeta = 1$, the imaginary component of $S_{12}$ is zero.) At non-zero frequencies, the imaginary component of $S_{12}(\Omega)$ may be interpreted as a frequency dependent time delay between the output twin beams, linked to their different cavity storage times when the cavity is unbalanced (see section II.g). At zero frequency, $S_{12}(\Omega)$ is real, meaning that $S_{1-2}(\Omega=0)$ is independent of cavity imbalance. This may be interpreted from the fact that the zero frequency spectrum corresponds to an intensity difference measurement over a time interval that is theoretically infinite. The effect of a time delay between the output twin beams that is finite, therefore, becomes negligible.

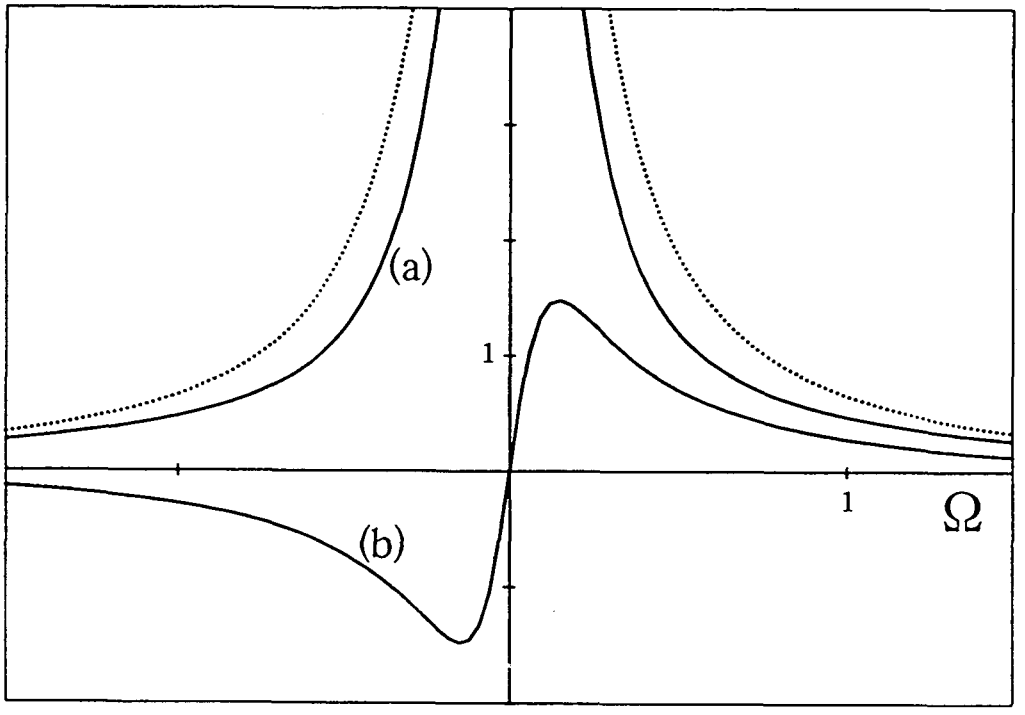


Figure 3.7: Real (curves a) and imaginary (curve b) components of $S_{12}(\Omega)$, with (solid) and without (dotted) a cavity imbalance of $\zeta = 0.5$.

The associated spectrum of the amplitude difference fluctuations $S_{1-2}(\Omega)$ is shown in fig. 3.8 without (solid line) and with (dotted line) cavity imbalance. Again, the effect of the imbalance is a reduction in the bandwidth where $S_{1-2}(\Omega)$ is below the shot noise level.

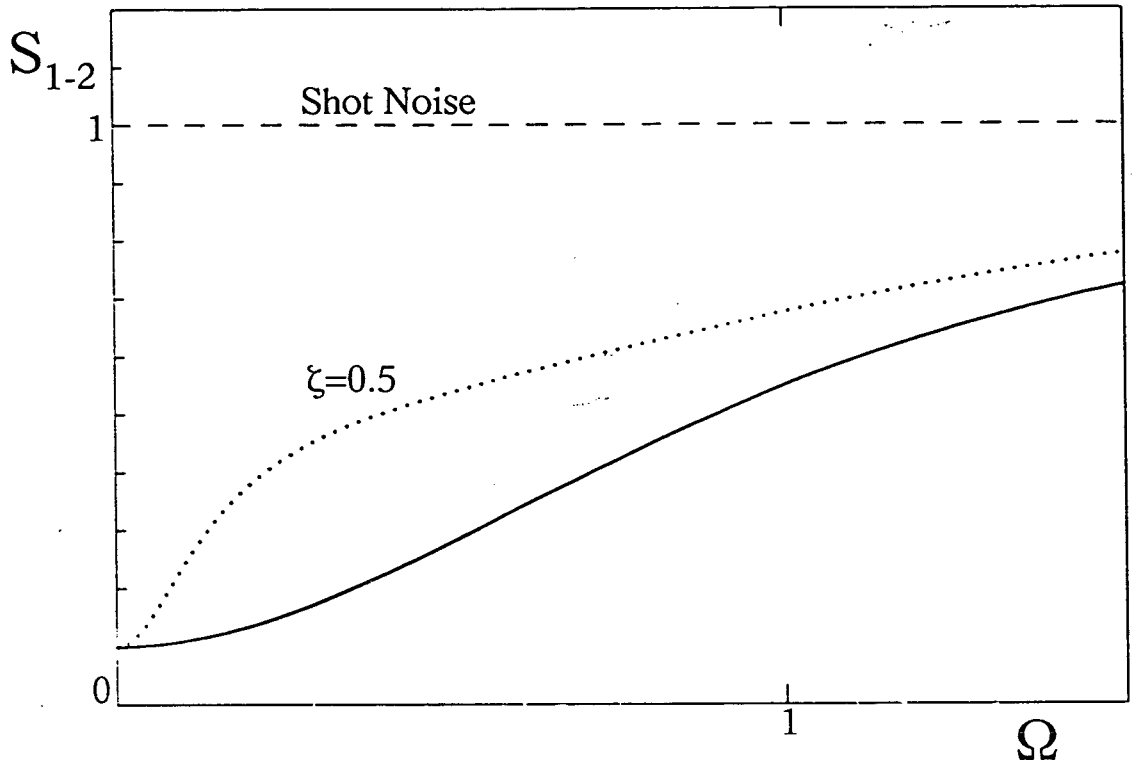


Figure 3.8: Amplitude difference spectrum $S_{1-2}(\Omega)$ with (dotted) and without (solid) cavity imbalance.

We note that when the twin beams are unbalanced, $S_{1-2}(\Omega)$ remains independent of pump or twin beam detuning. It varies slightly as a function of pumping, however, .and as $\sigma$ approaches 1, the bandwidth of the noise reduction becomes reduced. We note also from section II.? that when the twin beams are unbalanced, $S_{1-2}(\Omega)$ is only a measure of the amplitude difference fluctuations and no longer a measure of the intensity difference fluctuations. For this reason it cannot be measured directly and can only be inferred from a measurement of $S_1$, $S_2$, and $S_{12}$. We display for comparison in fig. 3.9 the amplitude difference spectrum $S_{1-2}(\Omega)$ (solid curves), and the *normalized* intensity difference spectrum $S_{I1-I2}(\Omega)$ (dotted curves) given by

$$S_{I_1-I_2}(\Omega) = \frac{1}{2}\left(\sqrt{\frac{\xi_1}{\xi_2}}\,S_1(\Omega) + \sqrt{\frac{\xi_2}{\xi_1}}\,S_2(\Omega)\right) - \mathrm{Re}S_{12}(\Omega) \qquad (3.39)$$

where $S_{I1-I2}(\Omega)$ is defined from eqtn. 2.54, divided by the shot noise level $2\sqrt{I_1 I_2}$. The curves are shown for the parameters $\sigma$=1.05, $\xi_1$=0.85, $\xi_2$=0.95, and $\zeta$=0.5 or 1. We observe in the intensity difference spectrum a significant increase in noise power at low

frequency due to the imperfect cancelling of the classical excess noise in the twin beams. At higher frequencies where the excess noise is smaller $S_{I1-I2}(\Omega)$ tends towards $S_{1-2}(\Omega)$.

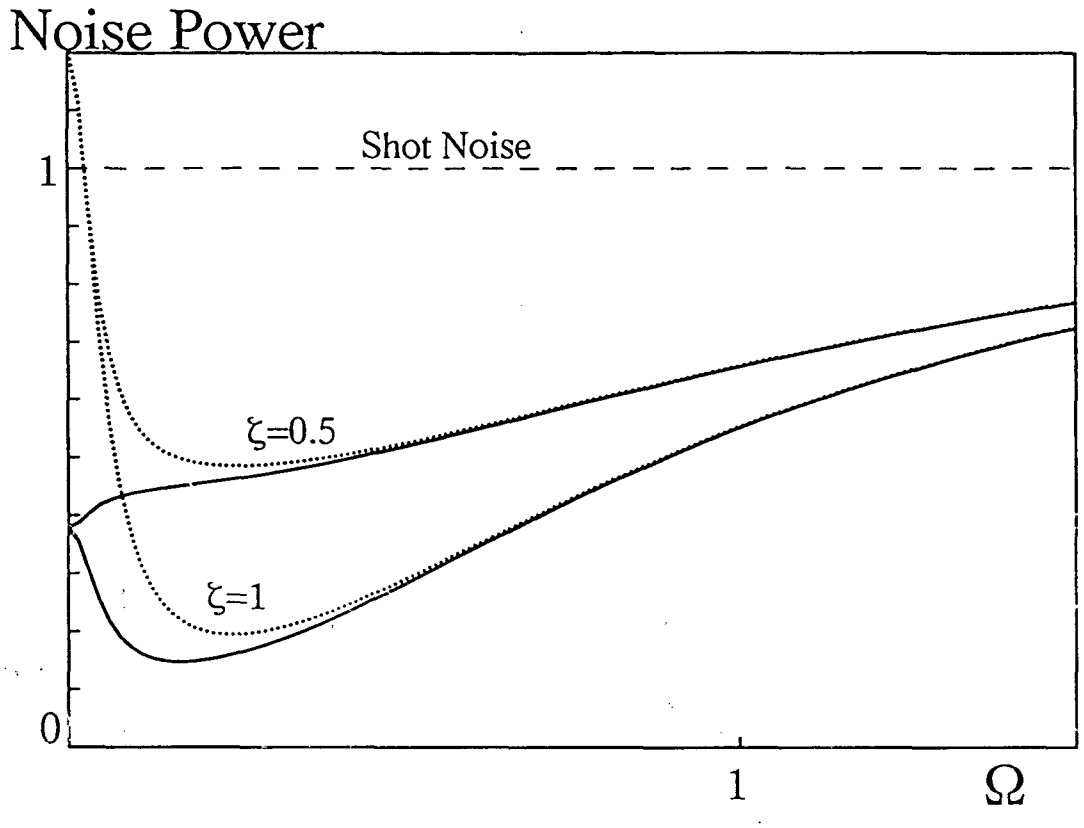


Figure 3.9: Amplitude (solid) and intensity (dotted) difference spectra with $\xi_1 = 0.85$ and $\xi_2 = 0.95$ ($\sigma = 1.05$).

In general, we find that both imbalance and detuning play only the minor role of introducing additional noise within the cavity bandwidth, and do not change the qualitative results of the previous section for the amplitude fluctuations in a balanced OPO. For the intensity fluctuations, they result in an increase in noise only at small frequencies. For the experiments which we will discuss below, imbalance and detuning are small (except for twin beam detuning), and to a good approximation their effects may be neglected at larger frequencies.

# IV. TWIN BEAM EXPERIMENT

The intensity correlations in OPO twin beams were originally verified to be below the shot noise limit in an experiment using an OPO made of a type II phase matched KTP crystal inside an optical cavity, for which a 30% quantum noise reduction was demonstrated in the twin beam intensity difference spectrum [Hei87]. Limits to this noise reduction stemmed principally from a low OPO output efficiency $\xi$ (see eqtn. 3.14). Improvements in the experiment resulted in progressively larger quantum noise reductions reported at 69% [Deb89] and finally at 86% in the experiment we present below. Much of the details of the former experiment are described in reference [Deb90], including also the design of the pump laser used in the former experiment. We briefly outline these and concentrate in this chapter on the improvements made to obtain an 86% noise reduction, as well as a verification of the quantum nature of the intensity correlations. This is presented in the reprint below, and is followed by supplementary experimental details on the pump laser, the OPO layout, the detection mechanism, and the twin beam separation mechanism.

****** Reprint: Optics Letters ******

# Improvements in the observed intensity correlation of optical parametric oscillator twin beams

J. Mertz, T. Debuisschert,* A. Heidmann, C. Fabre, and E. Giacobino

*Laboratoire de Spectroscopie Hertzienne, Université Pierre et Marie Curie, B.P. 74, F75252 Paris Cedex 05, France*

Received April 19, 1991

We report an observed quantum noise reduction of 86% (8.5 dB) near 3 MHz in the intensity difference between the twin beams generated by a nondegenerate type II optical parametric oscillator operating above threshold.

Over the years progressively larger amounts of quantum noise reduction have been reported. A particular line of interest has been in the generation of twin beams.[1] These exhibit intensity difference fluctuations that are reduced below the standard quantum level. A variety of methods have been used for the generation of twin beams, all of which rely on a mechanism of photon pair creation by parametric generation. Most experiments so far have used a $\chi^{(2)}$ nonlinearity, in which a single pump photon is downconverted into simultaneous signal and idler photons. The first experiments of this kind were limited to the low-intensity photon-counting regime, where the time correlation was analyzed in the parametric fluorescence of a crystal.[2,3] Intensity difference noise reduction was recently observed by using parametric fluorescence[4] and pulse amplification.[5,6] Alternative experiments were conducted in which the crystal was placed in an optical cavity and cw parametric oscillation was investigated. Noise reduction with an optical parametric oscillator (OPO) was first observed using a type II phase-matched crystal[7,8] and later with a type I phase-matched crystal.[9,10] Twin beams have also been generated by using parametric oscillation with a $\chi^{(3)}$ nonlinearity.[11]

In this Letter we present an improvement on our result for the type II phase-matching experiment using a $\chi^{(2)}$ nonlinearity and report an observed noise reduction of 86%. Particular attention is paid to loss mechanisms in our apparatus that deteriorate the pairwise detection of the twin-beam photons. We also include further verification that this noise reduction is robust with respect to the OPO parameters.

The quantum noise reduction in the signal and idler intensity difference spectrum is Lorentzian in profile. For noise frequencies outside the cavity bandwidth, the noise spectrum returns to the standard quantum (or shot-noise) limit. For zero noise frequency, the noise spectrum can ideally be reduced to zero. Degradations from this ideal are due to optical losses in the system, which occur both in the optical cavity, where the twin beams are generated, and in the photodiodes, where they are detected. The measured intensity difference spectrum, normalized to its associated shot-noise level, is[12]

$$S(\Omega) = 1 - \frac{\xi\eta}{1 + \Omega^2}, \tag{1}$$

where $\Omega$ is the noise frequency normalized to the cavity bandwidth, $\eta$ is the photodiode quantum efficiency, and $\xi = T/(T + L)$ is the OPO output coupling efficiency ($T$ is the transmission coefficient of the cavity coupling mirror and $L$ is the extraneous cavity loss coefficient). Improvements in the noise reduction are concomitant to improvements in both $\xi$ and $\eta$. We address these in turn.

The OPO in our experiment consists of a 7-mm-long KTP crystal inside an optical cavity. The intracavity loss coefficient $L$ is estimated to be 0.6% (double pass). This is fixed by unavoidable absorption in the crystal and imperfections in the optical coatings. A large output coupling efficiency $\xi$ is then obtained by an increase in the output transmission $T$ of the coupling mirror. A constraint is imposed by the fact that the OPO must remain above threshold for the available pumping power. The threshold pumping power scales approximately as $(T + L)^2/F_p$, where $F_p$ is the cavity pump finesse (assumed large). An increase in $T$ must be accompanied, therefore, by an increase in $F_p$. This supposes that the pump and downconverted modes are resonant for the same cavity length, which requires proper coating of the cavity mirrors. The cavity pump finesse is ~25, significantly higher than the finesse of ~5 in our previous experiment. For a larger pump finesse, heating of the KTP crystal becomes a problem, and the OPO could not be held triply resonant. The output mirror transmission coefficient is 6.3% for the infrared, which gives $\xi = 0.91$. (The input mirror is high-reflection coated for the infrared.)

The detectors are InGaAs p-i-n photodiodes with quantum efficiencies $\eta$ measured at 0.90. An improvement in these quantum efficiencies is obtained in this experiment by tilting the photodiodes in the polarization planes of the separated infrared beams so that they approach the Brewster angle. With a tilt angle of 45°, $\eta$ was measured near 0.94. Larger tilt angles gave rise to spurious edge effects.

0146-9592/91/161234-03$5.00/0 

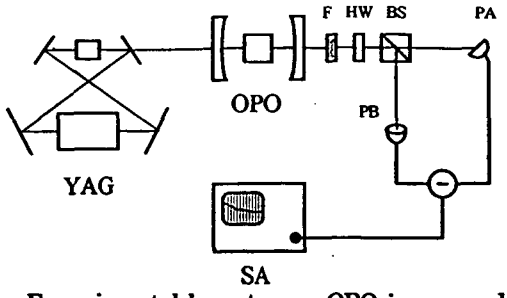


Fig. 1. Experimental layout: an OPO is pumped by an intracavity-doubled YAG laser. F, dichroic filter; HW, half-wave plate; BS, polarizing beam splitter; PA and PB, tilted photodiodes; SA, spectrum analyzer.

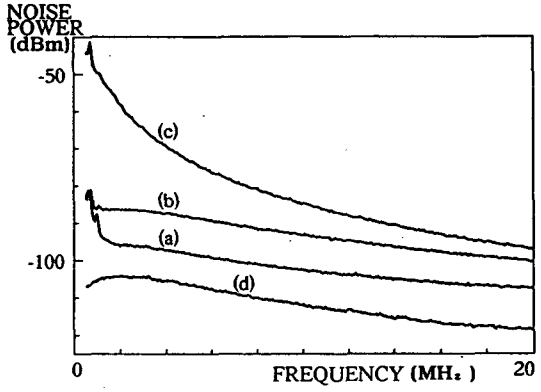


Fig. 2. Experimental results: curve (a), the twin-beam intensity difference power spectrum; curve (b), the associated shot-noise power spectrum; curve (c), a single-beam power spectrum; curve (d), the electrical noise floor.

The layout of the experiment is shown in Fig. 1. The OPO is pumped above threshold by a single-mode cw intracavity-doubled Nd:YAG laser with a power of 460 mW. The KTP crystal in the OPO is temperature stabilized and type II phase matched so that the downconverted twin infrared beams are cross polarized with nondegenerate wavelengths separated by less than 1 nm. The OPO cavity mirrors are 35 mm apart, with radii of curvature of 20 mm. A Nd:YAG laser was chosen over the previously used argon-ion pump laser for two reasons. First, the KTP crystal is phase matched to twice the frequency of a YAG crystal. The frequencies of the downconverted twin beams are therefore closer to degeneracy in this experiment, which reduces the imbalance between the twin-beam intensities to less than 2%. The second reason is that the upconverted pump light generated by the YAG is not cavity confined and is therefore insensitive to backreflections from the OPO, improving the OPO stability.

The pump beam passing through the OPO is blocked by a dichroic filter. The outgoing downconverted beams are separated by a polarizing beam splitter and monitored by the photodiodes. The dc portions of the photodiode signals (dc to 30 kHz) are added and used to actively stabilize the intensity of the twin beams, each held at 3 mW by piezoelectric control of the cavity length. The gain balance of the dc summing network is better than 1%. The ac portions of the photodiode signals (0.5–20 MHz) are subtracted, and the resultant ac intensity difference is recorded on a spectrum analyzer. The balance of the ac differencing network was verified by modulating the twin-beam intensities and observing the reduction in the modulation peak when the intensities were subtracted. The total optical and electrical common-mode rejection was found to be −35 dB up to 6 MHz and −30 dB up to 20 MHz. A half-wave plate is inserted before the beam splitter to rotate the polarizations of the twin beams. When these are turned 45° with respect to the axes of the beam splitter, the polarizing beam splitter effectively becomes a 50% beam splitter.[7] By rotating the half-wave plate, we conveniently toggle between a measurement of the intensity difference spectrum and a measurement of the shot-noise spectrum while remaining locked on the same OPO resonance.

The results of our experiment are shown in Fig. 2. Large single-beam excess noise is observed, owing to OPO pumping close to threshold. The intensity difference spectrum, normalized to the shot-noise spectrum (after both spectra are corrected for the electrical noise), is presented on a linear scale in Fig. 3. A noise reduction is observed up to 86% (±1%) below the shot-noise level, near 3 MHz. To our knowledge, this is the maximum amount of quantum noise reduction observed to date, comparable with the results reported by Richardson *et al.*[13]

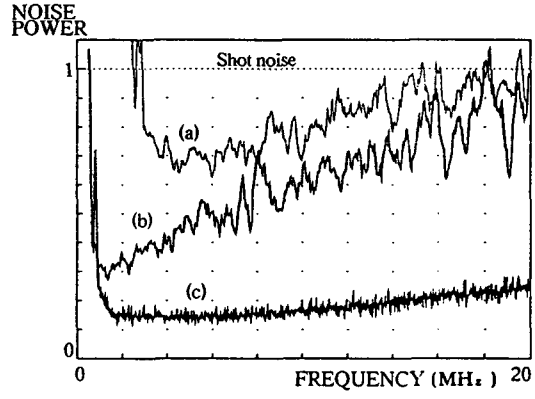


Fig. 3. Progressive increase in quantum noise reduction: curve (a), our results from 1987 ($\xi$ = 0.57, $\eta$ = 0.90); curve (b), our results from 1989 ($\xi$ = 0.77, $\eta$ = 0.90); curve (c), our present results ($\xi$ = 0.91, $\eta$ = 0.94).

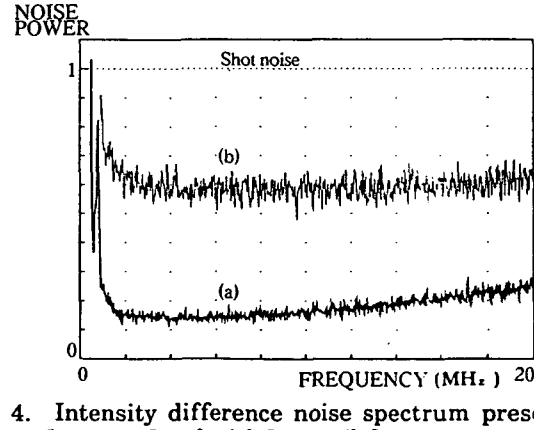


Fig. 4. Intensity difference noise spectrum presented without [curve (a)] and with [curve (b)] 50% attenuation of twin beams. The intensity incident upon the photodiodes is held constant.

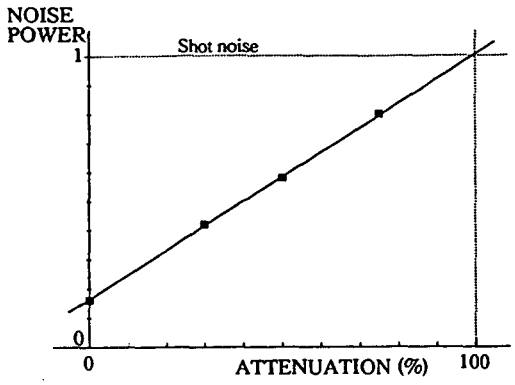


Fig. 5. Intensity difference noise spectrum at 10 MHz as a function of the attenuation of twin beams. The points are experimental data, and the solid line is a linear fit. OPO parameters are held constant.

If we correct for the photodiode efficiencies, this corresponds to a quantum noise reduction of 91% (11 dB) at the OPO output. Our present result is given along with our previous results[7,8] to illustrate the dependence of the noise reduction on the parameters $\xi$ and $\eta$. Note that our progressive improvement of $\xi$ is accompanied by a progressive improvement in the bandwidth of the noise reduction. Given the OPO parameters, our present noise reduction is expected to fit a Lorentzian of width 45 MHz. The rise in the noise reduction at low frequency is due to the imbalance in the twin-beam intensities.

We concentrate in this Letter on illustrating the quantum nature of the noise reduction by introducing calibrated losses in the twin beams before the beam splitter and observing the change in the resultant noise spectrum. It is well known that the intensity noise spectrum normalized to the shot-noise level tends linearly toward one with attenuation. Two conditions were examined: first, the intensity of the twin beams incident upon the photodiodes was held constant; second, the intensity of the twin beams immediately after the OPO was held constant.

In the first case, the OPO cavity detuning is adjusted to compensate for the attenuation in the twin beams. This changes the OPO oscillation threshold and effectively changes the OPO pumping level. Results in Fig. 4 are the normalized intensity difference spectra with and without attenuation. The gradual rise in curve (b) below 5 MHz may be attributed to a slight birefringence in the attenuation plate, which accentuates the imbalance between the twin beams. The threshold pump powers for the OPO oscillation are estimated to be 430 mW for curve (a) and 390 mW for curve (b). One observes that the noise reduction below the shot-noise level is exactly halved on attenuation (above 5 MHz), which verifies that the correlation in the twin beams is independent of OPO detuning or pumping level.

The second case examined is that for which the OPO detuning (and therefore the pumping level above threshold) is held constant. Insertion of auxiliary loss at the OPO output then measures properties strictly of the twin beams, since the source is unchanged. Figure 5 shows the power levels of the normalized intensity difference spectrum for various attenuations, measured at the noise frequency of 10 MHz. Again, one observes a linear dependence of the spectrum on attenuation. The shot-noise level is intersected for an attenuation extrapolated to 100%, as expected, providing an auxiliary verification of the calibration of this shot-noise level.

The results of this Letter represent a new performance level for quantum noise reduction and establish the OPO as a practical source of highly correlated twin beams. The correlation is robust and limited only by optical losses, which in this system are extremely low. Additional features that the generated output beams are laserlike and intense make OPO's particularly convenient for experimental applications, such as absorption spectroscopy[4,9,10,14] and the generation of nonclassical light by active control of one beam with the other.[15]

We are grateful to S. Reynaud and L. Hilico for helpful discussions. This research was partially supported by EEC contract ESPRIT BRA 3186, and the research of J. Mertz was supported by Direction des Recherche Etudes et Techniques contract 90/1333/A000. The Laboratoire de Spectroscopie Hertzienne is part of the Laboratoire de l'Ecole Normale Supérieure, which is associated with the Centre National de la Recherche Scientifique.

*Present address, Thomson CSF, Domaine de Corbeville, 91404 Orsay, France.

## References

1. S. Reynaud, C. Fabre, and E. Giacobino, J. Opt. Soc. Am. B **4**, 1520 (1987).
2. D. C. Burnham and D. L. Weinberg, Phys. Rev. Lett. **25**, 84 (1970).
3. S. Friberg, C. K. Hong, and L. Mandel, Phys. Rev. Lett. **54**, 2011 (1984).
4. J. G. Rarity and P. R. Tapster, in *International Conference on Quantum Electronics*, Vol. 8 of 1990 OSA Technical Digest Series (Optical Society of America, Washington, D.C., 1990), p. 8.
5. I. Abram, R. K. Raj, J. L. Oudar, and G. Dolique, Phys. Rev. Lett. **57**, 2516 (1987).
6. O. Aytur and P. Kumar, Phys. Rev. Lett. **65**, 1551 (1990).
7. A. Heidmann, R. J. Horowicz, S. Reynaud, E. Giacobino, C. Fabre, and G. Camy, Phys. Rev. Lett. **59**, 2555 (1987).
8. T. Debuisschert, S. Reynaud, A. Heidmann, E. Giacobino, and C. Fabre, Quantum Opt. **1**, 3 (1989).
9. N. C. Wong, K. W. Leong, and J. H. Shapiro, Opt. Lett. **15**, 891 (1990).
10. C. D. Nabors and R. M. Shelby, Phys. Rev. A **40**, 1428 (1989).
11. M. Vallet, M. Pinard, and G. Grynberg, Europhys. Lett. **11**, 739 (1989).
12. C. Fabre, E. Giacobino, A. Heidmann, and S. Reynaud, J. Phys. **50**, 1209 (1989).
13. W. H. Richardson, S. Machida, and Y. Yamamoto, in *International Conference on Quantum Electronics*, Vol. 8 of 1990 OSA Technical Digest Series (Optical Society of America, Washington, D.C., 1990), p. 395.
14. J. J. Snyder, E. Giacobino, C. Fabre, A. Heidmann, and M. Ducloy, J. Opt. Soc. Am. B **7**, 2132 (1990).
15. J. Mertz, A. Heidmann, C. Fabre, E. Giacobino, and S. Reynaud, Phys. Rev. Lett. **64**, 2897 (1990).

a: *Pump laser: experimental details*

The pump laser used in this experiment is a house built intracavity doubled cw Nd:YAG laser. The design of the laser is detailed in reference [Deb90]. The YAG head is a Micro-contrôle 904 model operating at 14 amps in a 50 cm figure eight oscillator (see fig. 4.1). A single circulation direction for the YAG beam is ensured by an intracavity Faraday element (15 mm Terbium Gallium Garnet rod) and Brewster plate. Single mode operation is ensured by an etalon of thickness 5 mm and spatial mode filtering by an aperture. Stabilization of the YAG frequency to an external Fabry-Perot etalon is maintained by piezoelectric control of the YAG cavity length using the Hänsch-Couillaud stabilization technique [Hän80]. The residual infrared frequency jitter was measured to be 125 kHz.

The intracavity doubling element is a 7 mm long KTP crystal, temperature stabilized to 26.6° C. This crystal is situated at a YAG beam waist with Rayleigh length adjusted to the length of the crystal The generated frequency doubled light has a wavelength 532 nm and a power in a linear polarization 500 mW.

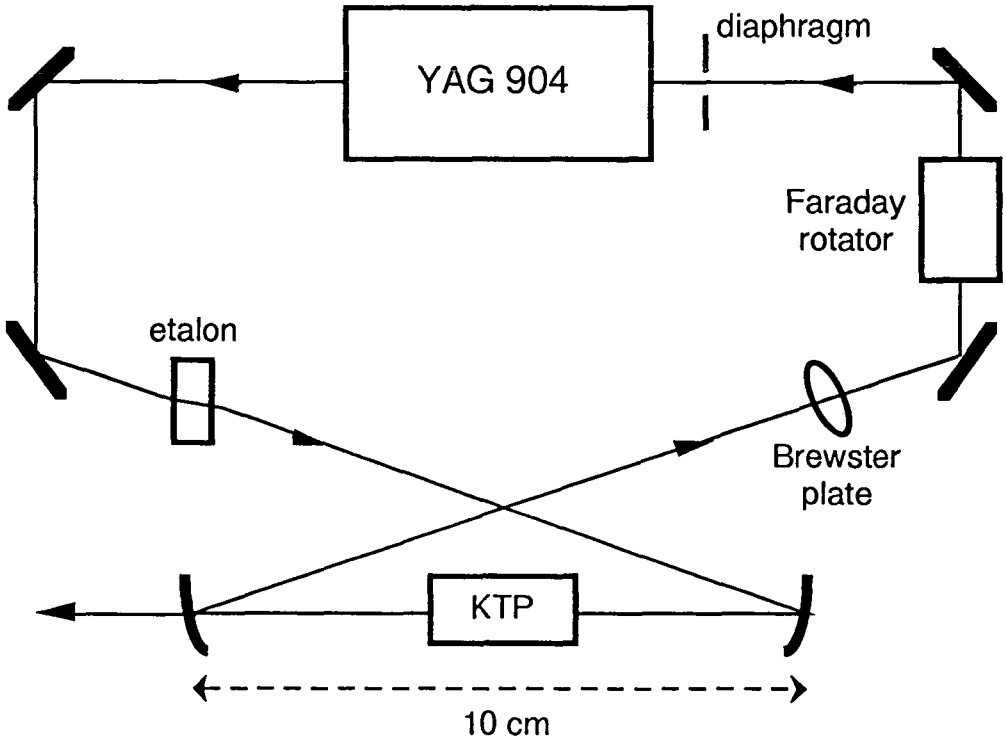


Figure 4.1: Intracavity doubled Nd:YAG laser.

**b: *OPO: experimental details***

The optical parametric oscillator used in our experiment is configured slightly differently than the one in fig. 3.1, in that the pump field is incident from one end of the cavity whereas the signal and idler fields exit out the other end (see fig. 4.2).

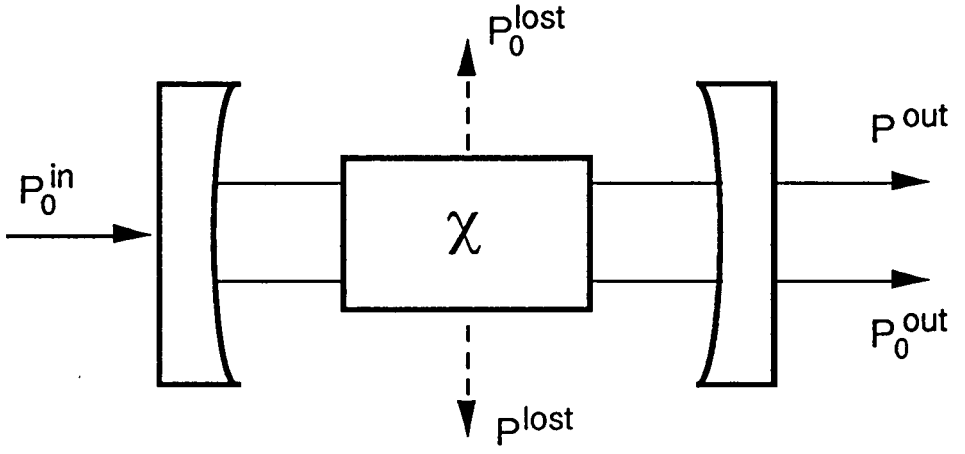


Figure 4.2: Input and output power balance.

We note here that the pump field damping term $\gamma_0'$ is now the sum of three damping terms

$$\gamma_0' = \gamma_0 + \mu_0 + \mu_0' \tag{4.1}$$

where $\gamma_0$ corresponds to damping due to the input port mirror, $\mu_0$ corresponds to damping due to intracavity losses, and $\mu_0'$ corresponds to the supplementary damping due to the output port mirror. Defining $P_0^{thresh}$ as the threshold pump power necessary for OPO oscillation on resonance ($\varphi_0=0$, $\varphi=0$), that is,

$$P_0^{thresh} = \frac{(\gamma'\gamma_0')^2}{8\chi^2\gamma_0} \tag{4.2}$$

such that on resonance for an input power $P_0^{in}$ we have

$$\sigma_{res} = \sqrt{\frac{P_0^{in}}{P_0^{thresh}}}\ , \tag{4.3}$$

then the respective powers of each field when the OPO is operating above threshold are

$$
\begin{aligned}
P^{out} &= 2\xi\xi_0 P_0^{thresh}(\sigma-1) && \text{per beam}\\
P^{loss} &= 2(1-\xi)\xi_0 P_0^{thresh}(\sigma-1) && \text{per beam}\\
P_0^{back} &= P_0^{in} - 4\xi_0 P_0^{thresh}\left(\sigma-\xi_0+\varphi^2(1-\xi_0)\right)\\
P_0^{loss} &= 4\left(\frac{\mu_0}{\gamma_0'}\right)\xi_0 P_0^{thresh}\left(1+\varphi^2\right)\\
P_0^{out} &= 4\left(\frac{\mu_0'}{\gamma_0'}\right)\xi_0 P_0^{thresh}\left(1+\varphi^2\right)
\end{aligned}
\qquad (4.4)
$$

where again $\xi_i=\gamma_i/\gamma_i'$ and the OPO is assumed balanced. Note that $P_0^{loss}$ and $P_0^{out}$ are independent of the pumping level. The experimental cavity parameters are $\xi$=0.91, $\xi_0\approx$0.4, $\mu_0/\gamma_0'\approx$0.3, $\mu_0'/\gamma_0'\approx$0.25. $P_0^{thresh}$ is estimated experimentally at 300 mW. Measurement of the powers in eqtns. 4.4 provides sufficient information, therefore, to determine the cavity detuning parameters.

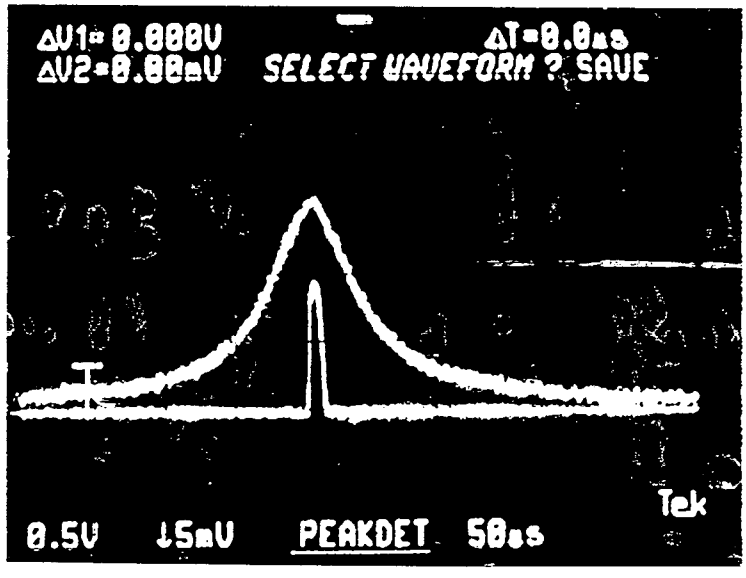


Figure 4.3: Pump (top) and signal (bottom) output powers as functions of swept cavity length.

The measured finesse for the pump field and the downconverted fields are ~ 25 and ~ 85 respectively. Due to these somewhat large finesses, the OPO must be resonant for the three fields for a same cavity length, as illustrated in fig. 4.3. This condition is not as stringent as it may appear since the OPO operation here is non-degenerate. The frequency difference in the down-converted modes is a free parameter, therefore, making it easier to satisfy simultaneously the resonance condition in the cavity and the phase matching condition in the KTP crystal. Since the OPO cavity is linear, however, it is important that the overlap of the pump and down-converted standing waves inside the crystal be optimized for maximum conversion efficiency. The cavity mirrors must be adapted for this

to present phase shifts on reflection so that the nodes in the down-converted modes correspond to the anti-nodes in the pump mode [Kim86], as is shown in fig. 4.4. The mirrors used in this experiment were supplied by LaserOptiks, Hanover.

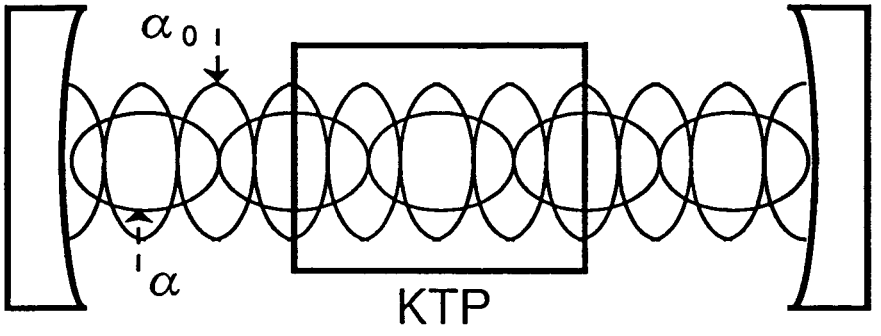


Figure 4.4: Optimal overlap geometry for pump and down-converted fields.

An external lens between the pump laser and the OPO is used to mode match the pump field to the intracavity fields. The intracavity beam waist is calculated at 40 μm with a Rayleigh length of 16 mm, so that the fields may be approximated as plane waves over the entire crystal length. The walk-off angle inside the crystal is 1.3 mrad for the wavelength 1.06 μm. The output port mirror is convex outside, with outside radius of curvature 10 mm so that the output signal and idler beams have a small angular divergence of 3 mrad.

The crystal is temperature stabilized to 31° C for optimal phase matching using a Peltier element and standard temperature controller. Unfortunately, the coupling between the crystal and the Peltier is weak and the temperature control is ineffective at compensating abrupt temperature changes due to heating of the crystal when the cavity is on resonance. Most of this heating stems from crystal absorption of the pump field. For pump finesses larger than ~ 25, separate variations of the pump and downconverted mode indices of refraction due to heating are too large, and the OPO can not be held triply resonant.

The DC output voltages of the signal and idler photodetectors are summed and compared to a battery supplied reference voltage. The total intensity incident on these photodetectors is stabilized by adjusting the OPO cavity detuning through piezoelectric control of the cavity length. The signal and idler intensities are held at 3 mW each. The gain of the control is limited by a mechanical piezo resonance at 1.5 kHz. Unity gain is crossed at approximately 1 kHz with a 9 dB/octave roll-off. A supplementary 18 dB/octave roll-off is included for frequencies below 200 Hz, obtaining higher low frequency gain (see chapter V for a brief review of these terms, and in particular section V.f). Note: in this stabilization scheme the signals DC and AC are taken from the same photodiodes (which differs from the previous schemes where separate photodiodes were necessary [Hei87, Deb89]). Although the YAG laser is equipped with its own frequency servo-control, it was found experimentally that the OPO intensity servo-control by itself was usually sufficient for stable OPO operation.

c: *Detection mechanism: experimental details*

The twin beams generated by the OPO are focussed onto the photodetectors to a spot size of 150 μm using aberration corrected lenses supplied by Melles-Griot. The photodiodes are Epitaxx 300 InGaAs *pin* diodes whose protective windows are removed. These are tilted in the respective polarization planes of the incident beams to approach the Brewster angle and improve the detection quantum efficiency to 0.94. Because the diode surfaces are AR coated to reduce reflection losses, the Brewster angle could not be predicted accurately. An optimum tilt angle was determined experimentally by locking the signal and idler intensities using one photodetector signal (not the sum) and observing variations in the second photodetector signal when the latter was tilted. A maximum increase in quantum efficiency of 3-4% was found for a tilt angle of 45°, whereas higher tilt angles gave rise to spurious edge effects. This increase in quantum efficiency was confirmed by a corresponding increase of 4% in the observed quantum noise reduction of the twin beam intensity difference. The specular reflection from the photodiode surface was measured to be far too low in power to explain such a 4% reflection loss. This loss is presumed therefore to be diffusive.

The detector pre-amplification circuitry is shown in fig. 4.5. This comprises basically two circuits, DC out and AC out, isolated from one another by the FET transistor BC109.

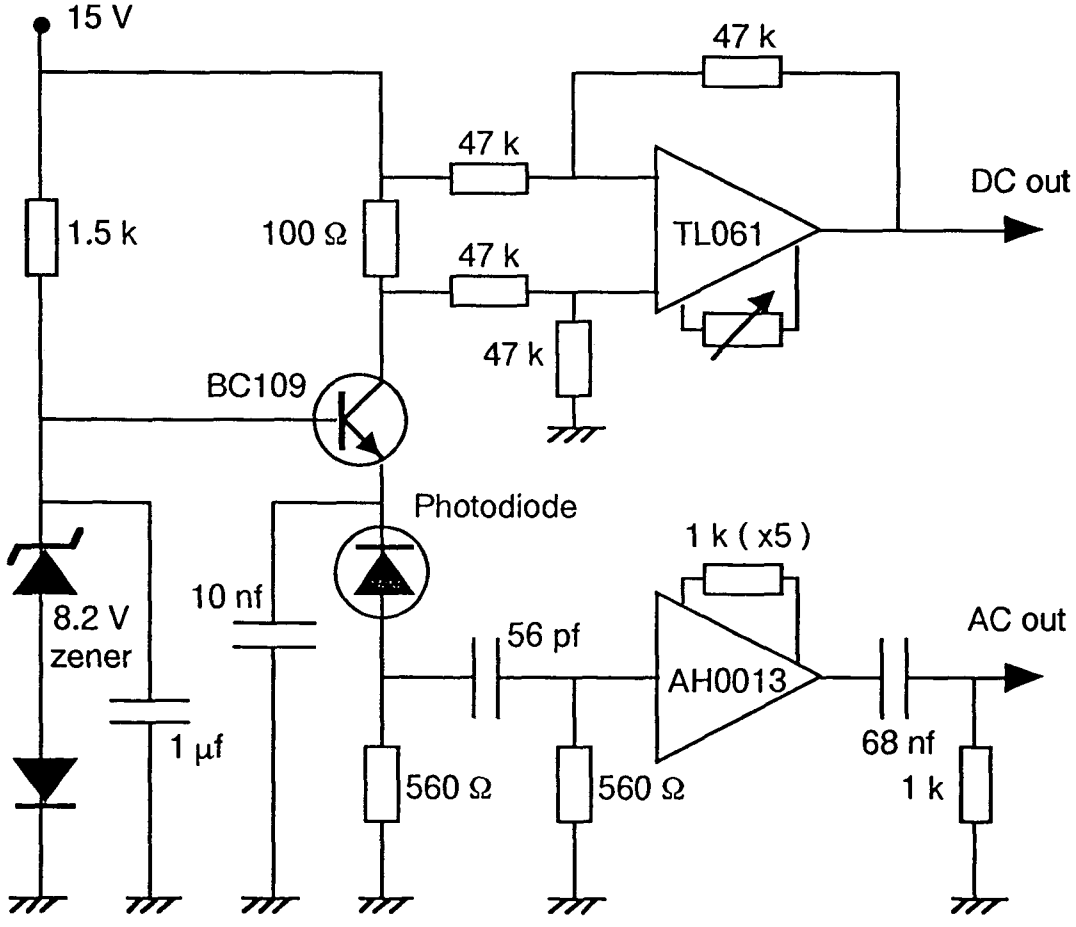

Figure 4.5: Photodiode AC preamp (bottom half) and power monitor (top half).

The DC out circuitry (top half of fig. 4.5) monitors the BC109 collector current by measuring the difference voltage across a 100 Ω resistor using a FET TL061 op-amp. This collector current is (approximately) the same as the emitter current defined by the photodiode. For a photodiode sensitivity $S$ (here 0.8 A/W at 1.06 μm), DC out measures then the optical power incident on the photodiode with a conversion factor $100S$. The photodiode is reverse biased and polarized to 8.2 V by imposing a Zener stabilized 8.8 volts at the BC109 base. The Zener voltage is compensated for temperature drift by a secondary diode, and its AC noise is capacitively shorted to ground. It was verified that the Zener supplied bias voltage contained no measurable excess noise compared with a battery supplied bias voltage. Additional AC shorting is included directly at the photodiode cathode by capacitors selected so that current variations up to 30 kHz in frequency could be monitored by the DC out circuitry (used for intensity stabilization).

The AC out circuitry (bottom half of fig. 4.5) monitors the AC voltage (0.5-20 MHz) at the photodiode anode. The amplifying element is an OEI AH0013 FET pre-amp with a gain set at 5. This is low noise ($2nV/\sqrt{Hz}$), and wideband (Gain Bandwidth Product = 100 MHz). 12 dB/octave high pass filtering is included below 50 kHz to prevent amplifier saturation resulting from the low frequency excess noise in the observed signals. Given the operating conditions of 3 mW per beam, the respective amplifier noise, Johnson noise, and shot noise power contributions scaled approximately as 1:2:50, meaning that the electronic noise floor was typically 4 to 12 dB below our signal of interest.

The AC output signals are subtracted using a Mini-Circuits ZSCJ-2-2 splitter (10 kHz - 20 MHz) with amplitude imbalance less than 0.1 dB and insertion loss less than 0.9 dB. The resultant difference signal is monitored using a Tektronix 2753P programmable spectrum analyzer whose resolution bandwidth determines the bandwidth B (see eqtn. 2.18) in the noise measurements. The spectrum analyzer is connected through a GPIB bus to a micro-computer for data processing.

**d:** ***Detection balance and linearity***

Important criteria for the evaluation of the intensity difference spectrum are detection balance (see section on twin beam separation below) and detection linearity.

The electrical DC imbalance was measured at less than 1% by comparing the DC output voltage levels of the two detectors for a common input current through the BC109 emitters when the photodiodes were removed. Minimization of this imbalance depended on resistor matching both in the emitter (load) sides and in the collector sides of the BC109s.

The electrical AC imbalance was measured in a similar manner by applying to the emitter loads an AC voltage from a sweep generator and measuring the common mode rejection ratio (CMRR) when the AC outputs were subtracted. It was important in this

procedure as well as in the actual experiment to run each detector off an independent power supply to avoid spurious signal correlations. The measured electrical CMRR was -40 dB up to 6 MHz and -35 dB up to 20 MHz, and was contingent on matching of the AC load networks, and of the AH0013 amplifiers and gain resistors. The total electrical and optical CMRR (including photodiode imbalance) was measured by sweep modulation of the OPO pump intensity and observation of the resultant modulation peaks in the down-converted beams both individually and on subtraction. This CMRR was found to be -35 dB up to 6 MHz and -30 dB up to 20 MHz.

The detection linearity was verified using two methods. The first method was a DC saturation measurement where the twin beam shot noise power level was observed to vary linearly with the total intensity incident on the photodiodes (see section VII.d for further details). The second was an AC saturation measurement, where an AC modulation peak was superposed to the output noise power of the OPO and observed to vary linearly with the modulation index. The latter measurement was reliable to 3%.

### e: *Twin beam separator: experimental details*

The beam separation mechanism at the output of the OPO consists of a half-wave plate followed by a polarizing beamsplitter (see fig. 4.6). The signal and idler beams are cross polarized and are rotated using the half-wave plate to make an angle θ with the polarizing beamsplitter axes.

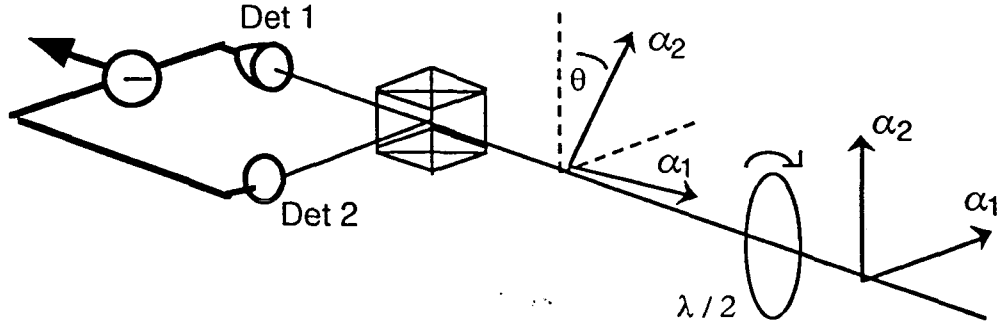


Figure 4.6: Layout for twin beam separator.

Writing the carrier frequencies of the signal and idler beams as $\omega_1$ and $\omega_2$, with $\Delta\omega=\omega_1-\omega_2$, the intensity fluctuations incident on detector 1 are given by

$$\delta I_1(\Omega) = \bar{\alpha}_1\left(\delta\alpha_1(\Omega) + \delta\alpha_1^*(-\Omega)\right)cos^2\theta + \bar{\alpha}_2\left(\delta\alpha_2(\Omega) + \delta\alpha_2^*(-\Omega)\right)sin^2\theta$$

$$-\bar{\alpha}_2\left(\delta\alpha_1(\Delta\omega+\Omega) + \delta\alpha_1^*(\Delta\omega-\Omega)\right)\frac{sin2\theta}{2}$$

$$-\bar{\alpha}_1\left(\delta\alpha_2(-\Delta\omega+\Omega)+\delta\alpha_2^*(-\Delta\omega-\Omega)\right)\frac{\sin 2\theta}{2} \tag{4.5}$$

and on detector 2 by the same expression with indices 1 and 2 interchanged and θ replaced by -θ. These intensity fluctuations comprise the beating of the carrier fields with their own fluctuation sidebands (first two terms) and the cross beating of the carrier fields with the other field fluctuation sidebands (last two terms), as illustrated in fig. 4.7. The OPO operation is non-degenerate with Δω much larger than the cavity bandwidth. The cross beating terms may therefore be considered as vacuum fluctuation terms (similar to the vacuum fluctuation terms entering through the unused port of an ordinary beamsplitter). For θ=0, beams 1 and 2 are separated by the polarizing beamsplitter into detection arms 1 and 2 respectively. For θ=π/4, they are distributed instead into detection arms 1 and 2 with equal proportions in each arm. In the latter case, the polarizing beamsplitter acts as a 50% beamsplitter.

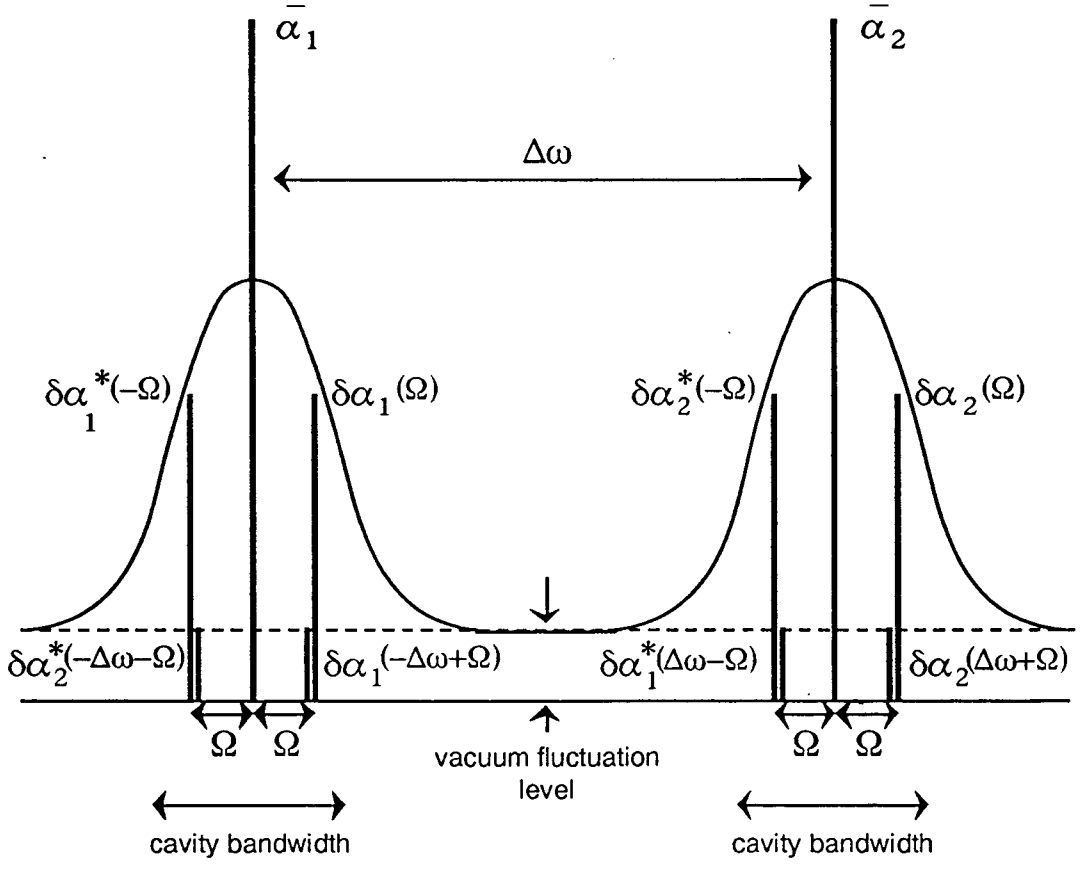


Figure 4.7: Schematic of modes coupled during detection. Non-degenerate twin beams are separated by frequency Δω. Ω is a noise frequency.

Before discussing the resulting intensity difference in both arms, we include considerations such as beam intensity imbalance and detector imbalance. The first we parametrize by δI/I, where δI is the half difference and I is the mean of the signal and idler intensities at the OPO output (typically 2%). The second we parametrize by ε, where the

common mode intensity difference signal is given at the amplifier input by $\varepsilon\eta I$. ($\eta$ is the mean detector quantum efficiency). As defined, $\varepsilon$ is the imbalance in the detection intensity-to-voltage conversion, which includes both a possible detector quantum efficiency imbalance and a possible electronic gain imbalance. It is given directly by the optical and electrical CMRR (see previous section), and is typically less than 2%. Using eqtn. 4.5 then, the observed intensity difference noise power $P_{1-2}(\Omega)$ becomes as a function of $\theta$:

$$P_{1-2}(\Omega) = 2\eta^2 I\left(S_{1-2}(\Omega)\cos^2 2\theta + \sin^2 2\theta + S_{1+2}(\Omega)\left(\frac{\delta I}{2I}\cos 2\theta + \varepsilon\right)^2\right) + 2\eta I(1-\eta) \quad . (4.6)$$

One finds that in the case of no imbalances, the observed intensity difference oscillates with $\theta$ between $2\eta I$ [$\eta S_{1-2}(\Omega)+1-\eta$] and the shot noise level $2\eta I$, providing a calibration for $\theta=0$ and $\theta=\pi/4$ respectively (see solid line in fig. 4.8). Departures from this oscillation are only to second order in the various imbalances, and are illustrated when these imbalances are greatly exaggerated (see dotted line in fig. 4.8). We note that these departures scale with $S_{1+2}(\Omega)$, which is large at low frequencies due to excess noise in each beam. Calibration of $\theta$ was effected therefore at high frequency (10 MHz) to minimize any errors. The observed normalized noise reduction $\tilde{S}_{1-2}(\Omega)$ is finally the intensity difference noise spectrum $P_{1-2}(\Omega, \theta=0)$ divided by the shot noise spectrum $P_{1-2}(\Omega, \theta=\pi/4)$:

$$\tilde{S}_{1-2}(\Omega) = \eta S_{1-2}(\Omega) + 1 - \eta + \Delta \qquad (4.7)$$

with an error

$$\Delta = \eta S_{1+2}(\Omega)\left(\left(\frac{\delta I}{2I}\right)^2 \pm \varepsilon\frac{\delta I}{I} + \varepsilon^2\eta\left(1 - S_{1-2}(\Omega)\right)\right) . \qquad (4.8)$$

Given the imbalance parameters for the experiment, this error is typically less than 1%.

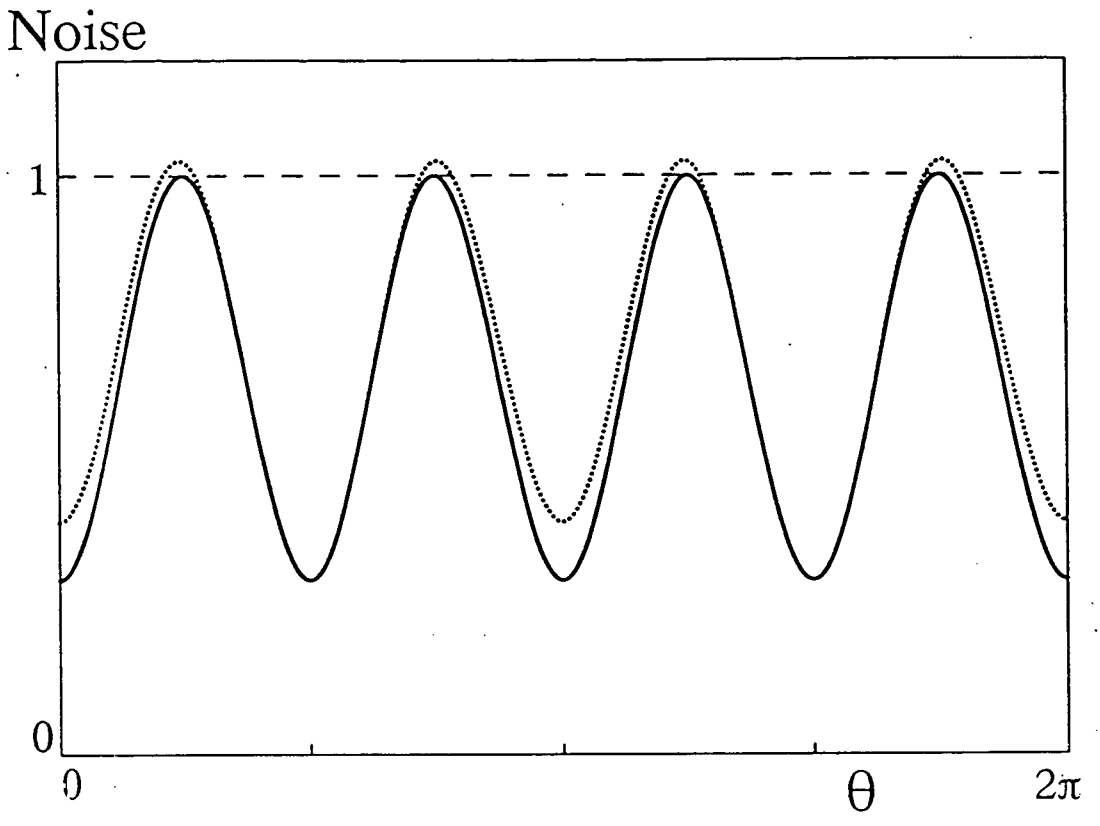


Figure 4.8: Intensity difference noise, normalized to $2\eta I$, as a function of half-wave plate rotation. $S_{1-2}=0.3$, $S_{1+2}=10$, $\delta I/I=10\%$, and $\varepsilon=5\%$. Note error periodicity of $\pi$.

**f:** *Conclusion*

We presented in the previous chapter the theory of twin beam intensity correlations. We verify here with experiment that these correlations are quantum in nature and can be large. The correlations are limited by the efficiencies in the twin beam generation ($\xi$) and in the detection ($\eta$). These efficiencies are shown to be exceptionally good for OPOs and for infrared photodiodes. At the current performance level, $\xi$ and $\eta$ are of the same order. Future improvements in the twin beam correlations should entail therefore a parallel improvement in both of these efficiencies.

For the remainder of the thesis we turn to an application of twin beam correlations to the production of a sub-Poissonian single beam via active control.

# V. CONTROL THEORY

We presented in the previous chapters a mechanism for the generation of twin beams whose intensities were correlated. We wish now to exploit this correlation to reduce the intensity fluctuations of a single beam by using active control from one beam to another. Before doing this, however, we introduce some basic ideas that will be necessary throughout the remainder of the thesis, and present in this chapter a brief review of control theory in general.

The standard formalism for control theory is an input-output formalism where an input parameter (for example, an intensity fluctuation) is "transferred" to an output parameter via a control network. In general, the desired effect of such a transfer is a regulation of the output parameter. In noise control applications, such a regulation entails a reduction in the fluctuations of the output parameter about some steady state value that is typically user controlled. As we will see below, however, conditions may arise when the transfer instead causes the output parameter to diverge at some instability frequency. We present here methods of evaluating the stability of a control network, where we limit ourselves to transfer responses that are linear. In particular, we concentrate on the example of a feedback control network since this is commonly used in experiment and will be examined in chapters VI and VIII for its applications towards twin beam control. Again, this chapter is only intended as a general review, and mathematical rigor will often be sidestepped.

### a: *Linear transfer*

We begin first by defining what is meant by the linear transfer of one variable to another. The variables are assumed measurable (ie. real) functions of time, and denoted $\alpha^{in}$ for the input variable and $\alpha^{out}$ for the output variable. $G$ is the transfer function linking one to the other (see fig. 5.1).

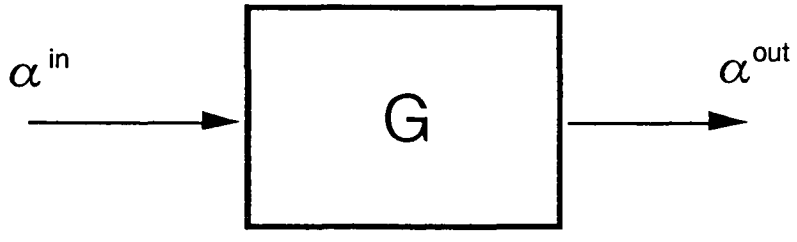


Figure 5.1: Linear transfer

In general, $\alpha^{out}(t)$ is a response to $\alpha^{in}(t')$, where t may be different from t'. $G$ is a function then both of t and t'. For stationary processes, however, it is a function only of $\tau = t\text{-}t'$. A linear transfer is defined by

$$\alpha^{out}(t) = \int d\tau\, G(\tau)\, \alpha^{in}(t-\tau). \tag{5.1}$$

Two restrictions will be applied to $G(\tau)$. The first stems from the measurability (reality) of $\alpha^{out}$ and imposes that $G(\tau)$ is real. The second stems from causality and imposes that $G(\tau) = 0$ for $\tau < 0$. That is, $\alpha^{out}(t)$ can only depend on $\alpha^{in}(t')$ if t' is prior to t.

In frequency space, the above integral equation becomes algebraic

$$\alpha^{out}(\Omega) = G(\Omega)\, \alpha^{in}(\Omega) \tag{5.2}$$

The measurability condition translates to the restriction

$$G(\Omega) = G^{*}(-\Omega). \tag{5.3}$$

The causality condition translates to the restriction that if $\Omega$ is extended into the complex domain (we use $\tilde{\Omega}$ to denote a complex frequency), then the poles of $G(\tilde{\Omega})$ occur only for $\mathrm{Im}(\tilde{\Omega}) \geq 0$. The latter restriction is somewhat artificial since in any experiment we are concerned only with real frequencies. Extension of $\Omega$ into the complex plane, however, provides a convenient tool for visualizing the stability of a transfer function, or its approach towards instability.

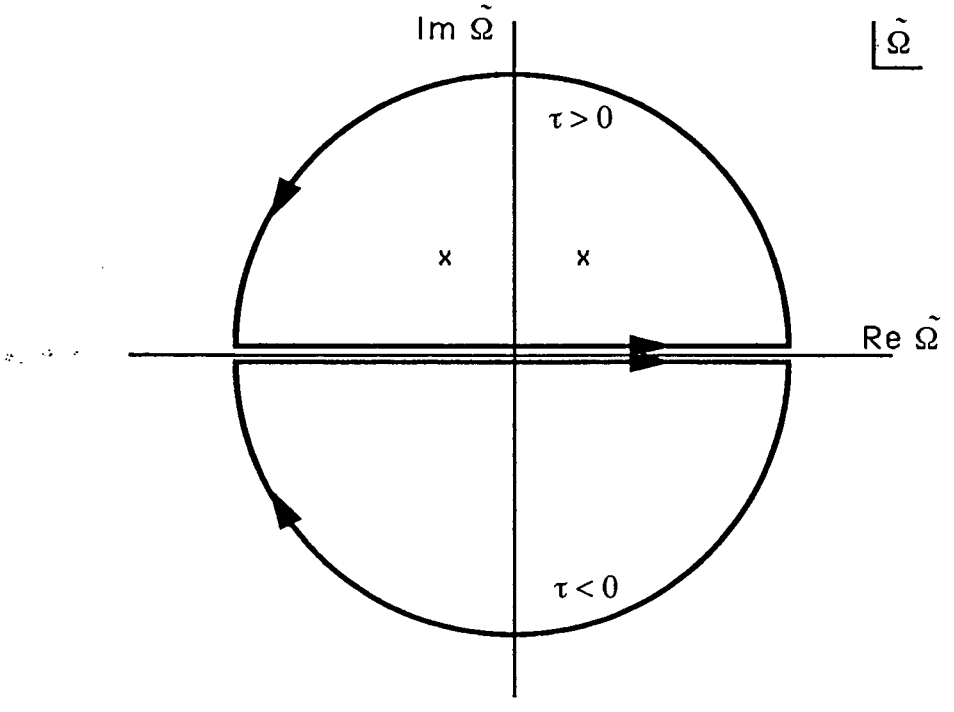


Figure 5.2: Integral over real $\Omega$ axis is equal to line integral over top contour ($\tau>0$) or bottom contour ($\tau<0$). Transfer is causal if there are no poles (marked x) inside bottom contour.

A simple way of understanding the restriction due to causality is from the Fourier transform relation

$$G(\tau) = \int \frac{d\Omega}{2\pi} G(\Omega)\, e^{i\Omega\tau}. \tag{5.4}$$

Assuming $G(\tilde{\Omega}) \to 0$ for $|\tilde{\Omega}| \to \infty$ (as is true of any realistic transfer function), then the above integral over the real $\Omega$ axis is the sum of the residues inside the contour shown in fig. 5.2, where the contour is different for $\tau < 0$ or $\tau > 0$. If, by causality, we impose $G(\tau<0) = 0$, then the sum of the residues in the $t < 0$ contour must be zero, entailing in general that poles of $G(\tilde{\Omega})$ in the lower half plane (l.h.p.) of $\tilde{\Omega}$ are forbidden.

In the event that a pole of $G(\tilde{\Omega})$ lies exactly on the real $\Omega$ axis, say at $\Omega_0$, then $\alpha^{out}(\Omega_0)$ becomes divergent for any non-zero $\alpha^{in}(\Omega_0)$, and the system is unstable. At this point, the linear transfer model breaks down and the instability gives rise to a spontaneous oscillation of the system at the frequency $\Omega_0$. The amplitude of this oscillation is typically governed by nonlinear effects such as saturation.

We give examples of three common transfer functions: the low-pass filter, the high-pass filter, and the time delay

$$G_{lp}(\Omega) = \frac{\Omega_{3dB}}{\Omega_{3dB} + i\Omega} \tag{5.5}$$

$$G_{hp}(\Omega) = \frac{i\Omega}{\Omega_{3dB} + i\Omega} \tag{5.6}$$

$$G_{td}(\Omega) = e^{-i\,\Omega\,\tau_d} \tag{5.7}$$

where $\Omega_{3dB}$ is a 3 dB roll-off frequency and $\tau_d$ is a time delay. The pole (x) and zero (o) locations of these transfer functions are shown in fig. 5.3 below. (For the time delay transfer function, these correspond to the locations where $G_{td}(\tilde{\Omega})$ diverges or vanishes respectively.)

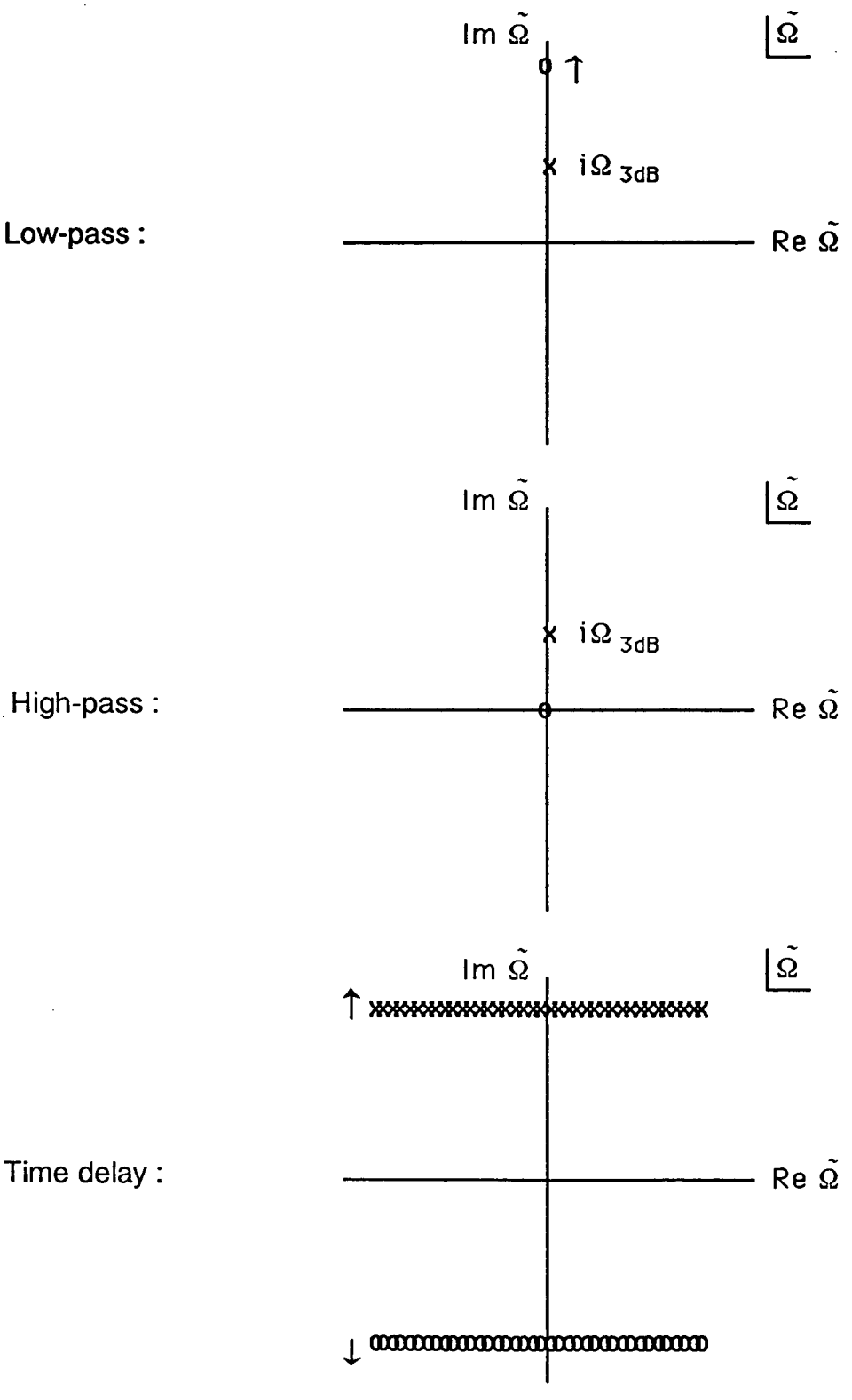


Figure 5.3: Transfer functions for low-pass filter, high-pass filter, and time delay. Poles = x; zeros = o.

**b: *Feedback***

So far, we have treated the transfer function $G(\Omega)$ as a black box linking an input variable to an output variable. We now examine the case when this black box is a feedback network comprising a direct transfer $A(\Omega)$ and a feedback transfer $gB(\Omega)$. We have chosen to separate out a parameter g from the feedback transfer function. This parameter will correspond to an experimentally adjustable variable which we will denote as the feedback gain. We also include in our model the possibility of a user specified reference level $\bar{\alpha}^{ref}$, assumed constant (see fig. 5.4).

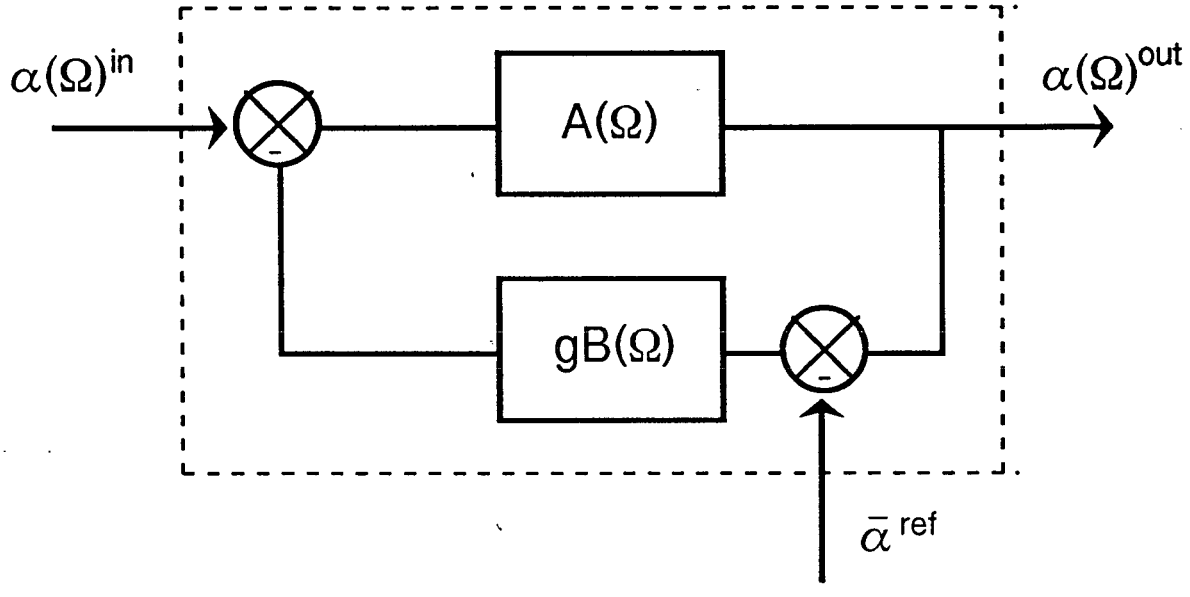


Figure 5.4: Feedback network.

For applications to noise control, we are particularly interested in the effect of feedback on the fluctuations in the input and output variables. These are separated out explicitly:

$$\alpha^{in}(t) = \bar{\alpha}^{in} + \delta\alpha^{in}(t) \quad ; \quad \alpha^{out}(t) = \bar{\alpha}^{out} + \delta\alpha^{out}(t) \tag{5.8}$$

where $\delta\alpha$ corresponds the fluctuations about the steady-state value $\bar{\alpha}$.

In a negative feedback configuration, the feedback is subtracted from the input and the respective equations governing the steady-state and fluctuation variables are:

$$\bar{\alpha}^{out} = A(0)\left[\bar{\alpha}^{in} - g\,B(0)\left(\bar{\alpha}^{out} - \bar{\alpha}^{ref}\right)\right] \tag{5.9}$$

$$\delta\alpha^{out}(\Omega) = A(\Omega)\left[\delta\alpha^{in}(\Omega) - g\,B(\Omega)\,\delta\alpha^{out}(\Omega)\right] \tag{5.10}$$

The global gain between the input and the output is known as the "closed loop gain", here equal to

$$G_{clg}(\Omega) = \frac{A(\Omega)}{1 + gA(\Omega)B(\Omega)}, \tag{5.11}$$

and total gain around the feedback loop is customarily known as the "open loop gain", here equal to

$$G_{olg}(\Omega) = g\, A(\Omega)\, B(\Omega). \tag{5.12}$$

Equations 5.9 and 5.10 may then be written in simpler form

$$\bar{\alpha}^{out} = G_{clg}(0)\,\bar{\alpha}^{in} + \left(1 - G_{clg}(0)\right)\bar{\alpha}^{ref}, \tag{5.13}$$

$$\delta\alpha^{out}(\Omega) = G_{clg}(\Omega)\,\delta\alpha^{in}(\Omega). \tag{5.14}$$

For effective noise control, it is clear that a small closed loop gain $G_{clg}(\Omega)$, or equivalently a large feedback gain g, is desirable. The steady-state output then tends towards $\bar{\alpha}^{ref}$ and the output fluctuations about this steady-state tend towards zero. In practice, however, ideal noise control such as this is typically approached only at relatively low frequencies for reasons which will delineated below.

c: *Nyquist analysis*

Equation 5.14 for the transfer of fluctuations in feedback control has the same form as equation 5.2. The same requirements imposed by causality therefore apply to $G_{clg}(\Omega)$.

Assuming $A(\Omega)$ and $B(\Omega)$ are themselves already causal, then the poles of $G_{clg}(\tilde{\Omega})$ occur in general for $\tilde{\Omega}$s that are solutions to the equation

$$G_{olg}\left(\tilde{\Omega}\right) = -1. \tag{5.15}$$

One can quickly determine whether or not $G_{clg}(\Omega)$ is causal then by mapping the region occupied by the l.h.p. of $\tilde{\Omega}$ (fig. 5.5 -- shaded region on left) into the corresponding region occupied by the open loop gain $G_{olg}(\tilde{\Omega})$ (fig. 5.5 -- shaded region on right). If the critical point $G_{olg}(\tilde{\Omega}) = -1$ is not covered by the latter region, then the poles of $G_{clg}(\tilde{\Omega})$ do not lie in the l.h.p. of $\tilde{\Omega}$, and $G_{clg}(\Omega)$ is causal. Note that the real $\Omega$ axis on the left is mapped to the contour of the shaded region on the right. This contour is called the Nyquist plot of the open loop gain; the above mentioned causality criterion is a (very) simplified version of the Nyquist stability criterion.

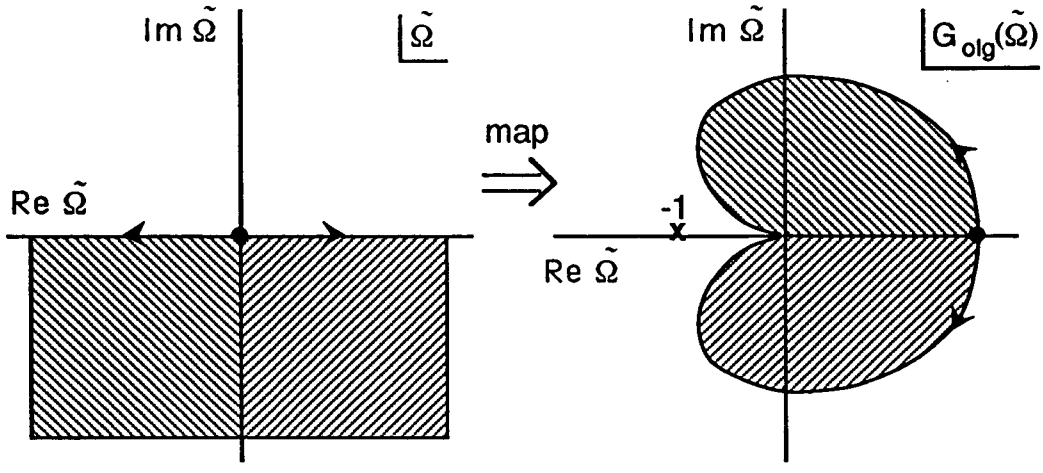


Figure 5.5: Nyquist map for typical feedback network.

In the following sections, we will examine in more detail what happens to $G_{clg}(\tilde{\Omega})$ as the feedback is "turned on", that is, as g is increased from 0. This we will do using two standard methods. The first is the root-locus method, in which the pole locations of $G_{clg}(\tilde{\Omega})$ are traced as a function of g. The second is the Bode method, in which the magnitude and phase of $G_{olg}(\Omega)$ are studied as a function of g. Both methods provide alternative ways of analyzing the feedback stability.

**d:** ***Root-Locus Analysis***

As noted above, the location of the poles of $G_{clg}(\tilde{\Omega})$ in the complex $\tilde{\Omega}$ plane provide information on the stability of $G_{clg}(\Omega)$. A pole location at $\tilde{\Omega}_0$, for example, appears as a resonance in $G_{clg}(\Omega)$ at the frequency $Re(\tilde{\Omega})$ and of width proportional to $Im(\tilde{\Omega})$. The closer this pole is to the real $\Omega$ axis, the sharper becomes the resonance peak, and the more unstable becomes $G_{clg}(\Omega)$ at the resonance frequency. A pole on the real $\Omega$ axis appears as a delta function in $G_{clg}(\Omega)$ where the system oscillates spontaneously.

We examine now the pole locations of the feedback loop transfer function $G_{clg}(\tilde{\Omega})$, defined by eqtn. 5.11. Again, these poles occur in general for $\tilde{\Omega}$s that are solutions to equation 5.15. We present a few rules of thumb governing their locations [DiS67, Gil71].

1) As the feedback is turned on, that is, as g varies from a small value to a large value, the pole locations of $G_{clg}(\tilde{\Omega})$ migrate from the pole locations of $G_{olg}(\tilde{\Omega})$ to the zero locations of $G_{olg}(\tilde{\Omega})$

2) There are an equal number of poles and zeros of $G_{olg}(\tilde{\Omega})$

3) The poles of $G_{clg}(\tilde{\Omega})$ tend to "avoid" one another. That is, they approach or depart from one another with radially symmetric directions, and their paths do not cross (although they may touch).

These rules will be made clear with some examples.

First we consider the simple case where $A(\Omega)$ is a low-pass filter (eqtn. 5.5) and $B(\Omega)=1$. In other words, the feedback transfer comprises only a linear gain g. The single pole of $G_{olg}(\tilde{\Omega})$ is at $\tilde{\Omega} = i\Omega_{3dB}$; the single zero is at $|\tilde{\Omega}| = \infty$. As the gain varies from a small value to a large value, the single pole of $G_{clg}(\tilde{\Omega})$ migrates from the former to the latter as shown in fig. 5.6. The transfer is stable for all values of g since the pole of $G_{clg}(\tilde{\Omega})$ remains in the u.h.p..

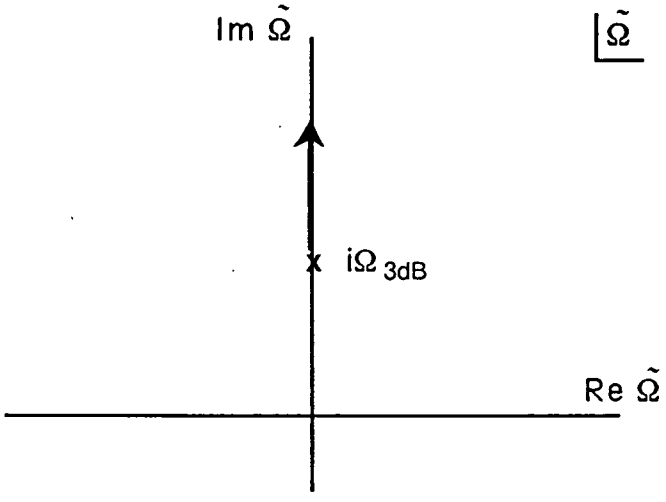


Figure 5.6: 1-pole feedback.

If $B(\Omega)$ now includes a low-pass filter with roll-off frequency $\Omega'_{3dB}$ (see eqtn. 5.5), then $G_{clg}(\tilde{\Omega})$ has two poles which migrate from the poles of $G_{olg}(\tilde{\Omega})$ to the zeros of $G_{olg}(\tilde{\Omega})$ as shown in fig. 5.7. The poles are degenerate at the mid-point between $i\Omega_{3dB}$ and $i\Omega'_{3dB}$. Note that the paths do not cross and that the poles approach one another from opposite directions both at this mid-point and also at infinity. Note also the symmetry of the pole locations about the imaginary axis. This is a consequence of the fact that $G_{clg}(\tau)$ is real (see eqtn.5.3). Again, the transfer is stable for all values of g.

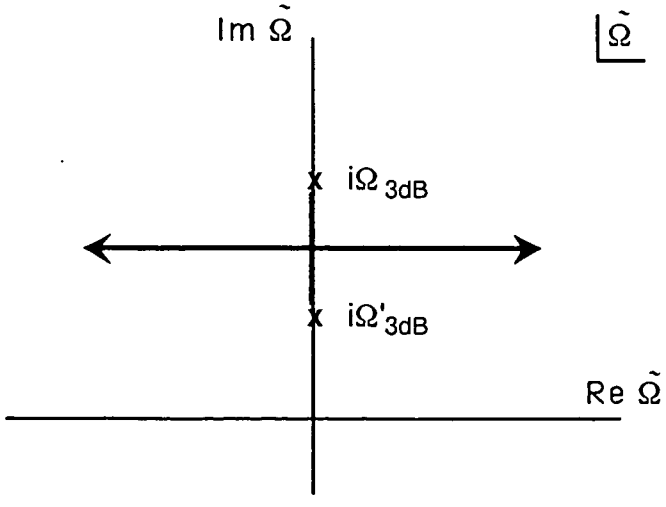


Figure 5.7: 2-pole feedback.

If $B(\Omega)$ now includes two low-pass filters, one at $\Omega'_{3dB}$ and one at $\Omega''_{3dB}$, then the situation is different. The poles of $G_{clg}(\tilde{\Omega})$ migrate as shown in fig. 5.8, again approaching infinity from radially symmetric directions, but this time two poles tend towards the l.h.p.. At a critical gain g, these poles touch the real $\Omega$ axis, and the system oscillates at the intersection frequency. Feedback gain beyond the critical g only aggravates the oscillation since in a causal system the poles are not allowed in the l.h.p. and must be held at the real axis. Again, the linear transfer model breaks down at this point and nonlinear effects must be taken into account.

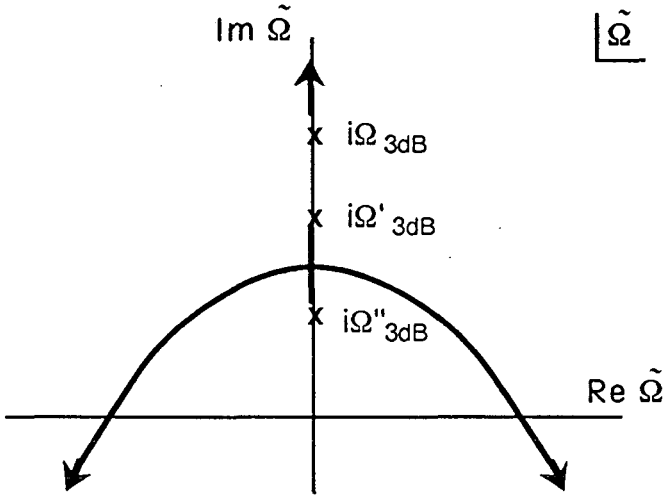


Figure 5.8: 3-pole feedback.

The performance of a feedback network in regulating an input parameter is dependent on feedback gain. From eqtns. 5.11 and 5.14, it is clear that a large feedback gain is desirable. For the control network described above, however, the gain is limited by a critical gain above which the system is unstable. The limit is imposed by the onset of oscillation at a resonance frequency. In some cases it may be possible to obtain higher gains simply by "pushing" the poles so that they intersect the real axis at higher frequencies, thereby increasing the frequency of oscillation. A possible method for this is to include high-pass filters (eqtn. 5.6) in the feedback loop. We will illustrate the example where two high-pass filters are included at $\Omega'''_{3dB}$ and $\Omega''''_{3dB}$. $G_{clg}(\tilde{\Omega})$ has five poles then which migrate as shown in fig. 5.9. Although the system still behaves essentially as a three pole network, the effect of the high-pass filtering is to push the deleterious poles farther apart so that the system oscillates eventually at a higher frequency. In general, this allows for a higher feedback gain. One observes again that the five zero's of $G_{olg}(\tilde{\Omega})$ (three at $\infty$ and two at 0) are approached from radially symmetric directions.

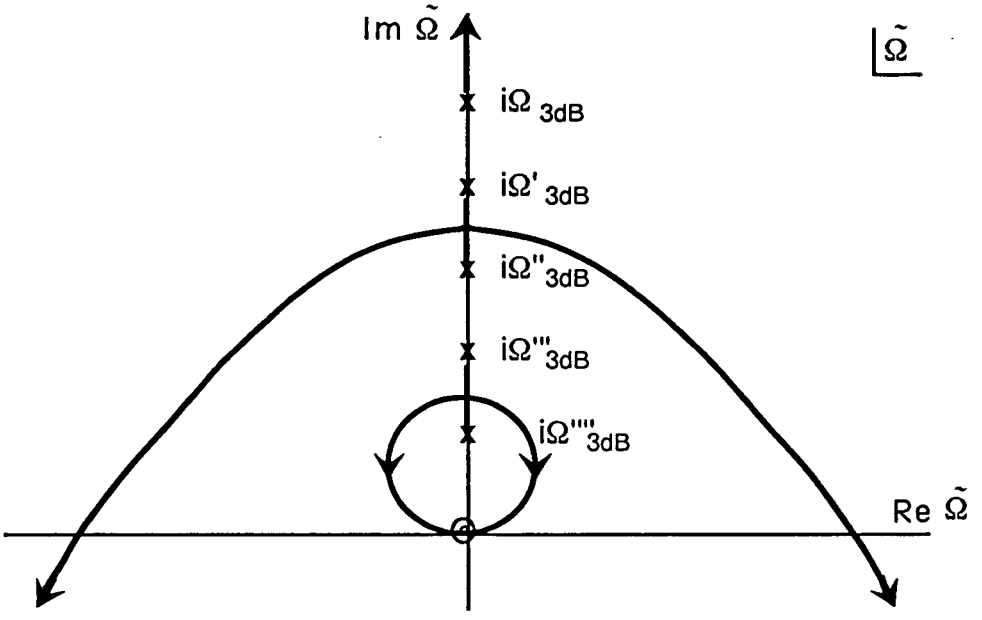


Figure 5.9: 5-pole, 2-zero feedback.

We note that the paths taken by the poles in the above figures are independent of whether the poles originate from low pass filtering or high pass filtering. For example, $\Omega_{3dB}$ and $\Omega''''_{3dB}$ could have been switched in fig. 5.9 without changing in any way the eventual oscillation frequency of the system. Such a switch, however, manifestly changes the global feedback response (see eqtn. 5.11).

**e:** ***Bode Analysis***

An alternative method for analyzing the stability of a transfer function is through the use of Bode plots. The Bode plot for a single pole low-pass filter is shown in fig. 5.10. Beyond the frequency $\Omega_{3dB}$ the roll-off in the transfer magnitude is 6dB/octave ($1/\Omega^2$ roll-off in power) and the transfer phase shift asymptotically approaches 90°. In general, one must add (subtract) a 6dB/octave roll-off and a 90° phase shift for every pole (zero) in the transfer function. The method for analyzing the stability of the feedback loop transfer $G_{clg}(\Omega)$ as defined by eqtn. 5.11 is similar to the one used in the root-locus analysis. As before, the system oscillates when the open-loop gain $G_{olg}(\Omega) = -1$, that is, when the magnitude of $G_{olg}(\Omega)$ is 1 (0 dB) and its phase is 180° (12dB/octave roll-off). A general rule, therefore, is that the system is stable if the open-loop gain magnitude does not cross the 0 dB line with a 12dB/octave roll-off *while the feedback is turned on.* For example, when $G_{olg}(\Omega)$ contains only a simple pole (see fig. 5.10), then $G_{clg}(\Omega)$ is always stable since there are no points at which the open-loop gain rolls off at 12dB/octave.

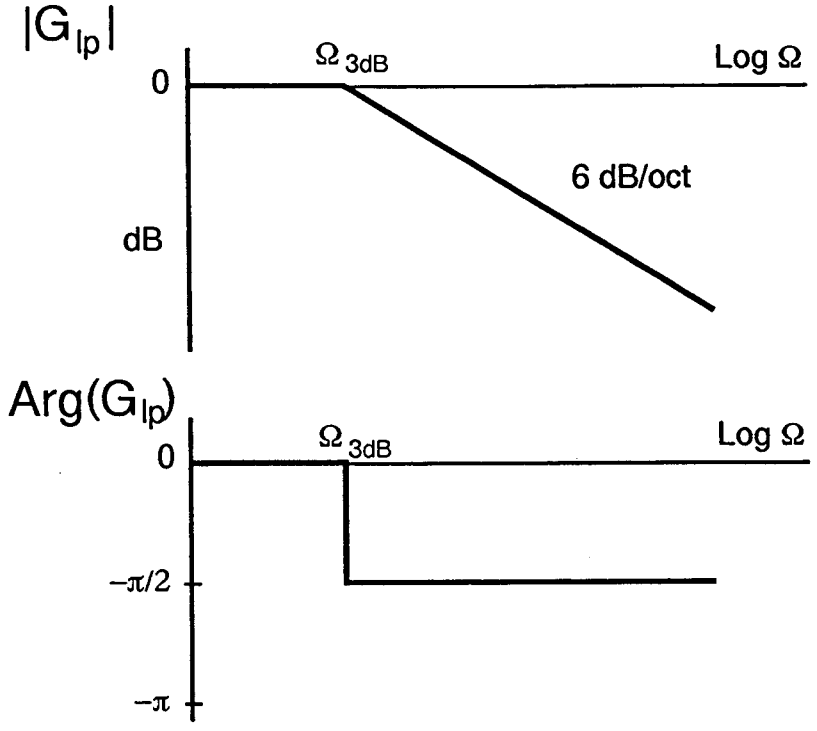


Figure 5.10: Bode plot for low-pass filter (asymptotic limits).

For the example shown in fig. 5.11 where the open-loop gain contains three poles at Ω' and two zeros at Ω", then even though the 0 dB line is crossed with a 6dB/octave slope, there was necessarily a point during the turn on process (g increased from zero) where the 0 dB line was crossed with a 12 dB/octave slope. The system, therefore, would have oscillated before it could attain the gain profile shown in fig. 5.11.

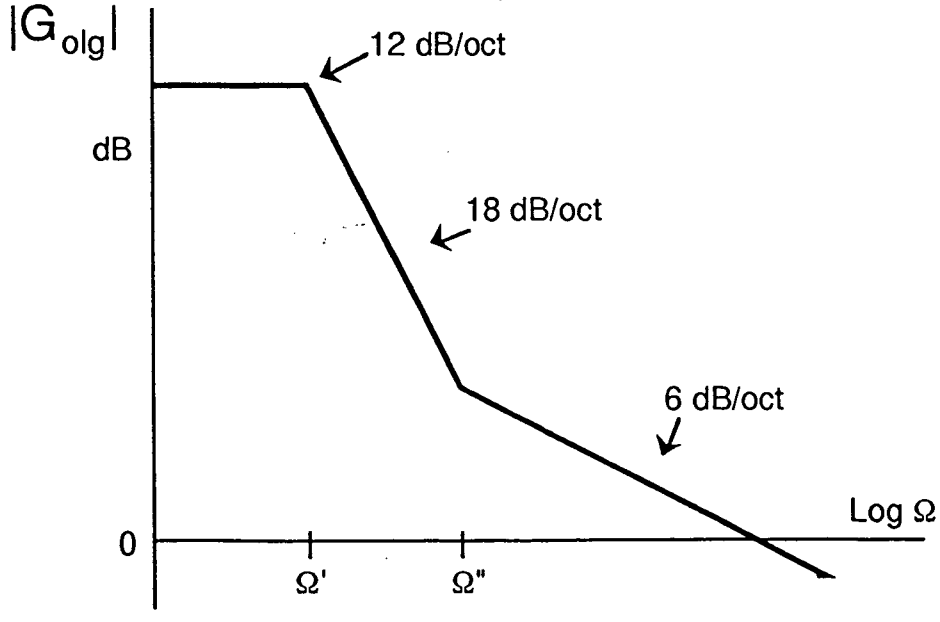


Figure 5.11: Bode plot for 3-pole, 2-zero feedback.

Two notes are in order here. The first is that, strictly speaking, a two pole feedback does not oscillate at unity gain since the phase shift only approaches 180° asymptotically (this is observed in fig. 5.7 as well). As will be shown below, however, only the slightest time delay in a two pole feedback is sufficient to push it into oscillation. For all intents and purposes, therefore, the 12dB/octave roll-off at unity gain is to be avoided. The optimal unity gain roll-off for good feedback response is generally accepted to be 9dB/octave.

The second note is that when control theory is applied to operational amplifiers, where $A(\Omega)$ is the amplifier gain (no feedback) and $gB(\Omega)$ is the feedback from the amplifier output to the amplifier input, the manufacturer specifications often confusingly refer to the amplifier gain $A(\Omega)$ also as the "open-loop gain" [Hor80]. We will stick here to our definition of the open-loop gain as $G_{olg}(\Omega)$. For the case of $A(\Omega) >> gB(\Omega)$, the open-loop gain is approximately equal to the amplifier gain divided by the closed-loop gain (see fig. 5.12). We note that this case is *not* a regime for effective noise reduction (inequality must be reversed), but instead is a regime for a regulated closed-loop gain. It applies to op-amps, where typically $A(\Omega)$ is $10^6$-$10^8$ at low frequency and $gB(\Omega) < 1$. An equivalent and commonly used criterion for feedback stability with op-amps, therefore, is that the amplifier gain should not meet the closed-loop gain with more than a 12dB/octave roll-off.

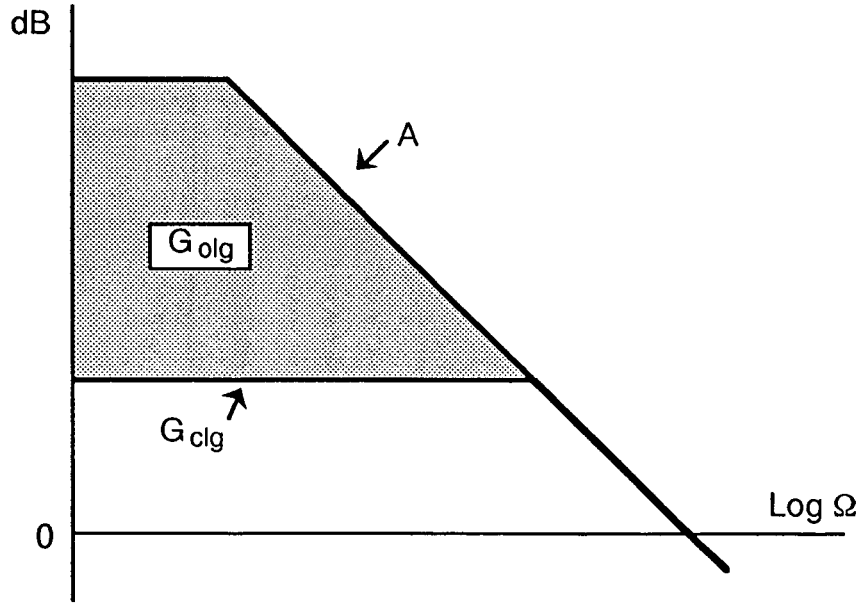


Figure 5.12: Feedback for op-amp.

**f: *Conditional Stability***

We have defined so far the "turning on" of a feedback loop as an increase of g from zero to some prescribed feedback gain. As observed in section V.d, and also in the last example above (fig. 5.11), one is usually limited in this turn on procedure to a maximum g before the system oscillates. In many cases, this maximum g falls short of the feedback gain desired. We noted in section V.d that a larger gain may be obtained then by pushing the feedback oscillation to a higher frequency. When this is impossible, however, one must resort to more elaborate procedures such as those described below.

Returning to the last example above, it is possible to obtain the open-loop gain profile of fig. 5.11 by activating the feedback in two successive steps instead of one. In the first step only a simple pole is turned on in the loop. g can be increased then to its desired value without danger of oscillation (see fig. 5.13). In the second step, the remaining poles and zeros are turned on simultaneously, obtaining finally the profile of fig. 5.11. When the above steps are taken in the prescribed order, the 0 dB line is never crossed by a 12dB/ octave roll-off, and the transfer function $G_{clg}(\Omega)$ is (conditionally) stable. Such is the procedure used to lock the intensity of the twin beams out of the OPO (see section IV.b), with the advantage that high feedback gains may be obtained at low frequencies.

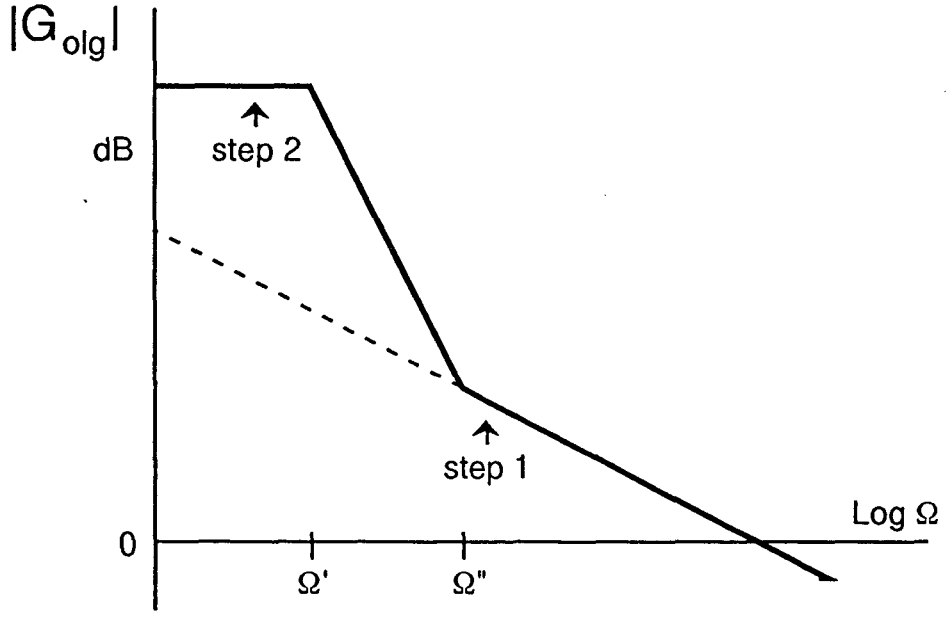


Figure 5.13: Turn-on procedure for conditionally stable feedback.

A similar result may be obtained by summing two feedback loops in parallel, as shown in fig. 5.14. The first is a simple pole filter with feedback gain g'. The second is a double pole filter with feedback gain g". By successively turning on the first loop and then the second loop, a global transfer is obtained with a gain profile similar to that in fig. 5.11. Again, to avoid oscillation, the order in which the loops are turned on must be respected. The advantage here of using two loops in parallel is that it allows independent control of the low frequency gain and of the high frequency gain. It also obviates the use of zeros in the second feedback loop. A similar mechanism to this will be used in the twin-beam feedback experiment which we will address in chapter VIII.

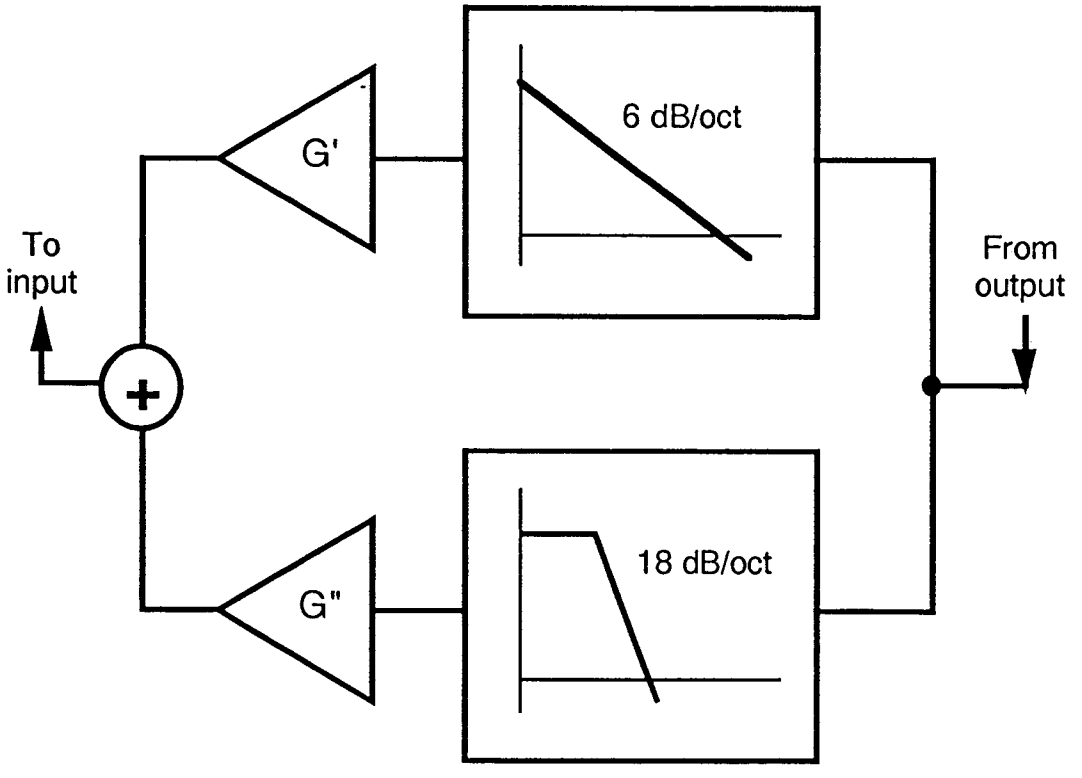


Figure 5.14: Conditionally stable parallel feedback.

### g: *Time Delay in Feedback*

The transfer function for a time delay $\tau_d$ is given by eqtn. 5.7. The qualitative difference between a time delay and a simple filter is seen by comparing the time delay Bode plot in fig. 5.15 to that in fig. 5.10.

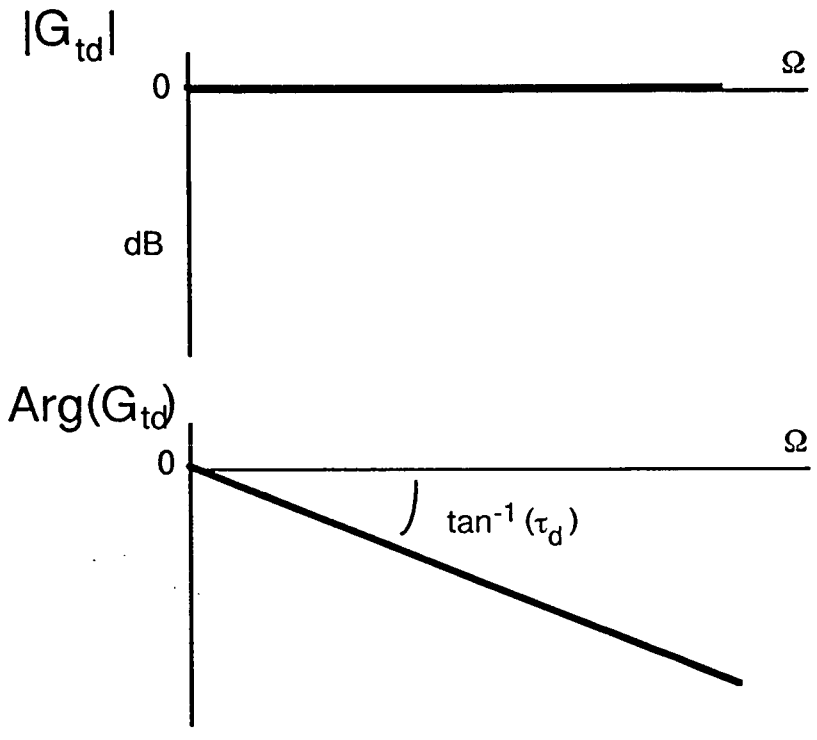


Figure 5.15: Bode plot for time delay.

Inside a feedback loop, a time delay by itself will render the loop unstable. In any physical system, however, a time delay is never by itself but is always accompanied by some kind of filter function either in $A(\Omega)$ or in $B(\Omega)$. A general rule then is that a time delay sets a limit to the maximum feedback gain allowed before the feedback system oscillates. For example, even for systems which are normally always stable, such as a simple pole feedback, a small supplementary time delay will limit the maximum gain allowed in the feedback to $g < 1/\Omega_{3dB}\tau_d$.

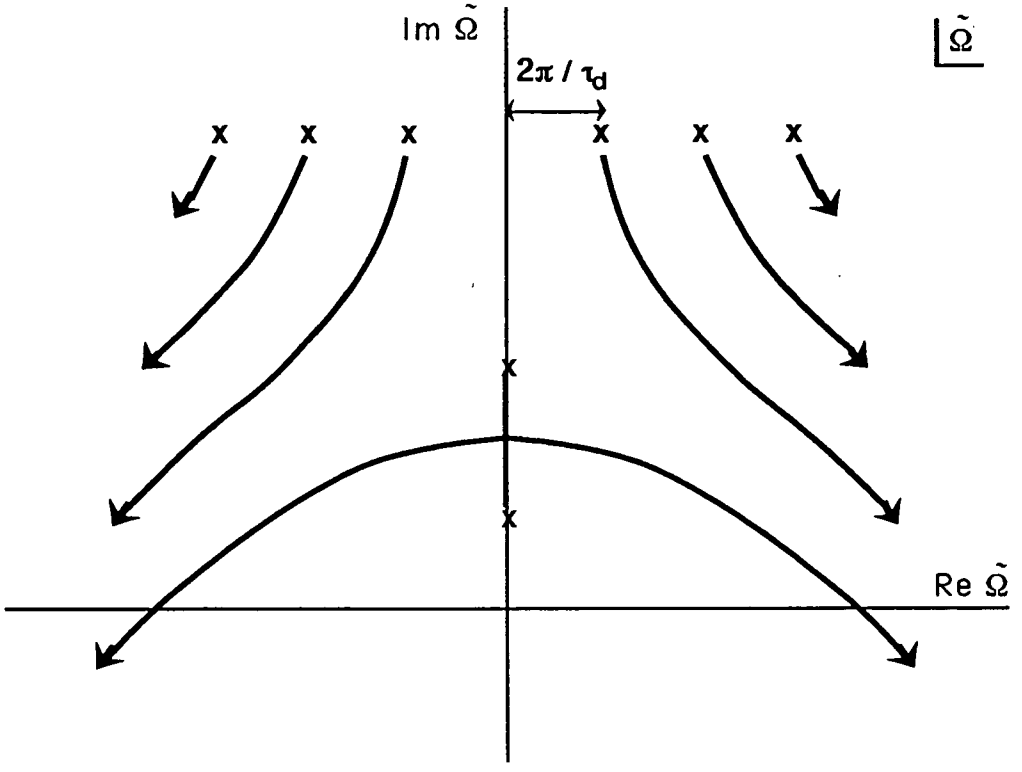


Figure 5.16: Root-locus plot for 2-pole feedback with time delay.

In fig. 5.16, this same effect is illustrated using a root-locus plot where the loop contains two poles at Ω' and Ω" (also normally stable -- see fig. 5.7). One observes here that the poles due to the filters are "nudged" into the l.h.p. by a series of poles due to to the time delay. The greater the time delay, the more pronounced this nudging. To allow for large feedback gain, therefore, it is necessary to minimize the time delay in the feedback loop. Note that the "poles" due to the time delay are discretized here to satisfy eqtn. 5.15, and no longer form a continuous line as in the bottom of fig. 5.3.

# VI. CONTROL USING TWIN BEAMS

We extend the formalism developed in the preceeding chapter and present a general theory for intensity noise reduction when one beam of light is used to control another. Although the theory is valid for any two beams, these will be assumed initially correlated to some degree. In the first part of the chapter we study to what extent the intensity fluctuations in one beam (beam 1) can be controlled by monitoring the intensity of a second beam (beam 2). We consider a general control mechanism where the transfer of intensity information from one beam to the other is linear. Again we use the semiclassical input-output analysis introduced in section II.f, and determine the conditions necessary for noise reduction below the shot noise level. Particular examples of opto-electronic control mechanisms will be given in the remainder of the chapter, where we apply our theory to the specific case of twin beams generated by an OPO.

The bulk of this chapter is taken from an article entitled "Generation of Sub-Poissonian Light using Active Control with Twin Beams" (J. Mertz, A. Heidmann, and C. Fabre) to be published in Physical Review A.

### a: *Basic model*

We consider a basic model for a control mechanism where the intensity fluctuations of beam 1 are corrected by a term proportional to the intensity fluctuations of beam 2 (no additive terms). Various refinements to this model will be made in later sections, but for now we restrict ourselves only to its essential features, described by

$$\delta\tilde{p}_1(t) = \delta p_1(t) - \int d\tau\, G(\tau)\,\delta p_2(t-\tau)\ . \tag{6.1}$$

The details of the control mechanism are contained in the transfer function $G(\tau)$, which we assume here only to be real and causal. The first term on the right represents the original (uncorrected) intensity fluctuations in beam 1. The second term on the right represents a correction term proportional to the intensity fluctuations in beam 2 at all times in the past. The tilde indicates post correction. In frequency space, this model simplifies to

$$\delta\tilde{p}_1(\Omega) = \delta p_1(\Omega) - G(\Omega)\,\delta p_2(\Omega) \tag{6.2}$$

where $G(\Omega)$ is the Fourier transform of $G(\tau)$ and mediates the transfer of fluctuations from beam 2 to beam 1 at frequency $\Omega$. The above equation can be written in terms of the intensity spectra

$$\tilde{S}_1(\Omega) = S_1(\Omega) + |G(\Omega)|^2 S_2(\Omega) - 2\,\mathrm{Re}\big(G(\Omega)S_{12}(\Omega)\big) \tag{6.3}$$

where $S_{12}(\Omega)$ is the correlation "spectrum" defined by eqtn. 2.44.

It is apparent here that $S_i$ and $S_{12}$ provide sufficient information on the two beams to determine the possible effectiveness of noise control. The maximum obtainable noise reduction in beam 1 at a frequency $\Omega$ is derived by minimizing $\tilde{S}_1(\Omega)$ as a function of the complex gain $G(\Omega)$. One finds

$$\tilde{S}_1^{opt}(\Omega) = S_1(\Omega)\left(1 - \frac{|S_{12}(\Omega)|^2}{S_1(\Omega)S_2(\Omega)}\right) \tag{6.4}$$

for an optimum transfer gain

$$G^{opt}(\Omega) = \frac{S_{21}(\Omega)}{S_2(\Omega)} . \tag{6.5}$$

We observe that the noise reduction can be perfect when $|S_{12}|$ is at its upper bound $\sqrt{S_1 S_2}$, for example when the two beams are initially perfectly correlated. On the other hand, if the two beams are initially uncorrelated ($S_{12}$=0) then the optimum gain is equal to zero, leaving the noise spectrum unchanged. It is best then not to bother with control in this case since it is impossible to effect any noise reduction.

It was pointed out in section III.d that when beams 1 and 2 are unbalanced (see definition in section II.g) then $S_{12}(\Omega)$ becomes complex for non-zero frequencies. This was interpreted as a frequency dependent time delay between the two output beams. From eqtn. 6.5 above, one finds that the optimal control gain must be complex as well and of phase opposite to $S_{12}(\Omega)$. This reflects the intuitive result that for the reduction in noise to be optimal, the control mechanism must compensate for the time delay between the output beams by introducing its own supplementary time delay on the monitor beam. Of course, for this mechanism to be causal, the monitor beam must be chosen as the output beam with the shorter time delay.

We note here that the optimal control gain described by eqtn. 6.5 may not be realizable, even in principle. Restrictions imposed by causality entail a well defined relation between the magnitude and the phase of any transfer function, known as the Kramers-Krönig relation [Toll56]. Eqtn. 6.5 is not guaranteed to satisfy this relation, as will become evident below. For this reason, it will be useful to consider the complex gain error defined as the difference between the realistic gain used in experiment and the theoretical optimum gain:

$$G_e(\Omega) = G(\Omega) - G^{opt}(\Omega) \tag{6.6}$$

The effect of this gain error, from eqtn. 6.3, is simply:

$$\tilde{S}_1(\Omega) = \tilde{S}_1^{opt}(\Omega) + |G_e(\Omega)|^2 S_2(\Omega) . \tag{6.7}$$

Deviations in either the real or the imaginary component of $G(\Omega)$ have the same effect on the noise control. The experimental control gain is optimized therefore by minimizing the *distance* in the complex plane between $G(\Omega)$ and $G^{opt}(\Omega)$. This distance, in fact, will serve as a gauge of the control gain performance.

**b:** ***Balanced beams***

We limit ourselves first to the simplifying assumption that beams 1 and 2 are balanced (same intensity and spectrum and no relative time delay -- see definition in section II.g). We observe from eqtn.6.5 and eqtn. 2.45 that $G^{opt}(\Omega)$ becomes a real function. The noise spectrum after correction with a general control gain $G(\Omega)$ can be written (from eqtn. 6.3)

$$\tilde{S}_1(\Omega) = (1 - Re(G))^2\, S(\Omega) + 2\,Re(G)\, S_{1-2}(\Omega) + Im(G)^2\, S(\Omega) \tag{6.8}$$

where $S_{1-2}(\Omega)$ is again the intensity difference spectrum defined by eqtn. 2.50.

One observes that for positive $Re(G)$, the noise $\tilde{S}_1(\Omega)$ after correction is the sum of three positive terms. The first term represents the incident intensity noise S, attenuated by the control mechanism. This vanishes when $Re(G)$ is set to 1. The second term represents a contamination noise introduced by the correction mechanism. This noise is proportional to $Re(G)$ and stems from the decorrelation between the incident beams. The last term represents an additional contamination noise due to the dephasing of G with respect to $G^{opt}$.

The optimum gain and optimum noise reduction are:

$$G^{opt}(\Omega) = 1 - \frac{S_{1-2}(\Omega)}{S(\Omega)} \tag{6.9}$$

$$\tilde{S}_1^{opt}(\Omega) = 2\, S_{1-2}(\Omega)\left(1 - \frac{S_{1-2}(\Omega)}{2S(\Omega)}\right) \tag{6.10}$$

It is clear that $\tilde{S}_1^{opt}(\Omega)$ is always less than $2S_{1-2}(\Omega)$. We examine the case when the twin beams are initially "classical", that is, $S(\Omega) \geq 1$. This is the usual case in experiment, and we wish to determine for this case the requirements on $S_{1-2}(\Omega)$ that are necessary to allow noise reduction below the shot noise level. Refering to eqtn. 6.10, we find

$$\tilde{S}_1^{opt}(\Omega) < 1 \quad \text{when} \quad S_{1-2}(\Omega) < \frac{1}{1+\sqrt{1-1/S}}\,. \tag{6.11}$$

When the excess noise in each beam is large ($S(\Omega) >> 1$), an initial quantum correlation of at least 50% ($S_{1-2}(\Omega) < 0.5$) is necessary to obtain sub-shot noise correction. The optimum gain is equal to one then, and the optimally corrected intensity noise becomes $\tilde{S}_1^{opt}(\Omega) \approx 2\, S_{1-2}(\Omega)$. When the excess noise in each beam is small ($S(\Omega) \approx 1$), a noise level less than $2S_{1-2}(\Omega)$ can be reached for an optimum gain smaller than 1. An initial quantum correlation of at least 50% is no longer necessary for sub-shot noise correction ($S_{1-2}(\Omega)$ can be greater than 0.5). If the beams are not initially correlated (or anti-correlated) at the quantum level ($1 \leq S_{1-2}(\Omega) \leq 2S(\Omega)-1$), then the control mechanism cannot correct below the shot noise and reacts only on the classical excess noise in beam 1.

These results can be understood alternatively by separating the beam fluctuations into the symmetric ($\delta p_+=(\delta p_1+\delta p_2)/\sqrt{2}$) and anti-symmetric ($\delta p_-$) components. One finds then

$$\tilde{S}_1(\Omega) = \tfrac{1}{2}\left[|1-G|^2\, S_{1+2}(\Omega) + |1+G|^2\, S_{1-2}(\Omega)\right] \qquad (6.12)$$

where $S_{1+2}(\Omega)$ is the noise spectrum of the symmetric fluctuation $\delta p_+$, defined in a similar way as in eqtn. 2.49. The fluctuations in beam 1 can be reduced to zero by subtracting the incident fields from one another (G=1) when they are perfectly correlated ($\delta p_-=0$), or by adding them (G=-1) when they are perfectly anti-correlated ($\delta p_+=0$). For intermediate cases when the beams are neither perfectly correlated nor perfectly anti-correlated, such a subtraction or addition of the two fields leaves a residual noise in beam 1 equal respectively to twice the symmetric or anti-symmetric noises. In general, this is not the optimal noise reduction. The noise can optimally be reduced further by making a compromise ($|G|<1$), leaving a residual noise in beam 1 containing both symmetric and anti-symmetric noise components.

### c: *Examples of control mechanisms*

Two general classes of control configurations will be examined: those where the control is effected after the two fields have been generated (feedforward correction) and those where the control is effected retro-actively at their source (feedback correction). Particular examples where the transfer channels are opto-electronic are shown in fig. 6.1. The transfer function $G(\Omega)$ comprises a transfer of intensity fluctuations to voltage fluctuations by detection of beam 2, a voltage gain, and a transfer of voltage fluctuations back to intensity fluctuations by analog modulation of beam 1 either downstream or at its source. Such channels are easily realizable in practice and will be elaborated on at length in further sections. In the present section, we examine the validity of the idealized model introduced above (eqtn. 6.2) by outlining some examples of its implementation.

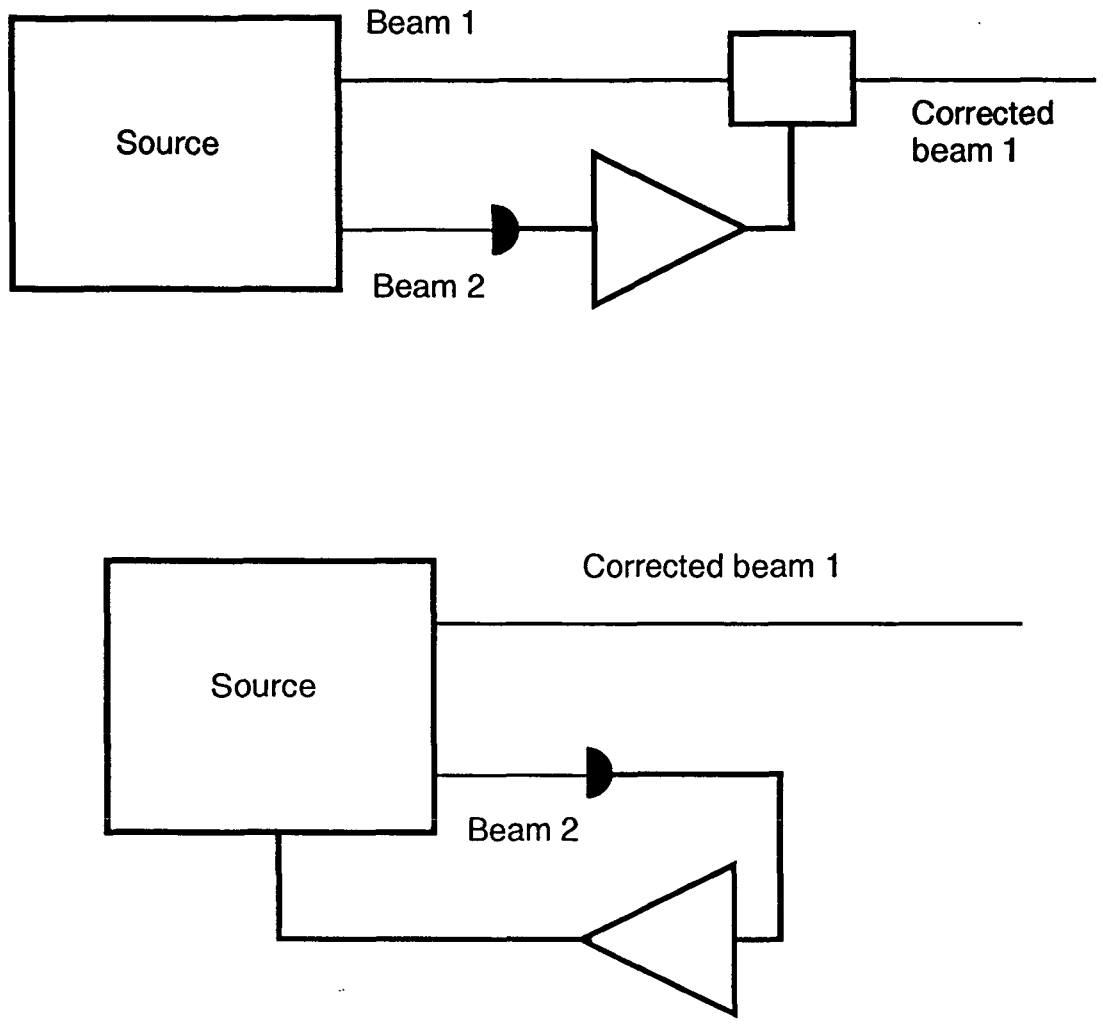


Figure 6.1: Feedforward (top) and feedback (bottom) control configurations.

We turn first to a feedforward configuration and adopt a simple transfer mechanism where beam 1 is subject to a loss proportional to the measured intensity of beam 2. Such a loss can be modeled as a simple beamsplitter with a variable transmission t:

$$t = \bar{t} - g\,\delta p_2 \tag{6.13}$$

where $\bar{t}$ is the bias of the beamsplitter ($\bar{t}$ must be less than one to allow the transmission to be increased or decreased by the control mechanism) and g is the gain of the control mechanism. In a semi-classical analysis, the incoming fluctuations $\delta p_1$ are coupled to vacuum fluctuations $\delta p_v$ entering through the unused port of the beamsplitter (as discussed in section II.f). The resultant outgoing fluctuations are

$$\delta\tilde{p}_1 = \bar{t}\,\delta p_1 - g\,|\bar{\alpha}_1|\,\delta p_2 + \bar{r}\,\delta p_v \ , \tag{6.14}$$

where $\bar{r} = \sqrt{1-\bar{t}^2}$ is the reflection coefficient of the beamsplitter.

This differs from the idealized model (eqtn. 6.2) in that beam 1 is attenuated by the bias $\bar{t}$ and there is an additional noise term (last term in eqtn. 6.14) associated with this loss in beam 1. Although the reflection coefficient r cannot be chosen arbitrarily small since the total transmission t (eqtn. 6.13) must be smaller than 1, it can be chosen of the order g $\Delta p_2 \approx \delta p_1 / |\alpha_1|$. The last term in eqtn 6.14 becomes negligible then and one recovers our idealized model. (In experiment, however, one is often constrained to keep this last term because of intrinsic losses in the beamsplitter mechanism. This is a drawback of feedforward control and degrades the amount of obtainable noise reduction, as we will discuss in section VI.i.)

The implementation of a feedback configuration is more complicated since it is necessary to consider the details of the beams' source. A general case is examined where we assume both beams are derived from a single driving field $\alpha_0$. In a linear fluctuation analysis, the amplitude fluctuations of the beams are related then to those of the driving field $\delta p_0$ through linear transfer functions $A_i$:

$$\delta p_i = A_i \, \delta p_0 + \pi_i \tag{6.15}$$

where $\pi_i$ are other possible additive noises uncorrelated with $\delta p_0$. Such a transfer is found for example in the case of parametric downconversion (see eqtn. 3.9).

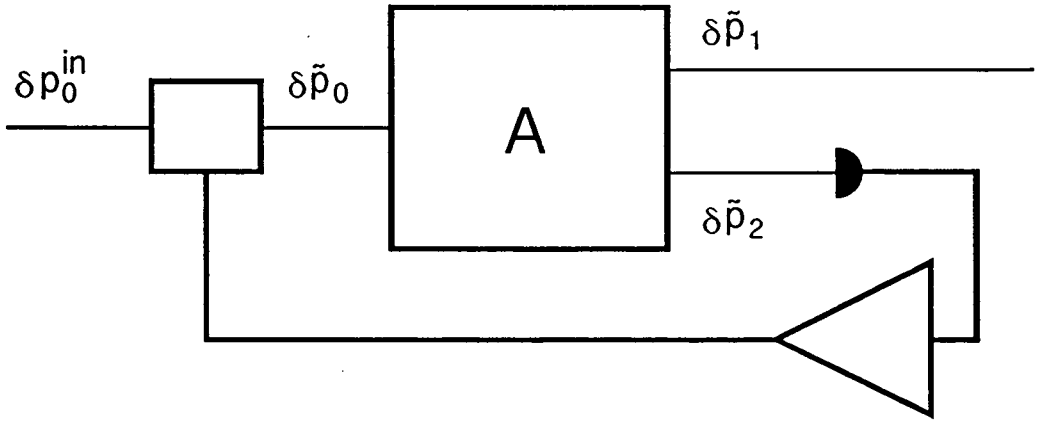


Figure 6.2: Feedback control configuration with a single driving field.

An identical mechanism to the one described above (eqtn. 6.13) is considered for the transfer of fluctuations from beam 2 to the driving beam (see fig. 6.2). The amplitude fluctuations $\delta p_0$ in eqtn. 6.15 become then

$$\delta p_0 \rightarrow \bar{t}\,\delta p_0^{in} - g\,|\bar{\alpha}_0|\delta p_2 + \bar{r}\,\delta p_v \ . \tag{6.16}$$

One can relate the fluctuations $\delta\tilde{p}_1, \delta\tilde{p}_2$ with feedback ($g\neq 0$) to the fluctuations $\delta p_1$, $\delta p_2$ without feedback ($g=0$):

$$\delta\tilde{p}_1 = \delta p_1 - \frac{gA_1|\bar{\alpha}_0|}{1+gA_2|\bar{\alpha}_0|}\,\delta p_2 \ , \tag{6.17}$$

$$\delta\tilde{p}_2 = \frac{1}{1+gA_2|\bar{\alpha}_0|}\,\delta p_2 \ . \tag{6.18}$$

One observes that for large gains g the amplitude fluctuations in the monitored beam 2 are completely attenuated by the feedback control (as in the Yamamoto experiment described in chapter I). This is not necessarily the case for the controlled beam 1 where the amplitude fluctuations are attenuated only to the extent that the two beams are correlated. The effect of feedback on beam 1, however, is the same as that described by our idealized model (eqtn. 6.3), independent of the noise terms introduced by the source ($\pi_i$) or by the transfer mechanism ($\delta p_v$). The feedback configuration presents therefore a relative advantage over the feedforward configuration that the transmission bias $\bar{t}$ can be arbitrary.

**d:** ***Channel imperfections***

Additional refinements can be made to our idealized model by including such imperfections as a non-ideal quantum efficiency $\eta$ in detector 2, and transfer channel noise. Loss in the detector is treated in the same manner as above, as a beamsplitter of transmission $\sqrt{\eta}$, and channel noise is treated by including additional fluctuation $\delta p_e$ at the input of the control mechanism, characterized by a power spectrum $S_e$. The measured fluctuations $\delta p_2$ are modified to

$$\delta p_2 \rightarrow \sqrt{\eta}\,\delta p_2 + \sqrt{1-\eta}\,\delta p_v + \delta p_e \tag{6.19}$$

where $\delta p_v$ represents the vacuum fluctuations coupled through the detector loss. From eqtn. 6.3, the effect of control becomes

$$\delta\tilde{p}_1 = \delta p_1 - \sqrt{\eta}\,G\,\delta p_2 - \sqrt{1-\eta}\,G\,\delta p_v - G\,\delta p_e \tag{6.20}$$

leading to

$$\tilde{S}_1 = S_1 + \eta|G|^2 S_2 - 2\,\mathrm{Re}\left(\sqrt{\eta}\,G\,S_{12}\right) + (1-\eta)|G|^2 + |G|^2 S_e \ . \tag{6.21}$$

Both refinements considered here have the similar effect of introducing additional noise terms in beam 1. These are the last two terms in eqtn. 6.21, associated respectively with non-ideal detector efficiency and channel noise. In addition, the gain G becomes effectively reduced by the factor $\sqrt{\eta}$, due to the loss incurred by beam 2.

The results derived from the previous sections still remain valid except that $S_2$ must be replaced by an effective spectrum:

$$S_2 \rightarrow S_2 + \frac{1-\eta}{\eta} + \frac{S_e}{\eta} \tag{6.22}$$

and G modified to $G/\sqrt{\eta}$. One finds the expected result that imperfections in the control channel tend to deteriorate the amount of attainable noise reduction.

**e:** ***Realization of variable attenuator***

It was shown in section VI.c that the transfer of fluctuations from one beam to another is possible using a variable attenuator (eqtn. 6.13). We consider here a specific example of a variable attenuator comprising an electro-optic modulator (EOM) followed by a polarizer aligned along the polarization plane of the control beam (see fig. 6.3). The neutral axes $\hat{x}$' and $\hat{y}$' of the electro-optic crystal are aligned at an angle $\phi$ from this plane. In a feedforward conguration, the control beam is beam 1. In a feedback configuration, the control beam is the pump.

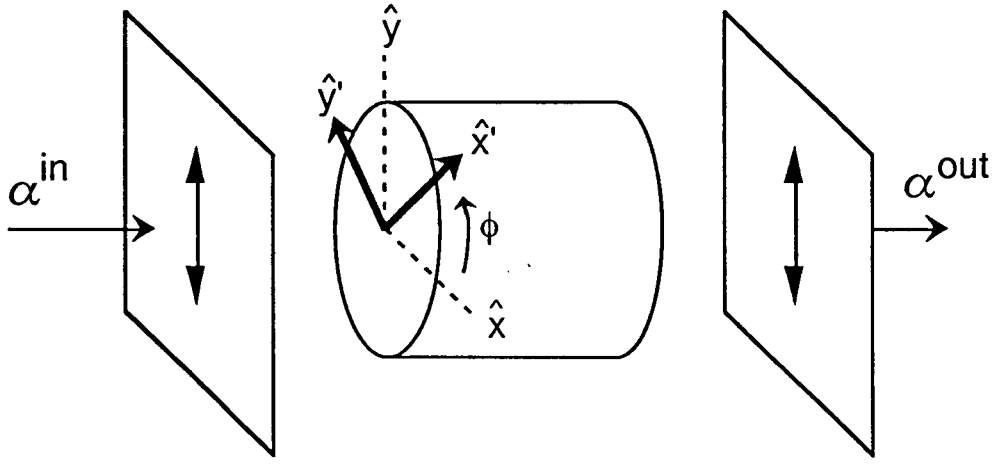


Figure 6.3: Variable attenuator made of EOM and polarizer.

We define $\Gamma$ as the phase shift after propagation through the crystal of a $\hat{y}$' polarized field with respect to an $\hat{x}$' polarized field. We write $\Gamma=\Gamma_0+\delta\Gamma$, where $\Gamma_0$ is a mean phase shift due to crystal birefringence or a voltage bias, and $\delta\Gamma$ is a fluctuating phase shift (assumed small) driven by the control mechanism. The incoming field $\alpha_i^{in}$ is assumed polarized along the $\hat{y}$ direction. $\delta\alpha_v^{in}$ are the incoming vacuum fluctuations polarized along the $\hat{x}$ direction. The transfer of the incoming field $\alpha_i^{in}$ to the outgoing field $\alpha_i^{out}$ (i=0 or 1) is

$$\alpha_i^{out} = \alpha_i^{in}\left(e^{i\Gamma}cos^2\phi + sin^2\phi\right) + \delta\alpha_v^{in}\left(sin\tfrac{\Gamma}{2}sin2\phi\right) \tag{6.23}$$

and is shown schematically in fig. 6.4, where we have assumed without loss of generality that the phase of the incoming mean field is real.

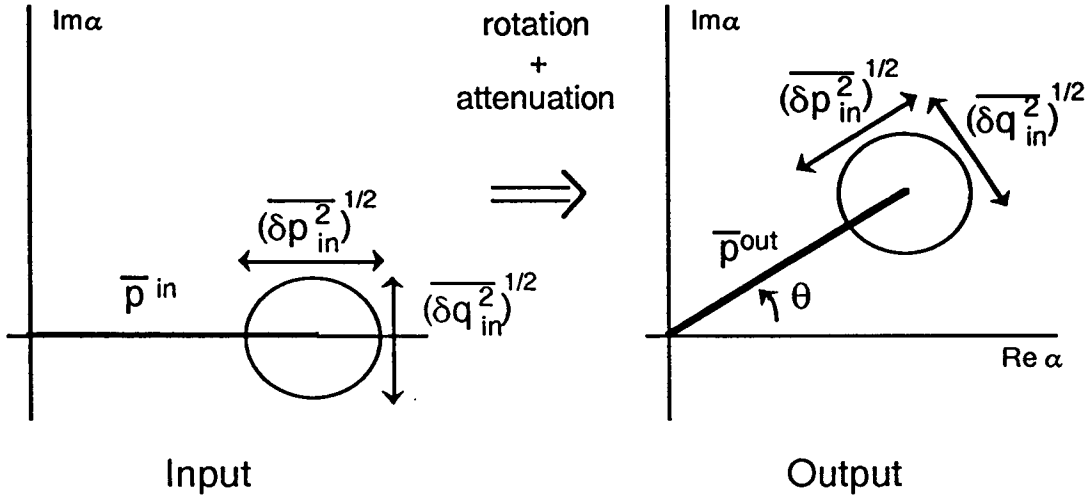


Figure 6.4: Input-output transformation in phase space.

The output field as a function of Γ is written to first order as

$$\alpha_i^{out}(\Gamma) = \alpha_i^{out}(\Gamma_0) + \left.\frac{\partial \alpha_i^{out}}{\partial \Gamma}\right|_{\Gamma=\Gamma_0} \delta\Gamma \tag{6.24}$$

from which we obtain

$$\bar{\alpha}_i^{out} = \bar{\alpha}_i^{in}\left(e^{i\Gamma_0}\cos^2\phi + \sin^2\phi\right) \equiv \bar{\alpha}_i^{in}\left(\bar{t}\,e^{i\theta}\right) \tag{6.25}$$

The mean field is therefore attenuated by a factor $\bar{t}$, which we define as the mean transmission of the modulator, and phase shifted by an angle θ. Separating the field fluctuations into amplitude and phase fluctuations (see fig. 6.3), these become respectively

$$\delta p_i^{out} = \bar{t}\,\delta p_i^{in} + \sqrt{1-\bar{t}^2}\,\delta p_v^{in} - \bar{\alpha}_i^{in}\sin(\Gamma_0-\theta)\cos^2\phi\,\delta\Gamma \tag{6.26}$$

$$\delta q_i^{out} = \bar{t}\,\delta q_i^{in} + \sqrt{1-\bar{t}^2}\,\delta q_v^{in} + \bar{\alpha}_i^{in}\cos(\Gamma_0-\theta)\cos^2\phi\,\delta\Gamma \tag{6.27}$$

The first terms on the right are the transmitted input fluctuations. The second terms are the attendant vacuum fluctuations due to transmissions less than 1. The third terms are the fluctuations induced by the controlled phase shift δΓ. For δΓ proportional to $\delta p_2$ and $\bar{t}$ close to 1, eqtn. 6.26 has the desired form of eqtn. 6.2. A side effect of the control here, however, is that it also modifies the phase fluctuations of the output beam. This may have a consequence in feedback control with an OPO, as we will discuss in section VI.i. We note finally that the control gain here is proportional to the control beam amplitude.

f: *Application to twin beams generated by OPO*

We now apply the above results to the case of balanced twin beams out of an OPO, and make use of the results in chapt. III. Using eqtn. 6.10 and refering to eqtns. 3.11 and 3.14, one finds the maximum noise reduction attainable for a single beam as a function of the OPO parameters (see examples in fig. 6.5 and fig. 6.6). This maximum is valid regardless of whether the control is feedforward or feedback. In a feedforward configuration, the intensity of beam 2 is monitored and used directly to control the intensity noise of beam 1. In a feedback configuration, the control is more complicated. Since the output fluctuations of the OPO are functions of the well identified input fluctuations, and since the input fluctuations of the pump beam in particular are readily accessible, a feedback loop can be realized where the output intensity fluctuations monitored at the output beam 2 are regulated by adjusting the intensity fluctuations of the pump. This has the effect of compensating not only the pump input fluctuations but all the other input fluctuations as well (see fig. 3.1), to within the feedback bandwidth. We note, however, that the pump fluctuations are not themselves necessarily reduced in feedback control.

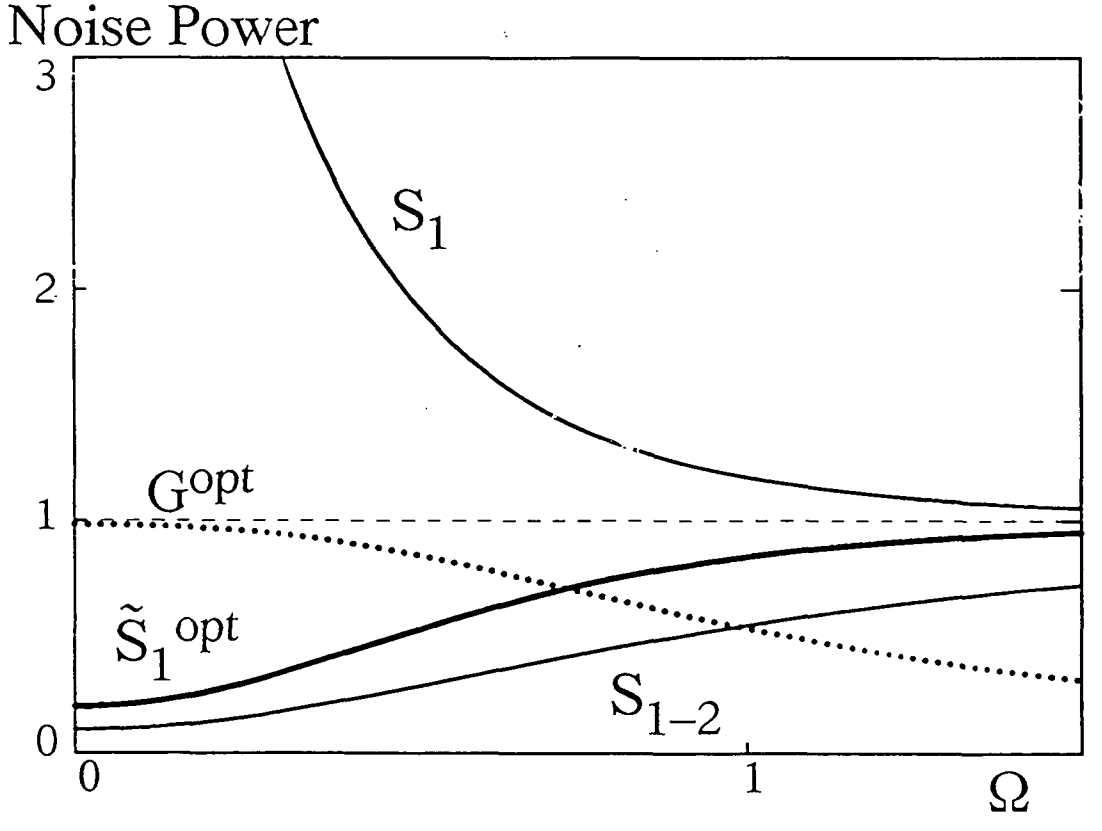


Figure 6.5: Optimal control with large single beam noise ($\sigma \approx 1$).

From eqtns. 3.9 and 3.10, one observes that the input pump fluctuations are coupled only to the symmetric fluctuations and not to the anti-symmetric fluctuations in each output beam. It is interesting to consider then why feedback to the pump beam cannot in

general completely eliminate the symmetric fluctuations, thereby reducing the noise in beam 1 to $S_{1-2}$, rather than $2S_{1-2}$. The difficulty is that both the symmetric and anti-symmetric output noise components are registered at beam 2. These are transferred to the pump beam by the feedback mechanism and even though the pump beam acts only on the symmetric noise, it contains deleterious information concerning the anti-symmetric noise. In effect, the more one tries to correct the output symmetric noise, the more one contaminates it with anti-symmetric noise. A compromise must be made in general for an optimum. In the limit when one tries to correct completely the symmetric noise, as in fig. 6.5 where it is dominant at low frequencies, one ends with twice the anti-symmetric noise in the controlled output beam, whereby $\tilde{S}_1^{opt}$ tends towards $2\,S_{1-2}$. Exactly the same result applies to feedforward control as well.

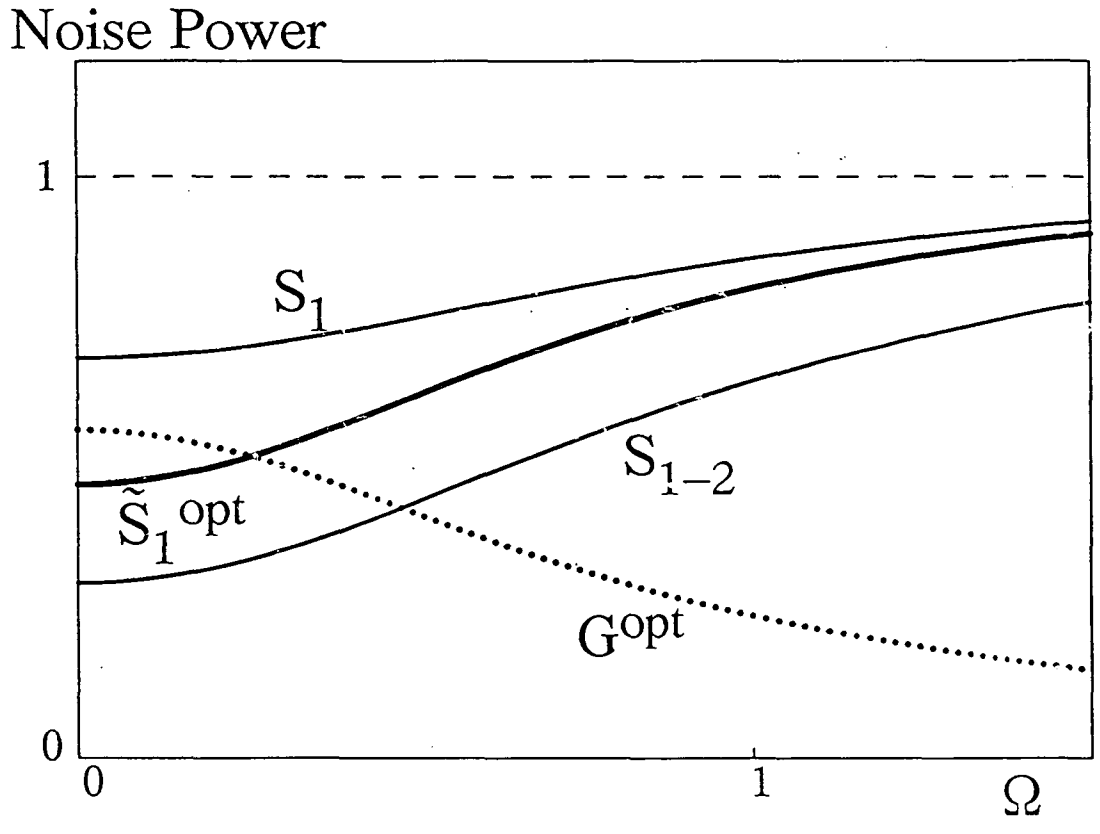


Figure 6.6: Optimal control with small single beam noise ($\sigma = 4$).

We emphasize here that as long as $G^{opt}$ is different from zero, that is, as long as beams 1 and 2 are even partially correlated or anti-correlated ($S_{1-2} \neq S$), then the optimal controlled noise spectrum $\tilde{S}_1^{opt}$ is smaller than the original noise spectrum S, and active control is advantageous. This is demonstrated even in the case of fig. 6.6 where S is already less than 1 (the OPO is operated very much above threshold).

In general, signal or pump detunings ($\varphi$, $\varphi_0 \neq 0$) and cavity imbalance ($\xi_1 \neq \xi_2$) produce only little effect on single beam control when excess noise is large and $\tilde{S}_1^{opt}$ is primarily dependent on $S_{1-2}$. Detunings only add to the excess noise without changing $S_{1-2}$.The effects of imbalance are similar and may be gleaned, for example, from fig. 6.7 where $\tilde{S}_1^{opt}$ is displayed as a function of the imbalance parameter $\gamma_1'/\gamma_2'$. One observes that at zero frequency, the optimum noise is left unchanged, since $S_{1-2}$ is independent of cavity imbalance at zero frequency (see discussion in section III.d). At higher frequencies, $\tilde{S}_1^{opt}$ tends to degrade as a result of a reduction in the bandwidth of the intensity correlations.

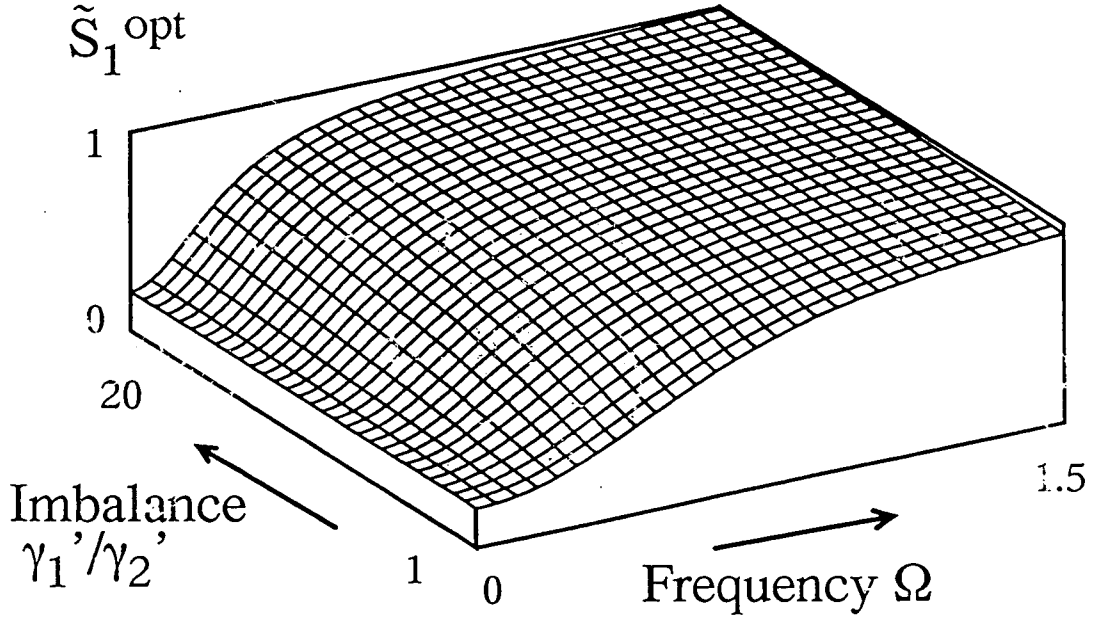


Figure 6.7: Optimal noise control as a function of imbalance ($\sigma$ = 1.3, $\xi$ = 0.9, $\gamma'$ constant)

g: *Gain error analysis*

For noise reduction to be optimal, the control channel must be tailored to produce a global control gain equal to $G^{opt}(\Omega)$. As mentioned in section VI.?, it is often impractical or even impossible to realize such a fit over all frequencies, and in general one must settle for optimal noise control only over a limited bandwidth. We examine the implications of a realistic control channel on noise reduction by studying first the effects of gain error. In the following section we will study the limitations imposed by a stability analysis.

To illustrate the essential features of a realistic control channel, we consider the example where it comprises a gain g, a simple filter of roll-off frequency $\Omega_0$, and a time delay $\tau_d$. The transfer function for this channel is:

$$gB(\Omega) = \frac{g\,\Omega_0\, e^{-i\Omega\tau_d}}{\Omega_0 + i\Omega} \,. \tag{6.28}$$

This channel may be used in a feedforward configuration or in a feedback configuration to provide a realistic control gain $G(\Omega)$ which we compare with an optimal control gain $G^{opt}(\Omega)$. We consider the case of balanced twin beams where $G^{opt}(\Omega)$ has the form shown in fig. 6.25.

In the feedforward configuration, $G(\Omega)$ is equal to $gB(\Omega)$. $G(\Omega)$ and $G^{opt}(\Omega)$ are shown then as a function of positive $\Omega$ in fig. 6.8. We note that $G^{opt}(\Omega)$ is always real whereas $G(\Omega)$ must deviate from the real axis due to restrictions imposed by the Kramers-Krönig relations. In other words, $G^{opt}(\Omega)$ is unrealizable here even in principle. The extent to which $G(\Omega)$ approximates $G^{opt}(\Omega)$ is characterized by its distance from $G^{opt}(\Omega)$ in the complex plane (see eqtn. 6.6). The resultant control performance is characterized by this distance squared (see eqtn. 6.7). The latter is plotted in figs. 6.9 and 6.10 for various parameters of the control channel. In fig. 6.9, g=1 and $\tau_d$=0 and the effect of the roll-off frequency $\Omega_0$ is isolated. One observes that a large bandwidth control is better adapted to $G^{opt}(\Omega)$ for low frequencies, but that its performance is worse for high frequencies above the cavity bandwidth. We note that the plot of $G(\Omega)$ for each of the cases (a), (b) and (c) is the same as that shown in fig. 6.8; only the rate with which this plot is traced out as a function of frequency is different. We also note that optimal control need not always be constrained to zero frequency and may be pushed to non-zero frequencies, as in the example shown in fig. 6.10 where g is less than 1 and $\tau_d$ is large.

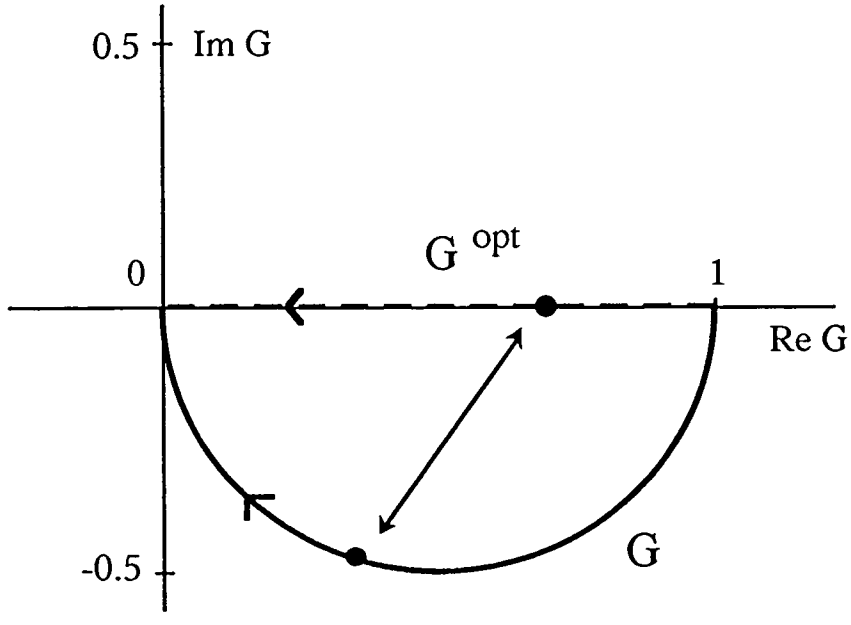


Figure 6.8: Feedforward control with low-pass filter (g = 1, $\tau_d$ = 0). Distance between G and $G^{opt}$ is shown by double-ended arrow.

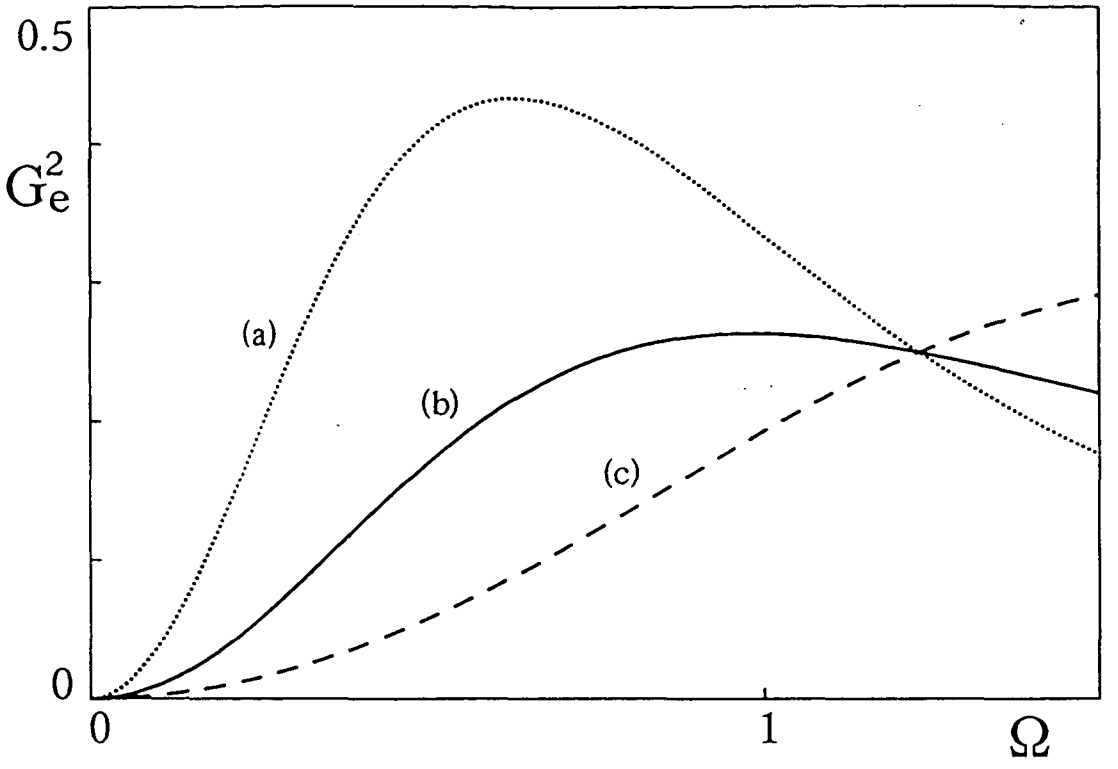


Figure 6.9: Gain error with low-pass filter feedforward control (g = 1, $\tau_d$ = 0). $\Omega_{3dB}$ equal to (a) half cavity bandwidth, (b) cavity bandwidth, and (c) twice cavity bandwidth.

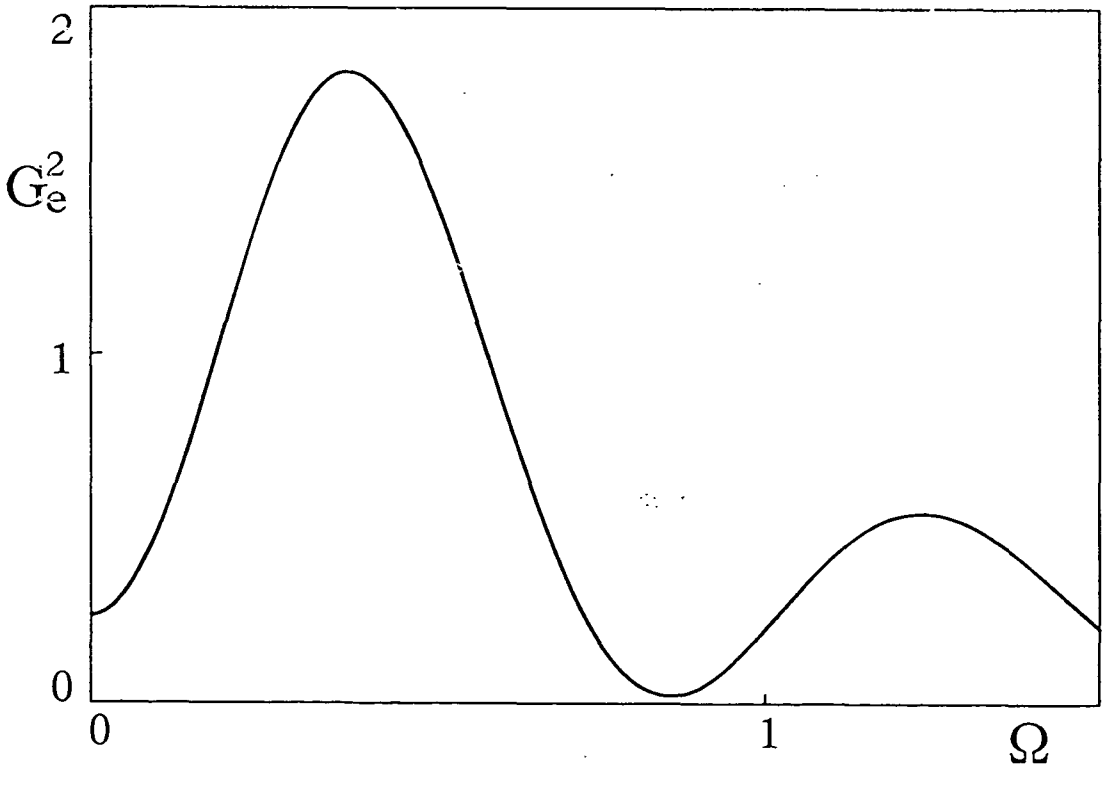


Figure 6.10: Gain error with feedforward control (g = 0.5, $\Omega_{3dB}$ = cavity bandwidth, $\tau_d$ = 5 x cavity bandwidth$^{-1}$ ).

We turn now to the feedback configuration, in which $G(\Omega)$ comprises both the transfer from beam 2 to the pump through the control channel and the transfer from the pump to beam 1 through the OPO cavity. We ascribe to the latter the transfer function $A(\Omega)$ (see eqtn. 6.15). For the example of a balanced, tuned OPO then

$$A(\Omega) = \frac{\sqrt{\xi\,\xi_0\,(\sigma-1)}}{\sigma - 1 + i\Omega} \tag{6.29}$$

(see eqtns. 3.9 and 3.10), and $A(\Omega)$ takes the form of a simple filter with roll-off frequency $\sigma$-1 (again, $\Omega$ is normalized to the cavity bandwidth).

Referring to eqtn. 6.17, the global transfer function for the feedback control becomes then

$$G(\Omega) = \frac{g\,A(\Omega)\,B(\Omega)}{1 + g\,A(\Omega)\,B(\Omega)}\ . \tag{6.30}$$

Note that $G(\Omega)$ is not the same as the closed loop gain defined by eqtn. 5.11, and goes to zero as $g \rightarrow 0$. We illustrate $G(\Omega)$ and $G^{opt}(\Omega)$ in fig. 6.11. At first glance, the feedback gain here may seem less effective than the feedforward gain shown in figure 6.8 because of the larger excursions from $G^{opt}(\Omega)$. At low frequency, however, the feedback gain is "stiffer" and spends more time in the vicinity of 1 than does the feedforward gain. This is observed from the corresponding feedback gain error $|G_e|^2$ in fig. 6.12.

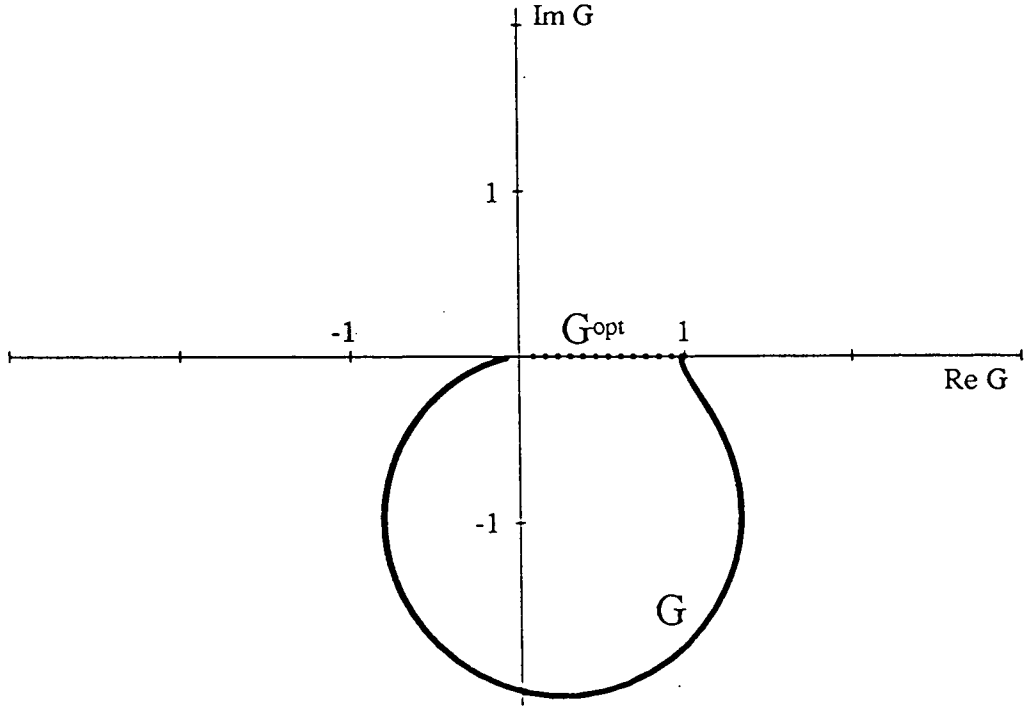


Figure 6.11: Feedback control with 2-pole network (g = 50).

When g is large, the feedback approaches optimal over a larger bandwidth than does the feedforward gain. At higher frequencies, however, the feedback gain error tends to diverge as the open loop gain $gA(\Omega)B(\Omega)$ approaches -1, limiting the bandwidth of effective control. This divergence is associated with feedback instability, which we will discuss below.

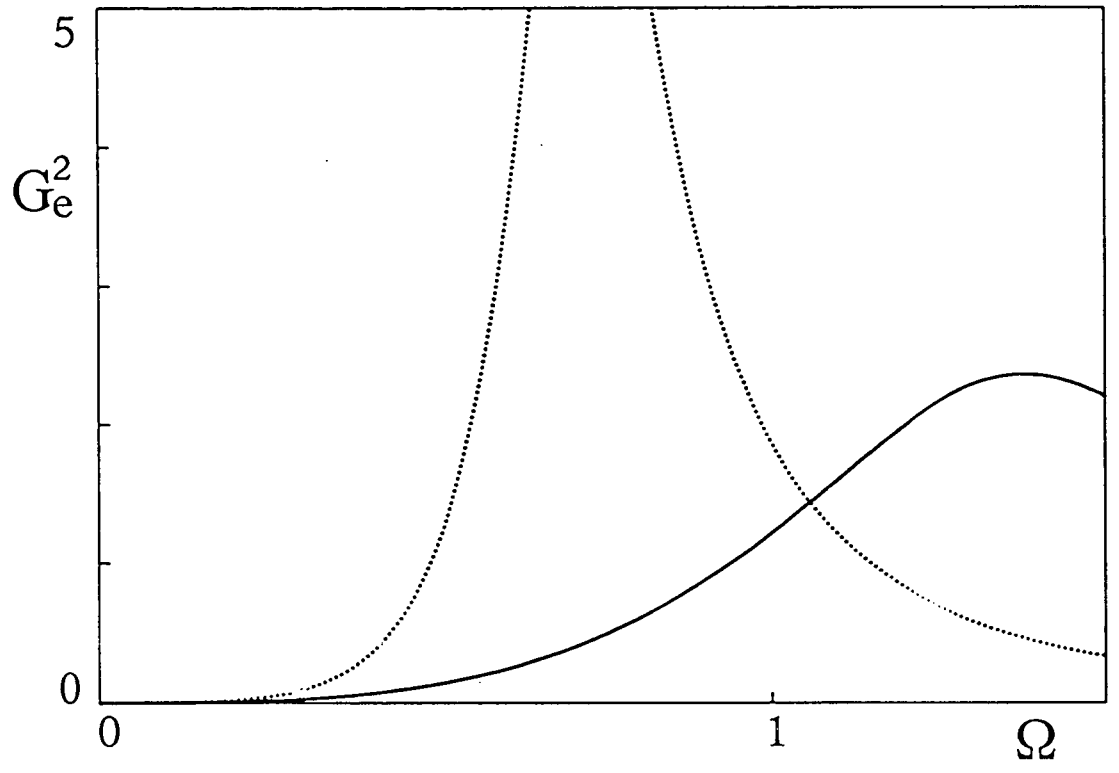


Figure 6.12: Gain error with 2-pole feedback control (g = 50, $\Omega_{3dB}$ = cavity bandwidth [solid] and cavity bandwidth/4 [dotted], OPO roll-off = cavity bandwidth / 10).

**h:** ***Stability analysis***

We consider now the same examples used above and examine the stability of the resultant control by using the root-locus method introduced in chapt. V. This method traces the migration of the poles of $G(\Omega)$ as the control gain is turned on, that is, as g is increased from zero. As we will see, the criterion that $G(\Omega)$ must remain stable can limit g and prevent $G(\Omega)$ from approaching $G^{opt}(\Omega)$.

When the control channnel described by eqtn. 6.28 is applied in the feedforward configuration, that is when $G(\Omega)=gB(\Omega)$, then the control is always stable. The poles of $G(\Omega)$ lie in the u.h.p. and remain fixed there independent of g. The resultant controlled intensity spectrum is illustrated in fig. 6.13a (again, for the example of a balanced, tuned OPO, where $G^{opt}(\Omega)$ is real). It is clear that the bandwidth over which the noise control is near optimal is smaller than the bandwidth possible in theory. As shown in the previous section, the noise control becomes optimal only at low frequencies where $G(\Omega)$ is real. In addition, it is only optimal for a specific value of g.

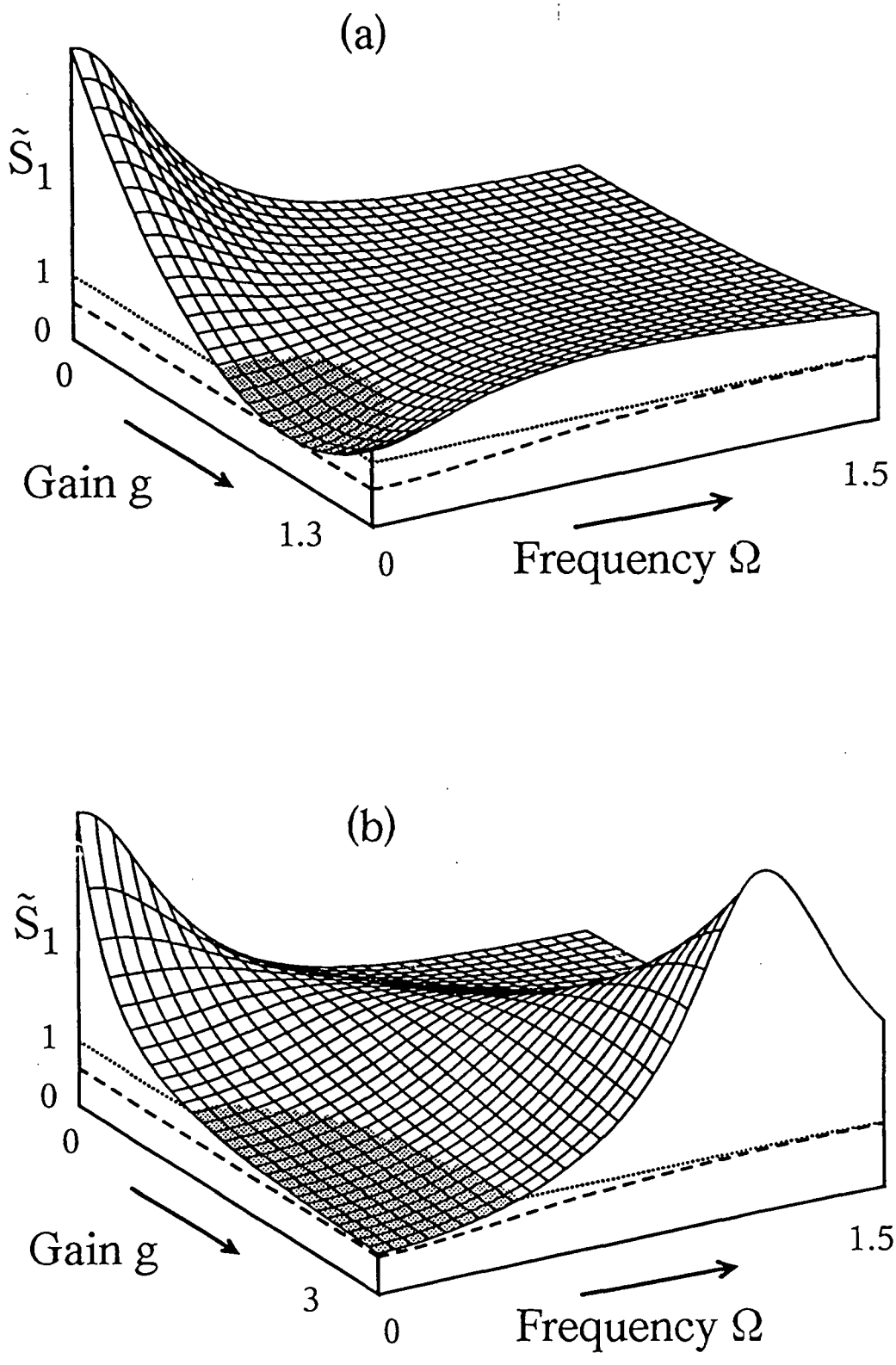


Figure 6.13: Noise reduction of OPO beam with (a) feedforward and (b) feedback configurations. $\Omega_{3dB}$ = cavity bandwidth, $\tau_c$ = cavity bandwidth$^{-1}$ /2. OPO is tuned and balanced ( $\sigma$ = 1.3, $\xi$ = 0.7). Dashed traces are theoretical optimum noise reduction.

When the control channel is applied in a feedback loop, then the global control gain is defined by eqtn. 6.30. The pole locations of $G(\Omega)$ are this time manifestly dependent on g, and although $G(\Omega)$ is slightly different from $G_{clg}(\Omega)$ presented in chapter V, the same methods for stability analysis apply. Using our simple model (eqtns. 6.28 and 6.29), $G(\Omega)$ becomes a two pole feedback network with a time delay. For small gains the pole locations of $G(\Omega)$ are in the u.h.p. and the feedback loop is stable. For larger gains, the poles are displaced and become "nudged" by even the smallest time delay $\tau_d$ towards the real axis (see fig. 5.16). At a critical gain, the loop is set into oscillation, which occurs when the open loop transfer function $gA(\Omega)B(\Omega)$ is equal to -1 (as in chapt. V). This oscillation sets an upper limit to the gain allowed in a feedback configuration. Illustrations of the resultant noise reduction are shown in fig. 6.13b, where the onset of oscillation is apparent. In many cases the maximum gain that is allowed before oscillation is not sufficient for the noise reduction in beam 1 to approach optimal. This maximum gain is largely governed by the location of the poles in filters $A(\Omega)$ and $B(\Omega)$. The lower these poles are in frequency, the lower the frequency of oscillation and, in general, the lower this maximum gain. For effective noise reduction, therefore, it is important to keep these pole locations at high frequencies. This usually entails maximizing the OPO pumping and bandwidth or working with fast electronics.

### i: *Feedforward versus feedback*

It was shown in section VI.c that the transfer of fluctuations from one beam to another is possible using a variable attenuator. A specific example of such an attenuator is given in section VI.e, where it consists of an electro-optic modulator followed by a polarizer. The intensity fluctuations in beam 2 are registered as voltage fluctuations which then pilot the EOM transmission and modify the intensity fluctuations either in the pump beam or in beam 1. A side effect of this type of channel is that it modifies also the phase fluctuations of the controlled beam (see eqtn. 6.27). This may pose a problem in the feedback configuration since the phase fluctuations of the pump beam are mixed into the intensity fluctuations of the signal and idler beams when the OPO is detuned (see eqtns. 3.9 and 3.10). We note, however, that the correlations between the signal and idler beams remain independent both of OPO detuning and of pump beam excess noise. The coupling of the EOM to phase fluctuations has a consequence, therefore, only on the signal and idler beam excess noises and not on their correlations. If these excess noises are already large, the coupling produces little effect on the noise control. In any case, one can circumvent the above problem by inserting into beam 1 a second modulator+polarizer run in parallel with the first modulator+polarizer but with opposite polarity. The transfer to intensity fluctuations is doubled then whereas the transfer to phase fluctuations is cancelled.

An advantage of feedback control over feedforward control is that the transfer function $G(\Omega)$ is less sensitive to variations in g. As observed in fig. 6.13b, for example, it suffices for optimal control that g be large (albeit not so large that the system oscillates). This

allows the noise control to be effective over a larger bandwidth than in a feedforward configuration, where g must take on a specific value.

A second advantage of feedback over feedforward is that beam 1 is left uncluttered of extraneous losses. It was shown in section VI.c that these losses could be reduced in theory to the point where the noise they introduced was negligible. This is often not the case in practice, and for a mean amplitude transmission $\bar{t}$ through the feedforward intensity modulator, the optimally reduced noise spectrum of beam 1 becomes degraded:

$$\tilde{S}_1^{opt}(\Omega) \rightarrow \bar{t}^2 \tilde{S}_1^{opt}(\Omega) + 1 - \bar{t}^2 \ . \tag{6.31}$$

A notable disadvantage of feedback, however, is its propensity towards oscillation. As illustrated in the above stability analysis, this imposes restrictions on the loop gain which hinder the effectiveness of the noise reduction. A feedback loop that is conditionally stable may be used to bypass these restrictions, obtaining higher gains below the oscillation frequency (see section V.f).

Experiments using feedforward and feeback configurations will be discussed in chapters VII and VIII, respectively.

# VII. FEEDFORWARD EXPERIMENT

We present here a twin beam control experiment using a feedforward configuration. The layout of the OPO is similar to the one presented in chapter IV. The intensity of beam 2 is monitored and used to directly regulate the intensity of beam 1 using an intensity modulator of the type described in section VI.e. The essential features of the experiment are presented in the publication below. The experiment was conducted prior to improvements in the OPO twin beam correlations (see chapt. IV) and benefited only of a 69% quantum noise reduction in the twin beam intensity difference spectrum. A similar experiment using an 86% quantum noise reduction is presently underway, the results of which will not be included in this thesis. Supplementary experimental details are given in this chapter on the pump laser, the feedforward channel, and the measurement of the single beam intensity noise spectrum.

****** Reprint: Physical Review Letters .******

# Observation of High-Intensity Sub-Poissonian Light Using an Optical Parametric Oscillator

J. Mertz, A. Heidmann, C. Fabre, E. Giacobino, and S. Reynaud
*Laboratoire de Spectroscopie Hertzienne de l'Ecole Normale Supérieure, Université Pierre et Marie Curie, 75252 Paris CEDEX 05, France*
(Received 23 February 1990)

We report the observation of high-intensity sub-Poissonian light using the correlated "twin" beams generated by an optical parametric oscillator. The intensity fluctuations in one of these beams are reduced by a feedforward correction mechanism that monitors the intensity of the second beam. The observed reduction in noise power is up to 24% below the shot-noise limit.

PACS numbers: 42.50.Dv, 42.65.Ky

Recently, the possibility of generating squeezed states by acting on the quantum fluctuations of the electromagnetic field has prompted much investigation.[1] These nonclassical states of light are characterized by a reduction in the fluctuations of some component of the field below the vacuum fluctuation level, making them potentially useful for improving the signal-to-noise ratio in experiments limited by the shot noise of standard laser light. Amplitude squeezed light, in particular, is defined by a reduction in the fluctuations of the amplitude component of the field. In the small-fluctuation limit it exhibits sub-Poissonian photon statistics, which is of interest for experiments involving direct intensity measurements.

Two techniques have been used so far in the generation of amplitude squeezed light. The first, a direct-conversion technique, relies on an inherently "quiet" source,[2-5] such as a constant-current–driven laser diode, where a maximum photon noise reduction of 26% was reported.[4] The second technique relies on external control of the amplitude fluctuations, using, for example, feedback correction. Large degrees of amplitude squeezing have been observed using "closed" configurations[6,7] where all the light is lost on detection to provide a feedback signal. The squeezed light in these systems is unavailable since it is restricted to internal paths of the loop, and several "open" configurations have been proposed for its extraction.[8-11] One such configuration makes use of the in-loop generation of two quantum-correlated light beams, one beam providing a feedback signal to stabilize the other beam below the shot-noise level. Recently, a quantum noise reduction of 22% has been observed in low-intensity incoherent light using feedback from spontaneous parametric down conversion.[12]

A particularly effective generator of quantum-correlated light beams is an optical parametric oscillator (OPO),[13] comprising a nonlinear crystal in an optical cavity. Such a device is based on the parametric down conversion of pump photons into pairs of signal photons, resulting in "twin" output beams whose photon numbers are nearly equal when counted over times longer than the cavity storage time.[14] In practice, the amount of correlation between the two output beams is limited only by spurious optical losses undermining the pairwise detection of the beam photons, and quantum noise reductions as large as 69% have been attained in the intensity difference between the beams.[15] The additional feature that the output beams are laserlike and of high intensity makes them particularly convenient for the generation of sub-Poissonian light using configurations where the control signal from one beam is either fed back to the pump or fed forward directly to the second beam. In this Letter, we report the first experimental observation of high-intensity sub-Poissonian light using an OPO in a feedforward configuration.

The experimental layout is shown in Fig. 1 and is similar to the one described in Ref. 15. An optical parametric oscillator is pumped above threshold by the 528-nm line of a single-mode cw argon-ion laser, isolated from OPO back reflections by an acousto-optic modulator (AO). The OPO cavity mirrors, 35 mm apart with the radii of curvature 20 mm, are transmitting in the visible and present a low finesse for the pump light. The nonlinear medium is a 7-mm-long potassium-titanyl phos-

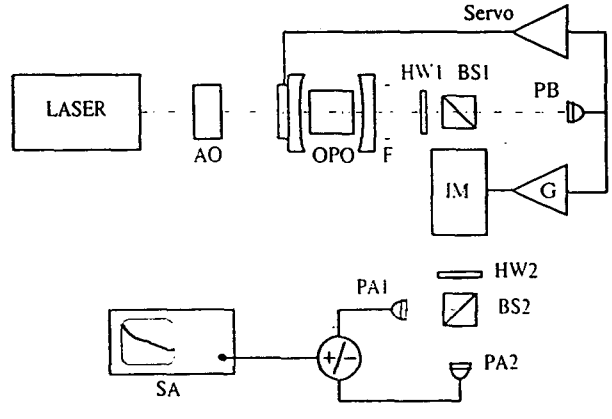


FIG. 1. Experimental setup. AO: acousto-optic modulator; F: dichroic filter; HW1,HW2: half-wave plates; BS1,BS2: polarizing beam splitters; IM: intensity modulator; PA1, PA2,PB: photodetectors; SA: spectrum analyzer.

 

phate ($KTiOPO_4$) crystal, type-II phase matched so the down-converted twin infrared beams are cross polarized with nondegenerate wavelengths $\lambda_1 = 1.048$ $\mu$m and $\lambda_2 = 1.067$ $\mu$m. The output mirror is 1.6% transmitting in the infrared and the total losses (including input mirror transmission and crystal absorption) are of the order of 0.5%, resulting in an infrared emission threshold at about 200-mW incident pump power.

A dichroic filter (F), placed at the output of the cavity, blocks the transmitted pump light while letting pass the two emitted infrared beams which are then separated by a polarizing beam splitter (BS1) into detection arms *A* and *B*. The detectors (PA1, PA2, and PB) are all reverse-biased Epitax 300 *p-i-n* photodiodes with quantum efficiencies measured near 0.9. The intensities of the infrared beams are sensitive to cavity detuning and are actively stabilized to 6 mW for an incident pump intensity of 420 mW, using the dc output (dc–30 kHz) from detector *B* to servocontrol the OPO cavity length.

The feedforward correction loop consists of a variable gain amplifier (G) driven by the ac signal (1–20 MHz) from detector *B*, and applied to an intensity modulator (IM) inserted in arm *A*. This modulator (an electro-optic modulator followed by a polarizer) acts as an analog shutter with a transmission proportional to the applied voltage from G. Total optical losses through path *A*, including losses due to the modulator transmission bias, are about 20%.

To calibrate the noise in beam *A* to its shot-noise reference level, a double-balanced detector is used in arm *A* made of a 50% beam-splitting mechanism (half-wave plate HW2 and polarizing beam splitter BS2) and two photodetectors (PA1 and PA2). The ac signals (1–20 MHz) from each photodetector can be either added or subtracted using an amplifier which is commuted between a summing or differencing configuration, and the resultant signal is observed on a spectrum analyzer (SA). The total noise in beam *A* and its associated shot-noise level are measured almost simultaneously by switching from one configuration to another.

The performance of the double-balanced detector *A* was carefully ascertained. The gain balance between the two configurations was checked by adding and subtracting two noises from independent electronic sources and observing the same result to within 1%. The total electrical and optical common mode rejection, measured by modulating the beam-*A* intensity and observing the reduction in the modulation peak when passing from the sum to the difference mode, was found to be $-30$ dB for a modulation frequency of 5 MHz, and no greater than $-25$ dB in the 1–20-MHz range. Linearity in the detection channel was also verified for optical powers up to 6 mW by inserting a variable attenuator in front of the double-balanced detector and plotting the shot-noise power as a function of the mean intensity in beam *A*.

Figure 2 shows various noise spectra of beam *A*, taken while stabilized on the same infrared resonance peak.

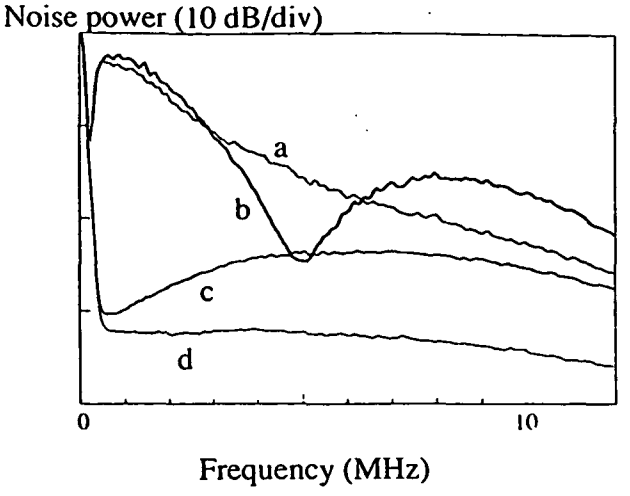


FIG. 2. Experimental noise spectra of beam *A* (curve *a*) without feedforward correction, (curve *b*) with feedforward correction, (curve *c*) associated shot-noise level, and (curve *d*) electronic noise.

Curve *a* is the total noise power in beam *A*, taken in summation mode (PA1+PA2), with no optoelectronic noise correction (feedforward gain G equal to 0). Curve *c* is the associated shot-noise level, taken in the differencing mode (PA1 $-$ PA2). It is clear from these spectra that the infrared beams generated by the OPO have a large amount of excess noise, due to the fact that the OPO is stabilized off resonance and close to oscillation threshold.[13] The excess noise at 5 MHz is typically 5 to 10 dB above the shot-noise level, depending on OPO cavity alignment and detuning. Curve *b* of Fig. 2 is the noise power in beam *A* when the optoelectronic feedforward correction is turned on. The observed noise reduction is sensitive to both the gain and phase lag of the feedforward correction signal. The latter is fixed by filters in the feedforward electronics that prevent low-frequency saturation, allowing the gain to be properly matched in a frequency range centered here about 5 MHz.

To evaluate the quantum noise reduction, we divide the noise power spectrum (Fig. 2, curve *b*) by the shot-noise spectrum (Fig. 2, curve *c*), having corrected both for electronic noise (Fig. 2, curve *d*). The resulting normalized noise power spectrum $S_{ff}(\Omega)$ is shown in Fig. 3, curve *a*. $S_{ff}(\Omega)$ drops below 1 over a 700-kHz frequency range around 5 MHz. The reduction in noise power is up to 24%($\pm$2%) below the shot-noise level.

These experimental results can be compared with a simple theoretical model, using a semiclassical input-output formalism.[16] Writing the semiclassical field-amplitude fluctuations of the two infrared beams at the OPO output as $\delta a_A$ and $\delta a_B$, the significant effect of the feedforward loop is to correct the fluctuations $\delta a_A$ of beam *A* by a term proportional to the fluctuations $\delta a_B$ of beam *B*. Neglecting losses in arm *A*, the field-amplitude

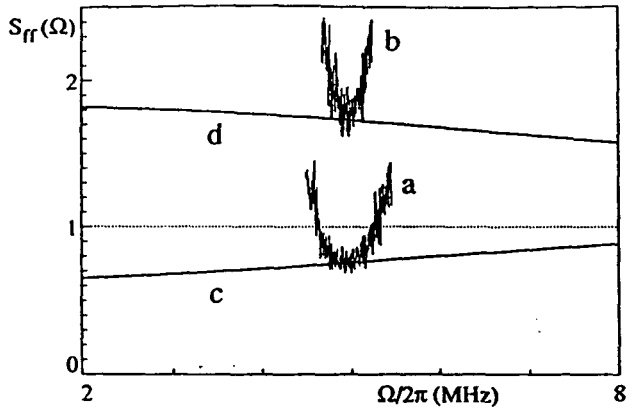


FIG. 3. Experimental noise spectra of beam $A$, normalized to the shot-noise level, (curve $a$) when the two beams at the OPO output are quantum correlated and (curve $b$) decorrelated by the beam mixer HW1+BS1. The largest noise power reduction is 24% below the shot-noise level (curve $a$). Theoretical curves ($c$ and $d$) represent the minimum obtainable noise powers for these cases when the gain is optimized at every frequency.

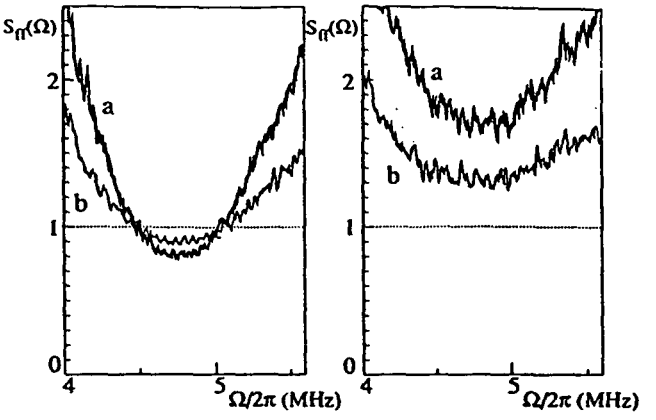


FIG. 4. Effect of a 50% attenuator inserted in beam $A$ after the intensity modulator, (left) when the two beams at the OPO output are quantum correlated and (right) decorrelated. Curves $a$ are the noise spectra of beam $A$ without attenuation, while curves $b$ are the noise spectra with attenuation. As expected, the attenuated noise tends toward the shot-noise level in proportion to the amount of attenuation.

fluctuations $\delta a_{ff}$ after correction become

$$\delta a_{ff} = \delta a_A - g\delta a_B , \tag{1}$$

where $g$ is a parameter related to the gain of the feedforward loop. The intensity noise spectrum $S_{ff}(\Omega)$, normalized to its shot-noise reference, is given directly by the variance of the field fluctuations $\delta a_{ff}(\Omega)$ at frequency $\Omega$:[17]

$$S_{ff}(\Omega) = \langle |\delta a_{ff}(\Omega)|^2 \rangle \tag{2a}$$

$$= (1-g)^2 S_I(\Omega) + 2g S_{A\text{-}B}(\Omega) , \tag{2b}$$

where $S_I(\Omega)$ is the intensity noise spectrum of a single beam at the OPO output (assumed to be the same for $A$ and $B$), and $S_{A\text{-}B}(\Omega)$ is the noise spectrum of the intensity difference between the output fields, characterizing the quantum correlation between the twin beams. $S_I$ and $S_{A\text{-}B}$ are normalized to their associated shot-noise levels. For an optimum gain,

$$g_{opt} = 1 - \frac{S_{A\text{-}B}(\Omega_0)}{S_I(\Omega_0)} , \tag{3}$$

the intensity noise $S_{ff}(\Omega_0)$ at frequency $\Omega_0$ reaches its minimum value,

$$S_{ff}(\Omega_0) = 2S_{A\text{-}B}(\Omega_0)\left[1 - \frac{S_{A\text{-}B}(\Omega_0)}{2S_I(\Omega_0)}\right] . \tag{4}$$

$S_{A\text{-}B}$ is less than 1 when beams $A$ and $B$ are correlated at the quantum level, and was measured to be around 0.35 at 5 MHz.[15] Neglecting losses, $S_I$ is identified with the noise spectrum of beam $A$ with no optoelectronic correction, and is everywhere greater than 1 for this experiment. The theoretical optimum intensity noise $S_{ff}(\Omega_0)$ is traced in Fig. 3, curve $c$, as a function of frequency $\Omega_0$, where factors such as intensity modulator loss, nonideal detection efficiency, beam imbalance at the OPO output, and electrical noise are taken into account.[18] The experimental result (curve $a$), shown superposed, effectively attains this optimum.

It is interesting at this point to consider a separate case where beams $A$ and $B$ are not correlated ($S_{A\text{-}B} = 1$). As shown in Fig. 3, curve $d$, the optimum feedforward gain for this case, while still correcting for much of the excess noise in beam $A$, does not reduce the noise even to the shot-noise level. This situation is readily attainable experimentally by inserting a half-wave plate (HW1 in Fig. 1) at the output of the OPO to rotate the polarization of each twin beam by 45°. Instead of separating the two cross-polarized infrared beams, the beam splitter BS1 then randomly distributes them into arms $A$ and $B$.[15] The resulting experimental noise reduction, with the feedforward gain optimized for a minimum noise around 5 MHz, is shown in Fig. 3, curve $b$. As in the case of correlated beams, the experimental results are in good agreement with theory.

For a last verification of the accuracy of the experiment an attenuator was inserted in beam $A$ immediately before the double-balanced detector. A specific signature of sub-Poissonian light is that the noise power normalized to its shot-noise level is increased with attenuation, whereas for classical light it is decreased or left unchanged. The normalized noise spectra of beam $A$ are shown in Fig. 4, when the beams at the OPO output are quantum correlated ($S_{A\text{-}B} < 1$, left figure) or decorrelated ($S_{A\text{-}B} = 1$, right figure) for the cases without attenuation (curves $a$) or with a 50% attenuator (curves $b$). It is

verified that the noise tends toward 1 in proportion to the amount of attenuation, and that quantum noise reduction is degraded by a factor of 2 (left figure). Note that the accuracy of the shot-noise calibration can be determined from these four spectra using linear extrapolation. One finds an uncertainty in the shot-noise level less than 1%.

In conclusion, a quantum noise reduction of 24% in the intensity noise of an intense light beam was observed. The generation of this amplitude squeezed light was obtained by optoelectronic feedforward correction, using the quantum correlation properties of twin beams generated by an optical parametric oscillator. Such a technique seems attractive for potential applications, particularly with the advent of monolithic OPO technology.[19] Moreover, larger noise reductions can be expected with improved OPO characteristics,[13] such as smaller cavity losses (or larger transmission of the output mirror) and higher pump power.

This work was partially supported by Direction des Recherches Etudes et Techniques Contract No. 87/091. We acknowledge the helpful assistance of T. Debuisschert and L. Hilico. Laboratoire de Spectroscopie Hertzienne de l'Ecole Normale Supérieure is a Laboratoire Associé au CNRS à l'Ecole Normale Supérieure et à l'Université Pierre et Marie Curie.

---

[1]See papers contained in J. Opt. Soc. Am. B 4, 10 (1987); J. Mod. Opt. 36, 6/7 (1987).

[2]M. C. Teich and B. E. A. Saleh, J. Opt. Soc. Am. B 2, 275 (1985).

[3]P. R. Tapster, J. G. Rarity, and J. S. Satchell, Europhys. Lett. 4, 293 (1987).

[4]S. Machida, Y. Yamamoto, and Y. Itaya, Phys. Rev. Lett. 58, 1000 (1987); S. Machida and Y. Yamamoto, Opt. Lett. 14, 1045 (1989).

[5]W. H. Richardson and R. M. Shelby, Phys. Rev. Lett. 64, 400 (1990).

[6]J. G. Walker and E. Jakeman, Proc. Soc. Photo-Opt. Instrum. Eng. 492, 274 (1985).

[7]S. Machida and Y. Yamamoto, Opt. Commun. 57, 290 (1986).

[8]Y. Yamamoto, N. Imoto, and S. Machida, Phys. Rev. A 33, 3243 (1986).

[9]F. Capasso and M. C. Teich, Phys. Rev. Lett. 57, 1417 (1986).

[10]H. P. Yuen, Phys. Rev. Lett. 56, 2176 (1986).

[11]G. Björk and Y. Yamamoto, Phys. Rev. A 37, 125 (1988).

[12]P. R. Tapster, J. G. Rarity, and G. S. Satchell, Phys. Rev. A 37, 2963 (1988).

[13]C. Fabre, E. Giacobino, A. Heidmann, and S. Reynaud, J. Phys. (Paris) 50, 1209 (1989).

[14]S. Reynaud, Europhys. Lett. 4, 427 (1987).

[15]A. Heidmann, R. J. Horowicz, S. Reynaud, E. Giacobino, and C. Fabre, Phys. Rev. Lett. 59, 2555 (1987); T. Debuisschert, S. Reynaud, A. Heidmann, E. Giacobino, and C. Fabre, Quantum Opt. 1, 3 (1989).

[16]S. Reynaud, C. Fabre, and E. Giacobino, J. Opt. Soc. Am. B 4, 1520 (1987).

[17]S. Reynaud and A. Heidmann, Opt. Commun. 71, 209 (1989).

[18]J. Mertz, C. Fabre, A. Heidmann, and S. Reynaud (to be published).

[19]C. D. Nabors and R. M. Shelby, Stanford University report, 1990 (to be published).

**a:** ***Pump laser: experimental details***

The pump laser used in the feedforward experiment is a Spectra-Physics model 171 argon ion laser with a model 270 power supply. This is different from the laser described in section IV.a. The laser cavity is fitted with a 1 cm long temperature stabilized etalon for single mode cw operation at the 528 nm. line, with about a 10 MHz free run jitter. Before being coupled to the OPO, the pump beam undergoes a 70 MHz frequency upshift through an AA MP 10 acousto-optic modulator. This effectively isolates the pump laser from any OPO backreflections, since these are no longer resonant with the laser cavity. The external frequency stabilization of the pump beam used in reference [Hei87] was found to be superfluous in this experiment due to improvements in the OPO intensity stabilization (see section IV.b), and was therefore omitted. The pump power incident on the OPO is 420 mW.

**b:** ***Feedforward channel: experimental details***

The feedforward channel is shown below (fig. 7.1). The intensity fluctuations of beam 2 are monitored by detector 2 and converted to voltage fluctuations. These are amplified and fed into electrode 1 of a transverse electro-optic modulator (Electro-Optic Design 810-2) followed by a polarizer. Electrode 2 is biased with a low impedance stabilized DC voltage adjustable to 1000 V. The electro-optic crystal is KD*P, oriented approximately 10° from the polarizer plane (see fig. 6.3). The bias voltage is adjusted so that the mean intensity transmission through the EOM (corrected for intrinsic losses) is about 93%. Transmissions closer to 100% are possible in principle (see discussion in section VI.c), but would have necessitated higher electronic gains in the feedforward channel to compensate for the attendant lower EOM modulation capability as the transmission approaches one. Such higher electronic gains would have run into the problem of amplifier saturation. Extra intrinsic losses in the EOM are 9%, and in the 50% beamsplitting mechanism are 3% (see section c below) -- amounting to a total optical losses of about 20% in beam 1 (before the photodiodes). Unfortunately, the intrinsic losses in the EOM used here are abnormally high and account for a large portion of these total losses, owing perhaps to a poor anti-reflection coating or index matching of the crystal immersion fluid. Referring to eqtn. 6.31, the total optical losses resulted in a degradation of the observed quantum noise reduction from a theoretical 30% to an observed 24%.

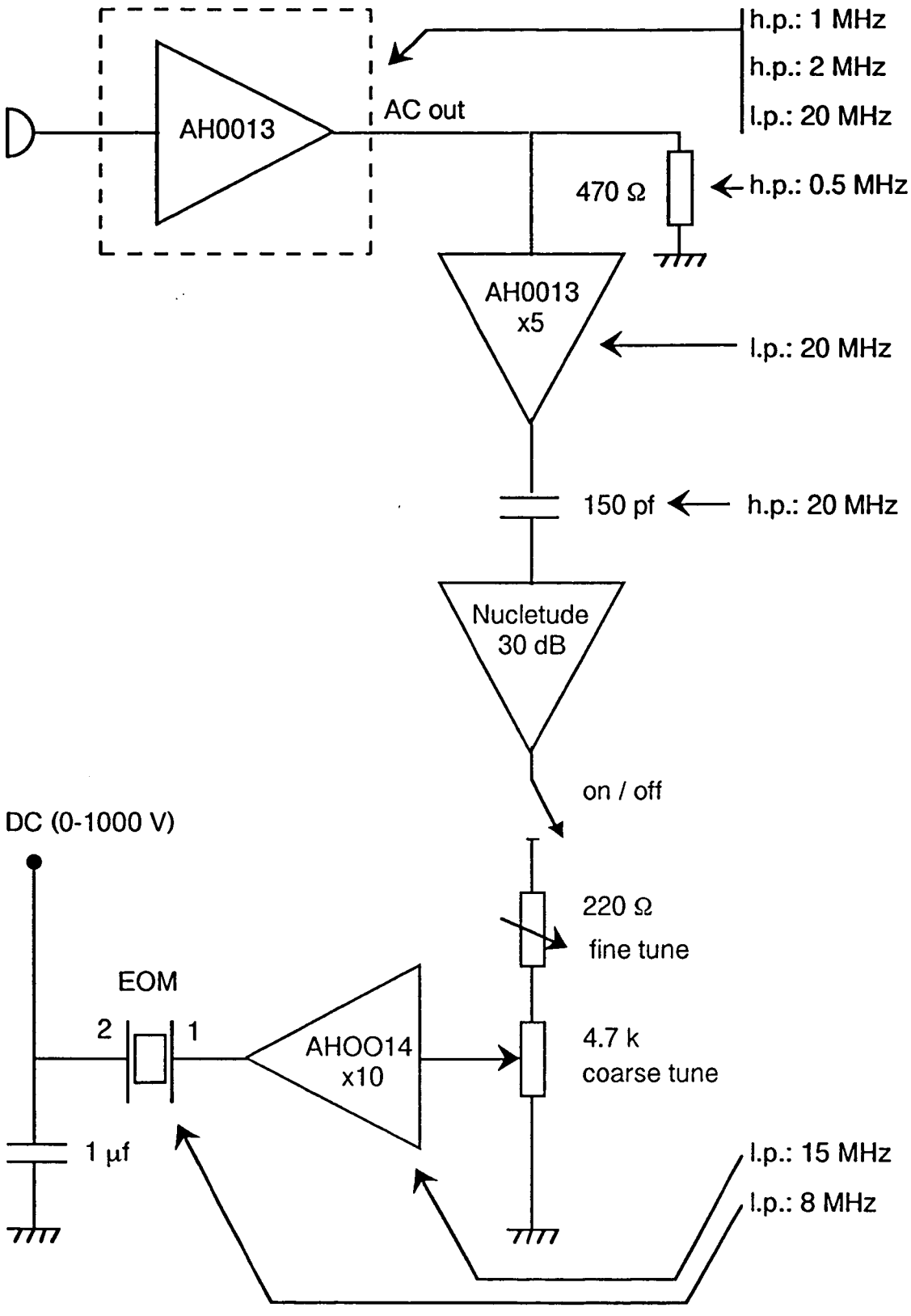


Figure 7.1: Feedforward circuitry.

The amplification of the photodetection signal occurs in four stages. The first stage is the AC out pre-amplification stage described in section IV.c. This is slightly different from the one shown in fig. 4.5 in that it is high pass with a 12 dB/octave roll-off below 1 MHz instead of 100 kHz. The AC out is loaded into 470 Ω and amplified by a ×5 OEI AH0013. This is capacatively coupled to a Nucletude model 5.30.1A modular amplifier of gain 30 dB (50Ω input impedance; noise figure 6.5 dB). A switch is used to turn the feedforward control on or off, followed by a potentiometer for control of the feedforward gain. The final amplification stage is an OEI AH0014 op-amp mounted with a non-inverting gain of 10. Several high pass filters in the circuit are necessary to prevent amplifier saturation due to the large single beam excess noise at low frequencies. The various filters throughout the circuit are identified in fig. 7.1.

The time delay associated with each amplification stage was measured independently using a pulse generator and comparing the arrival times of a reference pulse and an amplified pulse. This was found to be 5 ns for the AH0013/14 and 2 ns for the Nucletude. Along with the 30 cm electronic path length, the total time delay in the amplification portion of the feedforward channel is less than 15 ns.

The response of the EOM was determined independently by applying a sweep frequency to the EOM electrodes and observing the resultant optical modulation. The response is flat to 4 MHz and falls off progressively with a 3 dB roll-off at about 8 MHz. A slight piezo resonance was observed at 10 MHz. The reason for the poor EOM response at high frequencies is unclear and is perhaps related to poor impedance matching. (Recent EOM designs using ADP crystals forming 50Ω waveguides [???] are certainly better adapted but were unavailable for this experiment.) The time delay in the EOM response was inferred by measuring the phase shift as a function of frequency between the driving sweep voltage and the optical modulation, correcting for the supplementary delay of the detector amplifier. This was found to be approximately 15 ns, obtaining a total feedforward time delay on the order 30 ns.

We present in fig. 7.2 the theoretically obtainable spectrum $\tilde{S}_1^{opt}(\Omega)$ for beam 1 after optimal control. This is deduced by using eqtn. 6.10 using fits of the experimentally observed single beam noise spectrum $S_1(\Omega)$ and intensity difference noise spectrum $S_{1\text{-}2}(\Omega)$. The twin beams are approximated here as balanced.

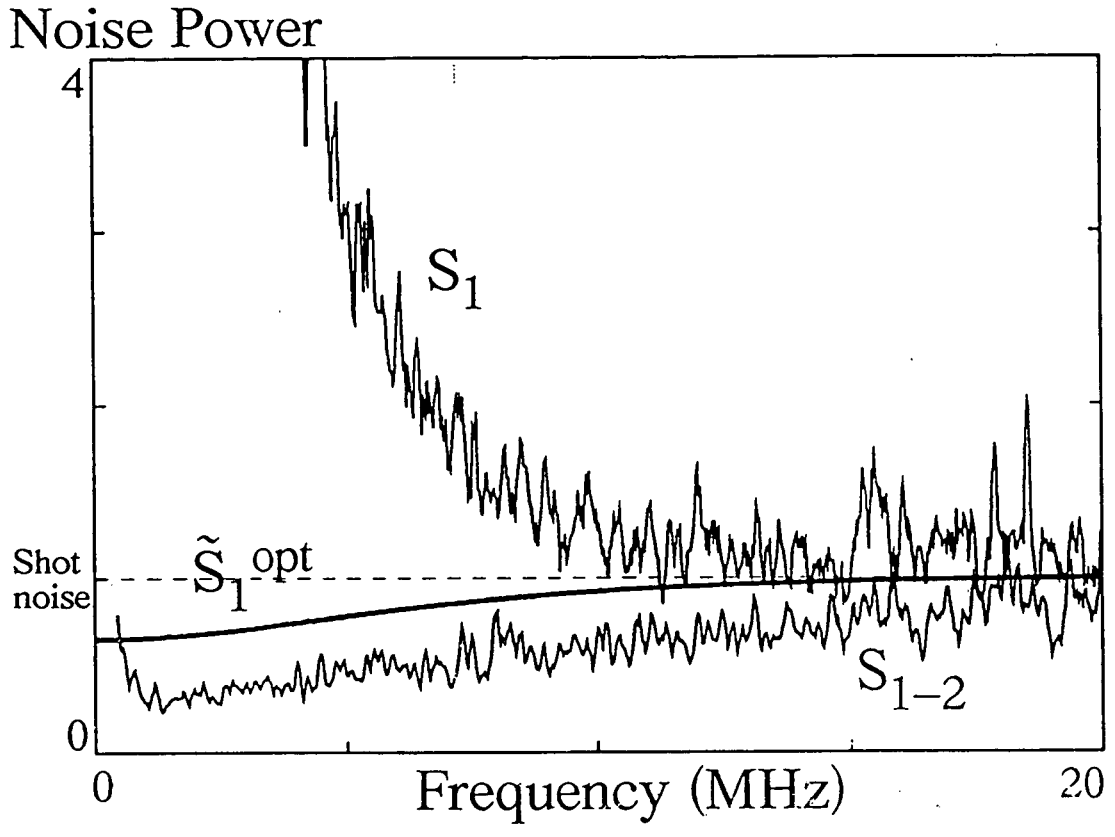


Figure 7.2: Experimental single beam ($S_1$) and intensity difference ($S_{1-2}$) noise spectra. Corresponding theoretical spectrum ($S_1^{opt}$) after optimal control.

The corresponding optimal control gain is presented in fig. 7.3 (dotted curve), and is compared with the actual control gain used in the experiment (solid curve). It is clear that the control gain used in the experiment is far from ideal, due primarily to the several high pass filters inserted in the control channel. We recall that the phase of the optimal control gain is zero (see chapt. VI). The phase of control gain used in the experiment is presented in fig. 7.4 (solid curve) along with the corresponding phase if the control gain were corrected for time delay (dotted curve). As expected, the effect of the time delay is to increase phase lag in the control channel (see section V.g). The frequency where the phase lag crosses zero can be adjusted by changing the various filter roll-offs in the feedforward channel. Ideally it should be chosen as small as possible, where the optimum noise reduction is better (see fig. 7.2). In practice, it was chosen to be 5 MHz by adjusting the capacitor value between the AH0013 and the Nucletude amplifiers. Optimal feedforward correction below this frequency was impossible because of amplifier saturation due to low frequency excess noise. The excess noise the OPO output beams is typically 6 to 10 dB above the shot noise level at 5 MHz. This is dependent on OPO detuning, which unfortunately was hard to control. Our best noise reduction was observed during runs when the excess noise was smallest.

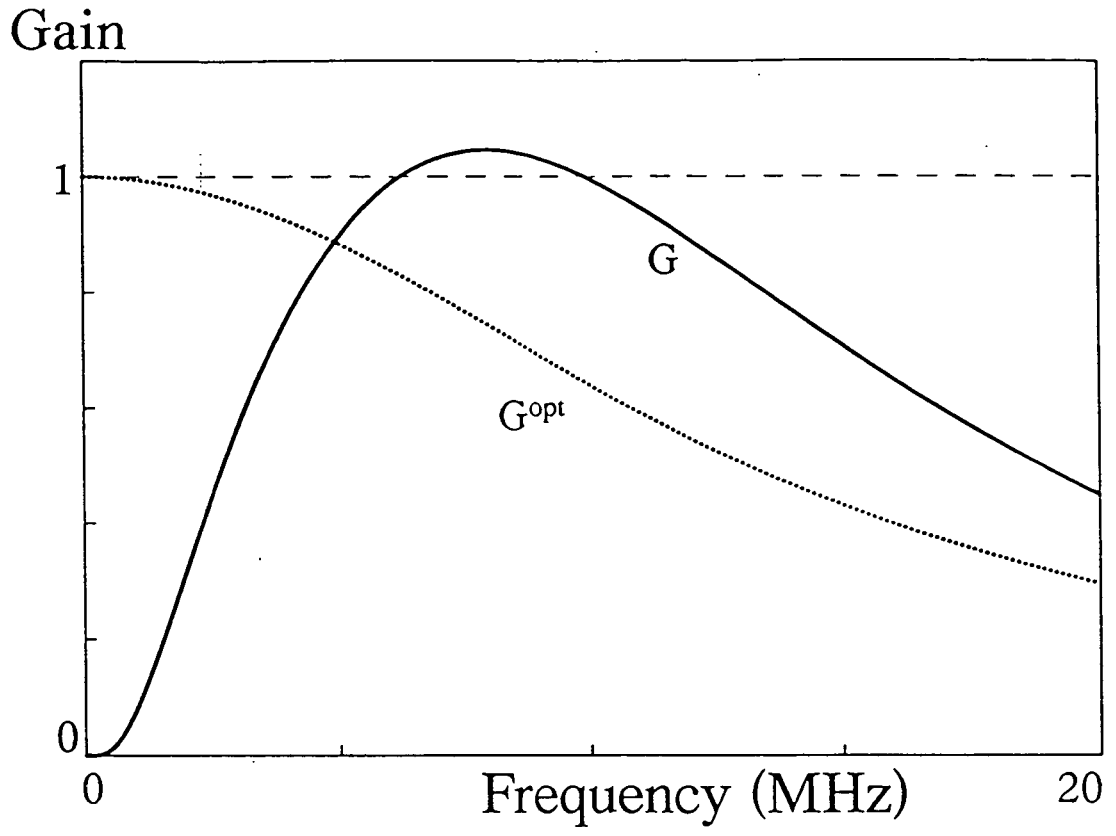


Figure 7.3: Experimentally used (solid) and theoretically optimal (dotted) feedforward control gain magnitudes.

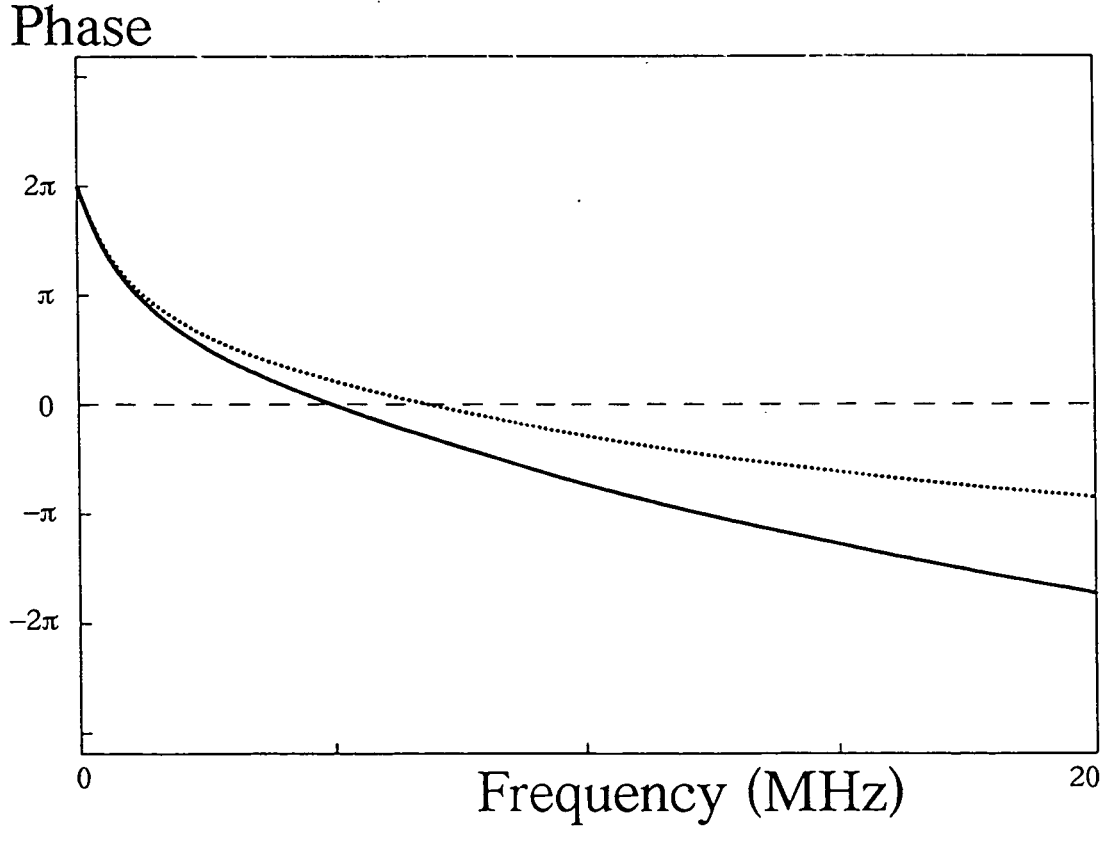


Figure 7.4: Feedforward control gain phase used in experiment (solid) and corrected for time delay (dotted).

We remind the reader that a control channel presenting the optimal gain shown in fig. 7.3 and the optimal phase of zero would have been impossible to design even in principle, because of restrictions imposed by causality (see chapt. VI). We must content ourselves here with optimal control only over a limited bandwidth. This is illustrated in fig. 7.5 comparing the experimentally observed and theoretically ideal single beam noise control. With proper adjustment of the feedforward channel gain (by using the potentiometers in fig. 7.1), optimal noise reduction of 24% below the shot noise level is effectively obtained at 5 MHz. The experimental control gain $G(\Omega)$, however, only fits the optimal control gain $G^{opt}(\Omega)$ over a small range centered about this frequency.

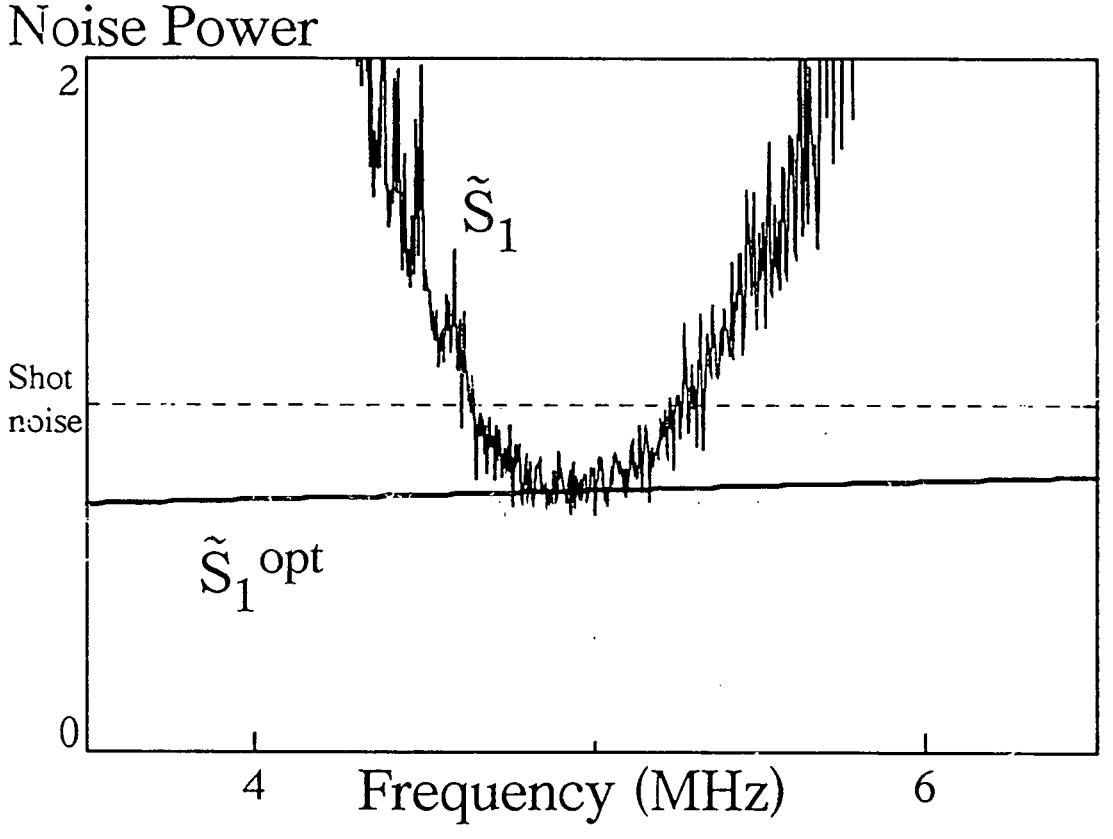


Figure 7.5: Experimentally observed and theoretically optimal control beam noise spectrum.

A comparison between $G(\Omega)$ and $G^{opt}(\Omega)$ is made (fig. 7.6) by plotting the two gains in the complex plane. $G(\Omega)$ intersects $G^{opt}(\Omega)$ at 5 MHz but deviates rapidly from the real axis primarily due to phase excursion. The corresponding plot of the gain error parameter $|G_e|^2$ (see section VI.a) is given in fig. 7.7. This may be compared with the controlled noise spectrum given in fig. 2 of the article at the head of this chapter.

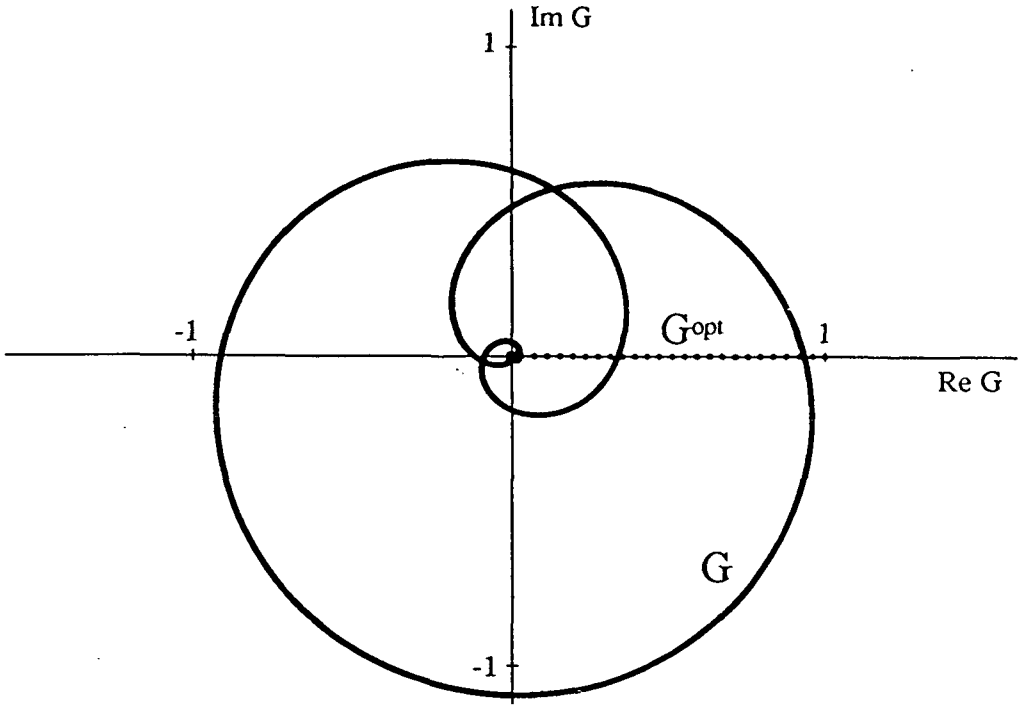


Figure 7.6: Traces of experimentally used (solid; runs clockwise) and theoretically optimal (dotted; runs right to left) control gains in complex plane. Intersection occurs at 5 MHz.

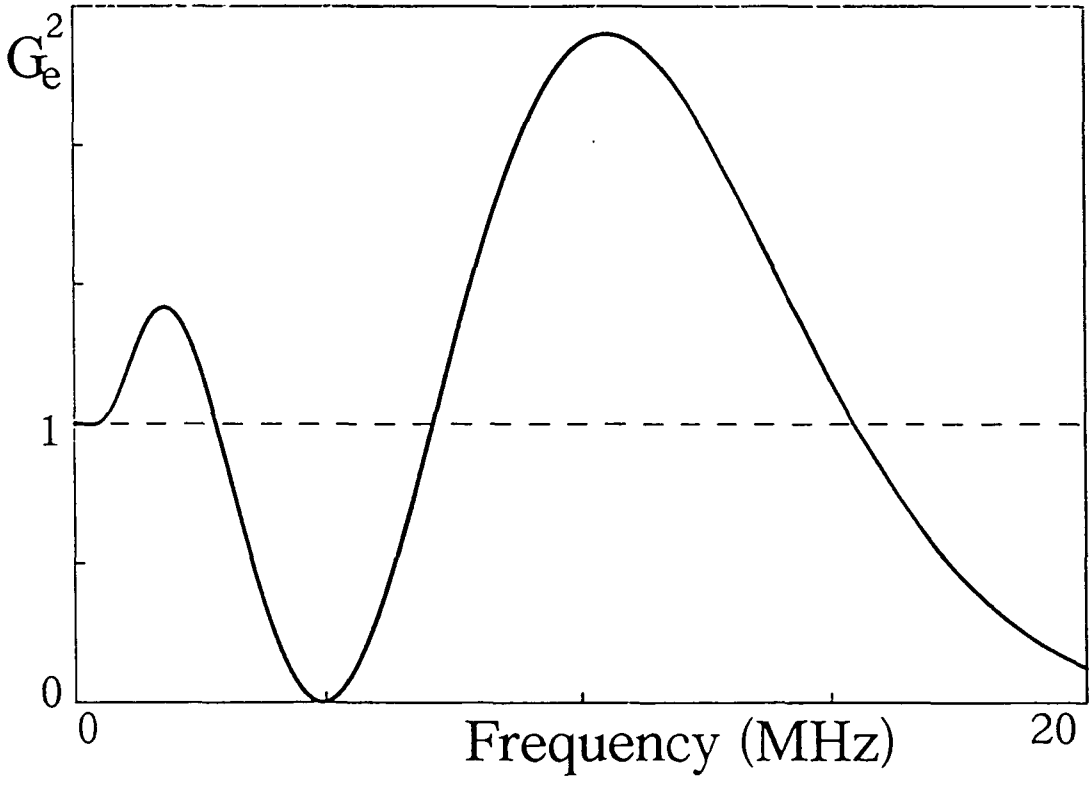


Figure 7.7: Experimental gain error parameter.

c: *Sum/difference circuitry*

After control, beam 1 is detected using a double balanced detector comprising a 50% beamsplitting mechanism and two balanced photodetectors. Note: in this experiment, the photodiodes are not tilted as described in section IV.c, and their quantum efficiency is only $\eta$=0.90. The 50% beamsplitting mechanism consists of a $\lambda/2$ plate followed by a low loss polarizing beamsplitter, where the $\lambda/2$ plate is adjusted for exactly 50% splitting. The AC outputs of the balanced photodetectors (see fig. 4.5) are added or subtracted to measure respectively the total noise in beam 1 or the shot noise in beam 1. The sum/difference circuit is shown below (fig. 7.8). When the commutator is down (as shown) the circuit is an inverting summing amplifier. When the commutator is up the circuit is a differential amplifier. The variable 100Ω resistor is used to match the non-inverting gain to the inverting gain. The gain experienced by $V_1$ and $V_2$ is about 5.7, independent of the commutator position. The effective gain "seen" by the AH0014, however, is twice this value. Although the AH0014 is internally compensated for gains larger than 10, an supplementary 6.8 pf was included to this compensation for smoother roll-off. The amplification bandwidth is about 12 MHz. The resistor values in the circuit are all relatively low to avoid coupling with stray capacitances. In addition, careful attention was paid to input impedance matching. The load into the circuit seen by $V_1$ and $V_2$ is 50Ω. The source impedance seen by the circuit is also 50Ω, independent of the commutator position. The AH0014 amplifier noise is specified at 3 $nV/\sqrt{Hz}$.

The matching of the inverting and non-inverting gain of the AH0014 was verified by applying two independent electronic noises to the inputs $V_1$ and $V_2$, and observing the output $V_{out}$ when these were added or subtracted. The input noises were near white in spectrum and obtained from the amplifier noises of cascaded AH0013s, such that their total electronic noise levels simulated approximately the optical noise levels observed in experiment. It was important in this verification procedure to run the AH0013s off separate power supplies to avoid spurious correlations. The change in the resultant output noise power of the AH0014 when in the sum configuration or in the difference configuration was imperceptible in the frequency range 2-12 MHz and estimated to be less than 0.05 dB.

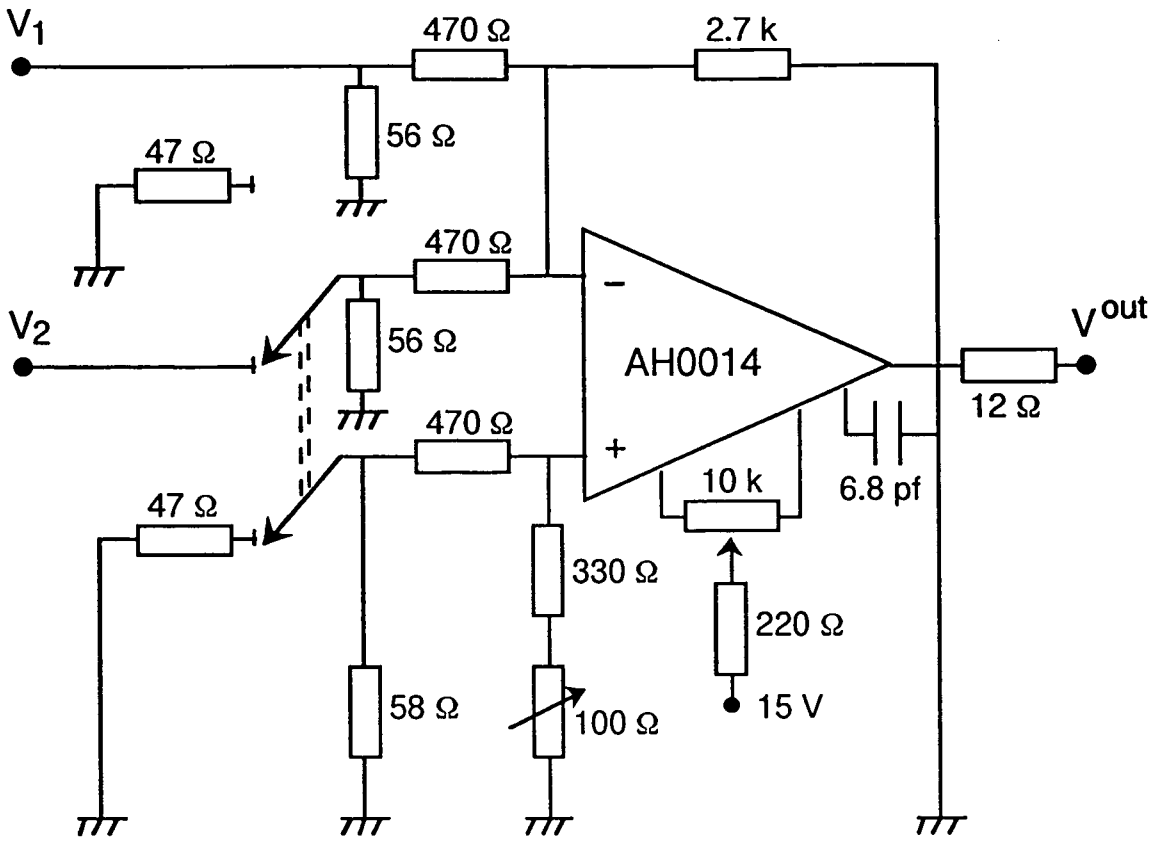


Figure 7.8: Sum/difference circuitry.

The electrical common mode rejection ratio in the difference mode was ascertained by applying a sweep frequency to the inputs $V_1$ and $V_2$ and observing the reduction in the amplified output signal when passing from the sum mode to the difference mode. This is -35 dB at 5 MHz. The total electrical and optical common mode rejection was ascertained in the same way as described in section IV.d, by modulating the intensity of beam 1. This is -30 dB at 5 MHz and no greater than -25 dB in the 1-20 MHz range. Given the level of single beam excess noise, such a rejection ratio is sufficient to ensure the calibration of the shot noise level at 5 MHz to within 2% (see eqtn. 4.6).

### d: *Detection linearity*

The linearity of the double balanced photodetector was verified using two procedures. The first was by inserting a variable attenuator before the 50% beamsplitting mechanism and plotting the shot noise power level of beam 1 (difference of AC outputs) as a function of mean intensity (sum of DC outputs). This is shown in fig. 7.9 where the shot noise power was monitored at 5 MHz. The linearity is manifestly assured well past the experimental operating intensity of 3 mW for each photodetector.

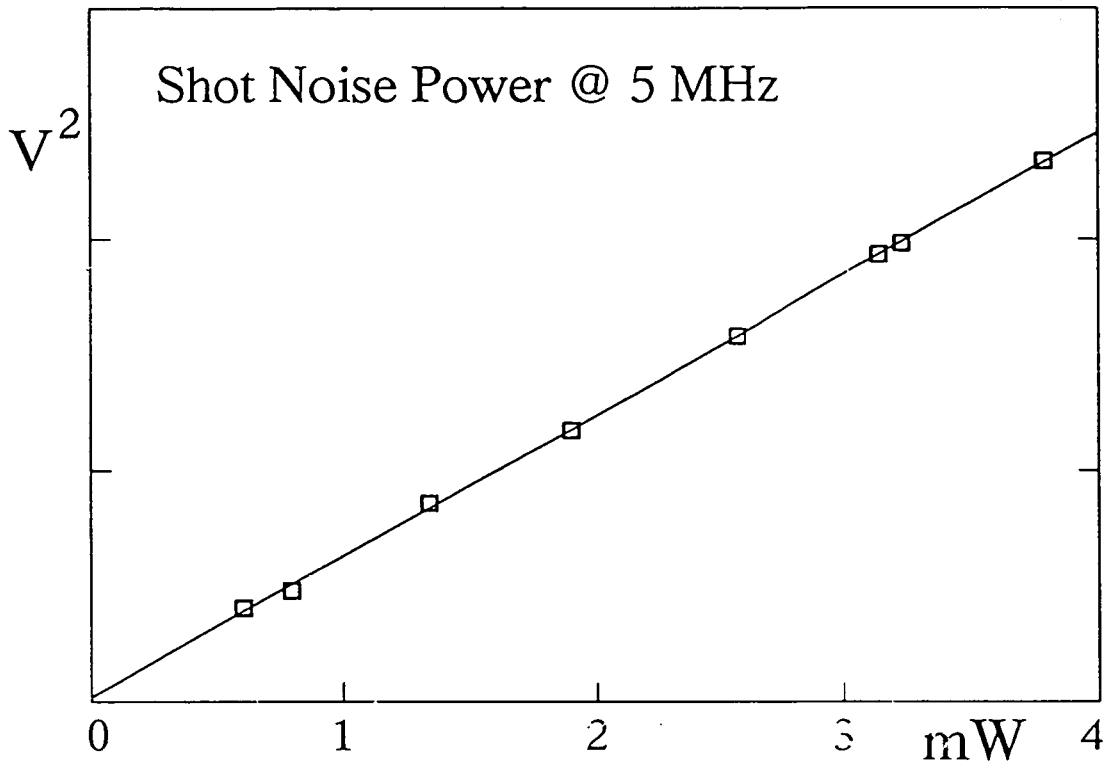


Figure 7.9: Shot noise power as a function of detected intensity at 5 MHz.

The second verification procedure consisted of observing the total noise power in beam 1 (AC outputs in sum mode) while toggling this power from one detector to another with the $\lambda/2$ plate of the 50% beamsplitting mechanism. Ideally one would expect the total observed noise power to remain independent of how the power was distributed over the individual detectors. Only slight changes of less than 0.1 dB were observed in this total noise power at 5 MHz when the optical power incident on the individual photodetectors was varied between 3 mW and 6 mW (total power 6 mW). These changes became imperceptible when the optical power on the individual photodetectors was varied between 1.5 to 3 mW (total power 3 mW), again assuring that the photodetectors do not saturate for experimental operating intensities.

**e:** ***Conclusion***

Although active control has been used in prior experiments [Tap88] to generate sub-Poissonian light, the results described here represent the first use of active control to generate such light with laser-like properties (high intensity, near monochromatic, well collimated, etc.). Possible improvements to the observed noise reduction are twofold in

nature. The first improvements rely on better characteristics of the twin beams, that is, increased intensity correlations and decreased excess noise. The second improvements rely on better design of the feedforward circuitry for a closer fit of the optimal control gain.

Feedforward experiments are currently underway using the upgraded OPO characteristics described in chapter IV. The twin beams in these experiments are better correlated but also contain more excess noise, and attention must be given to the feedforward channel design to avoid amplifier saturation. Channel designs that better fit the optimal control gain are also under investigation, along with the possible use of digital or nonlinear techniques. In any case, active control seems to be a promising candidate for optical noise reduction.

# VIII: FEEDBACK EXPERIMENT

As discussed in section VI.i, feedback control presents many advantages over feedforward control, including the possibility of noise reduction over a larger bandwidth. Optical losses due to the feedback control mechanism do not contaminate the controlled beam, and the feedback control is less sensitive to variations in channel gain. We present now an experimental attempt at feedback control. The operating conditions for the OPO are those described in chapter IV, where the twin beam intensity difference spectrum is 86% below the shot noise level near 3 MHz. From eqtn. 6.10 one expects then for ideal feedback control a reduction in the intensity noise of beam 1 of more than 70% below the shot noise level -- a significant improvement over the results of chapt. VII. Unfortunately, the feedback control was not ideal in this experiment. Although noise reduction was observed, the experiment was unsuccessful in reducing the control beam noise below the shot noise level, owing to problems elicited in chapter VI concerning feedback stability. A cursory analysis is given of the results along with an outline of the improvements necessary for sub-shot noise control.

### a: *Experimental layout and specifications*

The layout of the experiment is shown below in fig. 8.1. The noise in beam 1 is reduced by indirect control from beam 2 to the OPO pump.

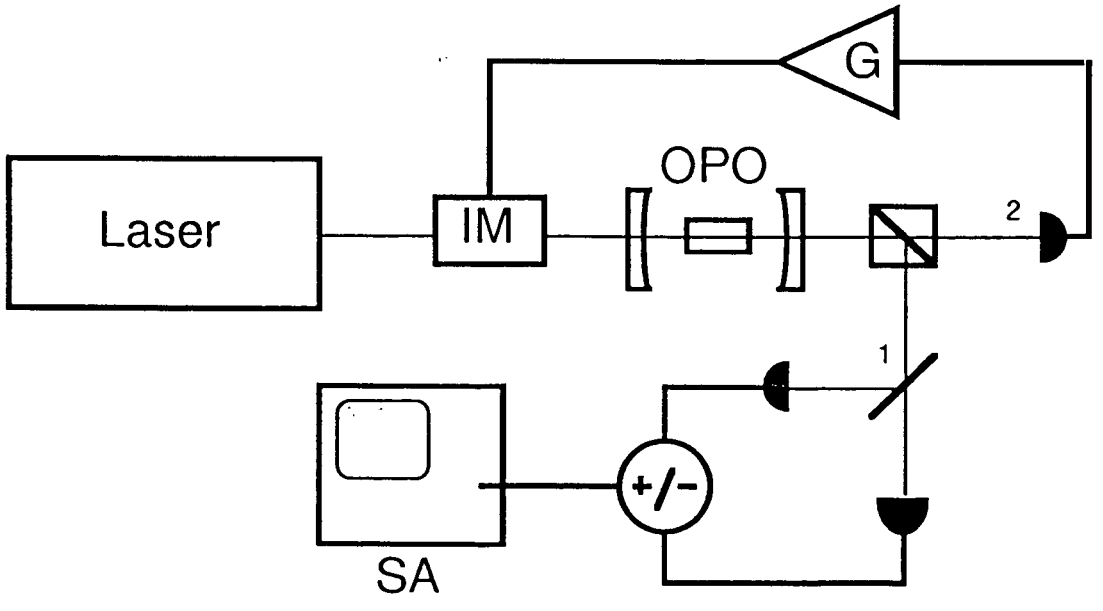


Figure 8.1: Experimental layout for feedback control.

The control gain transfer function is given by (see chapter VI)

$$G(\Omega) = \frac{gA(\Omega)B(\Omega)}{1+gA(\Omega)B(\Omega)} \tag{8.1}$$

where $A(\Omega)$ is the transfer function through the OPO and $gB(\Omega)$ is the transfer function through the control channel.

We first consider the transfer function through the OPO (eqtn. 6.29), given by

$$A(\Omega) = \frac{\sqrt{\xi\,\xi_0\,(\sigma-1)}}{\sigma-1+i\Omega} \tag{8.2}$$

where $\Omega$ is normalized to the cavity bandwidth, here about 45 MHz. $\xi = 0.91$ and $\xi_0 = 0.4$. It is difficult to accurately gauge $\sigma$, but this is estimated to be no greater than 1.02 given an OPO detuning such that the output twin beam intensity is 3 mW per beam (see eqtn. 4.4). The excess noise in the twin beams is dominant therefore over the shot noise over a large frequency range. As pointed out in section VI.g, $A(\Omega)$ resembles a low pass filter, with 3 dB roll-off frequency on the order here of 1 MHz. An increase in $\sigma$ is difficult because of limitations in the pump power. It is ill advised, in fact, because the attendant increase in the downconverted twin beam power would lead to detector saturation (see eqtn. 4.4).

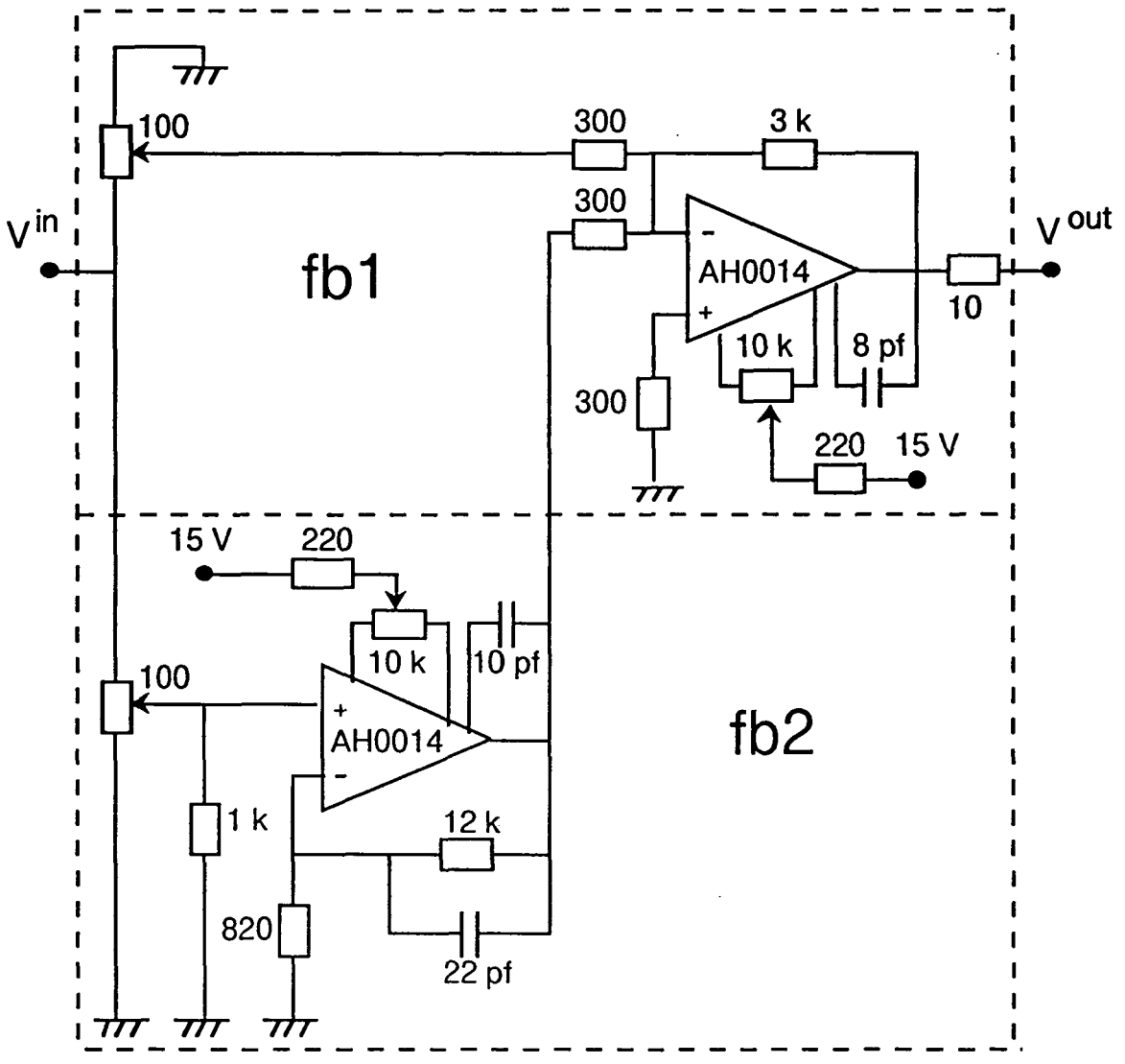


Figure 8.2: Circuit diagram for parallel feedback channels fb1 (top half) and fb2 (bottom half).

The details of the feedback circuitry are shown in fig. 8.2. The intensity of beam 2 is monitored by detector 2 whose AC output (see fig. 4.5) is loaded into 50Ω at $V^{in}$. The output of the feedback circuitry $V^{out}$ is fed directly into an EOM intensity modulator of the type described in sections VI.e and VII.b. We note here that because of YAG pump power constraints only a single EOM+polarizer mechanism is used in this experiment instead of two such mechanisms in series. A consequence of this is a coupling of the phase fluctuations into the intensity fluctuations of beam 1. As pointed out in section VI.i, however, this produces little effect on noise reduction when the excess noise in the twin beams is large.

As illustrated, the feedback channel comprises two parallel channels fb1 (top box) and fb2 (bottom box). The respective gains g1 and g2 of each channel are independent and adjustable with the 100Ω potentiometers. Channel fb1 contains a single AH0014 amplification stage. Channel fb2 contains a supplementary AH0014 amplification stage which is added to the fb1 amplification. For the present discussion, we do not consider the effects of fb2 and assume that its gain is set to zero. We will consider the (intended) effects of fb2 at the tail end of this chapter.

Referring to the specifications in chapt. IV, the control gain G(Ω) may be approximated as a five pole network comprising two high pass filters in the detector AH0013 pre-amplifier (roll-off frequencies at 50 and 500 kHz), and three low pass filters: one in the EOM response (roll-off frequency estimated at 8-10 MHz), one in the AH0014 amplifier (bandwidth 15 MHz), and one in the AH0013 pre-amplifier (bandwidth 20 MHz). The total time delay in the feedback channel is estimated at 25 ns.. We note that the roll-off frequencies of the high pass filters necessary to avoid amplifier saturation are lower in this experiment than in the feedforward experiment. This may seem contradictory in view of the fact that the excess noise in the twin beams is now larger, and that the channel gain g1 should also be large in theory for G(Ω) to approach $G^{opt}(\Omega)$. In practice, however, only a medium electronic gain was used since much of the feedback gain was supplied already by optical means, owing to the EOM modulation of a 400 mW pump beam rather than of a 1 mW signal beam (see comment at end of section VI.e). In any case, the feedback channel gain was limited by oscillation problems long before it was limited by amplifier saturation, as we will see below.

### b: *Results and discussion*

Experimental results for feedback control are shown in fig. 8.3. Curve (a) represents the beam 1 intensity noise prior to control. Curve (b) represents the beam 1 intensity noise with control (channel fb1 only). Curve (c) represents the associated beam 1 shot noise level. Curve (d) represents the electronic noise floor. One observes from curve (b) that the effect of an increase in the feedback gain is a reduction in the intensity noise below 4 MHz, along with a sharp increase in the intensity noise above this frequency, associated with the onset of oscillation. This curve is similar to the theoretical curve traced in fig. 6.13b. The feedback gain is limited here by a critical gain above which the system is unstable. As a result, the maximum noise reduction in the beam 1 is limited to only about 10 dB below its original level. Because of the large excess noise in beam 1, such a reduction is significantly short of attaining the shot noise level, by about 18 dB.

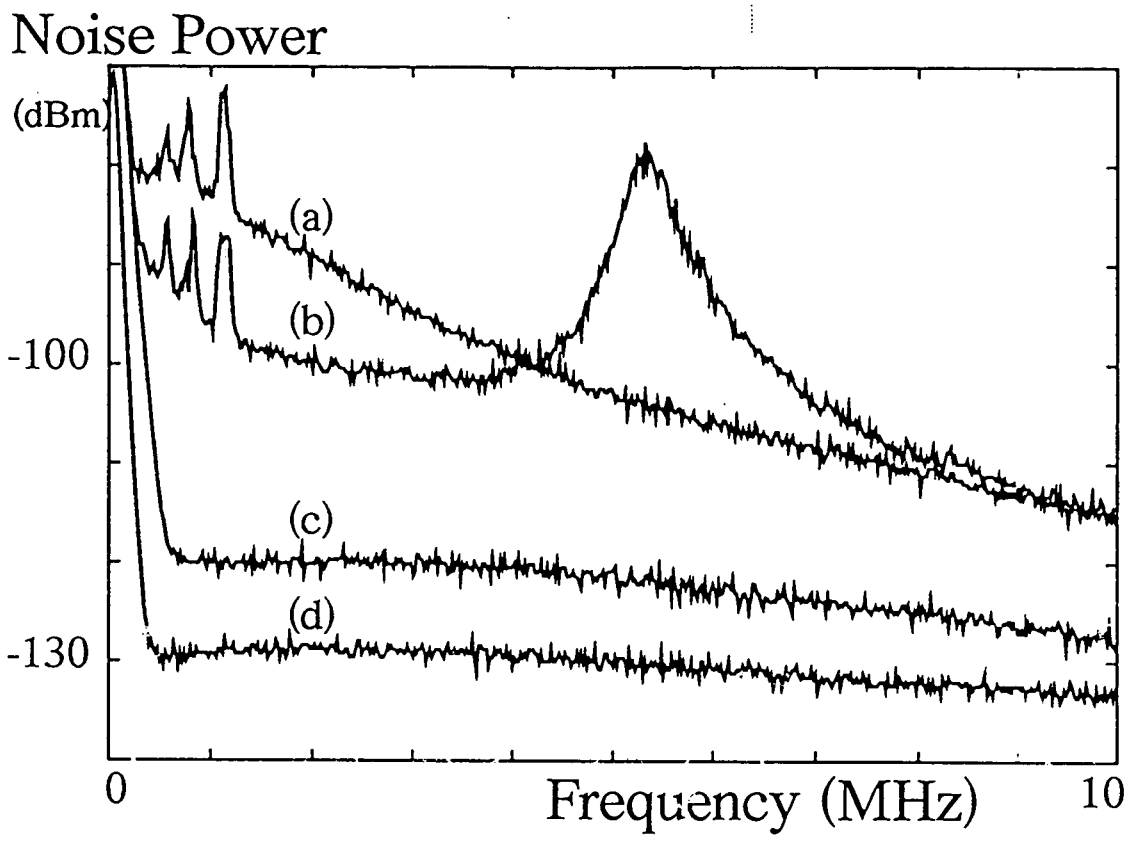


Figure 8.3: Experimental results for feedback control. (a) is single beam noise spectrum before control (g1=0). (b) is single beam noise spectrum after control (g1=0), (c) is single beam shot noise spectrum, and (d) is electronic noise floor.

It should be emphasized here that although the excess noise in this experiment is unfortunate, it does not in itself impose the limit to the observed noise reduction. This limit is imposed instead by the propensity of the system towards oscillation, setting an upper limit to the allowed feedback gain and preventing $G(\Omega)$ from approaching $G^{opt}(\Omega)$. A plot of both of these is given in fig 8.4, along with a plot of the gain error parameter $|G_e|^2$ (see section VI.a), which is given in fig. 8.5. The latter plot may be compared with curve (b) of figure 8.3. We note that even though the gain error may appear small below the oscillation frequency, it must be multiplied by the single beam noise spectrum (see eqn. 6.7), which is large. The gain error diverges as the system approaches oscillation.

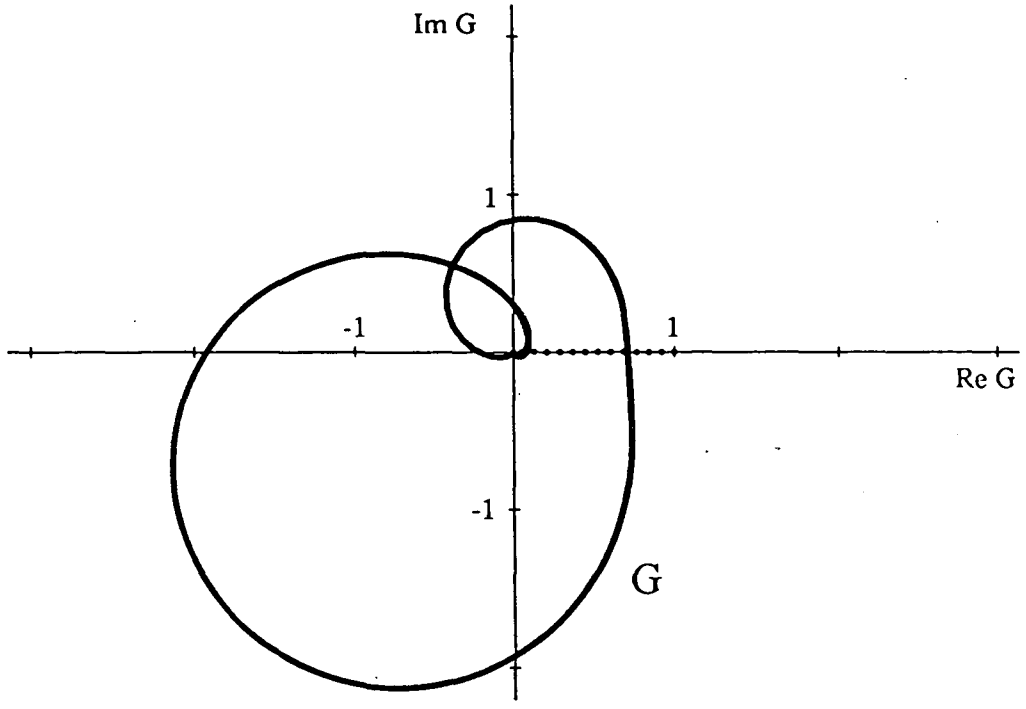


Figure 8.4: Traces of experimentally used (solid; runs clockwise; g1 = 5) and theoretically optimal (dotted: runs right to left) control gains in complex plane.

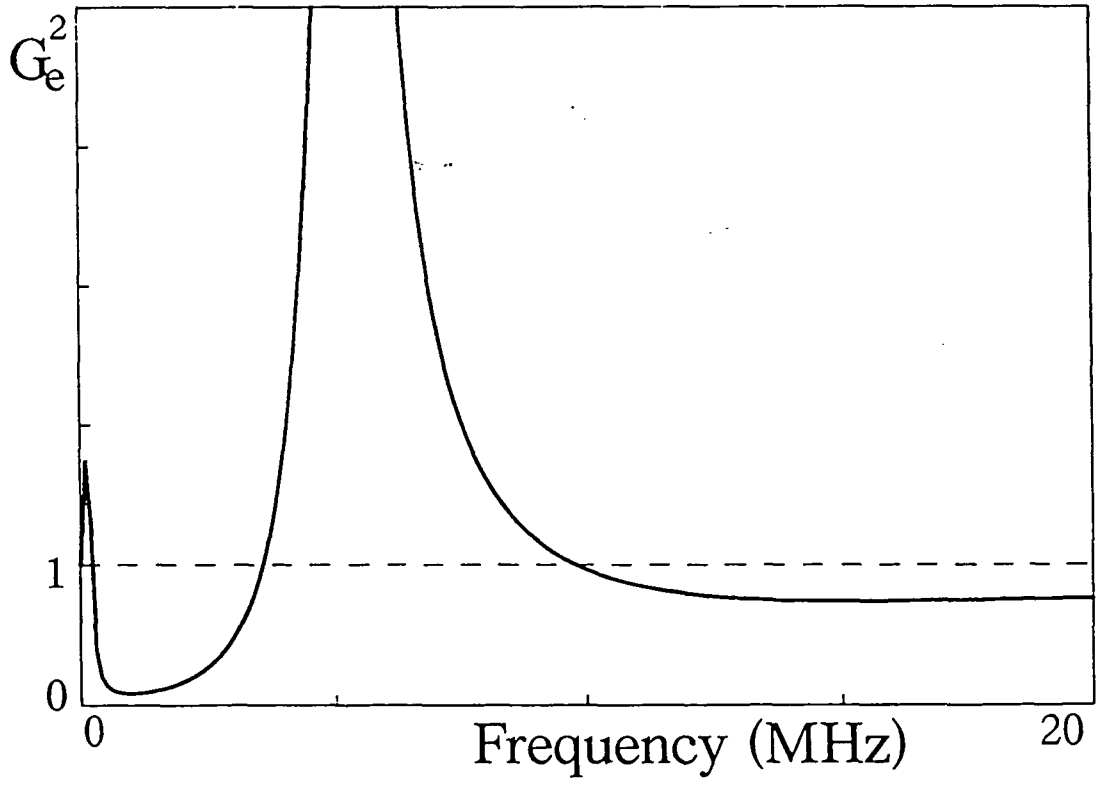


Figure 8.5: Experimental gain error parameter (g1 = 5)

We remind the reader that the plot of G(Ω) given in fig. 8.5 should not be confused with the Nyquist plot of the open loop gain, which evaluates feedback stability (see discussion in section V.c). For comparison, this Nyquist plot is shown in fig. 8.6 (for positive frequencies only). Depending on whether the point -1 is to the left or to the right of the contour, the feedback is respectively stable or unstable. A transition from one case to the other occurs as the channel gain g1 is increased. Two possible solutions may be envisaged to abate the problem of stability. These are addressed in turn.

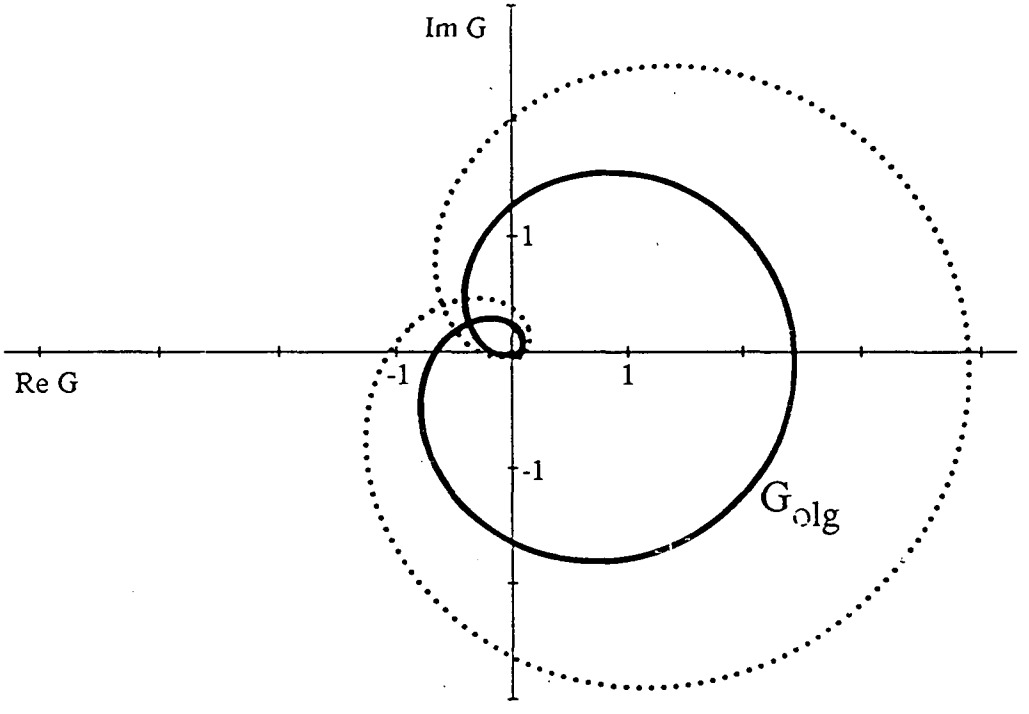


Figure 8.6: Nyquist plot of experimentally used open loop gain for g=5 (solid) and g=8 (dotted). Both traces run clockwise. Note, the former control is stable whereas the latter is unstable.

The first solution consists of pushing the feedback oscillation to a higher frequency. As illustrated in fig. 8.3, the oscillation in the system occurs here near 5.5 MHz. This is rather low, in particular because of phase excursions caused by the OPO pole (see eqtn. 8.2). Despite the large OPO bandwidth, this pole is dominant here because of the particularly low value of σ. An increase in σ would certainly be beneficial, both in increasing the feedback oscillation frequency and in reducing the twin beam excess noise. This would require a locking of the OPO closer to resonance as well as an increase in the photodetector power ratings (without an attendant decrease in their quantum efficiencies). The first of these is feasible, requiring perhaps an upgraded design of the OPO intensity stabilizer. The second of these requires perhaps the use of several photodetectors run in parallel.

Short of increasing the feedback oscillation frequency, an alternative solution may be contemplated where a secondary feedback channel fb2 is used to supply the additional desired feedback gain only at low frequencies. The general workings of such a feedback network with a parallel channel are described in section V.f. The gain of the channel fb1 is increased to just below oscillation threshold. The gain of the channel fb2 is then increased in turn to supply extra gain below the oscillation frequency. In theory, such a feedback is conditionally stable as long as the roll-off frequency of fb2 is sufficiently low (approximately an order of magnitude below the oscillation frequency of fb1). In practice, however, the oscillation frequency of fb1 in this experiment is too low for the fb2 to occasion any notable improvements in the observed noise control. Only a slight improvement (1-2 dB) was registered in the low frequency range below ~ 2 MHz.

The results presented in this chapter demonstrate that intensity noise reduction using feedback control with twin beams is possible. Although this reduction fell short of bettering the shot noise level, the limitations to the experiment are all well understood and technical in nature. Improvements to the control seem feasible. In particular, the results given here and in the preceding chapters may provide a starting point for the extension of twin beam control to include digital or nonlinear techniques. As a final note, although we restricted or experimental studies to the case where the twin beam source was an OPO and the control channel was electro-optic, the theoretical results we derived are general. They may be applied, for example, to all-optical channels or even to the case of a single beam where the control signal is provided by a QND measurement. OPOs present the experimental advantage, however, that they have already demonstrated their effectiveness in producing highly correlated light beams that are easy to manipulate. This makes them particularly adapted for further studies of active noise control.

# APPENDIX

Throughout the body of this thesis, we have used a semi-classical approach for the study of quantum fluctuations. The basic principle to this approach consists in replacing a quantum amplitude operator $\hat{a}$ by a classical amplitude variable $\alpha$ satisfying an appropriate probability distribution (see chapter II). We successfully applied this approach to the study of fluctuations in a weakly parametric OPO and to the study of the reduction of fluctuations using linear control with two beams. In the latter application, we adopted a control mechanism in which the intensity of one beam was monitored and used to modify the intensity of a second beam. In neither stage of the control was their recourse to the phase of the two light beams. This being the case, therefore, our noise control seems amenable to an alternative interpretation invoking a consideration only of the beam intensities and not of their amplitudes. This is the motivation for the remainder of this thesis. We present a model for intensity control based on an entirely different interpretation of photon noise, and based on simple photon counting arguments. Because this model does not fall under the domain of a semi-classical theory, it is included here as an appendix. We verify this model finally by Monte-Carlo computer simulation for simple cases.

### a: *Photon model*

We adopt a model in which a photon is considered as an event localized in time. Beams 1 and 2 are considered as streams of such events, with intensities

$$I_i = \sum_k \delta\left(t - t_{i,k}\right) \tag{a.1}$$

where $t_{i,k}$ is the event time of photon k in beam i. We will make no assumptions on the distributions of these event times, and $t_{i,k}$ need not be ordered in time. Note, as in chapter II, the intensity defined here has units of inverse time. To characterize the statistics of the beams we introduce the intensity auto-correlation function, defined as

$$C_i(\tau) = \frac{1}{\bar{I}_i}\left(\overline{I_i(t)I_i(t+\tau)} - \bar{I}_i^2\right) \tag{a.2}$$

and the cross-correlation function, defined as

$$C_{12}(\tau) = \frac{1}{\sqrt{\bar{I}_1\,\bar{I}_2}}\left(\overline{I_1(t)I_2(t+\tau)} - \bar{I}_1\,\bar{I}_2\right) \tag{a.3}$$

These are the same correlation functions as those defined in chapter II except that they are normalized to have units of intensity. If the photon arrival times within each beam are independent, that is, if the beam statistics are Poissonian, then $C_i(\tau)$ equals $\delta(\tau)$ [Rey90]. If

the photon arrival times in beam 1 are independent of the photon arrival times in beam 2, then $C_{12}(\tau)$ equals 0.

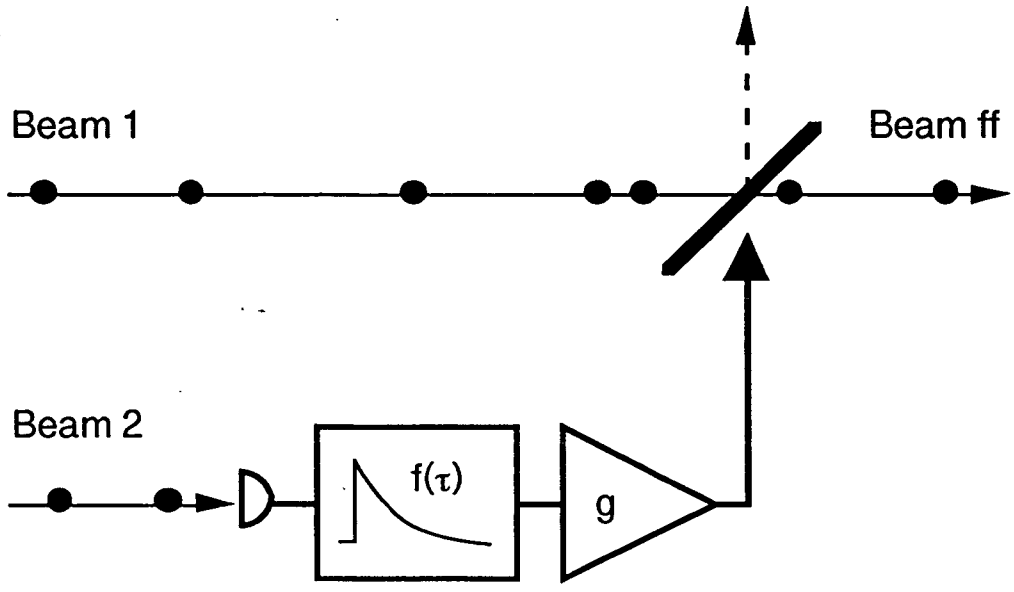


Figure a.1: Photon model of feedforward control. Intensity fluctuations in beam 2 are integrated over response filter $f(\tau)$ and amplified by gain g. Result is used to modify a modulator transmission in beam 1.

We consider the feedforward control mechanism shown above in fig. a.1 (the same as that considered in chapter VI). The intensity of beam 2 is monitored by a detector that integrates over a response filter $f(\tau)$. The difference between this monitored intensity (which is time dependent) and the average intensity (which is time independent) is used to adjust the transmission of an intensity modulator placed in beam 1, resulting in the controlled beam labeled ff in fig. a.1. Designating T(t) the transmission of the modulator as a function of time, this may be written as

$$T(t) = T_0 - \frac{g}{\bar{I}_2}\left(\int f(\tau) I_2(t-\tau)\,d\tau - \bar{I}_2\right) \qquad (a.4)$$

where $T_0$ (<1) is a transmission bias and g is a unitless gain factor. The term in parentheses is a measure of the intensity fluctuation in beam 2 at time t. We will assume this term is always small enough so that T(t) is never greater than 1 nor less than 0. The assumptions on $f(\tau)$ are only that it is causal and normalized, that is,

$$f(\tau < 0) = 0 \qquad \text{and} \qquad \int f(\tau)\,d\tau = 1\ . \qquad (a.5)$$

Photon k in beam 1 is either transmitted or reflected (lost) by the modulator at event time $t_{1,k}$. The instantaneous intensity of beam 1 after control can therefore be written

$$I_{ff}(t) = \sum_k \eta_k \, \delta(t - t_{1,k}) \tag{a.6}$$

where $\eta_k$ are independent stochastic variables equal to 0 or 1 with probability 1-$T(t_{1,k})$ or $T(t_{1,k})$ respectively.

We may calculate now the mean intensity of the controlled beam 1. This is

$$\bar{I}_{ff} = \overline{\sum_k \eta_k \, \delta(t - t_{1,k})} = \overline{\sum_k T(t_{1,k}) \, \delta(t - t_{1,k})} = \overline{\sum_k T(t) \, \delta(t - t_{1,k})} = \overline{T(t) \, I_1(t)}$$

$$= T_0 \, \bar{I}_1 - \frac{g}{\bar{I}_2} \int f(\tau) \, \overline{I_1(t) I_2(t-\tau)} \, d\tau + g \bar{I}_1 \tag{a.7}$$

We note that in the first line of the calculation T(t) becomes a function not of k but of time only, allowing it to be separated out from the summation. From eqtn. a.3, we may rewrite

$$\bar{I}_{ff} = T_0 \, \bar{I}_1 - g \sqrt{\frac{\bar{I}_1}{\bar{I}_2}} \int f(\tau) \, C_{12}(-\tau) \, d\tau \tag{a.8}$$

The first term on the right is the expected classical intensity reduction in beam 1 resulting from an average attenuation $T_0$. The second term on the right is a statistical correction term resulting from the twin beam correlations. When the mean intensity in beam 1 is much larger than the intensity fluctuations in beam 1 (as measured over the detection response $f(\tau)$ ), then we are in the semi-classical limit and the second term becomes negligible.

We now wish to evaluate the statistics of the controlled beam by calculating its auto-correlation function. Again, this is defined by

$$C_{ff}(\tau) = \frac{1}{\bar{I}_{ff}} \left( \overline{I_{ff}(t) I_{ff}(t+\tau)} - \bar{I}_{ff}^2 \right) \tag{a.9}$$

We must calculate for this

$$\overline{I_{ff}(t) I_{ff}(t+\tau)} = \overline{\sum_k \sum_{k'} \eta_k \, \eta_{k'} \, \delta(t - t_{1,k}) \, \delta(t + \tau - t_{1,k'})} \tag{a.10}$$

The above summation may be separated into a term where k = k' and a term where $k \neq k'$. The first term is

$$\sum_k \sum_{k'=k} \ldots = \overline{\sum_k \eta_k^2 \, \delta(t - t_{1,k}) \, \delta(\tau)} = \bar{I}_{ff} \, \delta(\tau) \tag{a.11}$$

where we have used the fact that $\eta_k^2 = \eta_k$.

Using the same procedure as used to obtain eqtn. a.7, the second term is

$$\sum_k \sum_{k' \neq k} \ldots = \overline{\sum_k \sum_{k' \neq k} T(t) \, T(t+\tau) \, \delta(t - t_{1,k}) \, \delta(t + \tau - t_{1,k'})} \tag{a.12}$$

The first term (a.11) arises from the auto-correlation of each photon with itself, resulting in an intensity noise equal to the shot noise level (see discussion in chapter II).The second term (a.12) arises from the auto-correlation of each photon with every other photon, resulting in deviations of the intensity noise from the shot noise level.

The second term may be rewritten as

$$\sum_{k}\sum_{k'\neq k}\ldots = \overline{T(t)\,I_1(t)\,T(t+\tau)\,I_1(t+\tau)} - \overline{T^2(t)\,I_1(t)}\,\delta(\tau) \qquad \text{(a.13)}$$

where we have written the right hand side of eqtn. a.12 as the summation when k and k' are independent minus the summation when k and k' are equal ($\delta(\tau)$ term).

Combining eqtns. a.11 and a.13, one arrives at

$$C_{ff}(\tau) = \frac{1}{\bar{I}_{ff}}\left(\overline{T(t)I_1(t)T(t+\tau)I_1(t+\tau)} - \overline{T(t)I_1(t)}^2\right) + \left[1 - \frac{1}{\bar{I}_{ff}}\overline{T^2(t)I_1(t)}\right]\delta(\tau) \qquad \text{(a.14)}$$

The term in parentheses is the "classical" result we would obtain if we were to consider $I_{ff}(t)$ simply as equal to $T(t)I_1(t)$. The term in brackets is a "quantum" correction term arising from the fact that events k=k' must be treated differently from events k≠k'. This quantum correction is a necessary consequence of our modelization of photons as discrete events.

Recalling that T(t) is a function of $I_2(t)$, we have effectively related here the photon statistics of the outgoing controlled beam to the photon statistics of the incoming non-controlled beams, which are presumably known. In this sense, our photon model becomes an input-output model. Our photon model differs however from the semi-classical model in that the outgoing beam statistics, characterized by an intensity correlation function to order 2, are related to incoming beam statistics characterized by intensity correlation functions to order 4 rather than only to order 2. This ensues from the fact that our photon model is non-linear whereas the semi-classical model is only linear in the intensity fluctuations.

If we restrict our photon model to the semi-classical limit in order to compare the two models, then the incoming beam statistics may be calculated by replacing $I_i(t)$ in eqtn. a.14 with the semi-classical intensity function

$$I_i(t) = \bar{I}_i + \delta I_i(t) \qquad \text{(a.15)}$$

where we assume $\delta I_i(t)$ is small compared to $\bar{I}_i$. We may write then

$$\begin{aligned}
\overline{I_{ff}} &= T_0\,\bar{I}_1 + O\left(\delta I^2\right) \\
\overline{T^2 I_1} &= T_0^2\,\bar{I}_1 + O\left(\delta I^2\right) \\
\delta(T I_1) &= T_0\,\delta I_1(t) - g\frac{\bar{I}_1}{\bar{I}_2}\int f(\tau)\,\delta I_2(t-\tau)\,d\tau + O\left(\delta I^2\right)
\end{aligned} \qquad \text{(a.16)}$$

where the terms of order $\delta I^2$ are neglected. Inserting the above relations into eqtn. a.14, we obtain

$$C_{ff}(\tau) = T_0 \left[ C_1(\tau) - \int G(\tau')[C_{12}(\tau - \tau') + C_{12}(-\tau - \tau')]\, d\tau' \right.$$
$$\left. + \int\int G(\tau')\, G(\tau'')\, C_2(\tau + \tau' - \tau'')\, d\tau'\, d\tau'' \right] + [1 - T_0]\, \delta(\tau) \qquad \text{(a.17)}$$

where we have made the substitution

$$G(\tau) = \frac{g}{T_0} \sqrt{\frac{\bar{I}_1}{\bar{I}_2}}\, f(\tau) \ . \qquad \text{(a.18)}$$

Again, eqtn. a.17 is the restriction of eqtn. a.14 to cumulants only of order 1 and 2. Cumulants of order 3 and 4 are neglected as small.

Converting to Fourier space, with the definitions

$$S_i(\Omega) = \text{F.T.}[C_i(\tau)] \ , \quad S_{12}(\Omega) = \text{F.T.}[C_{12}(\tau)] \ , \quad \text{and} \quad G(\Omega) = \text{F.T.}[G(\tau)] \qquad \text{(a.19)}$$

we obtain finally

$$\tilde{S}_{ff}(\Omega) = T_0 \left[ S_1(\Omega) - 2Re(G(\Omega) S_{12}(\Omega)) + |G(\Omega)|^2 S_2(\Omega) \right] + 1 - T_0 \qquad \text{(a.20)}$$

This result is obtained from the photon model in the semi classical limit. We observe that it is exactly the same as the result obtained from the semi-classical model (see eqtns. 6.3 and 6.31). In addition, we may note that the last term $1\text{-}T_0$ in $S_{ff}(\Omega)$ is attributed here to the quantum correction terms occasioned by the events k=k'. In the semi-classical model it was attributed instead to the vacuum fluctuations introduced into beam 1 through the unused port of the modulating beamsplitter.

**b:** ***Simulation algorithm***

We now describe a computer algorithm for a Monte-Carlo simulation of feedforward control. The algorithm is based on the photon model given above in which a photon is treated as a discrete event. A beam is simulated as a stream of such photons, and twin beams are simulated as streams of photon pairs. We discuss separately the algorithms for the generation of the twin streams, the control of stream 1, and the calculation of the resultant power spectrum of stream 1.

Twin stream generation:

Two separate statistics are involved in the generation of twin streams. The first are the statistics governing the generation of the photon pairs and the second are the statistics governing the decorrelation of the photon pairs. The first we characterize by a probability distribution $P(\tau_p)$ governing the delay times $\tau_p$ between successive photon pairs, assumed independent. The second we characterize by a probability distribution $D(\tau_d)$ governing supplementary decorrelation delay times for photons 1 and 2 in each photon pair, also

assumed independent. We note that $\tau_p$ and $\tau_d$ are always greater than 0. $D(\tau_d)$ is assumed the same for streams 1 and 2.

Denoting $t_{p,k}$ as the event time for the photon pair labeled k, the event times $t_{i,k}$ for the photons in streams 1 and 2 are generated from:

$$\begin{aligned} t_{p,k} &= t_{p,k-1} + \tau_p \\ t_{1,k} &= t_{p,k} + \tau_{1,d} \\ t_{2,k} &= t_{p,k} + \tau_{2,d} \end{aligned} \tag{a.21}$$

and are illustrated in fig. a.2.

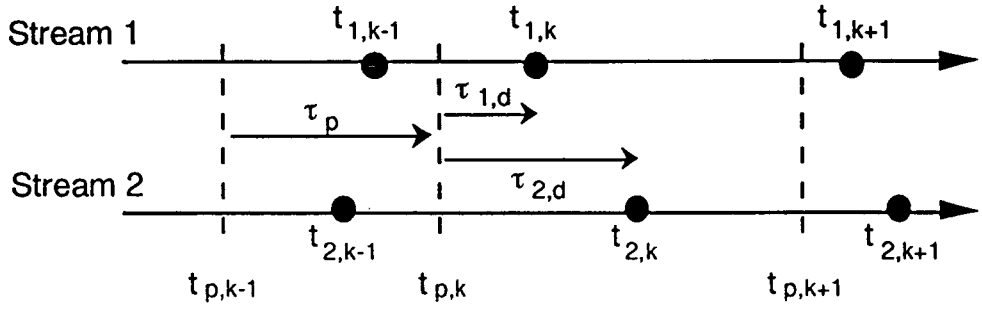


Figure a.2: $\tau_p$ is delay time between photon pairs (dashed lines are photon pair generation times). $\tau_{i,d}$ is supplementary individual photon delay.

The delays $\tau_p$ and $\tau_d$ are drawn for each photon pair using the method of uniform deviates [Pre86]. In this method, we define the functions

$$\tilde{P}(\tau) = \int_0^\tau P(t)\,dt \quad ; \quad \tilde{D}(\tau) = \int_0^\tau D(t)\,dt \tag{a.22}$$

The desired deviates $\tau_p$ and $\tau_d$ are generated according to

$$\tau_p = \tilde{P}^{-1}(u) \quad ; \quad \tau_d = \tilde{D}^{-1}(u) \tag{a.23}$$

where u is a system supplied deviate that is distributed uniformly between 0 and 1 ($P(t)$ and $D(t)$ are assumed normalized).

It is a easy matter in our simulation to introduce independent losses in each beam. For simplicity, however, we will neglect these losses.

Stream 1 control:

Once the twin photon streams are generated, we must decide for each photon k in stream 1 whether or not it is transmitted by the control mechanism. The control transmission coefficient depends at each time $t_{1,k}$ on the monitored intensity of stream 2. For the control mechanism to be causal, the monitored intensity can only depend on photons in stream 2 with event times $t_{2,k'}$ prior to $t_{1,k}$. The control mechanism is characterized by a response function $f(\tau)$ (assumed normalized -- see section above) such that the monitored intensity at time $t_{1,k}$ is equal to

$$I(t_{1,k}) = \sum_{\substack{k' \\ (t_{2,k'} < t_{1,k})}} f(t_{2,k'}) \qquad \text{(a.24)}$$

Once the monitored intensity is evaluated, we subtract from it the mean intensity of stream 2 (total number of photons divided by the total measurement time) to obtain a monitored intensity fluctuation. This is multiplied by a global control gain g and defines the transmission $T(t_{1,k})$ of the control mechanism, from which we draw whether or not photon (1,k) is transmitted. In the events that T is greater than 1 or less than 0, the photon is definitely transmitted or lost. These situations correspond to a saturation of the control mechanism. To compare our simulation results with our theoretical results (section A.a) we must select in our program a bias transmission $T_0$ so that these situations occur with only a negligible probability.

Power spectrum calculation:

By registering the event times of the transmitted photons in stream 1, a histogram can be made of the time delays between the transmitted photons. We note that a histogram of the time delays between only successive photons is insufficient here to characterize the statistics of the transmitted photon stream because the time delays between successive transmitted photons are no longer independent of one another. It is necessary therefore to construct a histogram of the time delays between *any* two photons in the transmitted stream. When the number of counted photons is large, this histogram approaches the auto-correlation distribution $C_{ff}(\tau)$.

After completion of the histogram $C_{ff}(\tau)$, the intensity power spectrum $S_{ff}(\Omega)$ is generated from the fast Fourier transform of $C_{ff}(\tau)$ [Pre86]. The frequency to which this spectrum is valid is one-half the inverse sampling time (channel width) of $C_{ff}(\tau)$. To avoid aliasing problems, however, we take the spectrum only to one-eighth the inverse sampling time.

The global flowchart for the above described algorithm is provided in fig. a.3.

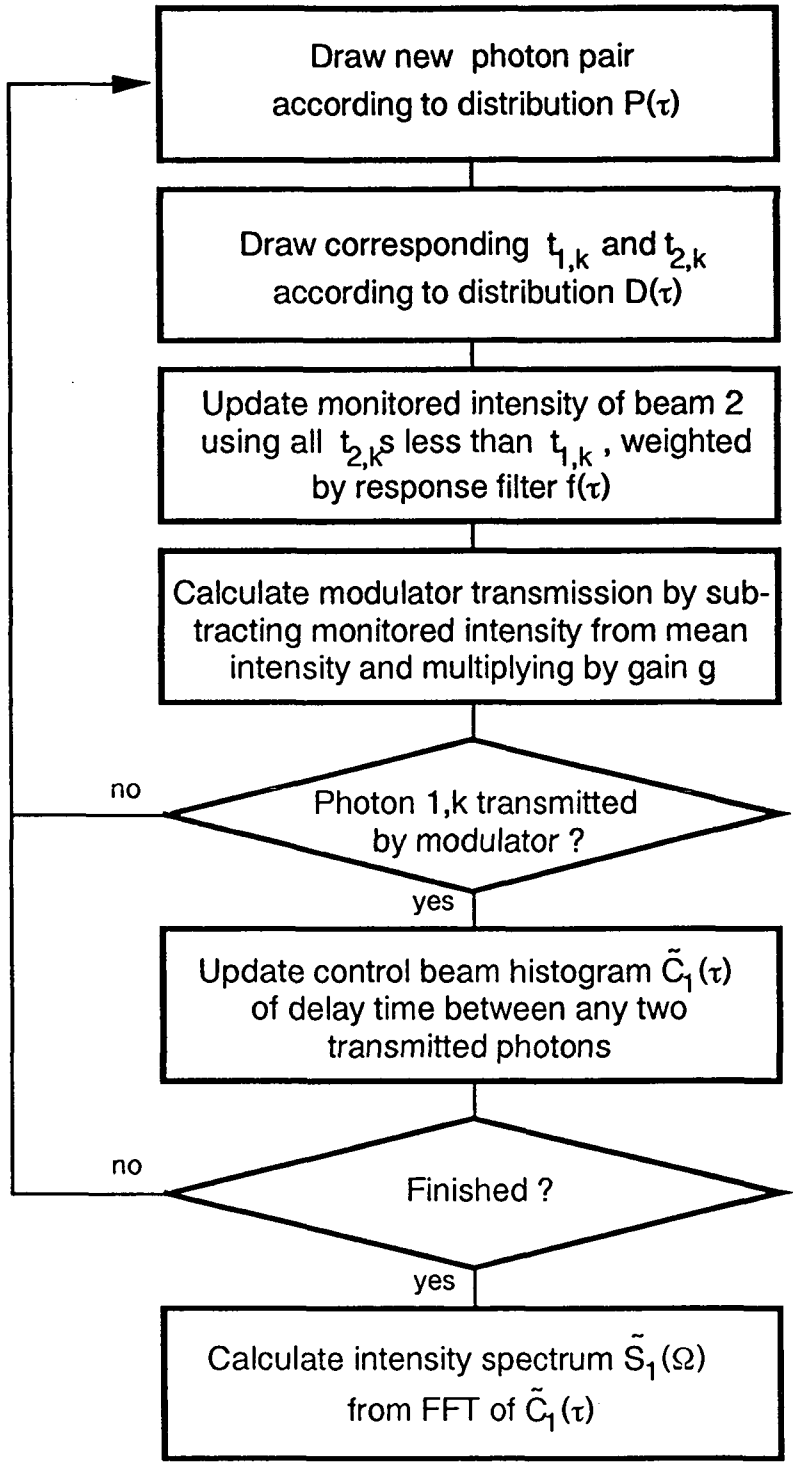


Figure a.3: Flow chart for computer simulation algorithm.

c: *Statistical parameters*

We wish to characterize the statistics of the incoming photon streams 1 and 2. These are balanced and have intensities:

$$I_i(t) = \sum_k \delta\left(t - t_{p,k} - t_{i,k}\right) . \tag{a.25}$$

The intensity average of each beam is $\bar{I} = \bar{\tau}_p^{-1}$ (equal to the inverse mean delay time between consecutive photons).

A calculation of the auto-correlation and cross-correlation functions can be made along the same lines as in section A.a, obtaining

$$C(\tau) = \delta(\tau) + \int d\tau_1 d\tau_2 \, D(\tau_1) D(\tau_2) \left[C_p(\tau + \tau_2 - \tau_1) - \delta(\tau + \tau_2 - \tau_1)\right] \tag{a.26}$$

$$C_{12}(\tau) = \int\int d\tau_1 d\tau_2 \, D(\tau_1) D(\tau_2) C_p(\tau + \tau_2 - \tau_1) \tag{a.27}$$

where we define $C_p(\tau)$ as the auto-correlation of the photon pair events. Again, the $\delta$-function terms in $C(\tau)$ correspond to the k=k' terms in our event summations.

We define $P(\Omega)$, $D(\Omega)$, and $S_p(\Omega)$ as the Fourier transforms of $P(\tau)$, $D(\tau)$, and $C_p(\tau)$. The power spectra associated with the above correlation functions become then:

$$S(\Omega) = 1 + |D(\Omega)|^2 \left(S_p(\Omega) - 1\right) \tag{a.28}$$

$$S_{12}(\Omega) = |D(\Omega)|^2 S_p(\Omega) \tag{a.29}$$

The photon pair power spectrum $S_p(\Omega)$ may be calculated from the photon pair delay spectrum $P(\Omega)$ using a simple relation which is valid when the time delays between successive photon pairs are independent [Rey90]. This is:

$$S_p(\Omega) = 1 + 2\,\mathrm{Re}\left[\frac{P(\Omega)}{1 - P(\Omega)}\right] - 2\pi \bar{I}^2 \delta(\Omega) . \tag{a.30}$$

Relating the computer simulated twin photon streams to the experimental example of twin beams generated by an OPO, the probability distribution $P(\tau_p)$ is associated with the down-conversion statistics in the parametric medium, and the probability distribution $D(\tau_d)$ is associated with the decorrelation statistics governed by the independent storage times of the twin beam photons in the optical cavity.

To our knowledge, the down-conversion statistics for an OPO operating above threshold have not been calculated. We will use in our program the statistics both of Poissonian light and of an example of super-Poissonian light. The first mimics an OPO much above threshold ($\sigma$=2). The second mimics an OPO slightly above threshold. We list

for these the delay time probability distribution $P(\tau)$, the uniform deviate inverse function $\tilde{P}^{-1}(u)$, and the corresponding normalized photon pair power spectrum $S_p(\Omega)$ [AS72]:

| | $P(\tau)$ | $\tilde{P}^{-1}(u)$ | $S_p(\Omega)$ |
|---|---|---|---|
| Poisson: | $\frac{1}{\bar{\tau}_p}\exp\left(-\tau/\bar{\tau}_p\right)$ | $-\bar{\tau}_p \ln(u)$ | 1 |
| >Poisson: | $\frac{1}{\sqrt{2\pi\tau\bar{\tau}_p}}\exp\left(-\tau/2\bar{\tau}_p\right)$ | $-2\bar{\tau}_p \ln(u_1)\sin^2(2\pi u_2)$ | $\frac{\lambda-1}{1+\lambda-\sqrt{2(1+\lambda)}}$ |

where $\lambda = |P(\Omega)|^{-1} = \sqrt{1+4\Omega^2\bar{\tau}_p^2}$ for the super-Poissonian statistics. Again, $\tau$ is restricted above to positive values.

For twin beams generated as photon pairs inside an optical cavity, the corresponding intensity difference spectrum $S_{1-2}(\Omega)$ outside the cavity has been calculated in reference [Rey87a]. This takes the profile of a series of Airy dips below the shot noise level.The separation between dips is equal to the cavity free spectral range. The width of the dips is equal to the cavity bandwidth $\bar{\tau}_d^{-1}$. We will only be concerned with the Airy dip around zero noise frequency. When the cavity is high finesse, as is the case in our experiment, the Airy profile tends towards a Lorentzian profile. We list the decorrelation time probability distribution $D(\tau)$, the uniform deviate inverse function $\tilde{D}^{-1}(u)$, and the corresponding normalized intensity difference noise spectrum $S_{1-2}(\Omega)$.

| | $D(\tau)$ | $\tilde{D}^{-1}(u)$ | $S_{1-2}(\Omega)$ |
|---|---|---|---|
| Correlation: | $\frac{1}{\bar{\tau}_d}\exp\left(-\tau/\bar{\tau}_d\right)$ | $-\bar{\tau}_d \ln(u)$ | $1-1/\left(1+\Omega^2\bar{\tau}_d^2\right)$ |

We remind the reader that we have neglected losses in the twin beams before the control. For this reason, $S_{1-2}(0)=0$.

Our model for the feedforward control response is a causal low pass filter with decay time $\tau_f$ ($\Omega_{3dB} = \tau_f^{-1}$):

$$f(\tau) = \begin{cases} 0 & \tau < 0 \\ \frac{1}{\tau_f}\exp(-\tau/\tau_f) & \tau > 0 \end{cases}$$

This response function is much simpler than the one used in experiment, and its effects will be more easily interpretable.

Finally, we include in our program the eventuality of a global time delay between beams 1 and 2, which we denote as $\tau_t$. In our numerical simulation this entails the simple addition of $\tau_t$ to every $t_{2,k}$. In our theoretical model it entails the simple multiplication of $S_{12}(\Omega)$ by $\exp(-i\Omega\tau_t)$.

Referring to eqtns. 6.3 and 6.31 or to eqtn. a.20, the above parameters may be used to predict the power spectrum of beam 1 after control, in the small fluctuation limit. We will compare this theoretical result from both our semi-classical and photon models to the Monte-Carlo results obtained by computer simulation.

**d:** ***Results***

We present the results of our numerical simulation. To ensure that we are in the semi-classical limit, the fluctuations $\delta n$ in the number of photons counted over the characteristic measuring time $\tau_f$ of the monitor detector must be small compared to the average number $\bar{n}$ of photons counted over the same time. In our simulation below, the intensity of photon stream 2 is monitored by counting over times containing an average of 20 photons ( $\bar{n} = \tau_f/\bar{\tau}_p = 20$ ). For Poissonian statistics, this corresponds to fluctuations about this count average on the order of $\delta n/\bar{n} = 20\%$. For a control gain equal to 1, we expect therefore $\delta T/\bar{T}$ to be on the order of 20% as well ($\delta T$ are the fluctuations in the control transmission, and $\bar{T}$ is the average control transmission). In the semi-classical limit $\bar{T}$ is approximately equal to the bias transmission $T_0$. To avoid large amounts of control saturation while maintaining the loss incurred in photon stream 1 to a minimum, we set in our simulation $T_0$ equal to 0.8.

In the results we present below the unit of frequency is $\tau_f^{-1}/2$, corresponding to the half-bandwidth of the monitor detector. The twin streams either remain perfectly correlated ($S_{1\text{-}2}(\Omega) = 0$) or are subject to a decorrelation with $\bar{\tau}_d = 2.5\ \tau_f$. The control gain $g/T_0$ is equal to 1. This is not necessarily the optimal control gain but will be chosen for purposes of comparison between the photon model and the semiclassical model. The total number of counted photons is equal to $10^6$. Because we are only approximately in the semi-classical limit, slight quantum effects may appear in the noise control. For example, the intensity of photon stream 1 after control typically ranges between 15.1 and 15.9 rather than being equal to the expected 16 (see eqtn. a.8).

In fig. a.4, the results are shown for the case of Poissonian photon pair statistics. Curve (a) represents the power spectrum of photon stream 1 before control. As expected, this is flat in frequency and equal to 1, by definition. Curve (b) represents the power spectrum of photon stream 1 with no decorrelation and after control. Ideally this should be flat and equal to 0.2, allowing for the bias losses in the control transmission. Because of the detector response time, however, the control is effective only at frequencies below the detector half-bandwidth. The detector obeys the response of a low-pass filter and the profile of the noise reduction is correspondingly Lorentzian. Curve (c) represents the power spectrum of photon stream 1 with decorrelation and after control. The decorrelation bandwidth is smaller here than the detection bandwidth and results therefore in a sharper degradation of the noise control. At low frequencies the noise in photon stream 1 is effectively reduced by the control mechanism, but at higher frequencies it becomes

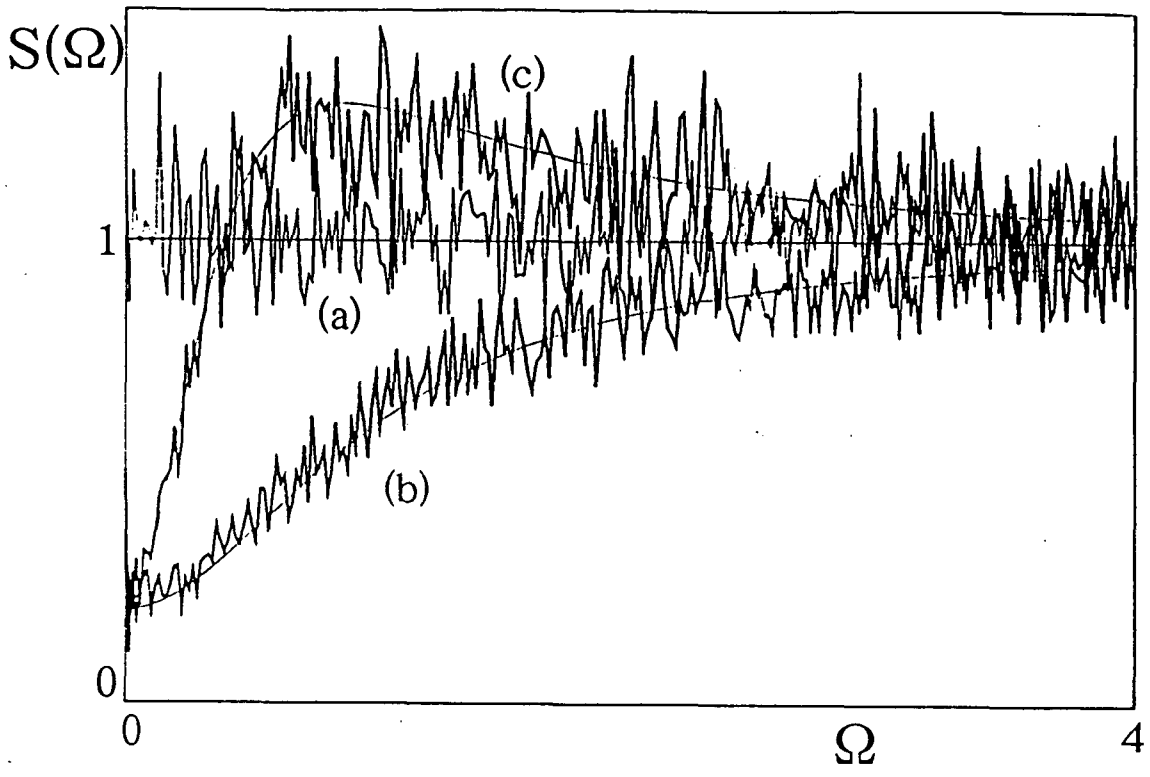


Figure a.4: Power spectrum of photon stream 1 before control (a), without decorrelation and after control (b), and with decorrelation and after control (c). Photon pair statistics are Poissonian.

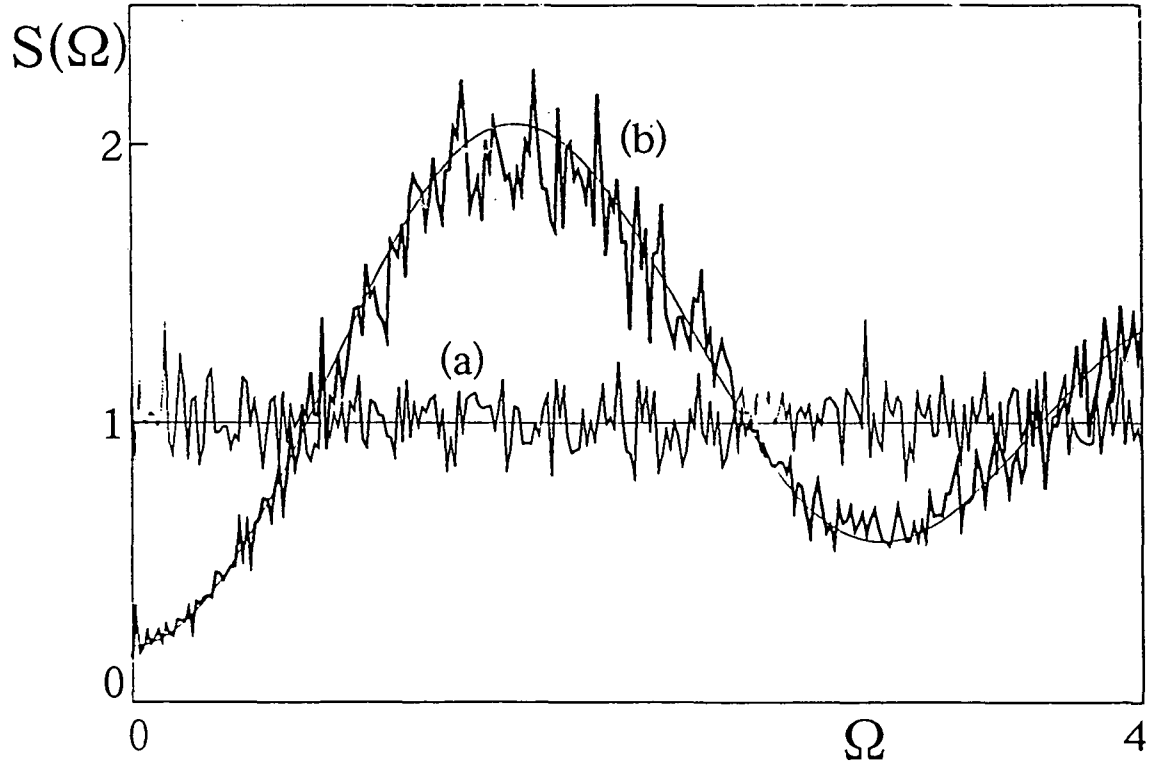


Figure a.5: Power spectrum of photon stream 1 before control (a), and after control with time delay (b). Photon pair statistics are Poissonian.

increased. The numerical results presented in curves (a), (b), and (c) are overlayed with the theoretical results obtained from eqtn. a.20. The results are observed to well agree.

In fig. a.5, the results are again shown for the case of Poissonian photon pair statistics. Photon streams 1 and 2 are perfectly correlated and photon stream 2 is subject to a global time delay $\tau_t = 2.5\ \tau_f$ with respect to photon stream 1. Curve (a) represents again the power spectrum before control. Curve (b) represents the power spectrum after control. The oscillation observed in curve (b) is characteristic of control with a time delay. The damping in this oscillation is the consequence of the finite detection bandwidth. We note that the effects of noise control extend here to higher frequencies than they do in curve (b) of fig. a.4. This may appear surprising but follows from the fact that the phase shift in the control due to the detection filter is compensated at certain frequencies by the phase shift due to the time delay, allowing the control to be more effective than before at those frequencies. Again, the numerical results compare well with the theoretical results.

In fig. a.6, the results are shown for the case of super-Poissonian photon pair statistics. Photon streams 1 and 2 are perfectly correlated. Curve (a) represents the power spectrum of photon stream 1 before control. Unfortunately, the statistics used in this simulation are such that the power spectrum remains essentially featureless over the displayed frequencies. Curve (b) represents the power spectrum of photon stream 1 after control. A slight discrepancy occurs at low frequencies between the numerical result and the theoretical result. This is attributable to control saturation, which is more important in the case of super-Poissonian statistics than in the case of Poissonian statistics (see transmission histograms below).

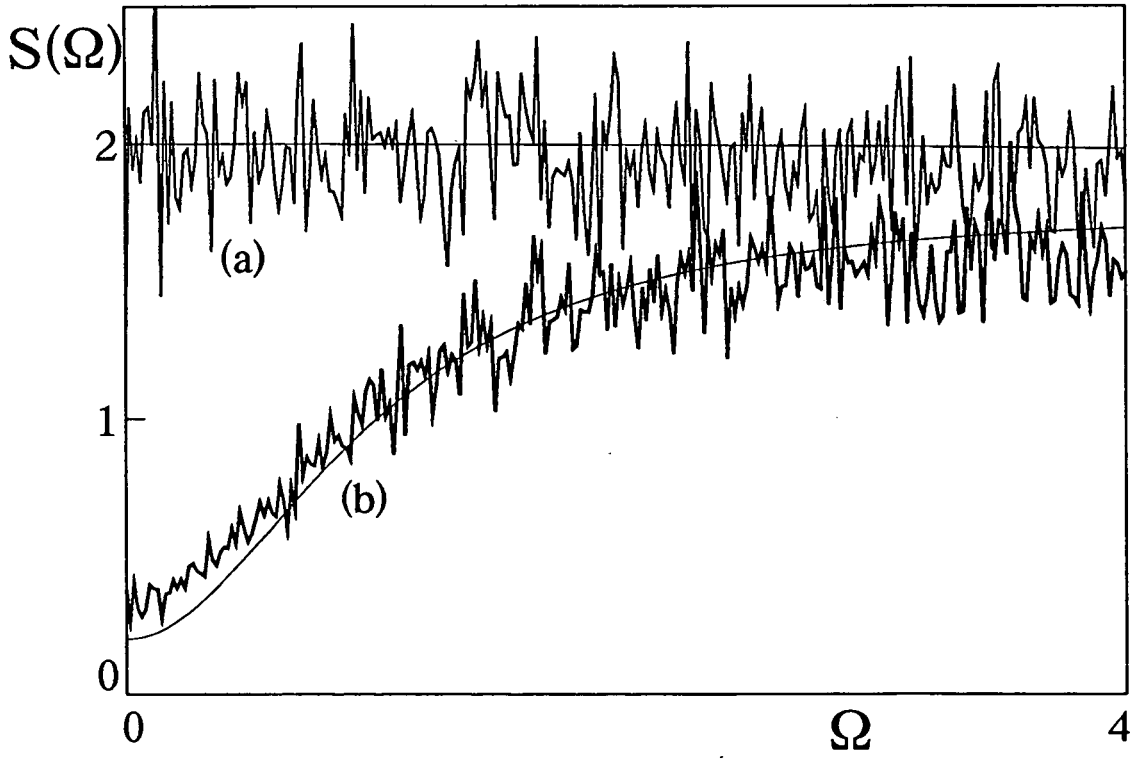


Figure a.6: Power spectrum of photon stream 1 before control (a), and without decorrelation and after control (b). Photon pair statistics are super-Poissonian.

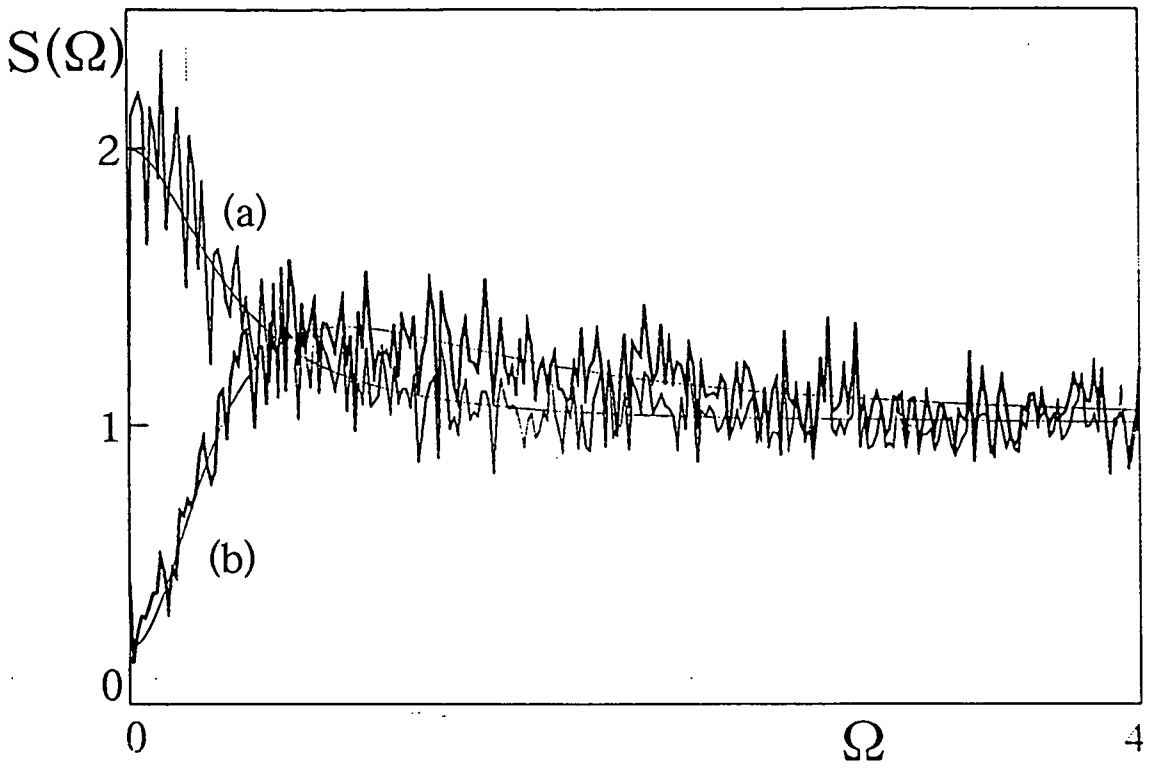


Figure a.7: Power spectrum of photon stream 1 before control (a), and after decorrelation and after control (b). Photon pair statistics are super-Poissonian.

In fig. a.7, the results are again shown for the case of super-Poissonian photon pair statistics. The photon streams are decorrelated this time, causing the photon statistics to revert to Poissonian statistics over small time scales (see eqtn. a.28). The simulation here is perhaps the closest to the actual experiment since it somewhat corresponds to photon pair generation in an OPO near threshold. Curve (a) represents the power spectrum of photon stream 1 before control. Curve (b) represents the power spectrum of photon stream 1 after control. The latter result differs in form of course from the actual experimental results because of the simplification in our model of the control gain response.

We present finally in fig. a.8 the histograms of the control transmissions for the cases when the photon streams are (a) Poissonian and (b) super-Poissonian (no decorrelation). Although the probability of control saturation is negligible in curve (a), it is less negligible in curve (b), resulting in the aforementioned discrepancies in the controlled stream power spectra at low frequencies. For larger values of $\bar{n}$ (average number of photons in detection time), the probabilities of control saturation diminish as do these discrepancies.

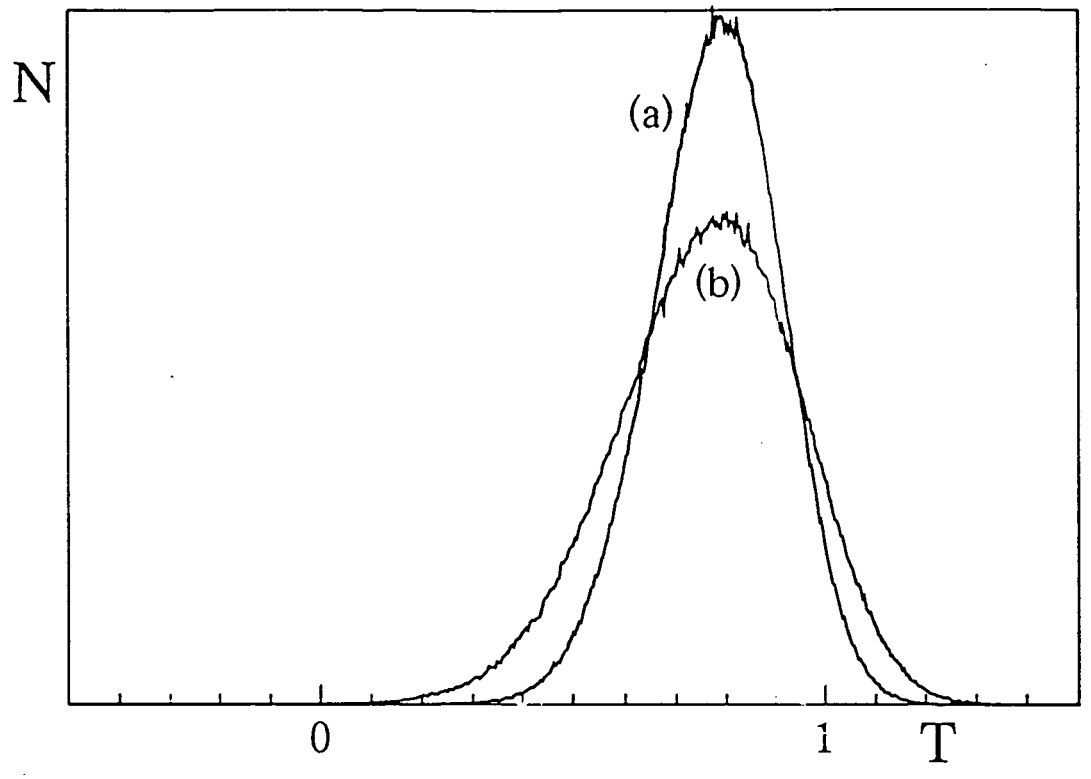


Figure a.8: Histogram of control transmission for Poissonian (a), and super-Poissonian (b) photon statistics (no decorrelation).

In conclusion, the essential result to be gathered from this appendix is the equivalence of the photon model in the semi-classical limit with the semi-classical model. This result is noteworthy insofar as the two models are based on entirely different interpretations of quantum noise. The photon model presents the advantage over the semi-classical model that it is not constrained to the semi-classical limit. In this way, it affords a more exact description of quantum noise. For example, it applies as well in the high intensity limit as in the low intensity limit. The photon model is constrained however to systems in which the phase of the photons do not intervene, and is therefore more limited in scope than the semi-classical model. For example, a description of the OPO when operating off resonance, that is, when the intensities and phases of the twin beams are coupled, would be impossible in the photon model. These differences notwithstanding, the two models complement one another and offer greater insight into the problem of noise control in optics.

# REFERENCES


[Abr87] I. Abram, R.K. Raj, J.L. Oudar, G. Dolique, Phys. Rev. Lett. **57**, 2516 (1987).

[AS72] M. Abramowitz, I.A. Stegun, *Handbook of Mathematical Functions*, (Dover 1972).

[Ayt90] O. Aytur, P. Kumar, Phys. Rev. Lett. **65**, 1551 (1990).

[Bjö88] G. Björk, Y. Yamamoto, Phys. Rev. **A37**, 125 (1988).

[Bru77] W. Brunner, H. Paul, "Theory of Optical Parametric Amplification and Oscillation", Progress in Optics XV. E. Wolf ed., (North Holland 1977).

[Bur70] D.C. Burnham, D.L. Weinberg, Phys. Rev. Lett. **58**, 2539 (1970).

[Cap86] F. Capasso, M. Teich, Phys. Rev. Lett. **57**, 1417 (1986).

[Cav89] C.M. Caves, in *Squeezed and Nonclassical Light*, P. Tombesi, E.R. Pike, eds., NATO ASI Series B190, (Plenum 1989).

[Cou91] J.Y. Courtois, A. Smith, C. Fabre, S. Reynaud, J. Modern Optics **38**, 177 (1991).

[Deb89] T. Debuisschert, S. Reynaud, A. Heidmann, E. Giacobino, C. Fabre, Quantum Opt. **1**, 3 (1989).

[Deb90] T. Debuisschert "Réduction des Fluctuations Quantiques de la Lumière à l'Aide d'un Oscillateur Parametrique Optique", Thesis Dissertation (Université Pierre et Marie Curie, Sept. 90).

[DiS67] J.J. DiStefano, A.R. Stubberud, I.J. Williams, *Theory and Problems of Feedback and Control Systems* (McGraw-Hill 1967).

[Dru81] P.D. Drummond, K.J. McNeil, D.F. Walls, Opt. Acta **28**, 211 (1981).

[Eke90] A.K. Ekert, P.L. Knight, Phys. Rev. **A42**, 487 (1990).

[Fab86] C. Fabre, E. Giacobino, S. Reynaud, T. Debuisshert, in *European Conference on Optics, Optical Systems and Applications*, SPIE Vol. 701, p. 488 (Florence, 1986).

[Fab89] C. Fabre, E. Giacobino, A. Heidmann, S. Reynaud, J. de Physique **50**, 1209 (1989).

[Fab90] C. Fabre, S. Reynaud, in *Fundamental Systems in Quatum Optics,* Les Houches Session 53, J. Dalibard, J.M. Raimond, J. Zinn-Justin eds. (Elsevier Science 1991).

[Fab90a] C. Fabre, E. Giacobino, A. Heidmann, L. Lugiato, S. Reynaud, M. Vadacchino, W. Kaige, Quantum Opt. **2**, 159 (1990).

[Fri84] S. Friberg, C.K. Hong, L. Mandel, Phys. Rev. Lett. **54**, 2011 (1984).

[Gia88] E. Giacobino, C. Fabre, S. Reynaud, A. Heidmann, R. Horowicz in *Photons and Quantum Fluctuations*, p. 81, E. Pike, H. Walther eds, Adam Hilger (Bristol 1988).

[Gib85] H.M. Gibbs, *Optical Bistability: Controlling Light with Light,* Academic Press (1985).

[Gil71] J.Ch. Gille, P. Decaulne, M. Pelegrin, *Théorie et Calcul des Asservissements Linéaires* (Dunod 1971)

[Gla65] R.J. Glauber, in *Quantum Optics and Electronics*, DeWitt, Blankin, Cohen-Tannoudji eds. (Gordon and Breach, 1965)

[Gra84] R. Graham, Phys. Rev. Lett. **59**, 1903 (1984).

[Gran86] P. Grangier, G. Roger, A. Aspect, Europhys. Lett. **1**, 173 (1986).

[Gran91] P. Grangier, J.F. Roch, Opt. Commun. **83**, 269 (1991).

[Han74] R. Hanbury Brown, *The intensity interferometer*, Taylor and Francis, London (1974).

[Hän80] T. Hänsch, B. Couillaud, Opt. Commun. **35**, 441 (1980).

[Haus86] H. Haus, Y. Yamamoto, Phys. Rev. **A34**, 270 (1986).

[Hei87] A. Heidmann, R. Horowicz, S. Reynaud, E. Giacobino, C. Fabre, G. Camy, Phys. Rev. Lett. **59**, 2555 (1987).

[Hong86] C. Hong, L. Mandel, Phys. Rev. Lett. **56**, 58 (1986).

[Hor80] P. Horowitz, W. Hill, *The Art of Electronics* (Cambridge University Press 1980)

[Jak85] E. Jakeman, J. Walker, Opt. Commun. **55**, 219 (1985).

[Kim86] H.J. Kimble, J.L. Hall in *International Conference on Quantum Optics*, Hamilton (New Zealand), J. Harvey, D. Walls, eds. (Springer Verlag 1986).

[LaP89] A. LaPorta, R.E. Slusher, B. Yurke, Phys. Rev. Lett. **62**, 28 (1989).

[Leo90] K. Leong, N. Wong, J. Shapiro, Opt. Lett. **15**, 1058 (1990).

[Lev86] M.B. Levenson, R.M. Shelby, M. Reid, D.F. Walls, Phys. Rev. Lett. **57**, 2473 (1986).

[Lou83] R. Loudon, *The Quantum Theory of Light*, Oxford University Press (1983).

[Mac86] S. Machida, Y. Yamamoto, Optics Commun. 57, 290 (1986).

[Mac87] S. Machida, Y. Yamamoto, Y. Itaya, Phys. Rev. Lett. **58**, 1000 (1987).

[Mac89] S. Machida, Y. Yamamoto, Opt. Lett. **14**, 1045 (1989).

[Nab90] C. Nabors, R. Shelby, Phys. Rev. **A42**, 556 (1990).

[Pap81] A. Papoulis, Probability, *Random Variables and Stochastic Processes*, McGraw Hill (Tokyo, 1981).

[Pre86] W.H. Press, B.P. Flannery, S.A. Teukolsky, W.T. Vetterling, *Numerical Recipes: The Art of Scientific Computing*, (Cambridge Univ. Press 1986).

[Rar87] J. Rarity, P. Tapster, E. Jakeman, Opt. Commun. **62**, 301 (1987).

[Rar90] J.G. Rarity, P.R. Tapster, in *International Conference on Quantum Electronics*, Vol. 8, p. 8 of 1990 OSA Technical Digest Series (Optical Society of America, Washington, D.C., 1990).

[Rey87] S. Reynaud, C. Fabre, E. Giacobino, J. Opt. Soc. Am. **B4**, 1520 (1987).

[Rey87a] S. Reynaud, Europhys. Lett. **4**, 427 (1987).

[Rey89] S. Reynaud, A. Heidmann, Optics. Commun. **71**, 209 (1989).

[Rey90] S. Reynaud, Annales de Physique **15**, 63 (1990).

[Ric90] W.H. Richardson, R.M. Shelby, Phys. Rev. Lett. **64**, 400 (1990).

[Ric91] W.H. Richardson, S. Machida, Y. Yamamoto, Phys. Rev. Lett. **66**, 2867 (1991).

[Sal85] B. Saleh, M. Teich, Opt. Commun. **52**, 429 (1985).

[Sha87] J. Shapiro, G. Saplakoglu, S.T. Ho, P. Kumar, B. Saleh, M. Teich, J. Opt. Soc. Am. **B4**, 1604 (1987).

[Shen84] Y.R. Shen, *The Principles of Nonlinear Optics,* Wiley-Interscience (1984).

[Slu85] R.E. Slusher, L.W. Hollberg, B. Yurke, J. Mertz, J.F. Valley, Phys. Rev. Lett. **55**, 2409 (1985).

[Sny90] J.J. Snyder, E. Giacobino, C. Fabre, A. Heidmann, M. Ducloy, J. Opt. Soc. Am. **B7**, 2132 (1990).

[Sque87] For review on Squeezed Light, see papers in special issues J. Opt. Soc. Am. **B4**, 10 (1987); J. Mod. Opt. **36**, 6/7 (1987).

[Sto86] D. Stoler, B. Yurke, Phys. Rev. **A34**, 3143 (1986).

[Tap87] P.R. Tapster, J.G. Rarity, J.S. Satchell, Europhys. Lett. **4**, 293 (1987).

[Tap88] P. Tapster, J. Rarity, J. Satchell, Phys. Rev. A37, 2963 (1988).

[Tei85] M.C. Teich, B.E.A. Saleh, J. Opt. Soc. Am. B2, 275 (1985).

[Toll56] J. Toll, Phys. Rev. **104**, 1760 (1956).

[Wal85] J. Walker, E. Jakeman, Opt. Acta 32, 1303 (1985).

[Wal85a] J.G. Walker, E. Jakeman, Proc. Soc. Photo-Opt. Instrum. Eng.**492**, 274 (1985).

[Val89] M. Vallet, M. Pinard, G. Grynberg, Europhys. Lett. **11**, 739 (1989).

[VanK81] N.G. Van Kampen, *Stochastic Processes in Physics and Chemistry*, (North Holland 1981).

[Wong90] N.C. Wong, K.W. Leong, J.H. Shapiro, Opt. Lett. **15**, 891 (1990).

[Wu86] L.A. Wu, H.J. Kimble, J.L. Hall, H. Wu, Phys. Rev. Lett. **57**, 2520 (1986).

[Yam86] Y. Yamamoto, N. Imoto, S. Machida, Phys. Rev. **A33**, 3243 (1986).

[Yar71] A. Yariv, *Introduction to Optical Electronics*, 2nd ed. (Holt, Rinehart, and Winston 1971).

[Yuen86] H. Yuen, Phys. Rev. Lett. **56**, 2176 (1986).

[Yur84] B. Yurke, J. Denker, Phys. Rev. **A29**, 1419 (1984).

**photon noise reduction using active control on twin beams generated by an optical parametric oscillator**

## ABSTRACT

We present two experiment that demonstrate intensity noise reduction in light below the standard quantum noise level. A first experiment establishes a reduction of 86 % in the intensity difference noise spectrum of twin beams generated by an Optical Parametric Oscillator. The second experiment exploits this intensity correlation between the twin beams and uses one beam to electro-optically control the other, generating a single beam whose intensity noise is reduced 24 % below the shot noise level. General theories are presented for both processes using a semi-classical input-output formalism. Control configurations are examined where the noise reduction is effected directly from one beam to the other (feedforward), or indirectly through the pump beam (feedback). We determine the maximum amount of noise reduction that may be obtained from active control and detail for these configurations the limitations imposed by constraints of causality and stability. Finally, we demonstrate the equivalence of the semi-classical model with a "corpuscular" photon model in the small fluctuation limit, which we substantiate using Monte-Carlo simulation.

**Réduction du bruit de photon à l'aide d'un asservissement sur des faisceaux produits par un oscillateur paramétrique optique**


## RESUME

*(Thèse en anglais)*

Nous présentons deux expériences qui mettent en évidence une réduction du bruit d'intensité de la lumière en dessous de la limite quantique normale. Dans la première expérience, nous avons mettons en évidence une réduction de 86 % dans le bruit mesuré sur la différence entre les intensités des deux faisceaux "jumeaux" produits par un Oscillateur Paramétrique Optique. Dans la seconde expérience, nous exploitons cette corrélation d'intensité entre les faisceaux jumeaux : la mesure de l'intensité d'un des faisceaux jumeaux est utilisée pour réduire les fluctuations d'intensité de l'autre faisceau par une méthode de correction électro-optique. Nous avons ainsi obtenu un seul faisceau dont le bruit d'intensité est réduit de 24 % en dessous du bruit quantique normal, ou bruit de grenaille. Nous présentons en outre une analyse théorique générale pour les deux expériences, en faisant appel à un modèle semi-classique de type entrée-sortie : sont étudiées successivement des configurations dans lesquelles la correction est appliquée directement sur l'autre faisceau (correction en aval), ou indirectement sur le laser de pompe (correction en amont). Nous calculons la réduction de bruit maximale qui peut être obtenue par de tels systèmes d'asservissement et détaillons les limites imposées par les contraintes de causalité et de stabilité. Pour terminer, nous démontrons l'équivalence, dans la limite des petites fluctuations, entre le modèle semiclassique et un modèle "corpusculaire" de description des photons. Une simulation numérique de type Monte-Carlo corrobore ce résultat.



**Mots clés**

Bruit quantique de la lumière
Compression de fluctuations quantiques
Oscillateur Paramétrique Optique
Méthodes d'asservissement électronique